An Electrostatic Ion-guide and a High-resolution Thrust-stand for Characterization of Micro-propulsion Devices

PAR

Subha CHAKRABORTY

ÉCOLE POLYTECHNIQUE
FÉDÉRALE DE LAUSANNE

Suisse
2015

Content

Content

Content

Acknowledgement

The world is full of generous people, extending their arms whenever someone is in need. The journey of PhD is full of ups and downs and I could not have come this far without some people guiding all along the path, some even pulling me along and some giving me the strength to step forward.

No words are sufficient to express my gratitude to my advisor, Prof. Herbert Shea. He extended his continued support through thick and thin, bestowed his faith in me when even I was not sure of myself. Herb, I cannot thank you enough for your patience with me, your invaluable advice and time.

Dan, I am not sure where I would have been without your relentless efforts to guide and motivate me. Among many other things, your keen eye for details is what I aspire most to achieve. Çağlar, you had been an inspiration since the day I joined LMTS, and without your priceless inputs, I would have been lost. Myriam, you helped me on so many occasions in so many ways that 'thank you' is too little a word for your kindness.

My friends and colleagues, past and present, in LMTS and SAMLAB, I am lucky to have had the opportunity to work alongside you; your valuable inputs and expertise helped me a lot to improve my work. Simon, Malick, Peter, Antony, Amir, Currit, Loïc, Massoud, Charlie, Bartjan, thank you for your valuable time and efforts whenever I asked for your help. Marie, Melody and Lucie, thank you for your continuous support all through. My friends, near and far, you know I don't often express it, but you have always been a great support and a great source of encouragement.

My family, there hasn't been a single occasion in my life you hadn't supported me, and being able to count on you, no matter what, has been the one biggest gain in my life. Reema, if I could find contentment even in the midst of despair, it was because of you.

The thesis jury committee, Prof. Volker Gass, Prof. Paulo Lozano, Prof. Peter Wurz and the jury president, Prof. Giovanni Boero, thank you for accepting to review this work. Thank you for sacrificing your time and efforts to help me improve it.

Subha
Neuchatel, 11.06.2015

Abstract

Interest in microthrusters has grown significantly in the last two decades for possible applications in small satellites and deep space missions. This thesis is motivated by the need of experimental setup for characterization of microthrusters.

In the first part of the thesis, a time-of-flight (ToF) mass spectrometer with an electrostatic ion-guide has been developed for characterization of electrospray microthrusters that can focus all mono-energetic emitted charges within about 23° emission half-angle on a small detector placed at a distance nearly 60 times larger than the diameter of the detector. This helps time-of-flight analysis from a large fraction of the emission in real time. Experiments performed with externally wetted tungsten emitters have shown up to 80% charge collection from a nearly 15° half-angle in positive and negative polarities of emission. From capillary emitters with about 40° emission half-angle, nearly up to 30% of the emission has been collected for ToF measurement. Despite accommodation of large beam spread and increase in flight time, flight time measurement has been possible quite accurately.

In the second part of the thesis, a nano-Newton thrust stand has been developed that can measure thrust up to about 100 μN with a resolution of 10 nN from different types of microthrusters. The operating principle of the thrust stand is different from other nano-Newton thrust stands developed in the last few years and it works by measuring impingement force of the emitted particles on a suspended plate with a sensitive force sensor. The suspended plate possesses a natural frequency around 50 Hz, and, by a homodyne thrust measurement scheme, avoids coupling of facility vibrations with the measurement. The resolution is among the best reported so far from thrust stands that measure thrust directly on the thruster and the first of its type to demonstrate less than 3 μN resolution. The setup has been characterized with the help of a cold-gas ejecting capillary and an electrospray device. Experiments with cold-gas ejector have shown that thrusts can be resolved with 10 nN resolution and a minimum thrust of about 10 nN can be detected. Measurements up to 2−3 μN from the electrospray device has been demonstrated with the thrust stand and the results are within 50−150 nN from that obtained from indirect beam diagnostics.

Keywords: Electrospray, micro-thruster, time-of-flight mass spectrometer (ToF-MS), ion-guide, nano-Newton thrust stand, thrust, sputtering

Résumé

L'intérêt pour les micro-propulseurs a considérablement augmenté au cours des deux dernières décennies pour des applications possibles dans de petits satellites et des missions dans l'espace lointain. Cette thèse est motivée par la nécessité d'appareils d'expérimentation pour la caractérisation des micro-propulseurs.

Dans la première partie de la thèse, un 'Time-of-Flight mass spectromètre' (ToF-MS) avec un guide-ion électrostatique a été développé pour la caractérisation des electrospray micro-propulseurs qui peuvent concentrer toutes les accusations mono-énergétiques émises dans 23° demi-angle a la détecteur placé à une distance près de 60 fois plus grand que le diamètre du détecteur. En recueillant grande fraction du émission, les ToF-MS fournit un rendement élevé sur une petite détecteur, réduit l'exigence de gain de l'amplificateur de transimpédance, et permet la mesure du temps de vol à partir de la grande fraction de émission. Les expériences réalisées avec des mouillés extérieurement émetteurs de tungstène ont montré la collection de charge de jusqu'à 80% à partir d'un demi-angle d'émission 15°. A partir de émetteurs capillaires avec environ 40° demi-angle, près jusqu'à 30% de l'émission ont été recueillies pour la mesure ToF. Malgré logements de grande fraction du propagation du faisceau et l'augmentation du temps de vol, la mesure du temps de vol a été possible avec assez de précision.

Dans la deuxième partie de la thèse, un système de mesure de poussée nano-Newton a été développé qui permet de mesurer la poussée jusqu'à environ 100 μN à partir de différents micro-propulseurs. Le principe de fonctionnement du Système de mesure est différent des autres poussée nano-Newton Système de mesure de poussée développé au cours des dernières années et il fonctionne en mesurant la force d'impact des particules émises sur une plaque suspendue avec un capteur de force sensible. La plaque possède une fréquence naturelle autour de 50 Hz, et, par un mesure homodyne de poussée, évite couplage des vibrations de l'installation avec la mesure. Le système a été caractérisée à l'aide d'un capillaire éjection de gaz froid jusqu'à environ 50 μN poussée dans l'air et un électro-spray micro-propulseur jusqu'à environ 3 μN poussée à l'intérieur une chambre à vide. Des expériences avec l'éjecteur à gaz froid ont indiquées poussées peuvent être résolus avec une meilleure résolution de 10 nN et une poussée minimale d'environ 10 nN peut être détectée. La résolution obtenue est parmi les meilleurs signalé jusqu'ici et le premier de son genre à démontrer moins de 3 résolution μN. A l'intérieur de la chambre à vide, la poussée a démontré environ 10 nN noise-floor et une poussée minimum d'environ 50 nN a été mesurée à partir de l'appareil électro-spray. Les résultats sont dans 50−150 nN à partir de celle obtenue à partir des diagnostics de émission indirects.

Mots-clés: Electrospray, micro-propulseurs, Time-of-Flight mass spectromètre(ToF-MS), guide d'ions, système de mesure de poussée nano-Newton, sputtering.

List of Figures

Figures

Figures

List of Tables

Tables

List of Symbols

EMI-BF$_4$	1-Ethyl-3-methyl-imidazolium tetrafluoroborate
EMI-Tf$_2$N	1-Ethyl-3-methyl-imidazolium bis(trifluoromethylsulfonyl)imide
NaI	Sodium Iodide
Cs	Cesium
In	Indium
H$_2$SO$_4$	Sulfuric acid
HCl	Hydrochloric Acid
NaOH	Sodium Hydroxide
He	Helium
Xe	Xenon
Al	Aluminium
m	Mass
q	Charge
v_e	Emission speed
V_{em}	Emission voltage
g_0	Acceleration due to gravity
I_{sp}	Specific impulse
Th	Thrust
I	Current
T_F	Flight time
L	Distance between source and distance
e	Electronic charge (1.602×10^{-19} C)
$K.E.$	Kinetic energy
$L.M.$	Linear momentum
Δm	Spreading in measured mass m
ΔL	Spatial spreading
$\Delta(K.E.)$	Kinetic energy spreading
$\mathfrak{R}$	Mass resolution $m/\Delta m$ of a ToF-MS
w	Arbitrary parameter
t	Time
D_c	Diameter of a detector
$\dot{m}$	Mass flow rate
R	Radius of a detector
r	Radial distance from axis
r_0	Radius of electrodes in stacked ring ion-guide

Symbols

θ_{em}	Emission half-angle
θ_{max}	Half-angle up to which, all charges can be focused
V_{lens}	Deflecting potential applied to the ion-guide
n	Arbitrary integer
d_1	Diameter of the first stage deflecting electrode of the ion-guide
l_1	Length of the first stage deflecting electrode of the ion-guide
η	Charge collection efficiency
η_{max}	Maximum charge collection efficiency
$(K.E.)_1$	Kinetic energy before fragmentation
$(K.E.)_2$	Final kinetic energy after fragmentation and further acceleration
$m_{monomer}$	Mass of a monomer
M_{dimer}	Mass of a dimer
v_z	Instantaneous axial speed of a charge in the flight tube
v_0	Initial axial speed of a charge
z	Axial distance from the emitter
I_{em}	Emitter current
I_{ex}	Extractor current
I_{det}	Detected current
V_{im}	Potential at the point of fragmentation inside the emitter accelerating region
$(K.E.)_{im}$	Kinetic energy of a monomer immediately after fragmentation
I_{em}^{+}	Emitter current in positive polarity of emission
I_{em}^{-}	Emitter current in negative polarity of emission
IR_n	Inner radius of the nth annular detector in 19-annular beam-shape measurement setup
OR_n	Outer radius of the nth annular detector in 19-annular beam-shape measurement setup
I_n	Current detected by the nth plate
J_n	Average current density on the nth plate
R_n	Mean radius of the nth annular detector in 19-annular beam-shape measurement setup
θ_n	Mean angle subtended by the nth annular detector in 19-annular beam-shape measurement setup on the emitter tip
D_s	Spot diameter of an emitted plume
F_{res}	Force resolution
d_s	Diameter of an arbitrary circular plate
m_p	Proof-mass of an accelerometer
a_c	Acceleration
F	Impingement force
d_{min}	Minimum detectable displacement with a displacement sensor
z_p	Forward movement of the force sensor to push on the plate
k_p	Spring constant of the plate
F_{OFF}	Offset force on the force sensor
z_f	Deflection of the force sensor probe by pushing on the plate
k_f	Spring constant of the force sensor
z_F	Deflection of the force sensor under applied external force

F_{meas}	Force measured by the force sensor
z_{n}	Final deflection of the force sensor due to pushing and applied external force on the plate
F_{Δ}	Resolution of the force sensor
F_{max}	Maximum external force that can be measured with the force sensor
$F_{\text{s,max}}$	Force range of the force sensor
L_{p}	Length and width of the particle intercepting plate
f_{p}	Natural frequency of the plate
δ	Minimum incremental motion of the translation stage
σ	Electrical conductivity
k_{sp}	Spring constant of the spring section of the particle intercepting plate
k_{pl}	Spring constant of the plate section of the particle intercepting plate
E	Young modulus
ρ	Density
M_{pl}	Mass of the plate
h	Thickness
h_{max}	Maximum thickness
I_{pl}	Moment of inertia of the plate section
L_{s}	Length of the spring in the particle intercepting plate
b	Width of the spring in the particle intercepting plate
f_{trd2}	Torsional natural frequency of a dual-beam spring configuration
G	Shear modulus
K	A function of b/h defined in Eqn. (5.21)
f_{spd2}	Translational natural frequency of a dual-beam spring configuration
f_{d2}	Frequency of fundamental mode of a dual-beam spring configuration
L_{min}	Minimum length of spring
k_{spd2}	Spring constant of the dual-beam spring configuration
k_{spd4}	Spring constant of the quad-beam spring configuration
k_{pld2}	Spring constant of the plate section in dual-beam spring configuration
k_{pld4}	Spring constant of the plate section in quad-beam spring configuration
f_{spd2}	Translational natural frequency of the springs in dual-beam configuration
f_{spd4}	Translational natural frequency of the springs in quad-beam configuration
k_{d2}	Overall spring constant of the dual-beam plate configuration
k_{d4}	Overall spring constant of the quad-beam plate configuration
f_{d4}	Frequency of fundamental mode of a quad-beam spring configuration
$L_{\text{min\_d2}}$	Minimum length of the spring in dual-beam plate configuration
$L_{\text{min\_d4}}$	Minimum length of the spring in quad-beam plate configuration
Y	Yield strength
R_{i}	Radius of curvature at the bending junction before removal of punch
R_{f}	Radius of curvature at the bending junction after removal of punch
d_{i}	Inner diameter of an indent
b_{i}	Space left on both sides of the indent
I_{arm}	Moment of inertia of the arms of the frame
I_{fr}	Moment of inertia of the frame

Symbols

k_{fr}	Spring constant of the frame
dA	Elementary area
z_N	Position of the neutral axis from the bottom of the frame
M_{fr}	Mass of the frame
L_t	Length of a torsion beam
b_t	Width of a torsion beam
δM	Increase in mass of frame without epoxy
ΔM	Total increase in mass of frame with epoxy
y	Oscillatory deflection of the plate
B	Final deflection of the plate under step force input
A	Amplitude of undamped oscillation of the plate
γ	Damping ratio
Φ	Phase
P_{in}	Pressure set at the pressure controller
A_{cap}	Cross-sectional area of the capillary
P_{inlet}	Inlet pressure of the capillary
P_{outlet}	Outlet pressure of the capillary
ΔP	Pressure drop in the capillary
$\dot{m}$	Mass flow rate
v	Flow velocity at the outlet of the capillary
P_0	Absolute ambient pressure
M_{inlet}	Mach number at the inlet of the capillary
Q	Volume flow rate
R_h	Hydraulic impedance
ρ_0	Density of air in ambient condition
P	Local pressure inside the capillary
r_{cap}	Radius of the capillary
ρ	Local density of air inside the capillary
v_z	Axial local velocity inside the capillary
v_r	Radial local velocity inside the capillary
μ	Dynamic viscosity of air
$\lvert K \rvert$	Coefficient of restitution
V_Δ	Differential output voltage of the force sensor corresponding to applied force
S_F	Sensitivity of the force sensor (Force per unit output voltage)
V_{OFF}	Force sensor output voltage when the plate corresponding to offset force
V_{NL}	No-load voltage output of the force sensor
F_d	Differential force measured by the force sensor when a force is applied on the plate
V_P	Power supply voltage
F_{up}	Force sensor output when looking upward
F_{down}	Force sensor output when looking downward
f_{ref}	Reference frequency for AC mode of operation
t_1	An instant of time

F_1	Force sensor output at time instant t_1
t_2	An instant of time
F_2	Force sensor output at time instant t_2
F_{in}	Input force for the lock-in amplifier
G	Square wave switching signal
C_n	n^{th} coefficient of the Fourier transform of $G(t)$
j	$\sqrt{(-1)}$
Φ_{in}	Fourier transform of F_{in}
$\delta(w)$	Unit impulse function
S	Amplitude of a sinusoidal signal
φ	Phase difference between the sinusoidal reference signal and the switching square wave signal
F_{out}	Lock-in amplifier output in units of force
Φ_{out}	Fourier transform of F_{out}
T_c	Time constant of lock-in amplifier
$f_{3\text{-dB}}$	3-dB frequency of the low-pass filter of the lock-in amplifier
R_{out}	R.m.s. voltage output of lock-in amplifier
X_{out}	X output of the lock-in amplifier
Y_{out}	Y output of the lock-in amplifier
X	x position of the thruster relative to the centre of the plate
Y	y position of the thruster relative to the centre of the plate
Z	z position of the thruster relative to the centre of the plate
R_{p1}	Non-repeatability of thrust measurement with the same plate
R_{p2}	Non-repeatability of thrust measurement with different plate
R_p	Overall non-repeatability of thrust measurement
E_{r1}	Thrust error due to response time of the plate
E_{r2}	Maximum thrust error due to distance of the thruster from the plate
E_{r3}	Maximum thrust error due to lateral offset of the thruster from the centre of the plate
E_{r4}	Thrust error due to uncertainty in k_p and k_f
E_{r5}	Thrust error due to misalignment of the force sensor
E_{r6}	Uncertainty in the relation between thrust and impingement force
E_r	Overall estimated maximum error in thrust measurement
I_{beam}	Beam current
t_0	Flight time of a monomer
t_1	Flight time of a dimer
t_2	Flight time of a trimer
f_0	Current fraction corresponding to monomer
f_1	Current fraction corresponding to dimer
f_2	Current fraction corresponding to trimer
Th_m	Thrust associated with a particular emitted charge species
Th_{ToF}	Thrust measured from time-of-flight measurement
γ_0	Thrust correction factor from time-of-flight measurement
$Th_{monomer}$	Thrust due to monomers emitted along the axis of the emitter

Symbols

θ	Emission angle (variable between 0 to θ_{em})
A_p	Area of a current probe
R_p	Distance of the current probe from the emitter
p	Fraction of total current detected by a current probe
J	Current density at the centre of the current probe
β_0	Angular spread correction factor for thrust
Th_{indir}	Indirect thrust obtained from ToF measurement, beam spreading and beam current
I_{ex}	Extractor current
A_a	Area of the aperture in the grid assembly
V_{gate}	Gate voltage
V_S	Voltage applied to the electrode adjacent to the gate electrode
E_G	Normal electric field on the gate electrode
E_P	Normal electric field on the plate
L_{SP}	Distance between plate and the first grid
L_{GS}	Distance between the gate electrode and the first electrode at -40 V
l_g	Spacing between the wires in the grid
d_g	Diameter of the wires in the grid
s	A parameter defined in Eqn. (7.12)
u	A parameter defined in Eqn. (7.13)
ς	A parameter defined in Eqn. (7.14)
ε_0	Permittivity of free space
F_{gate}	Force due to V_{gate} and V_S on the plate
ΔF_{gate}	Differential force due to pulsating gate potential on the plate
ΔF_0	Differential force due to pulsating gate potential on the plate in absence of V_S grid
α_i	Transparency of the three-electrode gate assembly
$Th_{\alpha i}$	Estimated thrust from the measured impingement force
I_{plate}	Plate current
Th_{dir}	Directly measured thrust from the thrust stand incorporating momentum transfer from the impinging particles
$(K.E.)_{out}$	Kinetic energy per unit atom of the sputtered atoms
$(K.E.)_{in}$	Kinetic energy per impinging ion
$\dot{N}_m$	Number density distribution over mass of ion impinging per unit area per unit time
Y_m	Yield in atoms/ion
m_{Al}	Mass of an aluminium atom
$\dot{p}_+$	Momentum rate of impinging ions
$\dot{p}_-$	Momentum rate of sputtered atoms
I_m	Current corresponding to ions of particular mass
p_m	Current fraction corresponding to ions of particular mass at a particular angle
f	Angle independent current fraction corresponding to ions of particular mass
Y_{tot}	Cumulative yield over the entire sputtering area

List of Abbreviations

LMTS	Microsystems for Space Technologies Laboratory
EPFL	École Polytechnique Federale de Lausanne
LEO	Low Earth Orbit
ES	Electrospray
FEEP	Field Emission Electric Propulsion
NASA	National Aeronautics and Space Administration
ESA	European Space Agency
MIT	Massachusetts Institute of Technology
GSFC	Goddard Space Flight Centre
ESTEC	European Space Research and Technology Centre
ARCS	Austrian Research Centres Seibersdorf
ToF	Time-of-Flight
MS	Mass Spectrometer
ST-7	Space Technology 7
DRS	Disturbance Reduction System
PIR	Pure Ionic Regime
CMNT	Colloid Micro-Newton Thruster
PPU	Power Processing Unit
DCIU	Digital Control and Interface Unit
DRIE	Deep Reactive Ion Etching
SOI	Silicon on Insulator
QMUL	Queen Mary University, London
TNO	Toegepast Natuurwetenschappelijk Onderzoek (Netherlands Organisation for Applied Scientific Research)
EU	European Union
SEM	Scanning Electron Microscope
ESI	Electrospray Ionization
EI	Electron Impact
FWHM	Full Width at Half Maxima
RPA	Retarding Potential Analyzer/Analysis
MALDI	Matrix-assisted Laser Desorption/Ionization
EAN	Ethyl ammonium nitrate
MES	Multiplexed Electrospray
ILIS	Ionic Liquid Ion Source
OPAMP	Operational Amplifier
FTMS	Fourier Transform Mass Spectrometer
LVDT	Linear Voltage Differential Transformer

Abbreviations

MERTS	Micro-pound Extended Range Thrust Stand
PET	Pulsed Plasma Thruster
AFRL	Air Force Research Laboratory
JPL	Joint Propulsion Laboratory
nNTS	Nano-Newton Thrust Stand
USC	University of Southern California
LDS	Linear Displacement Sensor
IPS	Interferometric Proximeter System
EMI	Electromagnetic Interference
MLTB	Magnetically Levitated Thrust Balance
DOF	Degree of Freedom
iEPS	Ion Electrospray Propulsion System
MFMI	Momentum Flux Measuring Instrument
CEM	Channel Electron Multiplier
MCP	Micro-channel Plate
FIB	Focused Ion Beam
RF	Radio Frequency
PCB	Printed Circuit Board
TEM	Transmission Electron Microscopy
MEMS	Micro-electro-mechanical Systems
AFM	Atomic Force Microscopy
UHV	Ultra High Vacuum
FEM	Finite Element Method
PMMA	Poly(methyl methacrylate)
TTL	Transistor Transistor Logic
PLL	Phase Locked Loop
BJT	Bipolar Junction Transistor
TRIM	Transport of Ions in Matter
QCM	Quartz Crystal Microbalance
IMS	Ion mobility spectrometry

List of publications

Journal publications:

1) S. Chakraborty, C. Ataman, D. G. Courtney, S. Dandavino, H. Shea**,** "A ToF-MS with a Highly Efficient Electrostatic Ion Guide for Characterization of Ionic Liquid Electrospray Sources", *Journal of The American Society for Mass Spectrometry*, vol. 25, issue 8, pp. 1364–1373, 2014.

2) S. Dandavino, C. Ataman, C. Ryan, S. Chakraborty, D. G. Courtney, J. P. W. Stark and H..Shea, "Microfabricated electrospray emitter arrays with integrated extractor and accelerator electrodes for the propulsion of small spacecraft", *Journal of Micromechanics and Microengineering*, 24(7), 075011, 2014.

Conference proceedings:

1) S. Chakraborty, S. Dandavino, C. Ataman, D. G. Courtney and H. Shea, "Development of a ToF setup with an ion-guide for characterization of electrospray microthrusters", 33rd International Electric Propulsion Conference, Washington, D.C., USA, pp. 4–11, 2013.
   (**Sessions best paper award**)

2) S. Chakraborty, C. Ataman, S. Dandavino and H. Shea, "Microfabrication of an Electrospray Thruster for small spacecrafts", PowerMEMS 2012, Atlanta, GA, USA, pp. 528-531, 2012.

3) S. Dandavino, C. Ataman, S. Chakraborty, H. Shea, C. Ryan, and J. P. W. Stark, "Design and fabrication of the thruster heads for the MicroThrust MEMS electrospray propulsion system". 33rd International Electric Propulsion Conference, Washington, D.C., USA., pp. 1–8, 2013
   (**Sessions best paper award**)

4) S. Dandavino, C. Ataman, S. Chakraborty, H. Shea, C. Ryan and J. P. W. Stark, "Progress Towards a Miniaturized Electrospray Thruster for Propulsion of Small Spacecraft", 48th AIAA/ASME/SAE/ASEE Joint Propulsion Conference and Exhibit, Atlanta, USA, pp. 1–13, 2012.

1 Introduction

This thesis is motivated by the need of experimental setup for characterization of microthrusters. The contribution of the thesis can be divided in two parts. The first part, comprising of Chapter 3 and Chapter 4 reports on development of a high throughput ion-guide for time-of-flight mass spectrometers that helps to measure the composition of emission from a particular type of micro-thruster, the electrospray thruster, by collecting a large fraction of the emission on a small detector. In the second part, comprising of Chapter 5 to Chapter 7, development a high resolution thrust stand is discussed that can measure thrust from different types of micro-thrusters.

Electrospray propulsion is one of the prospective candidates for small satellite propulsion applications and is a major subject of research in Microsystems for Space Technologies Laboratory (LMTS) at the EPFL, in Neuchatel. In this chapter, a brief account of electrospray propulsion technology is provided after a small review of small spacecrafts and micro-propulsion. Finally, the novelty of the thesis is discussed and the organization of the thesis is summarized towards the end of the chapter.

1.1.   Small spacecrafts and micro-propulsion

Interest in miniature satellites (< 100 kg mass) has grown significantly in the last two decades. With smaller spacecraft, launch cost can be significantly reduced and launch rates can be increased [1]. Many missions can be envisioned using miniature satellites with increased complexity and capability [2]. For example, instead of one large satellite, a scientific payload can be distributed among a fleet of small satellites to reduce mission risk, establish constellation of satellites and achieve redundancy in riskier operations without jeopardizing the whole mission [1]. Several small spacecrafts can be piggybacked on a relatively larger 'mothercraft' for interplanetary missions and released to form a distributed network or a spaceprobe to perform the critical operations [1]. They can also be used as 'micro-inspector' crafts that can be detached from a 'mothercraft' and inspect the latter for maintenance [3], or rendezvous with asteroids or relatively small space debris to de-orbit it [4]. Smaller satellites also enable students and universities to gain hands-on experience in space technologies [5], [6]. In Ref. [2], some examples of launches below 100 kg mass can be found till 2000, typically well within the volume of 1 m^3 and many of them within 20 kg of mass. In the last 14 years, the average mass of the satellites of this class has gone down to 5 kg, summary of which can be found in Ref. [5]. They are commonly categorized as nano-satellites, and number of such satellites has increased radically.

Beginning in 1999, *Cubesat*s, one of the smallest types of nano-satellites and with each unit defined within a volume of 10 cm × 10 cm × 10 cm, and mass within 1.33 kg [7], have been an attractive and economically viable option for academic and research institutes to gain access to space. Primarily aimed as technology demonstrators till date, many *Cubesat*

launches have taken place in the last decade [8]. Almost 10% of 2012 low earth orbit (LEO) launches is represented by *Cubesat*s [9]. Building up on the trend and success, *Cubesat*s are not any more just an easy-access-to-space provider; they are regarded as valuable science and technology assets [10], [11], grown beyond the interest of academic community to include industry and government entities. Single- or multiple-unit *Cubesat*s have been envisioned for lunar or interplanetary missions targeting different objectives, such as, mineral mapping of asteroids, solar system escape technology demonstration, Earth-Moon L2 quiet observatory etc. [10].

Till date, one of the main challenges limiting the escapade of small satellites has been a low cost and miniature propulsion system. Many *Cubesat*s are launched without active propulsion systems [12], where attitude control is achieved by, for example, a gravity boom [13], or not having attitude control at all [12], [14]. On the other hand, active propulsive capabilities are necessary for *Cubesat* applications like formation flying, inspector satellites or operations beyond earth's orbit [12]. The propulsion system, with the propellant and the other sub-systems, has to fit inside the limited size and mass that can be allotted for the propulsion system inside the small satellite and work within the available power on-board. Depending on the mission requirement, the thruster may need to deliver very low thrusts and/or high specific impulses. For example, atmospheric drag compensation for a *Cubesat* in LEO would require typically a few 10's of μN thrust [15]. On the other hand, extra-orbital missions employing *Cubesat*s would need several thousands of sec. specific impulse owing to high delta-*v* requirement and low propellant mass available [5]. Unfortunately, most of the existing propulsion technologies, developed and used for larger spacecrafts, cannot be efficiently scaled down to deem suitable for *Cubesat* applications. Miniaturization options for different existing thruster technologies have been investigated [1], [2], [16], [12] quite extensively. Electrospray propulsion is one of the key technologies that are potentially suitable for a wide variety of *Cubesat* missions, capable of providing high specific impulse and low thrusts in a small package.

1.2.   Electrospray propulsion

Electrospray propulsion works on the principle of electrospraying charged particle from a conductive liquid using high electric field. The concept of electrospray (ES) is nearly a century old [17], although a first analytical explanation came only in 1964 [18] from Sir Geoffrey Taylor. When a conducting liquid is brought in a region of strong electric field (usually through a capillary or by wetting a sharp tip), the meniscus of the liquid deforms into a conical shape and a very strong electric field near the tip of the cone, termed as the Taylor cone, extracts charged particles at a very high speed. The process of electrospray has found widespread application including mass-spectrometry, focused ion beam and propulsion, examples of which can be found since the 1960s [19]–[22].

A schematic of electrospray process is shown in Figure 1.1. In the figure, a conductive liquid inside a capillary is shown and an electric potential, V_{em}, is applied between the liquid and an extractor electrode. When the charged particles are accelerated by the applied electric field and if there is no other energy-loss mechanisms present in the extraction process, emission speed, v_e, can be found from conservation of energy as

$$\frac{1}{2}mv_e^2 = qV_{em}$$

(1.1)

where m and q are the mass and charge of the emitted particle. If only one type of charges are emitted along the axis of the capillary, the specific impulse and thrust can be written as [5]
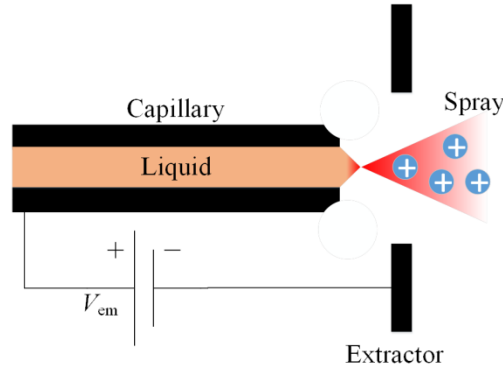
Fig. 1.1: Schematic of electrospray process from a capillary. High electric field between the conductive liquid and the extractor deforms the liquid meniscus into a conical shape and from the tip of the Taylor cone, charged particles are extracted.

$$I_{sp} = \frac{1}{g_0}\sqrt{2V_{em}\frac{q}{m}} \qquad (1.2)$$

$$Th = I\sqrt{2V_{em}\frac{m}{q}} \qquad (1.3)$$

where I is the emitted current, g_0 is acceleration due to gravity. It can be easily observed that, if the emitted charges have higher q/m, the specific impulse is higher, but thrust is lower. For example, typical $m = 87$ a.m.u. singly charged ion emitted from an electrospray source from ionic liquid EMI-BF$_4$ (discussed in section 1.2.2) at $V_{em} = 1$ kV and $I = 100$ nA can produce a thrust 4.2 nN and specific impulse 4700 s. If, on the other hand, droplets are emitted with, say hundred times higher m/q, for the same current level, the thrust can be ten times higher and specific impulse ten times lower. Depending on the geometry of the emitter, the type of conducting liquid, emission voltage and current, emission may comprise of only droplets, or a mixture of droplets and ions or pure ions, and thus a wide range of thrust and specific impulse can be achieved. Research on exploiting these traits of electrospray has been underway since the 1960s in form of field emission electric propulsion (FEEP) [21] and colloid thrusters [22], but, has accelerated since the 1990's with growing interest in small satellites.

While propulsion needs of small satellites are one of the key drivers for electrospray thruster research, *LISA pathfinder* is, on the other hand, an example, where such μN thrusters are required for much larger spacecrafts as well [23]. The Space Technology 7 (ST-7) Disturbance Reduction System (DRS) on the *Lisa Pathfinder* spacecraft employs colloid thrusters in the range 5 μN to 30 μN with specific impulse about 150 sec. to 275 sec. to compensate for all external drags [24], [25], [26].

1.2.1. FEEP thruster:

FEEP thrusters produce metal ions by field emission from the surface of a metal and inherently possess a high specific impulse. The earliest experiments on FEEP thruster were performed with cesium (Cs) propellant, which is a room temperature liquid metal (melting

point 28° C), fed in a 25 μm–200 μm inner diameter capillary tube using capillary forces [21]. Later on, FEEP research has been mainly focused in Europe, initially at European Space Research and Technology Centre (ESTEC) in the Netherlands [27], then at University of Pisa, Cetrospazio (later became Alta) in Italy [28], and Austrian Research Centres Seibersdorf (ARCS) in Austria [29], all under funding from ESA. The cesium FEEP thruster research in Alta led to slit emitters of varying slit widths, between 2 mm and 70 mm producing thrust from 40 μN to 1.4 mN with specific impulse around 9000 s [12]. The FT-150 FEEP thruster had been originally developed by Alta using cesium propellant for *Lisa Pathfinder* mission, capable of 0.3 μN to 200 μN thrust and specific impulse between 3200 s and 4500 s [30]. An image of the FT-150 FEEP thruster is shown in Figure 1.2.

Fig. 1.2: FEEP FT-150 emitter blade at first ignition [31]. Emission starts from few spots on the emitter blade, and it extends progressively to the whole active part of the slit during the initial thrust stabilization phase.

In contrast to cesium FEEP, ARCS developed needle type and capillary type FEEP emitters based on less reactive melted indium (In) as propellant (melting point 154° C) for the Space Technology 7 (ST-7) DRS system targeting missions like *LISA Pathfinder* and European *GOCE* mission [12]. Single ion emitter in these thrusters typically range up to 15 μN with specific impulse 4000 s−8000 s [29] and arrays of multiple emitters were developed for *LISA Pathfinder* and *GOCE* missions [32]. An image of a 4×4 thruster array of the indium FEEP devices is shown in Figure 1.3.

Fig. 1.3: Indium FEEP emitter array from ARCS [29]. 2×2 assemblies as well were extensively tested and characterized. 4 clusters of 9 emitters each (total 36 emitters) were also designed for *LISA pathfinder* program.

1.2.2. Colloid thruster:

Colloid thrusters use non-metallic conducting liquid of different types to emit ions or charged droplets or both and thus can range over a wide range of specific impulse and thrust. Earliest example of generating thrust by electrospraying from non-metallic conducting liquid can be traced back to 1960s [22] in which, a 250 μm inner diameter stainless steel needle was used to

electrospray charged droplets from octoil. Later on, multiple needle modules had been developed as colloid thrusters in a collaboration between TRW Systems Group and the Aero Propulsion Laboratory at Wright-Patterson Air Force Base [33]. Their colloid thruster consisted of 100 μm inner diameter and 360 μm outer diameter platinum capillaries and 19.3% by weight NaI solution in glycerol as propellant. With 60 capillaries, they had developed a colloid thruster with 800 sec specific impulse. Later on, annular slit colloid thruster was initiated by NASA Goddard Space Flight Centre (GSFC) by Stark and Sherman [34]. They tested forty eight different single emitter configurations with different propellants like glycerol doped with NaI, H_2SO_4, HCl and NaOH. Thrust and specific impulse were calculated by measuring the charge over mass ratio of emission using a time-of-flight mass spectrometer (ToF-MS), a tool, very commonly used even today for characterization of electrospray thrusters and is discussed in greater detail in section 2.1 in Chapter 2. Many other colloid research programs during the 1960s to 1970s can be cited, typically emitting charged droplets from capillary or slit-geometry emitters with thrust ranging in the μNs and specific impulse in the order of 100s of sec, an account of which can be found in [35].

1.2.3. Ionic liquid electrospray sources

Ionic liquid electrospray sources are a relatively newer subset of colloid thrusters employing ionic liquids as propellant. A revolution in colloid electrospray research took place in the 1990's together with increasing emphasis on small spacecrafts [1], [2], [16]. Novel ionic liquids gave the primary impetus on large-scale research activities on ionic liquid electrospray sources. A collaboration initiated between Prof. Martinez-Sanchez of MIT, Prof. Fernandez de la Mora of Yale University and Dr. Vlad Hruby of Busek Co. [35]. Romero-Sanz *et al* in 2003 showed that ionic liquid EMI-BF$_4$ can electrospray from 20 μm to 40 μm inner diameter silica capillaries in purely ionic regime with very low mass flow rates [36]. This was the first example of pure ion emission from non-metallic electrospray propellant where monomer, dimer and trimers were observed in the emission with no droplet current at higher m/q. Research activities in Yale continued towards investigation of different ionic liquids and effect of their properties on the emission characteristics. Investigation of electrospray properties with different ionic liquids have been reported from internally wetted 50 μm inner diameter stainless steel needles in [37] and externally wetted 0.5 mm diameter tungsten wires, electrochemically sharpened and roughened towards the emission tip [38], both published in the same year. The results in [37] generally suggest that ionic liquids with high electrical conductivity, high surface tension and low viscosity are favourable for pure ionic emission while ionic liquids with lower conductivity and surface tension, such as EMI-Tf$_2$N, produce mixture of ions and droplets from the internally wetted emitters. On the other hand, with externally wetted emitters [38], ionic liquids even with lower conductivity and surface tension can achieve pure ionic regime (PIR).

Different emitter geometries for ionic liquid electrospray sources have been studied over the last two decades. In MIT, Paulo Lozano, during his PhD, used commercially available pulled silica capillaries with 5 μm inner diameter with NaI-doped formamide solution and then 10 μm inner diameter distal coated needle emitter with EMI-BF$_4$ [39] and showed that PIR was achieved in the later with the emitted particles having very narrow kinetic energy spread. They had later used pulled silica capillaries with EMI-BF$_4$ and above 4000 sec specific impulse was recorded [40]. This research eventually branched to Busek leading to the development of the 5−30 μN range colloid micro-newton thruster (CMNT) to be used in ST-7

in *LISA pathfinder* mission [26]. A picture of the colloid thruster from Busek is shown in Figure 1.4.
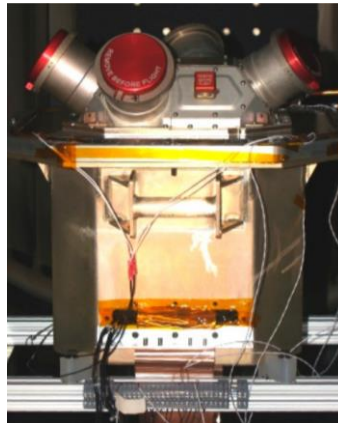
Figure 1.4: Picture of one of the two Busek colloid micro-newton thruster clusters taken from Ref. [26]. It consists of four independent colloid thruster heads, four propellant storage and feed systems, four power processing unit (PPU), one cathode neutralizer and one digital control and interface unit (DCIU). Each thruster comprises of nine parallel emitters, a heater and the extraction and acceleration electrodes.

While this colloid thruster is targeted for relatively low specific impulse application (~ 150 s) [26], many other different emitter configurations have been underway targeting pure ionic mode, and therefore, high specific impulse applications. In the following two sub-sections, two types of emitters are mainly discussed, which have been later used in Chapter 4 for characterization of an electrostatic ion-guide.

Externally wetted emitters:

MIT team moved on to developing externally wetted emitters. They used electrochemically etched tungsten wire emitters for understanding the emission properties and beam composition from ionic liquids [41], [42]–[44] as shown in Figure 1.5. These are 0.5 mm diameter tungsten wire chemically and electrochemically etched at the tip to create a sharp wettable emitter. The process steps of fabrication of the emitters can be found in detail in Ref. [44]. A reservoir loop to sustain liquid is created beneath the tip by spot welding another tungsten wire as shown. The tip is wetted by dipping it in ionic liquid and then depositing a small drop of the liquid at the intersection of the emitter and the loop, which works as a reservoir. Finally the prepared emitter is mounted on a copper block for electrical contact and is aligned with a 1.4 mm diameter aperture on a stainless steel extractor electrode.

Some of the interesting conclusions from their studies can be listed below.

- Externally wetted emitters produced purely ionic emission from EMI-BF$_4$ [43], [44] and EMI-Tf$_2$N [41] with widely different conductivity and surface tension values. These same emitters were later used in [38] for characterization of other ionic liquids [38].
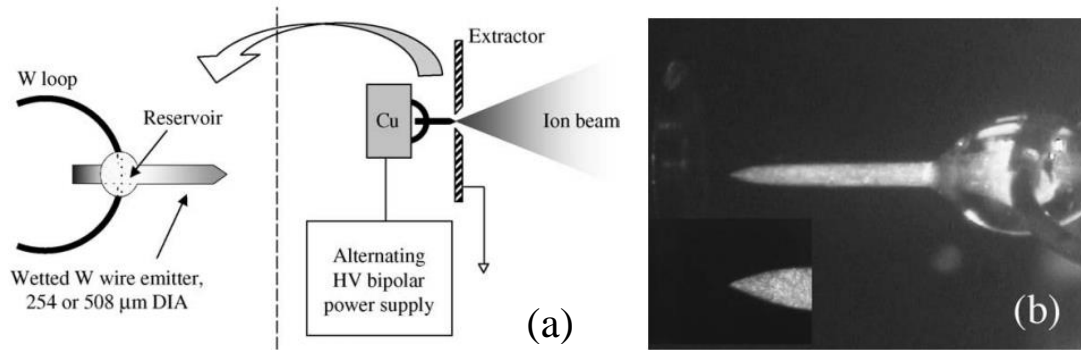
Figure 1.5: (a) Schematic of an externally wetted tungsten emitter taken from Ref. [44]. (b) Image of a tungsten emitter wetted with ionic liquid at the intersection of the loop reservoir. This image is taken from Ref. [43].

- In PIR mode from ionic liquids, a very narrow energy distribution and a very low energy deficit (typically within 1−3% of qV_{em}, V_{em} is the emitter voltage) are obtained in the emitted ions. These values are comparable to liquid metal ion sources. These emitters led to their development of ionic liquid focused ion beam applications [45]−[47].

- Continuous emission from the ionic liquid accumulates opposite charges on the liquid-metal interface and inhibits further emission by creating a double layer and eventually resulting in electrochemical degrading of the ionic liquid. This can be suppressed by alternating the polarity of emission at 1 Hz or higher and prolonged operation in bipolar mode can be achieved without degrading the ionic liquid [43].

The advantages of externally wetted emitters of emitting nearly mono-energetic pure ions had been combined with the advents of micro-fabrication to integrate multiple externally wetted silicon emitters [48], [49], porous nickel [50], tungsten [51] emitter arrays as shown in Figure 1.6 (a), (b) and (c) respectively. MIT recently reported on porous borosilicate glass array of emitters fabricated using laser ablation [52] as shown in Figure 1.6 (d); however, emission consisted of ionic current with a small trace of droplet current. Recently, porous borosilicate emitter strips have been fabricated in LMTS-EPFL by Dr. Daniel G. Courtney using milling machine and these devices have also shown highly ionic emission with several 10's of μN thrust [53]. These devices have been used in the thesis for characterization of the thrust stand and is discussed in section 7.1 in Chapter 7.

Micro-fabricated internally wetted emitters:

Many internally wetted capillary emitter arrays have also been developed over the years; a survey of the different types of emitters can be found in [5] and is avoided here. The micro-fabricated capillary emitters used in characterization of the ion-guide were fabricated in LMTS-EPFL by Dr. Ataman Çağlar and Dr. Simon Dandavino. In Figure 1.7, a schematic and a scanning electron microscope (SEM) image of the capillary emitters is shown from Ref. [54]. The capillaries are fabricated on silicon on insulator (SOI) wafer, using deep reactive ion etching (DRIE) process, details of which can be found in [54], [55]. Capillaries are typically of inner diameter between 5 μm and 10 μm and length 100 μm realized on the device layer of the wafer. A reservoir is created on the handle layer which, before electrospraying, is filled with ionic liquid, and the liquid reaches the tip of the capillary by

capillary process. An extractor electrode with aperture between 150 μm and 300 μm is micro-machined on another SOI wafer and these two are bonded together by wafer-level thermal compression bonding.
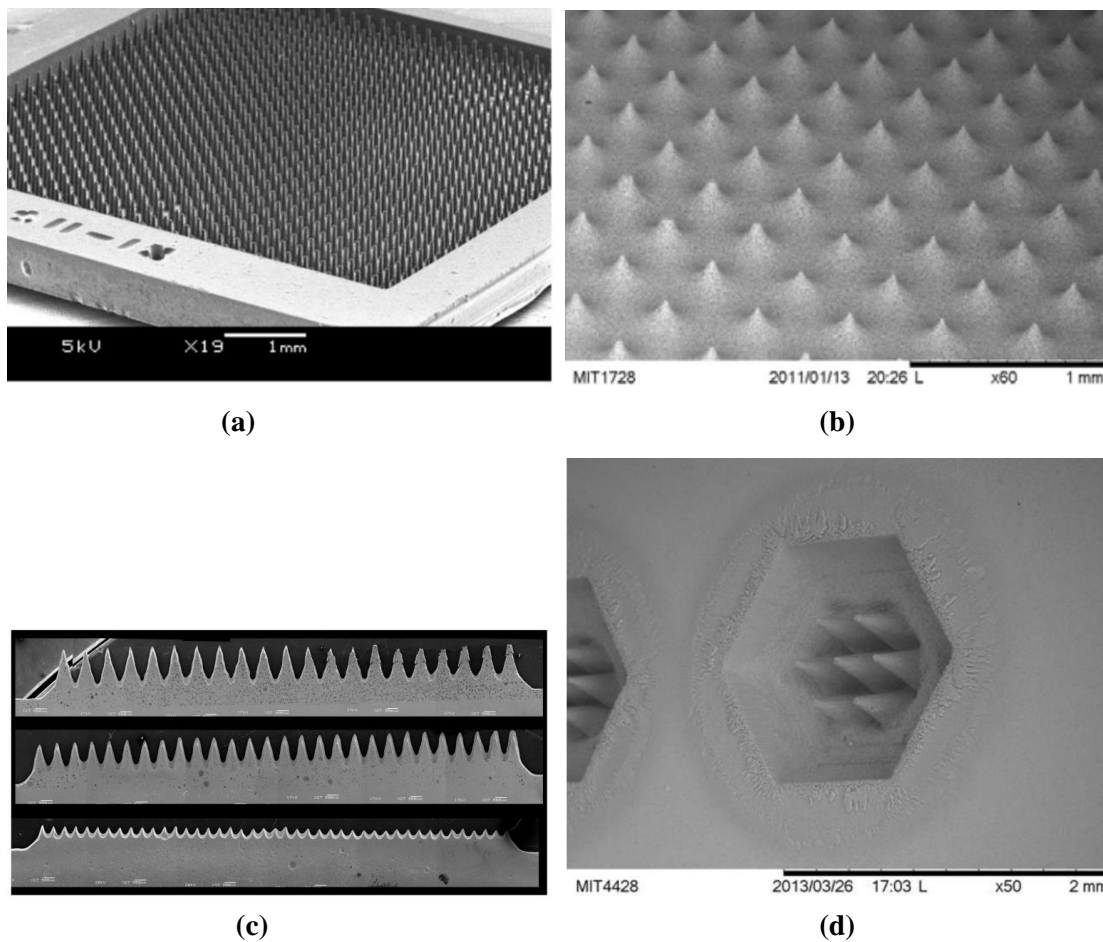
Figure 1.6: (a) Planer array of 1024 externally wetted silicon emitter array from Ref. [48]. (b) Planer array of 480 porous nickel emitters from Ref. [50]. (c) Linear array with different packing densities of porous tungsten emitters [51]. (d) Laser micro-machined porous borosilicate emitter arrays [52].
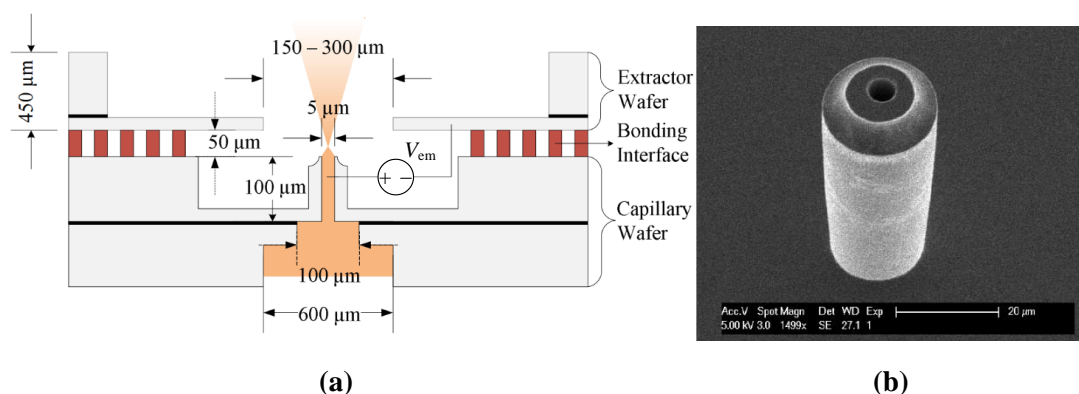
Figure 1.7: Schematic of an electrospraying micro-fabricated capillary emitter with extractor electrode and (b) a SEM image of the emitter, taken from Ref. [54].

These devices were developed over the progress made by Renato Krpoun in LMTS, who initially developed capillaries of diameter between 18 μm and 32 μm, details of which can be found in his PhD thesis [35]. The inner diameter of these devices was too large to provide sufficient hydraulic impedance and produce pure ionic emission. Later on, he devised a post-fabrication process of filling the capillaries with 5 μm silica beads to increase the fluidic impedance [35], [56] and could achieve pure ionic emission from EMI-BF$_4$. In Figure 1.8 (a) and (b), SEM image of a capillary emitter and bead-filled emitter taken from Ref. [35] are shown. He went on to demonstrating operation of a 19-emitter array configuration as shown in Figure 1.8 (c) and from time-of-flight measurements, estimated the specific impulse of 2000 sec to 4600 sec and thrust per emitter of 2 nN [57]. He also observed erosion of the extractor electrode after spraying for long time, indicating that the emitted spray may have a wide beam spread [57]. Kinetic energy measurement by retarding potential analysis (RPA) had shown that the kinetic energy of the emitted particles deficits by nearly 100 V over $V_{em} =$ 1200 V emission voltage [57], [35], intermediate between the nearly no-deficit case studied by Lozano with externally wetted emitters [41] and several hundred volts observed by Gamero-Castaño [58], [59] using metallic tube emitters. He also observed secondary kinetic energy peaks corresponding to fragmented ions [57] having resemblance to Lozano's observations [41].

(a)   **(b)**   **(c)**
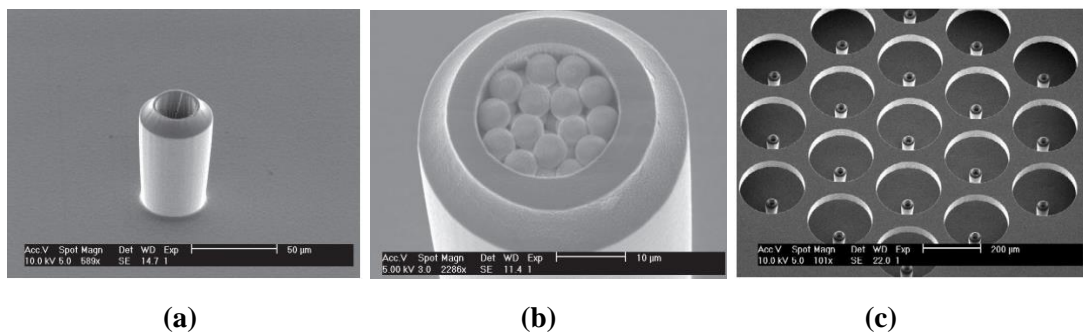
Figure 1.8: (a) Capillary emitter and (b) silica bead filled emitter fabricated by Krpoun [35]. The later achieved pure ionic emission from EMI-BF$_4$. (c) Array of nineteen emitters with the extractor electrodes [57].

Based on these developments, a collaboration among LMTS-EPFL, Queen Mary University London (QMUL), TNO (Netherlands), Nanospace (Sweden), SystematIC (Netherlands) and EPFL Space Centre (Switzerland) was initiated in 2010 with a project named Microthrust [60] funded by EU-FP7. The target of the project was to demonstrate an ionic liquid electrospray thruster breadboard module consisting of capillary emitter arrays, propellant handling, compact high voltage power supplies and neutralizer, packaged within the size constraints of nano- and pico-satellites [60]. The capillary devices shown in Figure 1.7 and used for characterization of the ion-guide in Chapter 4 are prototype devices fabricated during the development phase of the project. Experimental results on the beam composition on single capillary devices, performed with a ToF-MS at QMUL, had shown mixed ion-droplet mode of emission with specific impulse in the range of 100s of sec [55], even reaching 1100 sec [61] and thrust in the range of 100 nN or above. Later on, integrated accelerator stage was implemented on the next generation emitter arrays comprising of 91, 127 or 167 emitters on a single chip [5], [62], [63] as shown in Figure 1.9. These devices have shown typically more than 90% ionic content in the emission, more than 1000 sec specific impulse and several μN

total thrust [62], [63] by improved thrust vectoring and increasing exhaust speed of charges due to the additional accelerator stage.
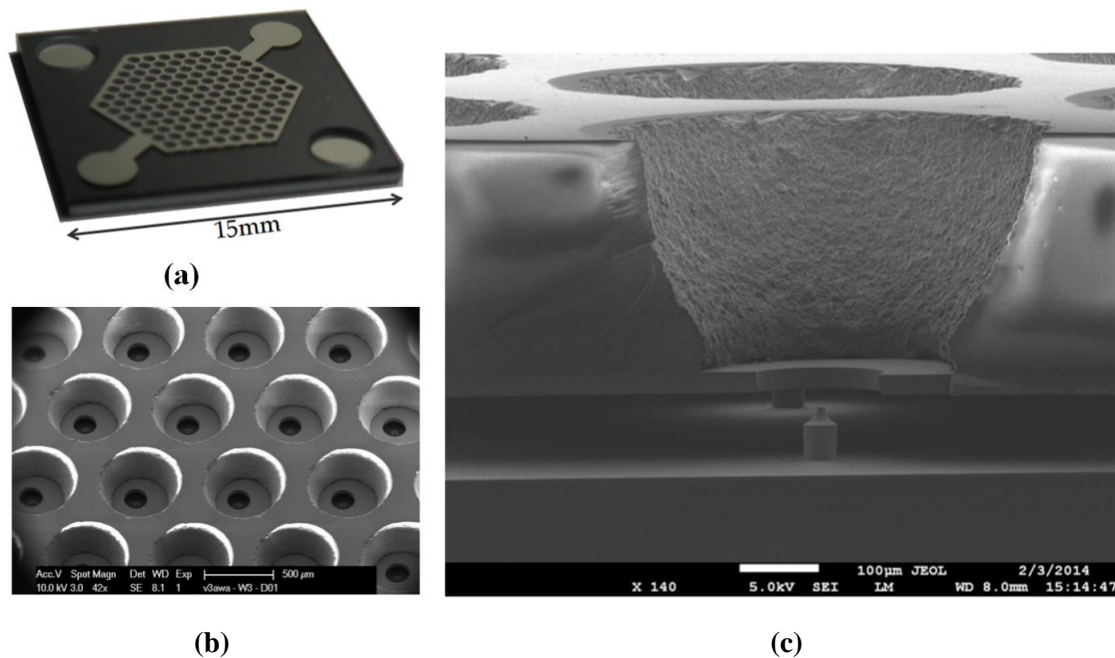
Figure 1.9: Optical (a) and SEM image (b) of micro-fabricated capillary emitter array with integrated extractor and accelerator. (c) Cross-section of the emitter array showing individual emitter aligned with extractor and accelerator electrodes [5].

1.3.   Characterization of electrospray microthrusters

Emission composition and measurement of thrust and specific impulse of electrospray propulsion devices is mainly performed with the help of time-of-flight (ToF) mass spectrometry of the emitted species, details of which are discussed in section 2.1 in Chapter 2. In ToF technique, the time-of-flight traces of emitted charged particles with different q/m are used for measuring the propulsive parameters, such as thrust and specific impulse, which are defined in Eqn. (2.6) to (2.8) in Chapter 2. From the emission, as is discussed in section 2.1 in Chapter 2, either a fraction of the emitted beam is collected without or by focusing on a detector typically placed at a distance 10 to 100 times the diameter of the detector, or the entire plume is collected on a large detector having diameter typically in the same order of magnitude as the flight length. In the first part of the thesis, i.e. in Chapter 3 and Chapter 4, a ToF mass spectrometer with an electrostatic ion-guide is discussed that can collect a large fraction of the emitted plume on a small detector by guiding the emitted charges through a flight tube nearly 60 times longer than the diameter of the detector.

Direct measurement of thrust from the microthrusters is a direct, but more challenging, approach in characterising microthrusters because of various reasons associated with reliable measurement of forces in the nN to µN orders, which is discussed in section 2.2 in Chapter 2. As reviewed in Chapter 2, this is typically achieved by mounting the thruster on a thrust stand that transduces thrust directly into another measurable signal or, alternatively and much less commonly, by measuring the momentum flux of the emitted plume on a plate. In the second part of the thesis, comprising of Chapter 5 to Chapter 7, development of a thrust stand of the second kind is discussed.

1.4.   Thesis novelty

The preceding sections were intended to provide a brief overview of characteristics of electrospray micro-propulsion devices. The first objective of the thesis was to develop a ToF-MS for beam composition characterization of the electrospray sources. The designed ToF-MS with the electrostatic ion-guide enables measurement of flight times during bipolar operation of the emitter and, at the same time, is capable of capturing charges over large emission half-angle on a small detector far downstream from the emission site. Although the concept of ion-guide is not new, and is discussed in section 3.1.5 in Chapter 3, the new design and application of the ion-guide in characterizing electrospray propulsion devices have been a key contribution in the thesis. Ion trajectory simulations have been performed to estimate the angular spread and the kinetic energy spread that the ion-guide can accommodate and to estimate the effects of the electric field distribution of the ion-guide on the flight trajectory of un-fragmented charges. It has been shown that the ion-guide can collect all charges within a 23° emission half-angle or a 30% kinetic energy spread irrespective of their q/m ratio on the small detector without having to scan the angular position of the emitter or using a very large detector in a large vacuum chamber. With emission from tungsten emitters up to 80% of the emitted charges could be collected, enabling not only real-time monitoring the mass spectra of the emission over a wide angle and energy range, but also reducing the gain requirements of the detection circuitry. Despite delaying the flight time and introducing additional spreading in the flight time traces, flight times of emitted particles could be measured quite accurately. Charge collection measurement from micro-fabricated capillary emitters has also been measured and above 30% maximum collection has been achieved despite having nearly 40° measured emission half-angle. The ion-guide concept used in the setup can also be potentially transferred to other mass spectrometric applications where real-time monitoring and quick attainment of the entire mass spectra is necessary, a few examples of which are discussed in section 2.1.4 in Chapter 2.

As a second part of the thesis, a compact nano-Newton thrust stand has been designed and characterized. The thrust stand can measure thrust from different types of micro-thrusters in the range of about up to 100 μN or more with resolution between 10 nN and 20 nN. The operating principle of the thrust stand is different from the existing thrust stands measuring thrust with the similar resolutions and is the first of its kind to demonstrate less than 3 μN resolution. This thrust stand measures thrust by intercepting particles emitted from a thruster on a spring-loaded plate and measuring the force on the plate with a sensitive force sensor. Measurement of thrust even up to 100 mN is potentially possible with the same thrust stand without having to modify or replace anything but the force sensor only with another force sensor from the same manufacturer with higher range. The design and manufacturing process of the particle intercepting plate have been carefully evaluated from mechanical and material point of view to make reproducible plates meeting some stringent requirements in order to be usable in the thrust stand. An analytical design methodology has been proposed in section 5.2 in Chapter 5 for the plate and has been verified with finite element simulation to finalize the optimum design. By its very principle of operation, the thrust stand is an isolated module from the thruster itself and hence can measure thrust from different types of micro-thrusters placed in front of it. Thrust measurements from a cold-gas ejecting capillary, emitting slow neutral particles in atmospheric conditions, and from an electrospray device, emitting high velocity charged particles in vacuum, have been demonstrated in Chapter 6 and Chapter 7 respectively. Thrust measurements from the cold-gas capillary using the thrust stand have

been compared with that measured directly on the capillary up to around 50 μN with about 90% accuracy. For electrospray device, the measured thrust is compared with that obtained from indirect beam diagnostics up to 2–3 μN with similar accuracy. Uncertainty in the relation between the particles' impingement force and the thrust generated on the thruster, and the spot size and location of the plume on the plate have been the two main sources of inaccuracy in the measured thrust and have been discussed in detail.

1.5. **Organization of the thesis**

The thesis is organized in the following chapters.

- **Chapter 1:** Chapter 1 provided a brief account of electrospray propulsion followed by a summary of the contribution of the thesis.

- **Chapter 2:** In Chapter 2, literature survey on time-of-flight mass spectrometry for characterization of electrospray propulsion devices and thrust stands for measuring thrust from micropropulsion devices in the range of μNs is provided in two separate sections.

- **Chapter 3:** In Chapter 3, design and experimental setup of a time-of-flight mass spectrometer with a high throughput electrostatic ion-guide is discussed. Qualitative and quantitative description of the performance of the setup is discussed.

- **Chapter 4:** In chapter 4, the experimental characterization of the ion-guide and flight time measurement from the two types of electrospray emitters are described.

- **Chapter 5:** In Chapter 5, development of the thrust stand is described. Constraints and targets of the thrust stand are described and analytical design approaches, parts of which are validated by finite element simulation, are provided.

- **Chapter 6:** In Chapter 6, atmospheric characterization of the designed thrust stand using a cold-gas ejecting capillary is described. It is shown that by using homodyne detection technique, a 10 nN thrust resolution can indeed be ensured with the thrust stand.

- **Chapter 7:** In this chapter, the performance of the thrust stand is evaluated using an electrospray propulsion device. The thrust measurements up to about 2–3 μN have been compared with expected thrust from beam diagnostics. Inaccuracies in the measurement creeping in due to impact mechanisms of the high speed particles on the plate are discussed.

- **Chapter 8:** Finally, the contributions of the thesis are summarized in this chapter. The major advantages and disadvantages are critically discussed and possible ways to address the shortcomings are attempted to address.

2 Literature survey: ToF-MS and nN thrust stand

Diagnostics of micro-thruster performances is a challenging endeavour. It has been mentioned in section 1.2 that electrospray propulsion is among the prospective candidates for small spacecraft propulsion and some of the conceived formation flying missions even with larger spacecrafts. These propulsion devices can deliver sub-µN to 100s of µN of thrust at moderate to high specific impulses.

Particularly for colloid thrusters, evaluating the q/m composition in the emission by time-of-flight (ToF) mass spectrometry has been a particularly interesting and conventional tool to estimate thrust and specific impulse. On the other hand, direct measurement of thrust in the range of µNs with sub-µN resolution from micro-thrusters, not limited to only electrospray thrusters, is a necessity that has been possible, with certain challenges, only recently.

In this chapter, a literature survey is provided on both, ToF measurement techniques for electrospray propulsion diagnostics and direct thrust measurement schemes. Time-of-flight mass spectrometers (ToF-MS) are widely used in chemical and biological mass-spectra analysis as well [64]; however, in section 2.1, the focus of the literature survey is primarily limited to those used for characterization of electrospray propulsion devices and effort has been made to address the key challenges in mass-spectral analysis of these propulsion devices. In section 2.2, thrust stands targeting direct measurement of µN order thrust are discussed. The operating principles of different thrust stands and the primary challenges in measuring such low thrusts are discussed.

2.1. ToF-MS for electrospray propulsion devices

Mass spectrometers are analytical instruments that separate charged particles based on their m/q ratio. A mass spectrometer can most generally be divided into three components, an ionization source, a mass analyzer and a detector, examples of each of which can be found in Table 1.1 in Ref. [64]. Time-of-flight mass spectrometers distinguish m/q of charged particles based on their velocity in a field-free drift region by measuring their flight times. In the simplest configuration, the ToF-MS consists of a source of temporally coherent charged particles, a field free drift tube and a detector as shown in Figure 2.1. For velocity v_e of the charged species, the flight time is simply given by,

$$T_F = \frac{L}{v_e} \tag{2.1}$$

where L is the flight length. ToF-MS are the simplest mass spectrometers and yet do not have any theoretical limits of measurable m/q [64] and the mass resolution is primarily limited by temporal and kinetic energy spread of the source and the speed of detection electronics. This

property of ToF-MS is particularly useful for characterization of electrospray propulsion devices, because, depending on the type of conducting liquid, the emitted charge species may possess a wide range of m/q ratios. For example, early examples of colloid thrusters using doped glycerol showed an emission m/q of around 34000 a.m.u./e (e = electronic charge) [34]. Monomer emission from ionic liquid EMI-BF$_4$ may have m/q as low as 87 a.m.u./e (corresponding to BF$_4^-$ ions) [44]. Emission in mixed ion-droplet mode from ionic liquids generates cations or anions of the liquid and much more massive charged droplets together [35]. Over the lifetime of the emitter, the spray property may vary with time due to electrochemical reactions [43] or instantaneous formation and annihilation of Taylor cone [15], [65]. By providing a real-time capture of all detected particles over a wide range of species mass comprising of individual ions and droplets, ToF-MS is therefore has been a logical choice for analysing electrospray propulsion systems.
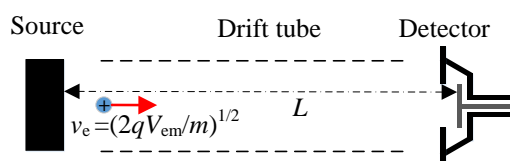
Figure 2.1: Schematic of time-of-flight measurement technique.

Capability of producing large molecular species by electrospray has been one of the key features of electrospray ionization (ESI) technique for mass spectrometric application in biological research [64]. J.B. Fenn [19] was awarded the Nobel Prize in 2002 for inventing ESI as an ionization technique for mass spectrometers. In his original setup, as shown in Figure 2.2, a stainless steel needle as the source is kept at 3500 V with respect to the cylindrical extraction electrode to generate charged droplets. The drying gas flow quickens evaporation of the solvent from the droplets to reduce their radius, finally desorbing quasi-molecular ions in gas phase [19]. Part of the ions enters the glass capillary to enable a supersonic jet into the first vacuum chamber. Although in Fenn's apparatus, a quadrupole mass spectrometer was used for analysing the m/q, ESI has since been used in tandem with many other mass analyzers [66]–[73] including ToF-MS [69], [70], [73], [74].
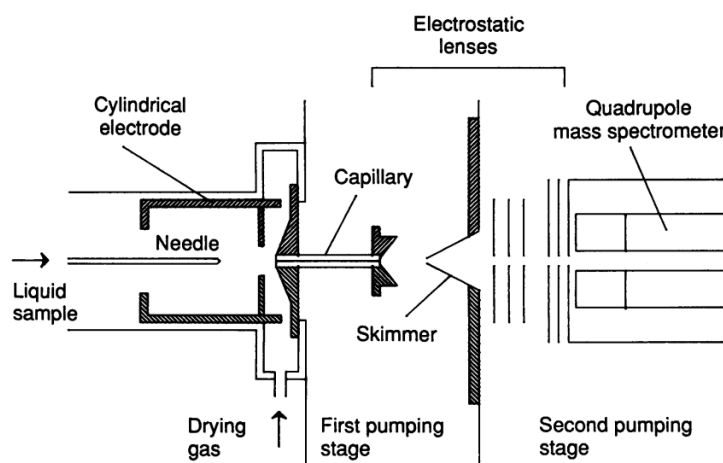
Figure 2.2: Schematic of the ESI mass spectrometer used by Fenn *et al* [19]

In a ToF-MS, when charges are generated with a constant kinetic energy (*K.E.*), the flight time of the charges over the length L of the flight tube can be written as

$$T_{\mathrm{F}} = L \left(\frac{m}{2(K.E.)} \right)^{1/2} \qquad (2.2)$$

Cameron and Eggers, in 1948, first built the ToF-MS, which they called the *ion velocitron* [75]. In their instrument, they used an electron impact (EI) source followed by accelerating and focusing electrodes to bring the emitted ions to approximately 500 eV kinetic energy for ToF measurement. Five years later, Wolff and Stephens constructed another ToF-MS [76] in which the ions were brought to constant linear momentum (*L.M.*) instead of kinetic energy (*K.E.*), by using extended accelerator field rings and ion extraction pulses so that the flight velocity is given by

$$T_{\mathrm{F}} = L \left(\frac{m}{(L.M.)} \right) \qquad (2.3)$$

In electrospray propulsion, if there is no other loss mechanisms, the emitted charges ideally possess the same kinetic energy given by Eqn. (1.1) in Chapter 1

$$\frac{1}{2} m v_{\mathrm{e}}^{2} = (K.E.) = q V_{\mathrm{em}} \qquad (2.4)$$

and hence,

$$T_{\mathrm{F}} = L \left(\frac{m}{2 q V_{\mathrm{em}}} \right)^{1/2} \qquad (2.5)$$

However, as discussed in section 1.2.3, deficit and significant spread in kinetic energy among the emitted charge species may exist in the emission spectra. With externally wetted emitters electrospraying from ionic liquids, a kinetic energy deficit and spread of typically 1−3% full width at half maxima (FWHM) has been reported in [41], [42]−[44]. With capillary emitters, operating in mixed ion-droplet mode, the spread in kinetic energy can be as high as 10% [5], [57], [35]. The kinetic energy of the emitted particles is usually measured with a retarding potential analyzer (RPA), in which, a potential is applied to an electrode in the path of the charges to stop them and the applied potential is a measure of the kinetic energy of the charge. Earliest example of using RPA for identification of macro-ions from electrospray sources can be traced back to 20 years before the invention of ESI mass spectrometer [77]. For kinetic energy analysis from electrospray propulsion devices, RPA is widely used [57], [35], [41], [42]−[44].

In general, when kinetic energy spread, temporal spread and spatial spread exist [64], the mass resolution $\mathfrak{R}$ of a ToF-MS can be written as

$$\frac{1}{\mathfrak{R}} = \frac{\Delta m}{m} = \sqrt{ 4 \left(\frac{\Delta T_{\mathrm{F}}}{T_{\mathrm{F}}} \right)^{2} + 4 \left(\frac{\Delta L}{L} \right)^{2} + \left(\frac{\Delta (K.E.)}{(K.E.)} \right)^{2} } \qquad (2.6)$$

where, Δw represents the spreading in the parameter w (m, T_{F}, L, $K.E.$). Therefore, this section will follow with divisions into three sections based on these spreading issues observed

in ToF measurements of electrospray propulsion devices. Finally, in section 2.1.5, the propulsive parameters will be defined in terms of the ToF traces.

2.1.1. Temporal spreading

The temporal spreading is partly associated with the time of ion formation or entrance into the drift tube, and partly to the limitation of ion detection and time-recording devices [64]. For electrospray propulsion devices, the operating voltage is typically around or above 1 kV. The speed of the emitted particles can be as high as several 10s of km/s for ions depending on its mass. In the early colloid thruster experiments at ESTEC, mean exhaust speed of 19 km/s was recorded from charged droplet emission at 5.5 kV potential difference between the capillary and the extractor [78]. For flight tube length of typically 1 m or less, the flight time of the fastest ions can be 50 μs or less. Therefore, the detector and ion generation mechanism need to be much faster in order to measure the flight times.

In matrix-assisted laser desorption/ionization (MALDI) sources, first developed by Karas and Hillencamp [79], and Tinkara *et al* [80] almost simultaneously, ion generation is intrinsically a fast ionization process, in which, laser pulses of width in the ns order are used to generate them. ESI is, on the other hand, a continuously ionizing source [64], and therefore, in order to integrate it into a ToF-MS and know the starting instant of the flight time, they need additional drawout or gating signal or both, such that a bunch of ions can be allowed into the drift tube with precise timing irrespective of their continuous formation at the source [64]. In the early examples of flight time measurement from electrospray propulsion devices, the emission power supply itself was abruptly switched off at a fast rate to find the flight time of the charges using an oscilloscope [34], [78]. In [78], a PL504 pentode valve was used to switch off the power supply within 1 μs. Ionic liquid electrospray devices can operate in bipolar mode in which the polarity of emission voltage is alternated to reduce electrochemical reaction [43] and switching of the emitter power supply can be a trigger for time-of-flight measurement; however, stabilization of the Taylor cone and associated stabilization time and start-up delay of the emission current [42] can be a cause of large time spread. In [42], the start-up delay and overshoot at the beginning of each transition is found to be a few ms with EMI-BF$_4$. Romero-Sanz *et al*, in their pioneering work on demonstrating ionic electrospray from ionic liquid [36] in 2003, utilized the instance of quick collapse of the Taylor cone as the reference time for flight time measurement. They grounded the emitter supply at reference time $t = 0$ and measured the flight times through a drift tube of length $L = 12.3$ mm. Recently, Lenguito has measured flight time by electrospraying ionic liquid ethyl ammonium nitrate (EAN) from multiplexed electrospray (MES) microthruster by interrupting the emission at 100 Hz [81] and measuring the flight times after collapsing the Taylor cone. In Figure 2.3, a schematic of the setup is shown. He used a fast electrometer to convert the current traces into voltage and measured the flight time using an oscilloscope.

In contrast to interrupting the emission from the electrospray source, the entrance of the emitted particles into the drift tube can be interrupted by using gating signals. In the first ToF-MS, the *ion velocitron* [75], Cameron and Egger used a gate drawout pulse of width around 5 μs to interrupt the emitted ions from entering the 317 cm long drift tube. In their experiment, the mass resolution was about 3 [64]. In the linear mass spectrometer, reported by Wolff and Stephens [76], a dual-gate scheme was implemented, in which, in addition to the drawout pulse in front of the drift tube, another ion extraction pulse was used at the end of the drift tube whose timing could be varied w.r.t. the drawout pulse and by scanning their timing

difference from 5 μs to 50 μs, the entire mass spectra could be achieved with a mass resolution about 20.
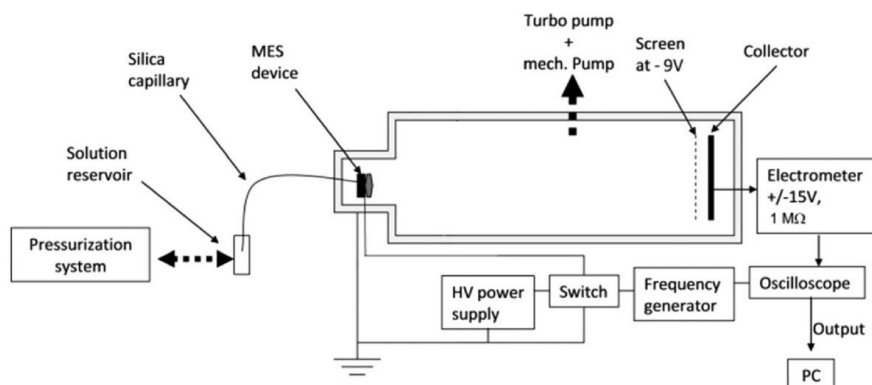
Figure 2.3: Schematic of ToF measurement setup used by Lenguito *et al* [81]. The emission is periodically interrupted using a switched power supply and ToF traces are recorded on an oscilloscope.

Both, single-stage and double-stage gating have been discussed and used in ToF measurement from electrospray propulsion devices by Lozano in his PhD thesis [39]. In Figure 2.4, a picture of the dual-gate configuration of the experimental setup used by Lozano is shown from [39]. In this setup, short opening pulse in gate 1 is followed by a short pulse in gate 2 with a variable phase shift to allow emitted particles with a narrow range of velocity to be detected by the Faraday cup detector at each scan. However, later on, this technique was abandoned due to large capacitive coupling between gate 2 and the detector, and signal to noise issues [39].
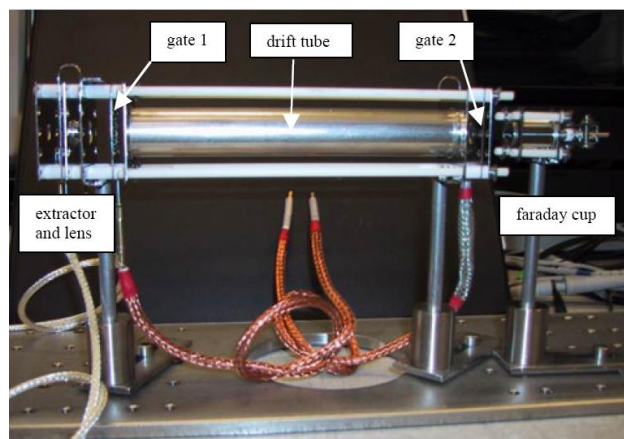
Figure 2.4: Picture of the dual-gate ToF measurement configuration used by Lozano [39]

Single gate configuration has been the most common configuration in ToF measurement from electrospray propulsion devices, a schematic of which is shown in Figure 2.5 (a) from Ref. [41]. Typical ToF traces with purely ionic emission from ionic liquid EMI-BF$_4$ using this setup with externally emitted tungsten emitter is shown in Figure 2.5 (b) from Ref. [44]. In this scheme, the gate, placed between the emitter and the drift tube, is opened or closed at a fast rate to allow or stop further entrance of the charged particles into the drift tube. In Figure 2.5 (a), an Einzel lens, comprising of three electrodes is also placed between the gate and the ionic liquid ion source (ILIS) for focusing the emitted beam, which will be discussed in more

detail in section 3.1.5 in Chapter 3. Lozano also described the effect of the electrostatic field of the gate on the kinetic energy of the particles during their passing through and around the gate electrode [39]. He concluded that for high q/m particles emitted from conductive liquids, the effect of the electric field is rather small on kinetic energy of the charges and hence on the flight time, because of their high speed and low residence time in the vicinity of the gate electrode. He later used a three electrode gate assembly for his experiments consisting of a central high voltage electrode powered by a high voltage pulse generator (DEI PVM-4210, pulse rise time < 15 ns [82]) and two adjacent grounded electrodes to reduce the stretch of the electric field of the gate signal further and reduce the particles residence time in the gate's electric field [39], [40]. In this configuration, and with a single electrode used as gate, the strong electric field normal to the plane of the electrode repels and back-scatters the high speed particles opposite to their initial trajectory when the gate is closed and part of the back-scattered particles may impinge on the emitter assembly with the possibility of damaging the emitter itself. Later they used a comb-type gate electrode with interleaved wires in the gate with successive wires at positive and negative potentials, as shown in Figure 2.5 (a), both driven by high speed pulse generator, such that a strong in-plane (to the electrode) component of electric field deflects the charges away from the axis of emission [41], [44], [83].

(a)   **(b)**
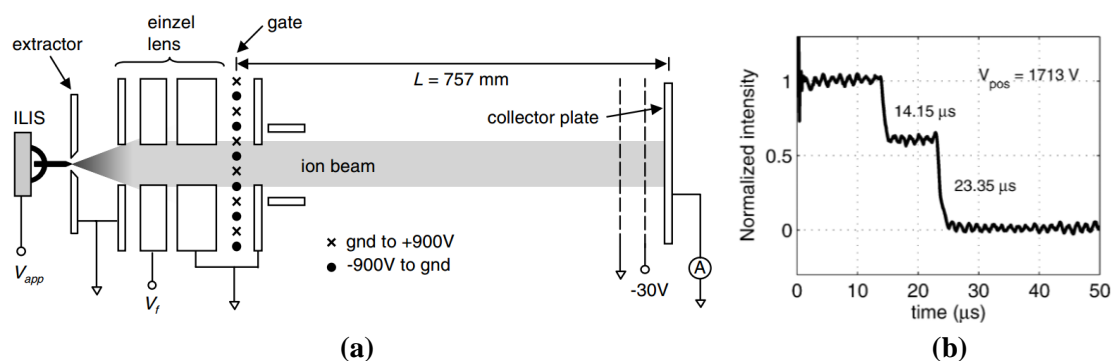
Figure 2.5: (a) Schematic of a single-gate ToF measurement setup from electrospray propulsion device, taken from Ref. [41]. (b) Typical time-of-flight traces of emission from ionic liquid EMI-BF$_4$ in positive polarity using externally wetted tungsten emitter, taken from [44] using the setup in MIT.

In QMUL, London, a ToF-MS is used for characterization of the micro-fabricated capillary electrospray emitters developed as LMTS, details of which can be found in [57], [35], [55], [61]–[63]. In Figure 2.6, a schematic of the setup is shown from Ref. [55]. In this setup, a three-electrode gate assembly is used as shown with the central electrode driven by high voltage pulse generator PVX-4150 (pulse rise/fall time < 25 ns [84]) for typically a few µs flight times to be measured.

Apart from fast switching of the entrance instant of the particles into the drift tube, the detection speed of the flight times is also an important parameter to reduce temporal spreading. Most classical time recording scheme for ToF-MS applications has been oscilloscopic traces or boxcar traces using an electron multiplier [64], [85]. The Bendix Mass Spectrometer was developed based on the magnetic electron multiplier used by Wiley and McLaren [85] in 1955. Modern digital oscilloscopes usually have several 10s of MHz bandwidth and around or above 1 GS/s sampling rate and measuring flight times of the order of a few µs is possible with them. However, a transimpedance amplifier to convert the current traces corresponding to arrival of charges into a measurable voltage is necessary and the

speed requirements are primarily attributed to this amplifier stage. Electrospray emission may take place over a wide emission angle [41], [86], [87] and only a small fraction of the emitted charges reach a detector placed after the drift tube if not focused and if the detector is small. As a result, gain bandwidth product of the transimpedance stage is a crucial parameter depending on the nominal flight time to be measured and the current reaching the detector. A trade-off study is provided in section 3.1 in Chapter 3 in designing a time-of-flight measurement setup with an electrostatic ion-guide to reduce the gain bandwidth requirement of the transimpedance stage when a small detector is used. Typically, high speed electrometers are used either with an ion-focusing arrangement, such as an Einzel lens, [39], [40], [43]–[47] or using a large detector to collect most of the emitted charges [36], [38], [83], [58], [59], [81]; or high speed transimpedance amplifiers, such as DHPCA-100, [88] are used without [55], [61], [63], or with [89], [90] focusing arrangement. In his thesis [39], Lozano used high-speed operational amplifier (OPAMP) based transimpedance amplifier with an asymmetric Einzel lens of 13° acceptance angle.
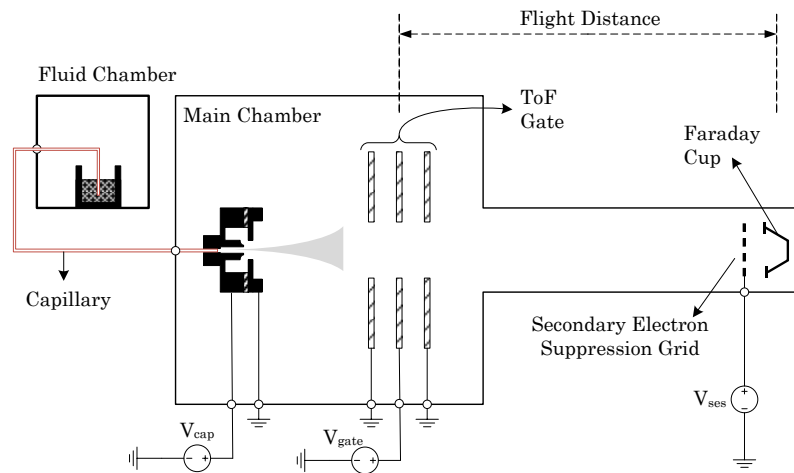
Figure 2.6: Schematic of the ToF chamber for characterization of electrospray devices in QMUL, London [55].

2.1.2. Spatial spreading

In general, spatial spreading may also arise from the lateral and axial spreading of ion formation in the source. With electrospray propulsion devices, however, this can be ignored since emission occurs from a tiny tip of a Taylor cone or a cone-jet structure whose length is much smaller than the flight tube length in general.

However, spatial spreading in electrospray source characterization may arise from the angular spread of the emitted species recorded particularly with a large flat collector. The different flight lengths the ions have to cover to reach the plate and associated spreading in the flight time traces can significantly contribute to spatial spreading. In Figure 2.7, a schematic of using a large flat plate collector is shown from Ref. [38]. In [81], a detector plate of diameter 19 cm is used, which collects emitted particles within 13° emission half-angle. In [83], a 20 cm diameter flat collector plate is used which subtends a 21.8^{o} angle on the emitter.

For a diameter D_c of the plate, placed at the end of the flight tube length L, the associated spatial spread can be written as

$$\frac{\Delta T_{\mathrm{F}}}{T_{\mathrm{F}}} = \frac{\Delta L}{L} = \left(1 + \frac{D_{\mathrm{c}}^2}{4L^2}\right)^{1/2} - 1 \tag{2.7}$$

between particles reaching the centre of the plate and those reaching the edge, assuming no kinetic energy spread, and for emission of only one type of charge species. $\Delta L/L$ can be considerably high depending on the ratio D_c/L. For the 13° and 21.8^o acceptance angles of the two examples discussed in the last paragraph, $\Delta T_{\mathrm{F}}/T_{\mathrm{F}}$ can be calculated to be 2.6% and 7.7% respectively. In [59], this spreading has been verified and addressed for purely ionic mono-energetic emission by evaluating $(1+\Delta T_{\mathrm{F}}/T_{\mathrm{F}})$ as a function of L. For single Einzel lenses used for focusing a small fraction of the emission on a detector far downstream, the detected particles are nearly parallel with very little contribution of the angular spread reflecting on the flight time traces. Also, Einzel lens allows only a narrow band of kinetic energies of the charges to pass through. As a result, contribution of an Einzel lens on the spreading of all the detected particles within a narrow emission angle and narrow kinetic energy range is usually very small. In [39], Lozano estimated the kinetic energy spread due to different flight times of charges along the axis and those close to the focusing electrodes of the asymmetric Einzel lens to be 0.6%. In contrast, the ion-guide described in section 3.2 in Chapter 3 and in [90], extends over the entire length of the flight tube and accepts a large angular spread of 23° in the emission to be collected on a small Faraday cup detector. A similar ToF spread factor has been introduced for the designed ion-guide in section 3.3.3, which can be as high as 36%. The difference in flight length of particles emitted at different angles from the axis causes the spread in the designed ion-guide.
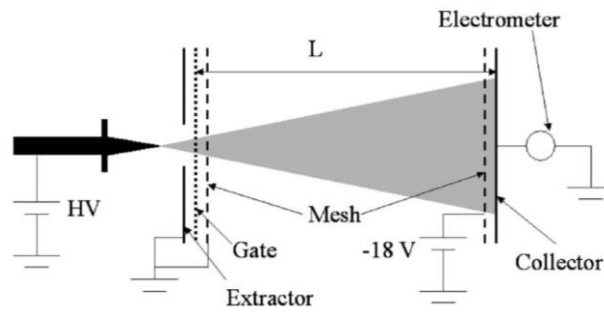
FIG. 1. ILIS experimental setup.

Figure 2.7: Schematic of a large plate collector used for ToF measurement from electrospray device. The image is taken from Ref. [38]

The uncertainty of axial position of an ion from the gate electrode plane may also induce uncertainty in the flight length. For example, with a gate signal switching from closed state to open state within, say 25 ns, a charge at speed, say 40 km/s, may be anywhere between 0 mm to 1 mm from the plane of the gate electrode to enter the drift tube. Also, finite width of the electrodes, the axial depth of a Faraday cup detector and overall uncertainty in the measured distance between the emitter tip and the detection plane may give rise to possible spreading in the flight length. Therefore, the flight tube length should be large enough such that this uncertainty is negligible. The ILIS characterization setup in MIT consists of a flight length of 75.7 cm [41], [43], [44]. On the other hand, in [59], a flight length, variable between 8.7 cm and 17.0 cm has been used to measure angular distribution of emission composition. The ToF setup in QMUL consists of a 40 cm long flight tube with the option of changing the relative position of a Faraday cup detector laterally [63] or axially [91].

2.1.3. Kinetic energy spreading

Kinetic energy spread, unlike temporal spread and spatial spread, is more a characteristic of the emission process itself. Apart from Ohmic losses in the emitter connections, finite conductivity of the electrospraying liquid, the potential distribution on the liquid meniscus, and energy required to bring neutral molecules in liquid phase to charged state in gas phase contribute to kinetic energy deficits [41], [39], i.e. $(qV_{em} - K.E.)$. Fragmentation of the solvated ions or droplets, space charge effect and self-repulsion among the charges themselves cause spreading in the axial speed and hence in kinetic energy of the individual particles [41], [39]. If fragmentation occurs inside the accelerating region of the emitter, the velocity distribution of the fragmented ions before exiting the extractor aperture reflects on the flight time. However, fragmentation in the field-free region does not change the axial velocity of the charge species further and hence does not add to further spread in the flight times. As mentioned towards the beginning of the section, this deficit and spread (FWHM), both can be as high as 10% for mixed ion-droplet emission and around 1−3% in purely ionic emission. The deficit and spread can be quantitatively measured with an optimally designed retarding potential analyzer consisting of five [5], [92] to seven [41] grids creating a smooth electrostatic potential barrier.

While RPA analysis provides information about the kinetic energy distribution among the particles, and can be used to correct for the deficit in actual kinetic energy of the emitted particles, this is difficult when there is large spread in the kinetic energy or different bands of kinetic energy with significant spreading, such as the case of mixed ion-droplet emission [35]. Energy focusing arrangements, such as a reflectron, first introduced by Mamyrin *et al.* in 1973 [93], can reduce the effect of kinetic energy spreading on the flight time spreading for the same q/m by allowing higher kinetic energy particles travel longer flight path. Reflectron or ion-mirror is widely used in modern ToF-MS systems as well. In Figure 2.8, schematic of Agilent G3250AA LC/MSD TOF System [94] is shown. It consists of five vacuum stages with the electrospray ionization source in the first stage, two octo-pole ion-guide stages for focusing and accelerating the ions, a beam shaping stage for parallelizing the beam and finally an ion-mirror based flight tube to produce a resolution of the order of several thousands.
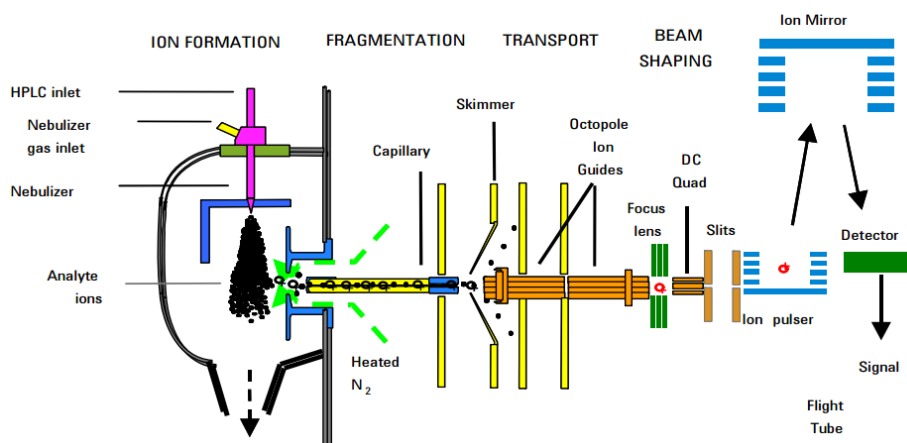
Figure 2.8: Schematic of Agilent G3250AA LC/MSD TOF System [94]

A study, based on inter-laboratory comparison research, has shown in 2003 [95] that, apart from other mass spectrometers like magnetic sector, Fourier transform mass spectrometer

(FTMS), modern ToF-MS can be potentially a high mass accuracy instrument routinely measuring down to around 10 p.p.m. mass accuracy. Ferrer and Thurman reported [96] an accurate ESI-TOF measurement of the mass of an electron. A list of commercially available ToF-MS instruments has been reproduced from different references in Table 2.1.

Table 2.1: List of some commercially available ToF-MS instruments and their mass resolution and mass range

ToF-MS	Mass resolution $m/\Delta m$ (FWHM)	Mass range in a.m.u./e^*	Ref.
Tofwerk HTOF	3000–10000	≤ 4000	[97]
Tofwerk CTOF	700–1000	≤ 4000	[97]
Waters LCT Premier	10000	18000	[98]
Agilent LC/MSD TOF	10000	7000	[98]
Bruker MicroTOF	10000	3000	[98]

$^*e$ = Electronic charge, 1.602×10^{-19} C

2.1.4. ToF mass resolution vs. mass range for electrospray propulsion devices

While mass resolution is a primary aspect in mass spectrometric analysis in biological research, there are several applications, where ability of ToF-MS to analyse the complete mass range rather than mass accuracy is utilized [99], [100]. Examples include chromatography, pyrolysis, desorption, on-line analysis of gas mixtures etc. [101], [102] where fast attainment of the entire mass spectrum is important because of rapidly changing sample composition. For example, investigation of kinetics and mechanisms of thermal decomposition and production of intermediate radicals in pyrolysis poses an essential criterion of real-time monitoring of the mass-spectrum [103], [104]. Monitoring time evolution of growing bacteria [105], [106] and their temporal characteristics, especially for bioterror agents, require mass spectra within minutes [107] for clinical and environmental applications. For high-speed ion-imaging applications, an entire mass spectrum is required from each pixel, and imaging an entire object requires very fast attainment of the entire spectra [108].

Electrospray propulsion devices fall in this category, where mass range, rather than mass resolution and accuracy, is more important. For a typical electrospray emission from ionic liquid EMI-BF$_4$, the minimum mass of an ion can be 87 a.m.u. for BF$_4^-$ ions. For mixed ion-droplet emission, droplets can be two or three order of magnitude heavier [39]. Therefore, a maximum mass resolution of the order of 1000 is required to characterize them if the emission consists of the entire range. For purely ionic emission, a much poorer resolution can be acceptable. In the electrospray characterization setup in MIT, a $T_F/\Delta T_F = 33$ is reported for characterization of PIR emission [41]. However, looking at Eqn. (1.3), since $Th \propto I \times m^{1/2}$ for a constant V_{em} a droplet with a given m can produce equal thrust as a hundred times lighter ion even if the corresponding current level is only 10% of that of the ion, and hence the mass range to measure is critical. Also time-variation of the spray properties of the source over its lifetime requires acquiring the mass spectra in quick time. Transmission of the emitted charges to the detector [72] is a primary requirement as well, mainly due to:

- Very low emission current levels from single emitters (can be as low as a few 10s of nA [44])

- Wide emission divergence (can be as high as 40° for micro-fabricated capillary devices [86]).

- Angular zones of ions and droplet emission with higher q/m usually away from the axis of emission ([109], [87])

Therefore, instead of a costly, high mass resolution ToF-MS, rapid and customized development of a ToF measurement system is usually preferred by electrospray propulsion research groups mainly for two diagnostics purposes:

- To know the spray composition, and thereby

- Estimate propulsive properties of the device.

In Chapter 3, design of an electrostatic ion-guide based ToF-MS for spray composition measurement from electrospray propulsion device is discussed. This ion-guide electrostatically guides the emitted charged particles with wide emission divergence along the flight tube axis to be detected on a small detector, thus increasing the transmission of the MS system. This reduces the gain limitation of a transimpedance amplifier for ToF traces and measures the emission composition over a large fraction of the emission to produce the mass spectra. However, the designed ion-guide introduces additional spreading in the ToF traces and reduces accuracy in estimation of propulsive parameters.

2.1.5. Propulsion parameters from ToF traces

ToF traces are used for evaluation of propulsive property from electrospray propulsion devices from the early stage of colloid thruster research. In [34], Stark and Sherman used ToF measurements as a means of calculating propulsive parameters like thrust and specific impulse. From the ToF current traces $I(t)$, the propulsion parameters, i.e. thrust, mass flow rate and specific impulse can be defined using the following equations [110]

$$Th = \frac{2V_{\text{em}}}{L}\int_0^\infty t\,\frac{\mathrm{d}I}{\mathrm{d}t}\,\mathrm{d}t \tag{2.8}$$

$$\dot{m} = \frac{2V_{\text{em}}}{L^2}\int_0^\infty t^2\,\frac{\mathrm{d}I}{\mathrm{d}t}\,\mathrm{d}t \tag{2.9}$$

$$I_{\text{sp}} = \frac{Th}{\dot{m}g_0} = \frac{L}{g_0}\frac{\displaystyle\int_0^\infty t\,\frac{\mathrm{d}I}{\mathrm{d}t}\,\mathrm{d}t}{\displaystyle\int_0^\infty t^2\,\frac{\mathrm{d}I}{\mathrm{d}t}\,\mathrm{d}t} \tag{2.10}$$

These equations intrinsically assume:

- The entire emission is unidirectional and all charged particles are emitted parallel to the axis of the spray, without any angular spread.

- The kinetic energy of the emitted particles is given by qV_{em}, i.e. there is no deficit and spread in kinetic energy. When energy deficit is known, *Th* can be better approximated by replacing V_{em} by *K.E./e*.

- No neutral particles generated in the acceleration region.

These assumptions are approximate for electrospray propulsion devices as the emission may take place over a wide emission angle and there might be a non-zero q/m gradient in the cross-section of the emitted beam. Error in kinetic energy deficit can be reduced by using measured kinetic energy by RPA method and considering the Ohmic losses. However, kinetic energy spread among the same q/m particles may intrinsically add error in the estimates. These issues are discussed in section 7.2 in Chapter 7 for comparing the measured thrust from the designed thrust stand with the estimated thrust from ToF traces. Finally, neutral particles may or may not generate during the acceleration time of a charged particle by fragmentation and the neutrals do not register on the ToF traces although they may generate significant thrust in the emission process.

It can be seen from Eqn. (1.2) and (1.3) in Chapter 1 that, for a mono-energetic emission of only one type of ions with a given m/q and constant current,

$$\left|\frac{\Delta Th}{Th}\right| = \left|\frac{\Delta I_{sp}}{I_{sp}}\right| = \frac{1}{2}\left|\frac{\Delta m}{m}\right| = \left|\frac{\Delta T_F}{T_F}\right| \tag{2.9}$$

With a high mass resolution of $m/\Delta m = 10000$ from the state-of-the-art ToF-MS (see Table 2.1 for example), thrust can be resolved with a resolution of 0.02% of the total range. For a 100 μN maximum thrust corresponding to the maximum detectable mass of the charged species, this corresponds to a resolution of 20 nN. However, with the ToF systems used in electrospray propulsion diagnostics, the resolution is expected to be much poorer. Moreover, the inaccuracies due to kinetic energy spread, angular spread in the emission and possibility of neutrals in the emission can be significant.

On the other hand, direct and accurate measurement of thrust from different types of micro-propulsion devices is underway in many research groups targeting sub-100 nN thrust resolution over several 10s of μN ranges. In the following section, a literature survey of different direct thrust measurement setups in the μN ranges with a resolution in the sub-μN and sub-100 nN ranges is provided.

2.2. Literature survey on nN-μN thrust measurement

With the growing interest in nano- and pico satellites, interest in small thrusters that can produce μN thrusts at high specific impulse is increasing as discussed in section 1.1. While indirect measurement of thrust as described in section 2.1.5 by ToF measurement of the emitted particles has been underway for a long time for electrospray propulsion devices, interest in development of thrust stands capable of directly measuring thrust from different types of micro-thrusters with sub-100 nN resolution is also increasing. Such precise thrust measurement is usually susceptible to effects such as facility vibrations, highway traffic,

personnel movement, ocean tide etc. [111] and in this section, the main emphasis is given to techniques of measuring μN thrusts and addressing the challenges in measuring direct sub-μN thrusts.

2.2.1 Early thrust measurement experiments

Since the early 70's of the last century, direct thrust measurement from micro-propulsion devices was based on converting the thrust into an inertial signal (e.g. displacement, rotation) and measuring the signal with inductive proximity probe, accelerometer, linear variable differential transformer (LVDT), differential plate capacitance systems etc., (reference to these can be found in [111]). During the 70's, one of the most sensitive μN thrust measurement facilities was developed by Goddard Space Flight Centre at NASA. Their micro-pound extended range thrust stand (MERTS), as shown in Figure 2.9, consisted of a torsional flexural pivot platform with two flexural pivots, a support tube and balance beam assembly between the pivots, a supporting frame where the thruster is mounted, a motorized counterweight mechanism, a magnetic damper to reduce transient vibration during steady-state thrust operation and a differential plate capacitance [112] readout system. The support tube works as an axis of rotation when thrust is generated. The counterweight enables the rotating structure to be statically balanced so that the noise output from the capacitor sensor due to external vibration can be minimized. The thruster is mounted 51 cm away from the axis of rotation for deflection that can be readout by the capacitor sensor. The targeted thrust level to measure was 4.4 μN–220 mN with a resolution 0.13 μN leading to an extremely large dynamic range which was not possible to measure with contemporary displacement or angular transducers except for a customized capacitive readout. Although the thrust stand met most of the design objectives, its performance was limited by the noise generated by building vibrations. The natural torsional frequency of the balance beam system was 84 mHz making the system susceptible to building vibrations in spite of several damping mechanisms.
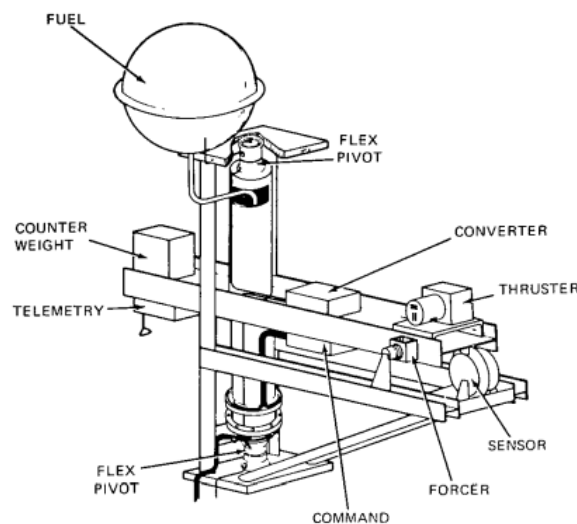
Figure 2.9: Schematic of the Micropound Extended Range Thrust Stand (MERTS) at Goddard Space Flight Centre at NASA [112]

Almost contemporarily, at MIT Lincoln Laboratory, a pendulum type thrust stand was developed [113], [114] for characterization of their pulsed electric thrusters (PET) LES-6,

capable of 2.7µN.s to 3.2 µN.s impulse. In this scheme, the thruster was mounted on a several inch long pendulum and was pulsed in synchronism with the oscillation frequency of the pendulum to observe the change in amplitude of oscillation of the pendulum as a measure of the impulse. To achieve nearly undamped oscillation of the pendulum, the setup was built inside a bell jar and pressure was set below 10^{-6} mBar and nearly 13 h of damping time was achieved. Before every run, it was ensured that the pendulum in its rest position is hung vertically without shift in its centre of mass so that there is no drift of the period of oscillation from run to run. Amplitude of oscillation of the resonating pendulum was measured with an aluminium pointer within 5% accuracy. The entire system was several metres in size and required very long experimental time due to prior adjustments to bring it to rest. The advantage of this resonant measurement is that it can eliminate the effects on the response due to external vibrations. However, this technique is limited to pulsed thrusters only as the pulse frequency can be synchronized with the pendulum natural frequency.

Only in the last two decades, direct thrust measurement of the order of 1 µN had been possible. These are particularly interesting for electrospraying colloid/ion thrusters. Apart from measurement down to µN to sub-µN levels, these thrusters also impose other requirements on the thrust stand such as

- These thrusters operate at kV order of potentials and in high vacuum conditions, typically of the order of 10^{-6} mBar or less. Apart from external noise sources discussed above, the vacuum pump generates strong vibration which can mask the low thrust output from the thruster.

- Rigidity of the high voltage cables and wiring on the thruster pose additional limitation of sensitivity of the thrust stand.

- Propellant flow connections.

Torsional balances have been used for very small force measurements in different fields of research. For example, Adelberger *et. al.* [115] used this principle for measuring force arising from the exchange of ultra-low-mass bosons. The main advantage of torsion balance is that it uses symmetric masses about the torsion axis to eliminate large gravitational offsets that may arise due to large weight to thrust ratio of the thrusters and only horizontal forces can be sensitively detected with proper adjustments. They are principally less sensitive to vibrations, capable of handling more thruster weight and simpler from the overall system point of view. For example, the thruster used in MERTS [112] had a weight 133 N and the minimum targeted thrust to be measured was 4.4 µN, giving a maximum weight to thrust ratio around 30×10^6. For µN to sub-µN thrust measurements as well, torsional balance have been indicated to be the most efficient and sensitive technique in Ref. [116], [117] for measurement of thrust from FEEP thrusters. Additionally, in [116], [117], complexity of feed-through to the thruster mounted on the torsion arm was significantly reduced by using the same tungsten wire as the suspending torsional spring and the electrical connection to the emitter. Optical readout was achieved using a mirror on the axis of torsion and homodyne detection scheme and down to 1 µN resolution was achieved. In another intuitive design, the torsional spring was a hollow wire also carrying the propellant to a colloid thruster [118].

Many torsional thrust stands have been reported in the last two decades with almost the same set of building blocks but different geometries and detection schemes for characterization of

different types of micro-thrusters. In [119], LES 8/9 PPT has been tested with a torsion balance with 0.59 m long torsion arm and 70 mHz natural frequency within 1% accuracy over 573 μN average thrust level. An LVDT was utilized for force transduction and was mounted between the stationary structure and the torsion arm to measure its deflection with a resolution of 500 nm. In order to remove unwanted thrust stand vibrations, the setup was electromechanically damped. Since the weight to thrust ratio was of the order of 10^5, small gravitational perturbations, slight horizontal misalignment and minute distortions in the vacuum facility significantly affect the performance and a typical zero-thrust drift of 1% of the total thrust was recorded which limited the accuracy of the measurements.

In a different approach, Princeton University developed a laser interferometric proximeter system (IPS) [111]. In this setup, the thruster was mounted on a swinging arm and deflection of the arm was measured using Michelson interferometer. This setup was potentially capable of resolving 10 μN thrusts and was particularly beneficial in removing electromagnetic interference (EMI) common in high current PPTs.

2.2.2   State-of-the-art: Towards sub-μN resolutions

In the last 15 years, several thrust stands have been reported successfully resolving below 1 μN thrusts. A summary of the performance of some of the sub-μN resolution thrust stands, some of which will be discussed in this section, is listed in Table 2.2 at the end of the chapter.

In European Space research and Technology Centre (ESTEC), a nulled-pendulum has been developed to characterize their FEEP thrusters in the range up to 100 μN with a targeted 10 nN resolution [120]. This setup is a twin balance with two identical pendula, one with the thruster under test and the other with a dummy load, so that external tilt and vibration affect both of them identically and by subtracting the thrust output from the two balances, the actual thrust can be measured. The deflections of the pendula are monitored using capacitive transducer. However, slight imbalance between the masses, differences in the feed-through assembly, the deflection monitoring system and undesired torsional vibrations in the two balances lead to detrimental effect on the resolution. Calibration performed with magnetic force suggested 0.3–0.5 μN to be the best resolution in a least disturbed environment, however, these values degraded by an order of magnitude under normal conditions. Later, a linear minimum mean-square error filter was implemented and 0.1 μN thrust resolution was achieved [121].

A quite similar approach has been reported in [122] where balancing is achieved by two separate identical plate-pendula suspended from an athermic spacer to nullify gravity, tilt and vibration, one of them carrying the thruster and the other a dummy identical load. However, the force transduction is achieved by using the distance between the plates under thrust as the cavity of a Fabry-Perot interferometer and measuring the frequency shift of a laser beam resonating in the cavity between the two plates.

A completely different approach from these previous examples and similar to the resonating pendulum configuration in MIT [113], has also been reported by Air Force Research Laboratory (AFRL) to potentially resolve 40 nN thrusts [123], however, thrust levels of no less than 5 μN had been tested.

At microthrust facility in JPL, a torsion balance was developed to adapt many types of microthrusters [124] and they tested many different types of microthrusters such as micro-

cold gas thruster, Indium FEEP [125], gas-fed PPT etc. They modified the design from Princeton University [111] IPS and used LVDT to measure thrust.

At ONERA, the French Aerospace Lab, a vertical pendulum thrust stand with counter-mass has been developed for sub-μN thrust resolution using capacitive sensor. A schematic of their vertical pendulum setup is shown in Figure 2.10 [126], [127]. They also use two accelerometers to for tilt and structure vibration measurement. They measured thrust from Indium FEEP thruster [126] and cold-gas thruster [127]. Recently they have reported a 100 nN resolution and 10 mN thrust range in their setup for ESA's GAIA cold-gas thruster evaluation [127].
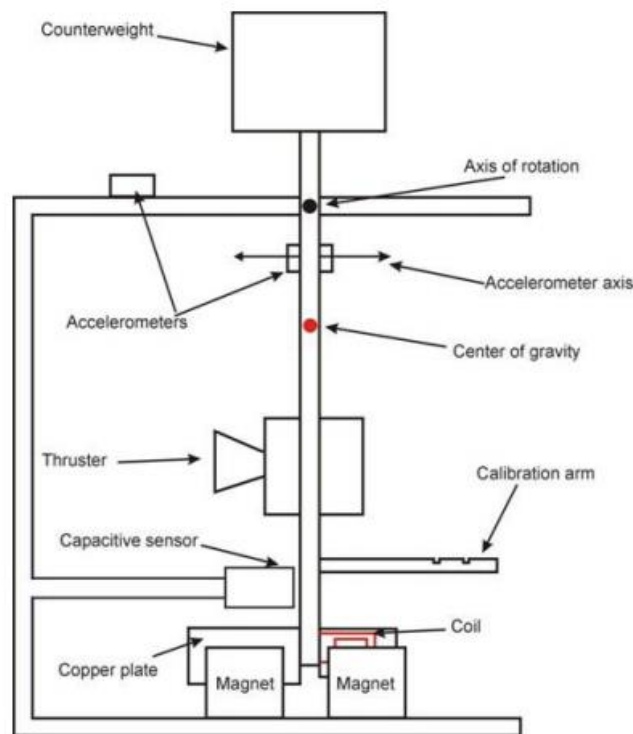
Figure 2.10: Schematic of the vertical pendulum thrust stand at ONERA, France [127]

In [128], another torsion balance was reported by Busek and MIT, principally identical to the MERTS [112] with two flexural pivots, 48 cm long torsion arms for the thruster and the dummy load and fibre optic displacement sensor. In order to remove undesired vibration and mechanical noise from the otherwise weakly damped system, an external damping circuit is implemented to derive the velocity of the arm under excitation and give a damping torque feedback to the arm to quickly achieve steady deflection. An electrospray needle is used as the thruster and 0.11 μN minimum thrust was measured with a potentially 10 nN achievable resolution. Till date, this is one of the best nN thrust stands reported. They later performed continuous thrust measurement from colloid thrusters and impulse bit measurement from PPTs [129]. A schematic of the torsion balance is shown in Figure 2.11.

In [130], [131] another nano-Newton thrust stand (nNTS), utilizing torsion balance with the two-flexure pivot arrangement is reported by University of Southern California (USC) and AFRL, USA. The thruster and the dummy mass are symmetrically mounted 25 cm away from the axis of rotation and an LVDT is located at 19.7 cm from the axis. For thrust levels below 1 μN, the LVDT is located at a distance 61 cm on symmetrically placed extended arms for

higher deflection. One of the key features of this thrust stand is use of a high-viscosity liquid baths as propellant feed-through for the thruster and also as a damper for steady state operation as shown in Fig. 2.12. The mechanical isolation of the feed-through achieved through this liquid bath reduces the critical constraint of feed-through driven forces on the thrust stand by not allowing direct mechanical solid contact. Calibration of the setup was performed using under-expanded helium (He) through a calibration orifice as a dummy thruster and comparing with a simulation model and very good agreement was obtained down to around 0.09 μN thrust level. The calibration facility described in the work was the first to perform under 1 μN thrust levels.
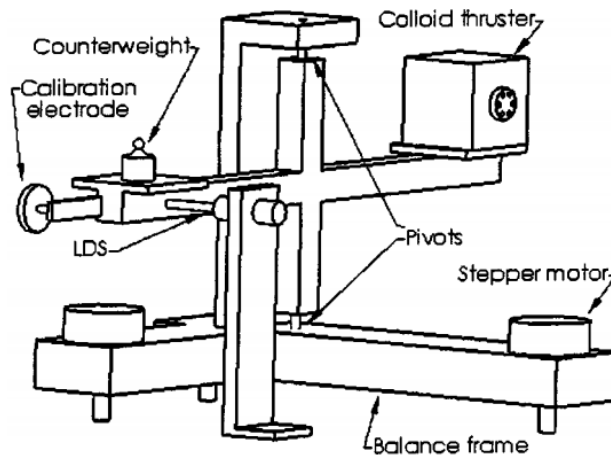
Figure 2.11: Schematic of the torsional balance developed in Busek and MIT [129].
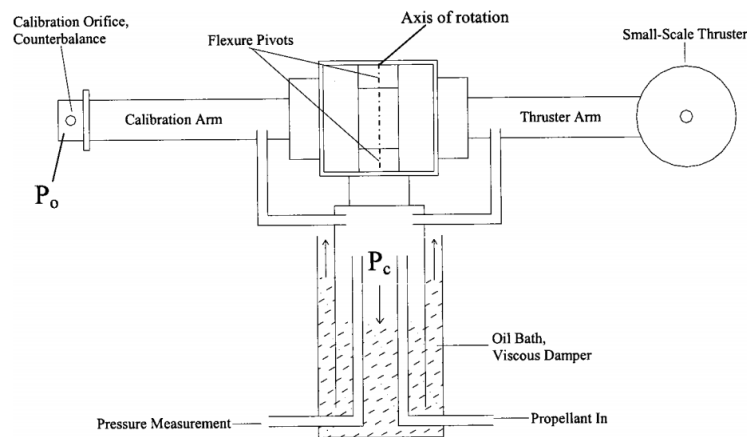
Figure 2.12: Schematic of the torsional balance nNTS in Ref. [131]

In Photonics Associates, New Mexico, a torsion balance was developed for characterization of laser ablation jet type thruster with 25 nN resolution. They used an angular deflection sensing technique using corner cube mounted on the axis of rotation of the torsion spring as shown in Figure 2.13 and measured thrust by observing the fringes from two reflected beams from the corner cube on a screen [132]. Implanting the interferometric element, the corner cube, on the thrust stand torsion bar was the only reported example of its type and was a modification to their earlier thrust stand [133] which could measure thrust with an accuracy of 1 μN. They also incorporated a critical damping oil bath in the new setup for removing transient rotations.
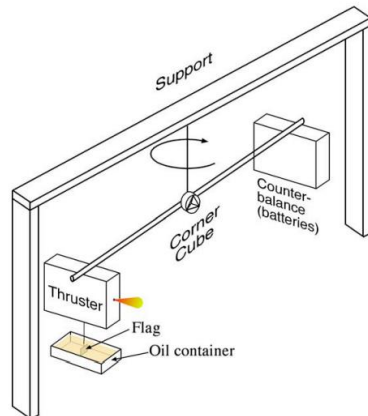
Figure 2.13: Schematic of the 25 nN resolution torsion balance type thrust stand in Photonics Associates [132].

Recently, a magnetically levitated thrust balance (MLTB) has been reported by MIT, a schematic of which is shown in Figure 2.14 [134]. In this test-bed, the small satellite with an ion electrospray propulsion system (iEPS) can be magnetically levitated to a zero friction environment and thrust is measured by monitoring the movement of the satellite free to rotate only in one rotational degree of freedom (DOF). The advantage of this technique is the thrust measurement limit is not limited by the stiffness of the pivots used in torsional thrust stands and rotational speed of the levitated satellite is the measure of thrust. However, an oscillation at around 4 mHz of the thruster due to imperfect magnets for levitation limits the noise floor of thrust measurement to 145 nN so far.
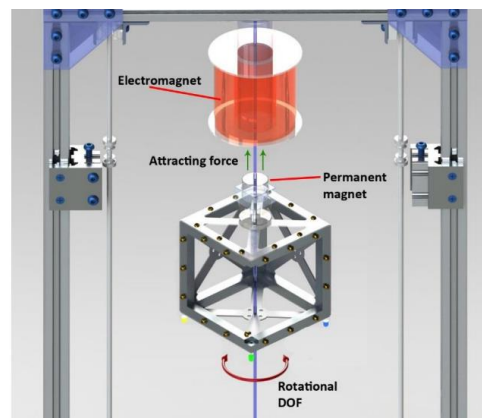
Figure 2.14: Magnetically levitated thrust balance (MLTB) at MIT [134].

Recently, Yang *et.al.* [135], Sony and Roy [136] also reported development of nano-Newton thrust stands using torsion balance with capacitive transducer and LVDT as sensing element respectively. However, the 10 nN resolution remains a bottleneck. Also, the minimum thrust level measured so far is reported to be around 0.09 μN [131] whereas the resolution is mostly derived from either the standard deviation of the measured thrust or from noise floor measurement without any thrust. This is partly because the calibration techniques used in most of the experiments could not generate reliable forces below 100 nN.

2.2.3 Challenges in resolving nN thrusts

From the survey, it can be seen different approaches have been used in resolving nN thrusts.

Torsion balance gains over other techniques such as hanging pendulum or inverted pendulum because the deflection is almost independent of the thruster mass, making it most sensitive to horizontal imbalance of the forces on the two arms even with very high weight to thrust ratios [137]. Hanging pendulums are usually simpler and highly stable with respect to external perturbations, however, nN sensitivity can be achieved only with very long pendulum arms [137]. Inverted pendulum approach provides better sensitivity than hanging pendulum in general and thus is suitable for moderate thrust to weight ratios, although stability is strongly dependent on the stiffness of the flexures, limiting its sensitivity to µN or above [119].

However, one of the difficulties with the torsional balance is that the horizontal, asymmetric or symmetric arms of the balance are quite large, typically in the range of 10s of cm, to generate measurable deflection generated by the torque of the thrust. As a result, the vacuum chamber required for such thrust stand is also quite large. With limitations in pumping capability and space and budget constraints, it is difficult to implement. Also, during experiments, it is often necessary to account and correct for the drifts and tilt of the thrust stand and hence tilt sensor, motorized tilt-adjustment, in-situ drift correction are often unavoidable complexity in the setup [137]. For example, the torsional thrust stand in Busek [129] comprises of 22 cm long arms and is equipped with two stepping motors to control inclination. In [136], the torsion arm is 28.5 cm long. The nNTS developed in USC [131] has 61 cm long arms and was installed in a 3 m diameter by 6 m long cryogenically pumped space simulation capable vacuum chamber. For the nulled pendulum configuration used in ESTEC is used a chamber with 1.2 m height and 1 m diameter [138].

The necessity of large torsion arms is mostly driven by the limitation of the angular or displacement sensor available and the torsional spring constant of the pivoted torsion spring. In most cases, the transducer is either a LVDT or a capacitive sensor or an optical displacement sensor for measuring thrust-end deflection or optical interferometry to measure angular or linear deflection. The pivots used in [128], [131], [136] had 0.0016 N.m/s spring constant. The LVDT used in [131] had sensitivity 260 mV/mm and with the implemented data recording and digitizing scheme, the minimum resolvable displacement was of the order of 10s of nm. Fibre optic Linear Displacement Sensor (LDS) has been used for displacement measurement with 5 nm resolution in [129], [136]. The IPS setup in Princeton University [111] had a 10 nm resolution. Capacitive displacement sensor used in [120], [121] had a resolution of 1 nm. As an order of magnitude calculation, if a 10 nN thrust is to generate a 1 nm deflection of the torsion arm with a 0.0016 N.m/s torsional spring constant of the pivot assembly, the required length of the arm is 12 cm. For lower sensitivity of the transducer, the required length will be higher.

One major challenge in measuring low thrusts is the response time of the arms during thrust build-up, where steady-state deflection of the arms is the measure of the average thrust. Due to large arms, the natural frequency of the stands is generally very low ranging from sub-Hz to Hz. Therefore, under normal conditions, the arms need several seconds to minutes before coming to rest and therefore the measurement speed is handicapped unless they are externally damped. In vacuum the problems are severer. For example, the thrust stand in Princeton University and JPL [111], [125], the natural frequency of the thrust stand was around 0.1 Hz. Busek thrust stand had a natural frequency of 0.4 Hz. The nulled pendulum stand at Busek had a natural frequency 3 Hz. As a result, different external damping mechanisms are implemented in the reported thrust stands. Magnetic damper is often used either to generate

Eddy current [136], [137] or to give a magnetic force feedback [121] to the thrust stand. Busek thrust stand [129] utilizes an electrostatic force on the arms to damp it from the same electrodes used for calibrating the thrust stand. On the other hand, as described earlier, vacuum compatible oil has been used to viscously damp the torsion of the pivot flexure in [131]. With damping the steady state can be achieved quickly, typically within 4−5 natural periods of the stand. However, the response times of the damped systems are still in a region susceptible to facility vibration, which is most prominent in sub-Hz to Hz ranges. As a result, drifts in the thrust stand output are one of the major problems. The slow drifts of the thrust stand output can be comparable to the minimum thrust levels to be detected and hence is a major challenge to eliminate. In MERTS [112], vibration isolation was implemented by suspending the thrust stand from springs, however, this introduced additional low frequency wandering of the entire thrust stand. In [120], twin balance was used for cancelling the vibration effects; however, improved results down to 0.1 μN could be achieved only after using a mean-square error filter algorithm. Vibration isolation table with active vibration velocity feedback can be implemented as suggested in [129]. Also, synchronous detection has been suggested by [116] to eliminate these low-frequency perturbations and drifts. The natural frequency of the torsional balance in [116] was 0.01 Hz, and to avoid resonance, FEEP thruster was excited at a frequency 0.1 Hz and 1 μN thrust accuracy was achieved with synchronous detection.

It might therefore be suggestive that operating in synchronous detection mode at higher frequencies might be one way of eliminating the low frequency vibrations and drifts. In this way, the thruster or the transducer can be excited at a known reference frequency and measurement can be done at the same frequency using a lock-in amplifier. However, this is limited by the low natural frequencies of the existing thrust stands and a higher natural frequency of the thrust stand will be desirable. For example, in [122], the deflecting plates were reported to have natural frequency 13.5 Hz and synchronous detection was implemented successfully. In this case, excitation of the low frequency vibrations can be isolated; also the high frequency transient oscillations of the thrust stand during thrust build up cannot couple to the locked-in output as long as the excitation frequency is widely away from the natural frequency. This also reduces emphasis on the damping mechanisms and ideally, can be removed to build a much simpler thrust stand. Present thrust stands are limited in their natural frequencies due to the long torsion arms required for the deflection detection capabilities of the transducers.

Another generic challenge in the sensitivity of thrust stands arises from the connectors and propellant supply to the thrusters mounted on the very sensitive torsion arm. The rigidity of the connectors, slight imbalance of their tension during operation etc. can lead to significant drift in the thrust measurement. Ingenious novelty has been found in dealing with these problems in literature. In [116]−[118], the electrical and propellant feed-through to the thruster were used as the torsion springs, thus reducing extra connectors. In the USC thrust stand [131] propellant feed-through to the thruster is provided through a viscous oil bath avoiding hard mechanical connection to the thruster. In ESTEC [116], all the pipelines coming into the vacuum chamber are rigidly cemented on the floor to avoid vibration coupling through them. However, most thrust stands are developed targeting and optimized for characterization of one particular type of thruster. For example, ESTEC primarily concentrated on characterization of their FEEP microthrusters. Again, the viscous liquid interface in the nNTS [131] can contaminate the ionic liquid propellant colloid thrusters

although it was not a problem for their gas dynamic calibration technique. Adapting a particular thrust stand for different types of thrusters is difficult because of their different weights, electrical and propellant feed-through. The JPL thrust stand [124] in particular has reported adapting their thrust stand for experiments with different types of thrusters in the sub-μN ranges. Onera thrust stand has been used for InFEEP and cold gas thruster.

2.2.4   Thrust measurement by measuring impingement force

One solution to this adaptability issue can be complete isolation of the thruster from the thrust stand, in which, the thruster is mounted separately and the thrust stand measures the impingement force by intercepting the emitted particles instead of directly on the thruster. By complete isolation, the electrical and propellant feed-through to the thruster will have practically no effect on the thrust stand. In this way, the thrust stand can be adapted to any type of thruster with wide thrust to weight ratio ranges without affecting the performance of the thrust stand. Also as the thrust stand does not have to carry the thruster; it can be made smaller and lighter and designed with high natural frequency.

However, this is not a direct thrust measurement method and the accuracy of the measured thrust depends on the accuracy with which the relation between the impingement force and the thrust is known, which may be different for different types of thrusters, and at different exhaust speeds. Unfortunately, this relation is difficult to obtain unambiguously for different types of thrusters. In section 6.1.3 in Chapter 6 and section 7.4.4 in Chapter 7 more details on these relations will be presented for a low Mach number cold-gas ejecting capillary and for ionic liquid electrospray thrusters respectively, although, it can be emphasized here that these correlations are not completely accurate and depend on the type of thruster, the type and speed of the impinging particle etc.

Over the last few years, a few articles have been reported measuring thrust using this 'indirect' method [139]–[144], although at mN thrust ranges with resolution limited to a few μN to several hundred μN. In Figure 2.15, a schematic of the basic principle and that of the experimental setup used by Wu *et al* [139] for indirect thrust measurement is shown. In their experiments, cold nitrogen gas thruster at atmospheric pressure, and at low pressure (between 21.9 Pa and 66.9 Pa) and hot plasma from arc-jet thruster were used to generate the plume of particles which was intercepted by a plate. Impingement force on the plate of the order of 100 mN or above was measured with a pitot-type pressure probe and a pressure tap placed at the centre of the plate. They had also computed the relation between the impingement force and the thrust using Fluent software and had shown that these two are nearly same at atmospheric condition and at low pressure with cold nitrogen jet.

In [140], a similar method using an optical detection scheme has been presented and they obtained the similar relation between the computed thrust and measured impingement force from cold xenon and argon. However for hot gas (1500 K), the ratio of impingement force and the calculated thrust was significantly lower, around 0.3 for hot xenon and 0.6 for hot argon. They reported a resolution of 3 μN of their thrust stand. In [142], a momentum flux sensor has been reported by University of Houston, University of Michigan, Ann Arbor, Ad Astra Rocket Company and NASA Marshall Space Flight Center with 100 μN resolution. Force on a graphite coated disc was measured with a strain gauge from emission of a 5 kW xenon (Xe) Hall Effect thruster and compared   with   an   inverted   pendulum   thrust   stand measuring thrust on the thruster directly. In [143], West *et al* reported a momentum flux

measuring instrument (MFMI) with a 15 μN resolution and 20–500 μN range, measuring impingement force from cold gas flow and with a discharge ignited using argon propellant.

(a)   (b)
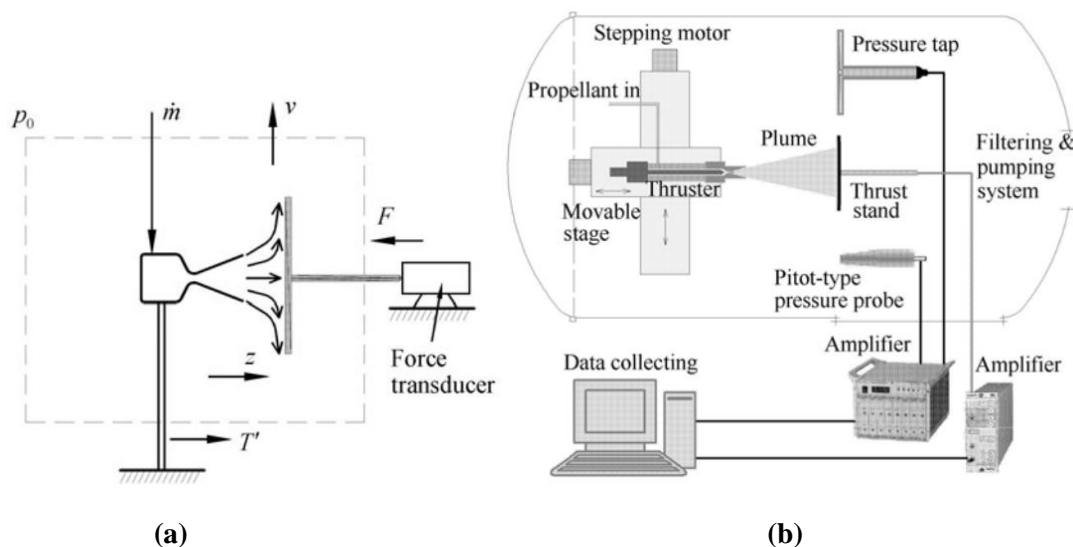
Figure 2.15: Schematic of the basic principle and (b) the test setup for indirect thrust measurement used by Wu *et al* [139]

In all the indirect thrust measurement techniques by measuring impingement force, the relation between the impingement force and thrust is the main source of inaccuracy in the thrust. However, the isolation between the thruster and the thrust stand allows for adaptation of the thrust stand to various types of thrusters. In the designed thrust stand in Chapter 5 of this thesis, this indirect approach has been taken with the aim of bringing the resolution down to 10 nN over a 100 μN force range and capability of adapting to different types of thrusters. In Chapter 6 and Chapter 7, thrust measurements with a cold-gas ejecting capillary and from an electrospray thruster are presented with the designed thrust stand. However, as seen in Chapter 6 and Chapter 7, the inaccuracy of the measured thrust in this method has been rather large, around 10%, although impingement force with around 10 nN to 20 nN resolution could be measured.

2.3. Summary

In this chapter, a literature survey on ToF-MS techniques for characterization of electrospray propulsion devices and thrust measurement techniques for micro-propulsion devices has been presented. The different time-of-flight measurement experimental setups for electrospray propulsion devices have been discussed on the basis of temporal, energy and spatial spreading. The propulsion parameters based on time-of-flight measurements have been defined which are used as means of finding thrust and specific impulse of the thrusters. However, the accuracy of thrust and specific impulse measurement from ToF measurement can be limited by the following reasons:

- Kinetic energy deficit and spread among the emitted species.

- Angular spread of emission.

- Distribution of q/m over emission cross-section.

- Unaccounted neutral particles

The first three issues can be approximately corrected for by RPA analysis and angle resolved measurement of ToF spectra. However, large kinetic energy spread among particles with same q/m, particularly for mixed ion-droplet emission from ionic liquid electrospray devices, can lead to large errors. Angle resolved spectral analysis by scanning over the beam cross section may be time consuming and lack sensitivity due to low signal at the detector and also does not work if the properties of the emitter changes with time. Focusing most of the charges or collecting most of the charges with a large plate accommodates a large fraction of the emission to be analysed in one scan, however, they cannot account for the effect of angular spread on the thrust, especially if there is a q/m gradient in the emission cross-section, and lead to increased spreading in the mass spectra.

In Chapter 3, design of a ToF-MS setup with an electrostatic ion-guide is presented that increases sensitivity of measurement by increasing throughput, i.e. by accommodating a large fraction of the emitted charged species on a small detector for ToF measurement; however, it will be shown that despite higher accommodation of the emitted beam for flight time measurement with a small detector, the ion-guide introduces additional spreading in the flight times to be measured and hence reduces resolution.

In the second part (section 2.2), a literature survey on different thrust stands for directly or indirectly (by measuring impingement force from the emitted particles) measuring thrust from micro-thrusters has been provided. The key challenges in direct thrust measurement in the μN ranges can be summarized below:

- Susceptibility to ambient vibrations, vibration from connectors and feed-through to the thruster.

- Requirement of damping, peripheral sensors to monitor tilt, drift etc.

- Adaptability to different types of thrusters.

- Large size of the thrust stand.

- Low natural frequency.

Indirect method, in which, thrust can be measured by measuring impingement force from the emitted plume can overcome some of these problems, but they have the following problems:

- Sub-μN resolution has not been reported so far.

- Accuracy limited by the relation between the impingement force and the generated thrust.

In Chapter 5, design of an indirectly measuring thrust stand is described that attempts to meet some of the challenging issues with directly measuring nN thrust stands and achieve nN level resolutions. Thrust measurement has been performed with cold-gas ejecting capillary and electrospray thruster in Chapter 6 and Chapter 7 respectively. However, it will be discussed in Chapter 6 and Chapter 7 that the inaccuracy in the relation between the impingement force and the actual thrust generated on the thruster head leads to inaccuracy in the measured thrust although the resolution of force measurement is around 10 nN to 20 nN.

Table 2.2: A list of thrust stands with sub-µN resolution.

Manufacturer [Ref]	Thrust stand type	Thruster used	Measurement principle	Resolution (µN)	Range (µN)
ONERA [126], [127]	Vertical pendulum	InFEEP, Cold gas	Capacitive	0.1	10000
ESTEC [120]	Twin pendula	InFEEP	Capacitive	0.3–0.5	10–100
Busek/MIT [128]	Mass balanced torsion arm	Colloid, FEEP	LDS	0.01	–
USC/AFRL [130]	Mass balanced torsion arm	FMMR	LVDT	0.014	0.08–1
AFRL [123]	Swinging gate pendulum	µPPT	LVDT	0.04	> 5
Busek [143]	Mass balanced torsion arm	Colloid, µPPT	LDS	0.03	–
NASA-JPL [124]	Torsional pendulum	Various	LVDT	< 1	200
Politecnico di Torino [122]	Nulled pendulum	–	Interferometer	0.01	100
Padova/ESTEC [121]	Nulled pendulum	FEEP	Capacitive	0.1	220
Photonic Associates [132], [133]	Mass balanced torsion arm	µLPT	Interferometer	0.025	0.1–500
H. U. S. T. [135]	Mass balanced torsion arm	PPT	Autocollimator	0.09	264

3

Design and Experimental setup for an ion-guide for electrospray propulsion sources

I t has been discussed in section 2.1 in Chapter 2 that time-of-flight mass spectrometers (ToF-MS) have been historically the most common tool to characterize electrospray sources for propulsion application. In contrast to MS systems that sample spectral intensities by scanning the mass range, ToF-MS can yield a complete spectrum of all detected particles with each measurement, thereby enabling analysis in real time. Depending on the speed of emitted particles from the electrospray source, the charges take different times to reach a detector placed at the end of a ToF tube and accordingly the current traces at the detector provides information about the different q/m ratio in the emission. However, the length of the flight tube and the detection sensitivity with a small detector are inversely related due to angular spreading of the emitted particles over the length of the flight tube. In this chapter, design of an electrostatic ion-guide based ToF-MS for collecting a large fraction of the emitted charged particles for flight time measurement is discussed. The design in this chapter, and the experimental results discussed in Chapter 4 have been published in the following article:

> S. Chakraborty, C. Ataman, D. G. Courtney, S. Dandavino, H. Shea, "A ToF-MS with a Highly Efficient Electrostatic Ion Guide for Characterization of Ionic Liquid Electrospray Sources", *Journal of The American Society for Mass Spectrometry*, vol. 25, issue 8, pp. 1364–1373, 2014.

In this chapter, first a trade-off is made in section 3.1 between the sensitivity requirements and spreading of the emission. Based on the study, the ion-guide design is discussed in section 3.2. The ion-guide consists of cascaded electrostatic lenses in the entire ToF path to continuously guide the charges parallel to the axis of the ion-guide, thus increasing the amount of charges reaching the detector. It is shown in section 3.3 that, for a given deflecting electric potential applied to it, the ion-guide can collect all mono-energetic charges over nearly 23° emission half-angle on a small Faraday cup detector placed at a distance nearly 60 times the diameter of the detector. However, accommodation of different flight lengths of the emitted particles, the ion-guide introduces spreading in the flight times for a given q/m and thus affecting mass resolution. Finally the details of the ToF-MS experimental setup with its different components are described in section 3.4. The experimental results with the ion-guide for two different types of electrospray sources are discussed in Chapter 4.

3.1.   Trade-offs for the ToF-MS

From the survey of ToF-MS systems for characterization of electrospray propulsion devices, it can be generally observed that it typically consists of at least the following sub-systems

shown in Figure 3.1.

1. The emission from the electrospray source is electrostatically gated with an electrode (or an assembly of multiple electrodes as discussed in section 2.1.1 in Chapter 2) with a response time much faster than the time-of-flight to be measured.

2. The ToF traces are recorded on an oscilloscope having fast sampling speed.

3. The current traces due to the different types of charge species in the emission is converted to a measurable voltage to be recorded with the oscilloscope with a transimpedance amplifier.

The transimpedance amplifier needs a bandwidth sufficiently high to respond much faster than the flight time to be measured; at the same time, its transimpedance gain needs to be sufficiently high to convert the detected current into a measurable voltage trace on an oscilloscope. Therefore, choice of the sub-systems is dominated by the current detected by the detector and the flight time to be resolved, which, in turn, is dictated by the m/q to be resolved. In the following sub-sections some trade-offs are made in the design on the ToF-MS. A summary of the trade-offs has been listed in Table 3.4 at the end of the section.
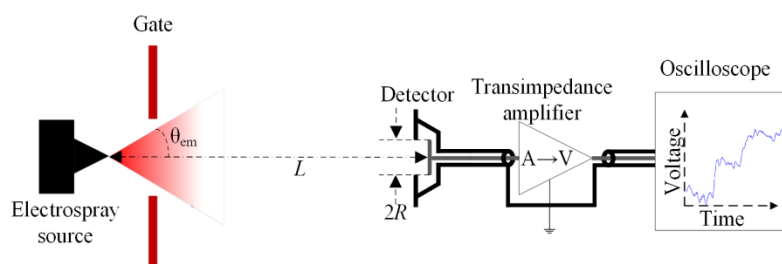
Figure 3.1: Schematic of a typical ToF measurement setup for electrospray propulsion devices. It consists of a gate in front and a detector at the end of a flight tube followed by a transimpedance amplifier for converting beam current into voltage. The output voltage traces of the transimpedance amplifier are monitored with an oscilloscope.

3.1.1. Electrospray sources to characterize

As discussed in section 1.2.3, two types of ionic liquid electrospray sources are used for mass spectrometric characterization. In Table 3.1, the typical reported characteristics of emission from these two types of devices have been summarized. Measurement of the emission-half-angle of the capillary emitters ($\sim 40^{\circ}$) in Table 3.1 is discussed in section 4.2.2 in Chapter 4 and more details can be found in the Ref. [86]. The geometries of the two types of emitters are discussed in section 3.4.1 in this chapter later. There are several ionic liquids which are potentially capable of use in ionic liquid electrospray sources, [35], [37]–[39], [44], [63], however, EMI-BF$_4$ is used as the ionic liquid with two different types of electrospray sources.

3.1.2. Flight time and flight tube length requirement

The smallest ion, BF$_4^-$, from EMI-BF$_4$ has a mass 87 a.m.u.. For the highest operating voltage $|V_{em}| = 2$ kV chosen for operation, the maximum speed of the BF$_4^-$ ion can be calculated from Eqn. (1.1) in Chapter 1 to be 66.6 km/s which corresponds to the minimum flight time to be measured with the ToF-MS. In design of the ToF-MS, this minimum flight time is chosen to

be ≥ 10 μs for BF_4^- ions if they are not further accelerated or decelerated in the drift tube after emission. It is shown in section 3.3.2 that the ion-guide continuously decelerates and accelerates the charges inside it, thereby increasing their flight times. The required flight tube length to ensure a minimum 10 μs flight time of BF_4^- ion at $|V_{em}| = 2$ kV can be calculated from Eqn. (2.5) to be $L = 66.6$ cm. This flight length is 9.1 cm shorter than the 75.7 cm used in [41], [44], [46] with an Einzel lens to focus the emitted ions, more than five times longer than the flight length used in [36] and four times longer than the maximum flight length used in [59], both with a large plate collector, and more than 50% longer than the flight length used in [55] with a Faraday cup detector FC-72A [145]. With this flight length, all other ions or droplets emitted at $|V_{em}| \leq 2$ kV will have flight times higher than 10 μs. It can be noted from Ref. [44] that, other ionic liquids potentially suitable for ionic liquid ionic source (ILIS), such as EMI-[F.2.3HF], can emit lighter ions (59 a.m.u.) and at the same operating V_{em} the minimum flight times may be smaller than 10 μs with this length; however, for most other ionic liquids, flight times will be higher than 10 μs.

Table 3.1: Type of electrospray sources used for characterization of the ToF-MS

Property	Value	
Emitter type	Externally wetted tungsten emitter	Micro-fabricated capillary emitter
Operating voltage, $|V_{em}|$	Up to ± 2 kV	Up to ± 1 kV
Emission half-angle	~ 15°	~ 40°
Operation regime	Purely ionic	Mixed ion-droplet
Current (at room temperature)	~ ± 100 nA	~ ± 1 μA
Reference	[44]	[61], [86]
Pressure	~ 10^{-6} (mBar) or less	
Ionic-liquid used	EMI-BF$_4$	
Mass of the smallest ion (BF_4^-)	87 a.m.u./e	

3.1.3. Transimpedance amplifier

As mentioned in section 2.1.1 in Chapter 2, flight times ≥ 10 μs can easily be detected from oscilloscopic traces. However, depending on the detected current level, the responsibility of the preceding transimpedance amplifier is to convert the current into a measurable voltage at the input channel of the oscilloscope. Both, transimpedance gain and available bandwidth of the transimpedance stage, are therefore required to be high. Commercial pico-ammeters can measure pA currents [146], but their sampling speed is too low for measurement of flight times in the μs order. High speed electrometers [36], [38]–[40], [43]–[47], [58], [59], [81] or commercial transimpedance amplifier DHPCA-100 [55], [61], [63] have been used in electrospray propulsion device characterization setups when the detected current level is of the order of 10 nA or higher. For the designed ToF-MS in this chapter, state-of-the-art DHPCA-

100 transimpedance amplifier has been chosen. In Table 3.2, a list of properties of DHPCA-100 is reproduced from Ref. [88]. It can be seen that, 10^6–10^7 V/A gain with above 1 MHz 3-dB bandwidth can be achieved with rise/fall time within 2% of the flight time to be measured. However, voltage signal at the input of the oscilloscope depends on the amount of current reaching the detector.

Table 3.2: Available gain and bandwidth settings of a FEMTO DHPCA-100 high speed transimpedance amplifier reproduced from Ref. [88]

Setting	Low noise						High speed					
Gain (V/A)	10^2	10^3	10^4	10^5	10^6	10^7	10^3	10^4	10^5	10^6	10^7	10^8
3-dB bandwidth (MHz)	200	80	14	3.5	1.8	0.22	175	80	14	3.5	1.8	0.22
Rise/fall time (10%–90%) under step input (ns)	1.8	4.4	25	100	200	1600	2	4.4	25	100	200	1600

3.1.4. Detector

It can be noted that for the chosen flight length of 66.6 cm, the required diameter of a detector plate to capture all charges emitted from a microfabricated capillary emitter over 40° emission half-angle is 111.8 cm. This size of the detector is impractically large given a limited size of a vacuum chamber and pumping capability. This required size is nearly 8.5 times larger than the plate used in [36], [59] with much smaller flight lengths. On the other hand, in [41], [44]–[46], instead of a large plate detector Einzel lens is used to focus the ions on a Faraday cup detector. If no focusing arrangement is used, the fraction of charges collected on the small detector is given by the ratio of solid angle subtended by the detector on the emitter to the solid angle of emission, assuming a uniform current density over the entire emission half-angle, i.e. charge collection fraction is

$$\eta = \frac{\left[1 - \cos\left\{ \tan^{-1}\left(\frac{R}{L} \right) \right\} \right]}{\left[1 - \cos\theta_{em} \right]} \tag{3.1}$$

where $R = D_c/2$ is the radius of the detector. In Table 3.3, the expected current detected by a FC-72A Faraday cup detector with a standard 1 cm^2 circular detection aperture [145] are listed for $L = 66.6$ cm if no focusing is used. The half-angle subtended by the small FC-72A detector with 1 cm^2 circular aperture on the emitter is only 0.5° and the current detected by the detector is only in the range of 100 pA. With the DHPCA-100 transimpedance amplifier, the 100 pA current can be converted to only 100 μV to 1 mV with 10^6–10^7 V/A transimpedance gain, which are not sufficient for reliable ToF measurement using the oscilloscope. At higher gain (10^8 V/A) around 10 mV signal output can be achieved, the 3-dB bandwidth is only 220 kHz and a rise/fall time 1.6 μs, as high as 16% of the minimum flight time to be detected.

The small Faraday cup detector can be replaced by a channel electron multiplier (CEM) or micro-channel plate (MCP) [147] of similar detection area (typically 2–6 mm outer diameter) that can pre-amplify the current by a factor of 10^4–10^8 at a very fast speed and hence the gain requirement on the transimpedance amplifier can be greatly relaxed for the desired bandwidth. They are widely used in mass spectrometric applications and work on the principle of avalanche of secondary emission triggered by the incident high energy particle [148]. Use of CEM in characterizing electrospray propulsion sources has been demonstrated by Lozano in his PhD thesis [39].

Table 3.3: Expected detected current for a flight length $L = 66.6$ cm and circular detector size of 1 cm^2 assuming uniform current density over the emission half-angle

Emitter type	Emission half-angle	Expected emission current (µA)[*]	Expected detected current (µA)
Externally wetted tungsten emitter	~ 15°	0.1	~ 105×10^{-6}
Micro-fabricated capillary emitter	~ 40°	1.0	~ 154×10^{-6}

[*]From Table 3.1

However, in the design of the ToF-MS, instead of amplifying a small fraction of emitted current, alternative approach of collecting a large fraction of the emitted current is considered for the following reasons.

- There may be non-uniform distribution of q/m over the emitted beam cross-section. Especially for mixed ion-droplet emission, evidence exists of localized angular zones of emission with high q/m particles typically away from the axis of emission [41], [59], [109], [87]. Analysis only from a small fraction of the emission may not reveal the entire mass spectra in the emission.

- Emission may be asymmetric w.r.t. the axis of the flight tube, due to misalignment of the emitter axis, or local formation of Taylor cone away from the tip of the emitter, or unstable due to instantaneous formation or annihilation of Taylor cones [15], particularly for externally wetted tungsten emitters [65].

The q/m distribution over the entire beam cross-section can be evaluated by varying the angular position of the emission axis with respect to the axis of the flight tube [58], [149]; however, covering the entire beam cross-section would require several scans depending on the size of the detector and the angular spread of emission and the following possible scenarios may inhibit the scan over the entire angular spread.

- The emission property may change due to electrochemical reaction, instantaneous formation or annihilation of Taylor cones.

- The prototype devices may not spray for the entire duration of the experiment.

A compromise can be made between the size of the detector and the time required in the entire angular scan; alternatively, the emitted particles can be focused on a small detector. In design of the ToF-MS in this chapter, the second approach is taken and a small Faraday cup detector FC-72A with $R = 5.64$ mm radius aperture (1 cm^2 area) is chosen at the end of the flight tube where the transmission of the emitted particles to the detector is attributed to the focusing capabilities of an ion-focusing arrangement.

3.1.5. Ion focusing

Ion-focusing can be achieved by electrostatically or electromagnetically deflecting the charges towards a desired axis of detection. Cylindrical Einzel lenses are particularly useful in electrostatically deflecting the charges towards its axis and have been used in mass-spectrometric applications [150]–[153] including ionic liquid electrospray device characterization [39], [40], [43]–[47]. An Einzel lens typically consists of three electrodes with a deflecting potential applied to the central one and the other two electrodes grounded as shown in Figure 3.2 from Ref. [154].
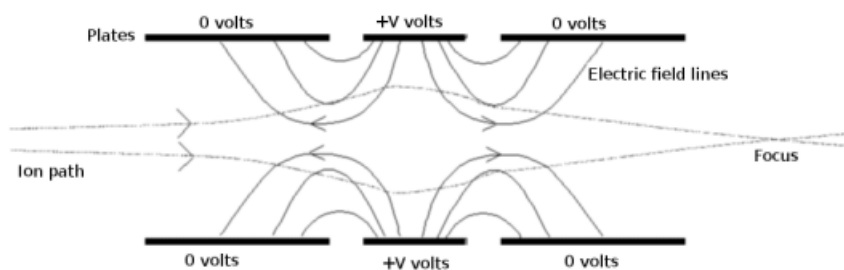
Figure 3.2: Schematic of a three-electrode Einzel lens taken from Ref. [[154]. Deflecting potential is applied go the central electrode and the other two electrodes are grounded.

In principle, a strong radial electric field in the Einzel lens deflects the charges towards the axis. The focusing capability of an Einzel lens is independent of the incident q/m and hence can focus a wide range of q/m with the same kinetic energy per unit charge [39]. The Einzel lens configuration reported in [39] was capable of focusing mono-energetic charges within 13° half-angle from its axis on a detector 15 cm away. Later, focusing capabilities of the Einzel lens has been used for ionic liquid based focused ion beam (FIB) applications from nearly mono-energetic emission from ILIS sources as well [45], [46]. In [39], detailed study with different kinetic energies of incident charged particles has been conducted. It can be generally concluded that for a given deflecting potential applied to the Einzel lens, kinetic energy within a narrow range can be focused whereas kinetic energy higher than the acceptable range are under-focused and kinetic energies below the acceptable range are over-focused, both diverging from the axis of the lens along the flight tube, a phenomenon similar to chromatic aberration in geometrical optics. Also, charges too close to the deflecting electrode surface are deflected differently than those close to the axis, similar to spherical aberration. Due to chromatic and spherical aberration, a wide range of kinetic energy and wide angular spread in the emitted particles cannot be focused for a given deflecting potential applied to the lens.

In Ref. [155], study of different geometric configurations of such three-electrode Einzel lenses have been performed for finding their chromatic and spherical aberrations. It has been observed that minimum spherical and chromatic aberration do not occur at the same

deflecting potential for the studied lens systems; and reducing spherical aberration by varying the deflecting potential increases chromatic aberration and vice versa.

Ion-guide

One modification to using a single-stage Einzel lens for accommodating higher kinetic energy spread and angular spread can be thought of by using cascaded electrodes in form of an extended multi-stage Einzel lens system. In principle, each stage can focus within a small angle and energy spread, while reducing the angle for the charges with higher kinetic energy. The succeeding stages accept the already focused charges and the under-focused charges with reduced angle from the previous stage. Thus in every stage, the lenses can reduce the angle of the charges that it can accept and guide them parallel to the axis of the ion-guide, thereby increasing the overall charge collection fraction.

(a)	**(b)**
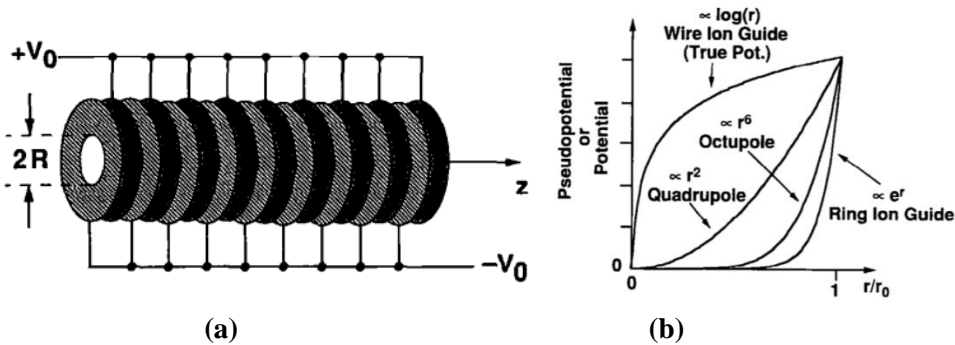
Figure 3.3: (a) Schematic of a stacked-ring electrostatic ion-guide. (b) Comparison of radial electrostatic potential of a wire ion guide and the pseudopotentials of multipole and stacked-ring ion guides versus ion radial position (r) normalized to the radius r_0 of the rings. The stacked-ring guide produces the broadest and flattest electric field-free region and a sharply defined potential well to confine ions as they travel through the guide. Both the images are taken from Ref. [158].

The concept of electrostatic ion-guide has been reported in several articles [156]–[162]. In [159]–[162], a radial electric field is created using a central wire along the length of the flight tube. On the other hand, ion-guides based on spatially inhomogeneous radio-frequency (RF) potential on a multi-pole ion-guide have also been reported [163], [164]. Closely related to a multi-pole RF ion-guide is a stacked-ring RF-only ion-guide, details of which can be found in [165]. An RF field is applied between each pair of neighboring rings in a stack of ring electrodes; a 'pseudo-potential' well is created inside the rings with steep radial gradients to confine slow charges radially [158]. In an inverse approach, stacked rings, with positive and negative static potentials applied to alternate rings, work on an analogous principle on fast ions [158]. In this case, the alternating spatially inhomogeneous electric field is generated by an ion that moves past static-potential electrodes of successively opposite sign rather than a time-oscillating potential applied to ions that move slowly [158]. In Figure 3.3 (a), a schematic of such a stacked-ring electrostatic ion-guide is shown from Ref. [158]. In Figure 3.3 (b), a qualitative comparison of the electrostatic potentials of different types of ion-guides has been shown from Ref. [158]. The ring-guide provides the broadest and flattest electric field-free region as the radial distance (r) is increased and a sharp electric field close to the wall of the ring (at $r = r_0$).

Table 3.4: Summary of the trade-offs discussed in section 3.1

Property	Value	Comment
Maximum operating voltage	± 2 kV	–
Ionic liquid	EMI-BF$_4$	Other ionic liquids possible
Electrospray source	Externally wetted, internally wetted	For typical properties, see Table 3.1
Minimum flight time	10 μs	Corresponds to BF$_4^-$ ions at $V_{em} = -2$ kV
Transimpedance amplifier	DHPCA-100	–
Detector	FC-72A	Faraday cup with 1 cm^2 detection aperture
Ion focusing	Electrostatic ion guide	Design in section 3.2 for collecting particles with wide range of kinetic energy and wide angle spread

3.2.   Ion-guide design

The ion-guide designed in this chapter is conceived from the perspective of a cascade of single-stage Einzel lenses with deflecting potential and ground connected to alternate electrodes all along the length of the flight tube.

3.2.1. Goals

The goals of the design of the ion-guide are listed below:

- For a given deflecting potential, maximize the acceptable half-angle for collection with the small Faraday cup detector.

- For a given deflecting potential, maximize the acceptable kinetic energy spread among the charge species for collection with the small Faraday cup detector.

As a baseline, the ion-guide should transmit all charges emitted from the externally wetted tungsten emitters, which emit nearly mono-energetic charges over around 15° half-angle. For mixed ion-droplet emission from micro-fabricated capillaries, there may be nearly 10% energy spread (FWHM) as discussed in section 2.1 in Chapter 2 and in [5], [57], [35], and emission half-angle as high as 40°. The ion-guide should be able to transmit charges with this energy spread from a large acceptance angle as well.

3.2.2. Constraints

The following constraints are enforced on the design of the ion-guide due to practical issues.

- The parts of the ion-guide are commercially available for ease of development. The grounded electrodes are metallic plates with central aperture and the deflecting

electrode in between is a hollow cylinder supported on metallic plates as shown in Figure 3.4.

- The individual Einzel lens components of the ion-guide are cylindrically symmetric. Also the individual Einzel lenses are considered symmetric about the radial plane going through the centre of the central deflecting electrode. The chosen set of symmetric configurations is a sub-set of the several symmetric and asymmetric Einzel lens configurations that can be considered [39], [155] in general.

- The long ion-guide along with the Faraday cup detector can sit inside the flight tube without additional need of mounting it along the axis of the tube.

- Only one power supply for the deflecting central electrode of all the cascaded stages of the ion-guide.
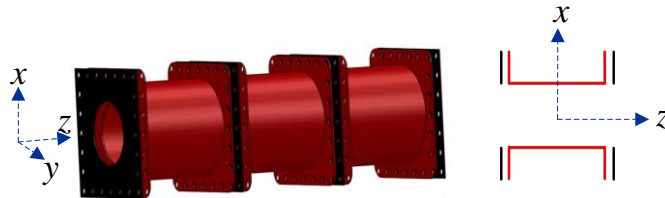
Figure 3.4: Schematic of the Einzel lens stages in the ion-guide. The central deflecting electrode (in red) is a hollow cylinder supported on metallic plate and the ground electrodes (in black) are metallic plates with circular aperture. The individual Einzel lens stages are axially symmetric w.r.t. the axis of the emitter. Also, individual Einzl lens stages are symmetric about the radial plane going through the centre of the central electrode.

It has been discussed in section 3.1.2 that a flight length L = 66.6 cm is required for a minimum 10 µs flight time of BF_4^- ions at $|V_{em}|$ = 2 kV. A commercially available flight tube with L = 65 cm is chosen which has a 73 mm inner diameter. It can be noted that the FC-72A Faraday cup detector has a square grounded plate of 50.8 mm sides (71.8 mm diagonal) [145]. Also, the square plates for the individual Einzel lenses are chosen from commercially available dimensions from KimballPhysics [166] with 50.8 mm sides (71.8 mm diagonal) and circular central aperture. In this way the entire ion-guide, once designed and assembled, can simply slide inside the flight tube and is supported on the edges of the square plates. In this way, the ion-guide axis is nearly coaxial with the flight tube and no further alignment and mounting are required for the long ion-guide.

3.2.3. Simulation for the design

With this length L = 65 mm of the flight tube, and radius R = 5.64 mm of the Faraday cup detector, the charge collection fraction can be simulated for designing the ion-guide. Since the building block of the ion-guide is single-stage Einzel lenses, first, the charge collection fraction of a single-stage Einzel lens is considered. The distance between the high voltage tubular electrode and the grounded aperture electrodes is taken as 3 mm for practical considerations of spacers, wiring etc. In Figure 3.5 (a) and (b), schematic of the ToF-MS setup with the single-stage symmetric Einzel lens and that with the ion-guide are shown. The

electrospray source is considered at a distance 6 mm from the first ground electrode of the Einzel lens so that a gate electrode can be inserted in between. All the grounded electrodes are considered to have a 25 mm aperture to restrict the analysis to a specific set of dimensions. In the figure, angle θ_{em} is the assumed total beam half-angle and θ_{max} is the half-angle up to which, all charges can be focused by the focusing system on the Faraday cup 65 cm away.

(a)

(b)
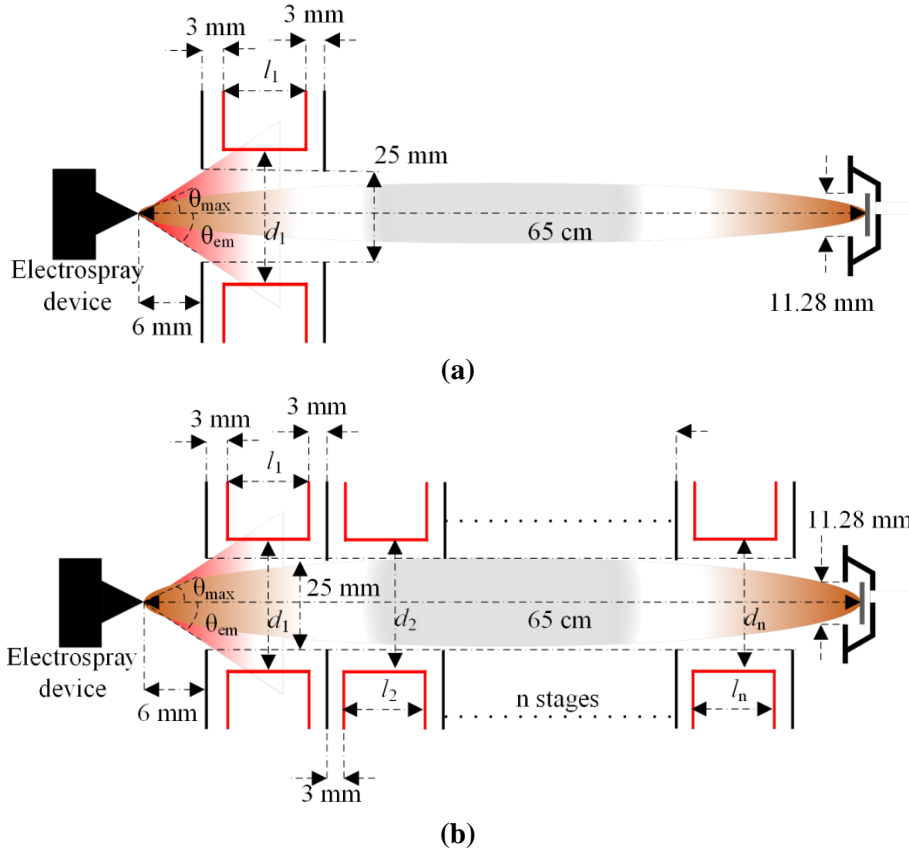
Figure 3.5: Schematic of a ToF-MS system with a (a) single stage Einzel lens and (b) with the ion-guide with n stages. The distance between the electrospray source and the first electrode of the focusing system is 6 mm. The distance between two successive electrodes is 3 mm. The diameter of the aperture in the grounded plate-electrodes is 25 mm. Faraday cup detector FC-72A is places at 65 cm from the emitter. The red coloured electrodes are the deflecting electrode with potential V_{lens} and the black coloured electrodes are grounded.

In Figure 3.6, the half-angle up to which all emitted charges that can be focused inside the 5.64 mm diameter Faraday cup detector at the end of the 65 cm long flight tube is plotted against the ratio of the applied focusing voltage V_{lens} to the emission voltage V_{em} for three different symmetric single-stage Einzel lens configurations. Simulations have been performed with SIMION ion trajectory simulator (version 8.0) assuming mono-energetic charge emission with energy qV_{em}. The dimensions are chosen from the available plate and hollow cylinder dimensions from KimballPhysics [166].

It can be seen that, charges within only up to 9° from the axis of emission can be focused on the detector with the three different configurations. However, the focusing potential at which all charges within this 9° are collected is a function of the dimensions of the deflecting central electrode of the Einzel lens. In Figure 3.7 (a), (b) and (c), the ion trajectories of three different

kinetic energies, $1.2 \times qV_{lens}$, $1.1 \times qV_{lens}$ and $0.9 \times qV_{lens}$ are shown respectively for the case $d_1 = l_1 = 25$ mm. Here, emission of charges uniformly distributed over the 9° half-angle is assumed. It can be seen that the $1.2 \times qV_{lens}$ ions are under-focused, although their angle with respect to the axis of the lens is reduced, allowing them to enter a subsequent stage with lower angle. The ions with $1.1 \times qV_{lens}$ are focused in a way that the particles are paraxial after emerging from the lens and hence can travel to the detector parallel to the axis without being affected by subsequent stages, if any. The ions with low kinetic energy $0.9 \times qV_{lens}$ are over-focused and hence their angle increases after emerging from the stage, making them less acceptable for any subsequent stage.
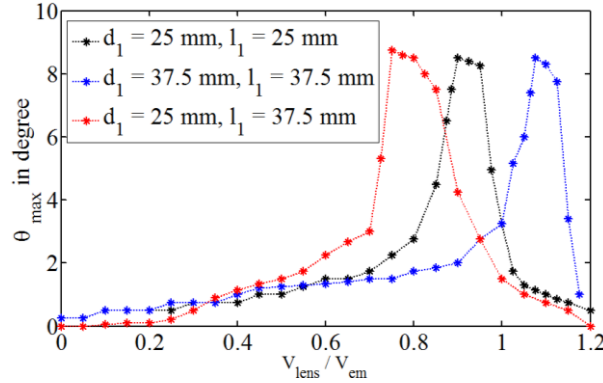
Figure 3.6: Simulated plot of the maximum half-angle up to which a single-stage Einzel lens can collect 100% emitted charges as a function of the ratio of the lens voltage and emitter voltage. Up to 9° half-angle can be collected with these single-stage symmetric configurations.

(a)   **(b)**   **(c)**
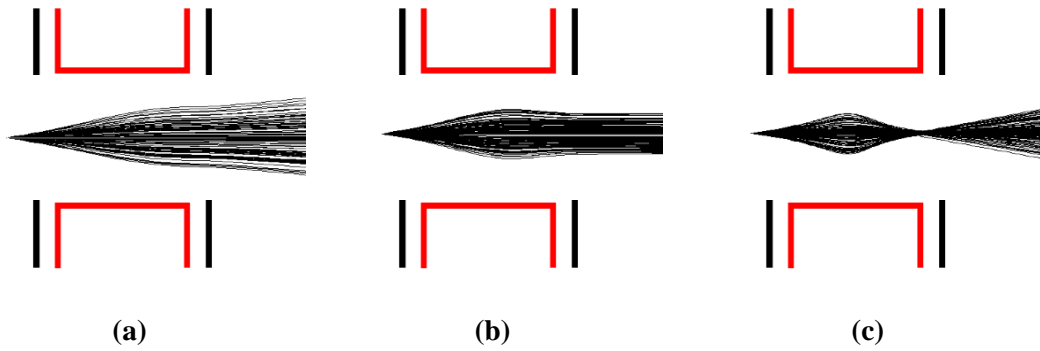
Figure 3.7: Ion trajectories in a single-stage Einzel lens with $d_1 = l_1 = 25$ mm with kinetic energies (a) $1.2 \times qV_{lens}$, (b) $1.1 \times qV_{lens}$ and (c) $0.9 \times qV_{lens}$. The $1.2 \times qV_{lens}$ ions are under-focused, $1.1 \times qV_{lens}$ are suitably focused and $0.9 \times qV_{lens}$ are over-focused.

One relevant inference that can be taken from Figure 3.6 is that, for a given focusing potential, the different configurations of the single-stage lens can focus charges with different kinetic energies. For example, if the focusing voltage V_{lens} is set to 1 kV, the configuration with $d_1 = l_1 = 25$ mm can focus all charges within 9° with the kinetic energy between 1.05 keV and 1.11 keV; for other kinetic energies, charges only very close to the axis are collected. The configuration $d_1 = l_1 = 37.5$ mm can focus charges with kinetic energy between 0.89 keV and 0.93 keV and $d_1 = 25$ mm, $l_1 = 37.5$ mm configuration between 1.21 keV and 1.33 keV within the approximately 9° emission half-angle. For each of these configurations, kinetic energies

higher than the corresponding ranges are under-focused and lower kinetic energies are over-focused, both diverging away from the axis of emission and not being collected by the small detector. Therefore, if the emission consists of a widespread kinetic energy distribution and wide emission angle, significant reduction in the charge collection is expected.

If two different types of single-stage lenses, say $d_1 = l_1 = 25$ mm and $d_1 = l_1 = 37.5$ mm, are cascaded one after another, the first stage having a peak on the left of the second stage in Figure 3.6, for the same applied focusing voltage V_{lens}, significant improvement in the collection fraction can be expected. The first stage can focus emitted particles with kinetic energies between $0.89 \times V_{lens}$ and $0.93 \times V_{lens}$ within 9°. Higher kinetic energies and higher emission angles are under-focused, but enter the second stage with reduced angle with respect to the axis of the second stage. The second stage can focus the higher kinetic energies, between $1.21 \times V_{lens}$ and $1.33 \times V_{lens}$ from the 9° elevation angle, but the population within this 9° is already increased due to reduction in angle from the previous stage. Therefore, if for a given emission voltage V_{em}, focusing voltage is set to an appropriate value, significant improvement in charge collection from a wider kinetic energy spread and angular spread can be expected.

3.2.4. Final dimensions of the ion-guide

Based on the above argument, the following dimensions for the ion-guide have been chosen as described in Table 3.5. To cover the total length of 65 cm of the flight tube, a total n = 13 stages are required.

Table 3.5: Dimensions of the designed ion-guide

Element	Length of deflecting cylinder	Diameter of deflecting cylinder	Diameter of opening in the ground electrodes	Spacing between electrodes	Voltage applied to the deflecting cylinder
1st stage	$l_1 = 25$ mm	$d_1 = 25$ mm	25 mm	3 mm	V_{lens}
nth (13 ≥ n ≥ 2)	$l_n = 37.5$ mm	$d_n = 37.5$ mm	25 mm	3 mm	V_{lens}

In Figure 3.8 (a), an image of the 3-D model of the designed ion-guide is shown where the red electrodes are at deflecting potential V_{lens} and the black electrodes are connected to ground. In Figure 3.8 (b) the electrical connections to the electrodes are explicitly shown. On the same figure is superimposed the ion-trajectories simulated from SIMION with kinetic energy per unit charge equal to $1.1 \times V_{lens}$. It can be seen that the charges are guided along the axis of the ion-guide by continuously deflecting them towards the axis of the tube all along its length and the nearly periodic nature of the ion trajectories is in accordance with the qualitative explanation provided in section 3.1.5 "Ion Guide" section.

3.3.   Expected performance of the ion-guide

Based on the design described above, the expected performance of the ion-guide has been analysed below. The charge collection efficiency of the ion guide and increase and spreading

in flight times to be measured have been discussed and quantified based on specific assumptions which are discussed in the course of the analysis.

(a)

(b)
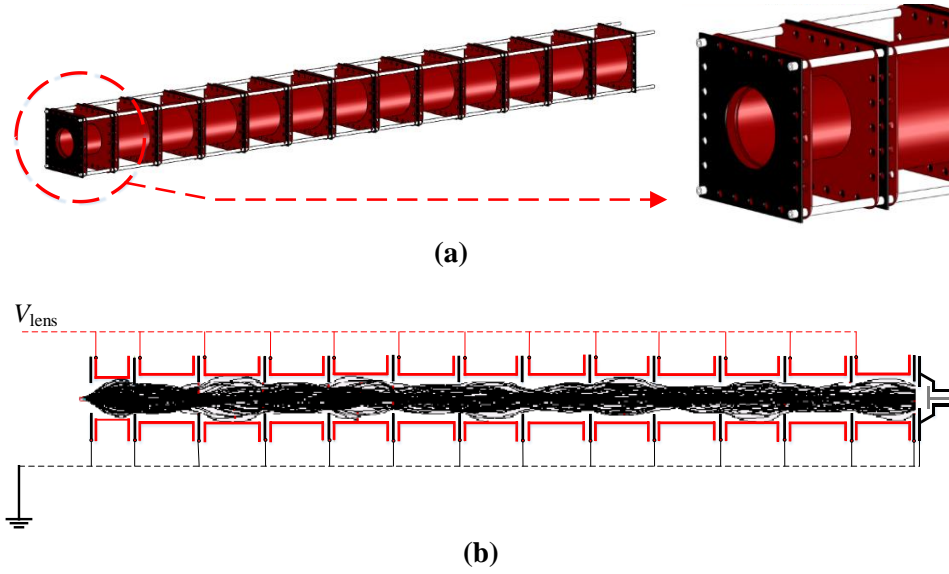
Figure 3.8: (a) Image of the 3-D model of the designed ion-guide. Red electrodes are at deflecting potential V_{lens} and the black electrodes are connected to ground. (b) Electrical connections to the ion-guide. V_{lens} is connected to the red tubular electrodes and the black plate electrodes are grounded along with the shield of the Faraday cup detector on the right side of the figure. The black curved lines are simulated ion trajectories of the charges.

3.3.1. Charge collection fraction

In Figure 3.9 (a) and (b), the surface plot of the charge collection fraction by only the first stage of the ion-guide and that by the entire ion-guide with emission half-angle θ_{em} and the ratio V_{lens}/V_{em} are shown. Simulations have been performed in SIMION ion trajectory simulator (version 8.0). Here, the emitted charges are assumed to be uniformly distributed over the entire half-angle θ_{em} and with constant kinetic energy qV_{em}. The colour bar in the figures represents the percentage of emitted charges that can be collected by the FC-72A Faraday cup detector. The ion-guide can collect 100% of a mono-energetic emitted beam at qV_{em} for up to 23° emission half angle when the deflecting potential $V_{lens} = 0.95 \times V_{em}$. The maximum accepting half-angle $\theta_{max} = 23^o$ for the ion-guide is nearly 2.5 times more than that from the first stage for the same flight length, 1.8 times more than that obtained with a single-stage Einzel lens in Ref. [39] with a 4.3 times longer flight tube and 8° more than the stacked-ring ion-guide described in Ref. [158]. For any emission half-angle θ_{em}, the maximum fraction of charges collected can be written (assuming uniform charge distribution over the entire emission solid angle) as

$$\eta_{max} = \frac{(1-\cos 23^0)}{(1-\cos \theta_{em})} \qquad (\theta_{em} > 23^o) \tag{3.2a}$$

$$\eta_{max} = 1 \qquad (\theta_{em} \leq 23^o) \tag{3.2b}$$

when V_{lens} is set to 0.95 times the kinetic energy per unit charge of the mono-energetic

emission. Here the ratio in (3.2a) is the ratio of solid angles subtended by the 23° acceptance angle of the ion-guide (within which, all mono-energetic charges can be collected) and the solid angle of emission. It can be obtained that for a 40° emission half-angle, nearly 34% of the charges are within the 23° acceptance angle if charges are uniformly distributed over the entire emission half-angle and hence can be collected, had there been only mono-energetic emission at kinetic energy qV_{em} and had the deflecting potential been set to $0.95 \times V_{em}$.

(a)   (b)
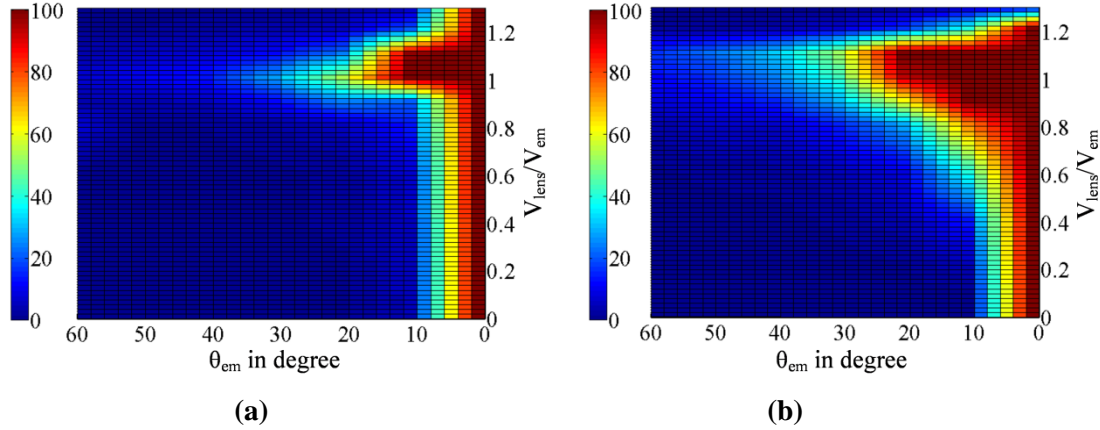
Figure 3.9: Simulated surface plot of the charge collection fraction by (a) only the first stage of the ion-guide and (b) that by the entire ion-guide with emission half-angle θ_{em} and the ratio V_{lens}/V_{em}. The colour bar in the figures represents the percentage of emitted charges that can be collected by the FC-72A Faraday cup detector. The ion-guide can collect 100% of a mono-energetic emitted beam for up to 23° emission half angle. The kinetic energy range and angular spread that can be transmitted is much broader for the ion-guide than for the single-stage.

Some specific mono-energetic cases can be studied with the ion-guide relevant to the two types of electrospray emitters discussed in Table 3.1. For a tungsten emitter, nearly mono-energetic emission within $\theta_{em} \approx 15^{\circ}$ with a beam-shape as reported in [44] can be considered. The beam-shape from these sources is later described to be nearly parabolic [167]. For microfabricated capillary devices, as discussed in Chapter 4, section 4.2.2, the emission half-angle can be considered $\theta_{em} \approx 40^{\circ}$. Again, retarding potential analysis (RPA) of these devices has previously shown that the kinetic energy of emission can have nearly 10% deficit from the applied emitter potential V_{em} [57], [35]. There can also be secondary peaks [57], [35] corresponding to fragmentation in which charged droplets or solvated ions can break into neutral molecules and smaller ions during their acceleration or post-acceleration and share the kinetic energy according to the ratio of their masses. More detailed discussion on fragmentation is provided in section 4.1.2, 4.1.3, 4.2.3 and 4.2.4 in Chapter 4 while interpreting the experimentally obtained charge collection fractions from tungsten emitters and capillary emitters. For simplicity, the emission from capillary sources is assumed here to comprise of equal proportion of charges at two kinetic energies, one corresponding to the energy deficit of 10% and other corresponding to fragmentation of a dimer into monomer post-acceleration, namely,

$$(K.E)_1 = 0.9 \times qV_{em} \tag{3.3}$$

$$(K.E)_2 = \frac{m_{monomer}}{m_{dimer}} \times (K.E)_1 \tag{3.4}$$

where $m_{[w]}$ is the mass of the ion type [w]. Here $(K.E.)_1$ represents the kinetic energy of an originally emitted monomer and $(K.E.)_2$ the kinetic energy of a monomer generated due to fragmentation from a dimer which had a kinetic energy $(K.E.)_1$ before break-up. The beam-shape corresponding to each of the monomer types can be taken from Figure 4.11 (b) at $V_{em} =$ -740 V for example, which shows the measured current density distribution over angle from a micro-fabricated capillary source at different emission voltages in negative polarity of emission. For negative polarity of emission from EMI-BF$_4$, the ratio of masses can be taken as $m_{monomer}/m_{dimer} = 0.3$.

Accordingly, five cases have been considered for the case-study as described in Table 3.6. Case 1 is a mono-energetic emission with kinetic energy qV_{em} uniform over a 15° emission half-angle. Case 2 is the same, but considering a beam-shape reported in [44] instead of a uniform distribution, equivalent to a realistic emission from an externally wetted tungsten emitter. Case 3 is a mono-energetic emission with kinetic energy qV_{em} uniform over a 40° emission half-angle. Case 4 corresponds to a situation of emission of mono-energetic emission at qV_{em} from capillary device, but with a beam-shape described in Figure 4.11 (b). Case 5 is a special, but more realistic, case that takes into account the fragmentation of dimers into monomers emitted from capillary device and hence monomers of two different kinetic energies $(K.E.)_1$ and $(K.E.)_2$ defined in (3.3) and (3.4), each having a beam shape identical to Case 4.

Table 3.6: Details of case study on expected charge collection fraction

Case	Emission voltage	Kinetic energy of charges	Total number of charges for simulation	Beam half-angle θ_{em} (deg.)	Beam-shape
1	V_{em}	qV_{em}	10000	15°	Uniform
2	V_{em}	qV_{em}	10000	$\sim 15^o$	Ref. [44]
3	V_{em}	qV_{em}	10000	40°	Uniform
4	V_{em}	qV_{em}	10000	$\sim 40^o$	Figure 4.11 (b)
5	V_{em}	$(K.E)_1 = 0.9 \times qV_{em}$ $(K.E)_2 = 0.3 \times (K.E)_1$	5000 5000	$\sim 40^o$ $\sim 40^o$	Figure 4.11 (b) Figure 4.11 (b)

In Figure 3.10, the corresponding charge collection fractions for the five different cases have been plotted against the ratio V_{lens}/V_{em}. It can be seen that for the case of tungsten emitters, emitting within 15° emission half-angle, all the emitted mono-energetic charges can be collected with the help of the ion-guide if the focusing voltage V_{lens} is set between $0.75 \times V_{em}$ and V_{em}. Conversely, if there is a kinetic energy spread, for a given V_{lens}, the kinetic energy of between qV_{lens} and $1.33 \times qV_{lens}$ can be collected from emission within 15° half-angle. For capillary devices, with as wide as 40° emission half-angle, a maximum of 34% charges can be collected from a uniform angular distribution, which has been described on the basis of Eqn. 3.1 before. For an assumed mono-energetic emission with the defined beam-shape profile in Figure 4.11 (b), the collection fraction can reach 65%; and more than 40% over a range of kinetic energies between $1.04 \times qV_{lens}$ and $1.39 \times qV_{lens}$.

For a more practical situation of multiple kinetic energy peaks separated by a large factor, such as in Case 5, the maximum collection fraction depends on the fraction of charges at a given kinetic energy. For the special case of 1:1 ratio of monomers with kinetic energies $0.90 \times qV_{em}$ and $0.27 \times qV_{em}$, the maximum collection for each species reaches 33% at different V_{lens}, with more than 20% collection of kinetic energy spread over 40% around the individual kinetic energies. If there is a kinetic energy spread around the peak kinetic energy $0.90 \times qV_{em}$ due to fragmentation inside the accelerating region of the emitter, by setting $V_{lens} \approx 0.75 \times qV_{em}$, all of these charges can be collected from within 23° emission half-angle while rejecting the charges fragmented post-acceleration. However, for capillary emitters, emitting mixture of ions and droplets, many other possible fragmentation situations may arise with kinetic energies spread over a wide range, not limited to only $0.90 \times qV_{em}$ and $0.27 \times qV_{em}$ which are discussed in section 4.2.3 in Chapter 4.
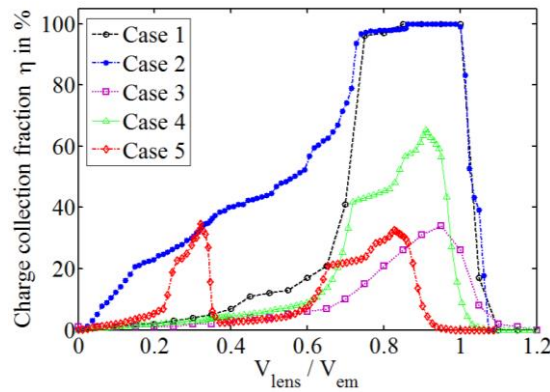
Figure 3.10: Simulated charge collection fraction vs. the ratio V_{lens}/V_{em} for the five cases described in Table 3.6.

3.3.2. Increase in flight time

The ion-guide leads to increase in the flight time of the charges compared to the value obtained from Eqn. (2.5). For a given flight tube length, flight time is inversely proportional to the axial speed of the charges. The axial component of the electric field in the focusing arrangement leads to change in the instantaneous axial speed by decelerating and accelerating the particles within the length of the lens. In a single-stage lens, the change in average axial speed of the particles is typically negligible since the deceleration and acceleration take place over the length of the lens, which is much shorter than the length of the flight tube. For the ion-guide, the charges are decelerated and accelerated all along the length of the flight tube and as a result the average axial speed of the charges is lower than the initial speed. In Figure 3.11 (a), the simulated instantaneous axial speed v_z of a BF_4^- ion normalized to its initial speed v_0 is plotted against the distance from the source, z, normalized by length of flight tube, L, along the flight tube for the first-stage only and for the entire ion-guide respectively. The initial kinetic energy of the ion is assumed to be $qV_{em} = qV_{lens}$ i.e. V_{lens} is set to V_{em}, the kinetic energy per unit charge and the ion is assumed to be emitted along the axis of the flight tube. It can be easily observed that for the single-stage lens, v_z decreases and then increases to $1.05 \times v_o$ in the single-stage case, slightly higher than the initial speed contributed by the overall axial acceleration from the Einzel lens. For the ion-guide, the instantaneous axial speed periodically changes between $0.48 \times v_o$ and $0.83 \times v_o$ as the ion traverses along the ion-guide. After emerging from the final stage, the axial speed increases slightly until it hits the Faraday

cup. As a result of the reduced average speed of the ion through the ion-guide, the flight time is expected to increase from its otherwise unaltered flight time given by (2.5). In order to estimate the change in flight time due to the ion-guide, a ToF correction factor, which depends on the lens voltage, is defined as

$$\text{ToF correction factor} = \frac{T_{\text{F}}(V_{\text{lens}})}{T_{\text{F}}(V_{\text{lens}} = 0)} = \frac{T_{\text{F}}(V_{\text{lens}})}{L\left(\dfrac{m}{2qV_{\text{em}}}\right)^{1/2}} \tag{3.5}$$

<table>
<tr><td>(a)</td><td>(b)</td></tr>
</table>
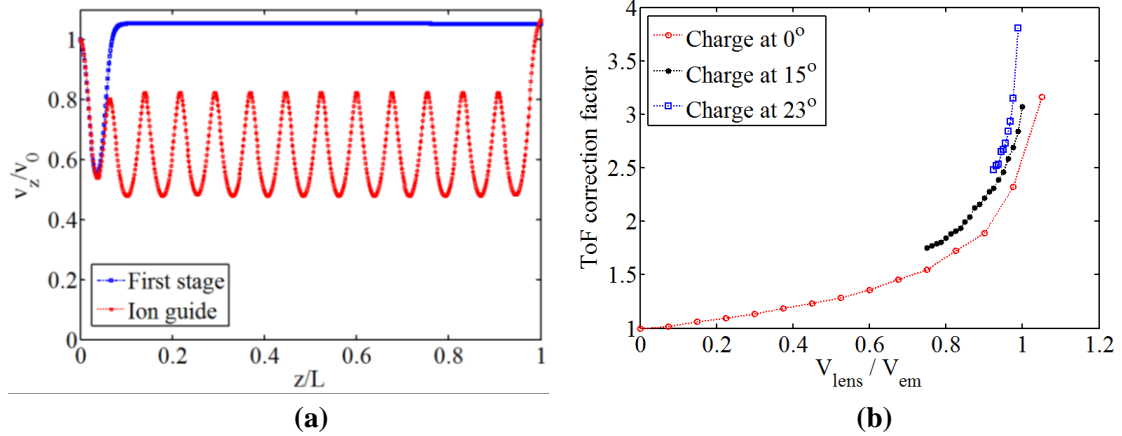
Figure 3.11: (a) Simulated instantaneous axial speed v_z of a BF_4^- ion normalized to its initial speed v_0 is plotted against the distance from the source, z, normalized by length of flight tube, L. The initial kinetic energy of the ion is assumed to be $qV_{\text{em}} = qV_{\text{lens}}$ and the ion is assumed to be emitted along the axis of the flight tube. For the single-stage lens, the axial speed is constant over most of the flight path whereas for the ion-guide, the axial speed periodically changes. This leads to an increase in flight time in the ion-guide. (b) Simulated ToF correction factor vs. the ratio $V_{\text{lens}}/V_{\text{em}}$ for three different initial angles of the BF_4^- ions. A three-times increase is observed for the axial ion. For an off-axis ion, the ToF correction factor is larger than that for the axial ion. For different initil angles, the correction factor is different leading to spreading in the ToF traces even for the mono-energetic charges with same q/m

In Figure 3.11 (b), the simulated value of ToF correction factor for charges at three different initial angles are shown. This value is found to be independent of the q/m and is a function of the ratio $V_{\text{lens}}/V_{\text{em}}$. For axially directed charges, the ToF increases by a factor of about 3 from its otherwise unaltered value given in (2.5) as the ratio $V_{\text{lens}}/V_{\text{em}}$ increases from 0 to 1. This is equivalent to having a flight tube nearly three times longer as well, without actually increasing the length of the tube. As the initial angle increases, the off-axis charges begin to reach the detector for higher V_{lens} and show different ToF correction factors for different angles. This is a drawback of the setup as this directly leads to spreading in the ToF traces for the same q/m with same kinetic energy emitted at different angles. This issue is discussed in the following section.

3.3.3. Spreading in flight times

For ions at different initial angles, the ToF correction factor is different as seen in Figure 3.11 (b). For a charge emitted at the maximum acceptable angle of 23°, the ToF correction factor is

nearly 36% higher than that for an axial charge. Consequently, a ToF spread factor can be defined here as

$$\text{ToF spread factor} = \frac{T_F(V_{lens}, 23^o)}{T_F(V_{lens}, 0^o)} - 1 \approx 0.36 \qquad (\theta_{em} > 23^o) \qquad (3.6a)$$

$$\text{ToF spread factor} = \frac{T_F(V_{lens}, \theta_{em})}{T_F(V_{lens}, 0^o)} - 1 \qquad (\theta_{em} \leq 23^o) \qquad (3.6b)$$

For an ion at 15°, i.e. at the typical maximum angle from the emitters, nearly 20% increase in the ToF is expected from the axial ion with the same kinetic energy and q/m. Therefore, for an externally wetted tungsten emitter, a 20% uncertainty is expected on the measured time of flight of a particular ion species emitted between 0° and 15°. For micro-fabricated capillary device, this spread can be as high as 36%. This significantly limits the use of the ion-guide in achieving mass resolution above 1.5 according to Eqn. (2.6) even if there is no kinetic energy spread. For kinetic energy spread among the charges of same q/m, further spreading is expected according to Eqn. (2.6). As a result, although ToF mass spectra can be achieved from a broad section of the emission, the ion-guide provides poor resolution mass analysis of the emission. For example, dimers $(EMI\text{-}BF_4)BF_4^-$ and trimers $(EMI\text{-}BF_4)_2BF_4^-$ from EMI-BF_4 in negative polarity of emission have a mass ratio 0.59:1 and for a given emitter voltage, a flight time ratio 0.77:1 when the ion-guide is not used. However, dimer emitted at an angle 23° may have flight time higher than that of a trimer emitted axially when the ion-guide is used and hence they may coincide on the ToF traces making them unresolvable. However, for emission predominantly limited to a much lower angle, the effect may be smaller as the current density is primarily concentrated within a narrower solid angle.

3.4. The ToF-MS experimental setup

The designed ToF-MS with the ion-guide is developed in LMTS-EPFL, Neuchatel for characterization of electrospray sources. In Figure 3.12 an image of the 3-D model of the ToF-MS is shown. The stainless steel parts of the vacuum chamber are purchased from Lewvac [168]. The main chamber is a DN160CF cubic six-way cross. On one side of the chamber, the flight tube of length 65 cm and inner diameter 73 mm is attached. The chamber is bolted on a laboratory table. Two DN160CF view-ports are installed on the vacuum chamber as shown in Figure 3.11. The electrical, nitrogen (for venting) and ionic liquid feed-through are accommodated on a custom-manufactured flange on top of the vacuum chamber. The ionic-liquid is reserved in a separate vacuum chamber, always kept in vacuum (~ 1 mBar), and is transported to the ToF-MS chamber using a glass-capillary tube and nano-port feed-through, N-124S from Idex [169] for electrospraying from the capillary devices. For the externally wetted tungsten emitters, the emitter is wetted with the ionic liquid outside the vacuum chamber separately. The vacuum chamber is pumped with an Edwards TIC pumping station [170] consisting of EXT75DX turbomolecular pump and a XDD1 diaphragm backing pump.

In the following sections, the following components of the ToF-MS experimental setup are discussed.
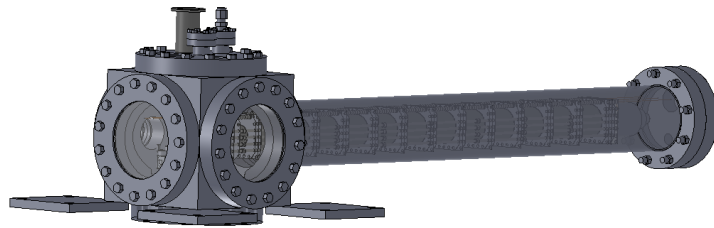
Figure 3.12: 3-D view of the ToF-MS. The main vacuum chamber is a cubical six-way cross with the flight tube attached to one side of it. The ion-guide slides through and sits inside the flight tube.

1. Two different types of electrospray propulsion devices discussed in Table 3.1.

2. The ion-guide.

3. The electronic setup consisting of the high voltage switched power supplies, the transimpedance amplifier and the oscilloscope.

In addition, the setup is also adapted for measurement of spray angular divergence of the electrospray devices and this setup is also discussed.

3.4.1. Electrospray source

As mentioned in section 3.1, two different types of electrospray propulsion devices have been used with the ionic liquid EMI-BF$_4$ for characterization of the ion-guide.

1. Electrochemically etched tungsten emitter

The emitters are fabricated with the help of Dr. Daniel Courtney using 3 cm long and 0.5 mm diameter tungsten wires from KimballPhysics [166] using an electrochemical process described by Lozano and Martinez-Sanchez from MIT in Ref. [44]. In Figure 3.13 (a) and (b), scanning electron microscope image of one of the fabricated tungsten emitter is shown. The emitter is mounted on a 6 mm thick polyoxymethylene (POM) plate, cut to 5 cm side square shape with 0.5 mm diameter hole at the centre to mount the emitter. A stainless steel plate with 1 mm diameter circular hole at the centre is used as the extractor electrode as shown in Figure 3.13 (c) and (d) and the emitter is aligned to the extractor aperture using an optical microscope. Evidences exist that decreasing the distance between the emitter tip and the extractor electrode increases stability of emission current [171] and in this case, the emitter tip is brought to the same plane as the inner plane of the extractor electrode through the aperture. A tungsten wire loop is created nearly 5 mm beneath the tip of the emitter as shown in [44] so that a reservoir drop of ionic liquid can be sustained there due to capillarity and can externally wet the sharp tip of the emitter with the ionic liquid.

2. Microfabricated capillary device

The microfabricated capillary electrospray devices are fabricated on silicon-on-insulator (SOI) wafers using deep reactive ion etching (DRIE) process by Dr. Çağlar Ataman and Simon Dandavino at LMTS-EPFL as described in [54], [55]. The extractor electrode with aperture diameter between 150 μm and 300 μm are fabricated on another SOI wafer and these two wafers are aligned and bonded. In Figure 3.14 (a), a scanning electron microscope image

of the capillary electrospray device is shown. In Figure 3.14 (b) and (c), the mounting assembly of the capillary electrospray device is shown. The ionic-liquid is dropped from the ionic liquid feed-through capillary to fill-up a reservoir created just behind the capillary emitter assembly as shown schematically in Figure 3.14 (c). By capillarity, the liquid reaches the tip of the capillary after filling a micro-machined reservoir on the emitter device.

(a)   (b)

(c)   (d)
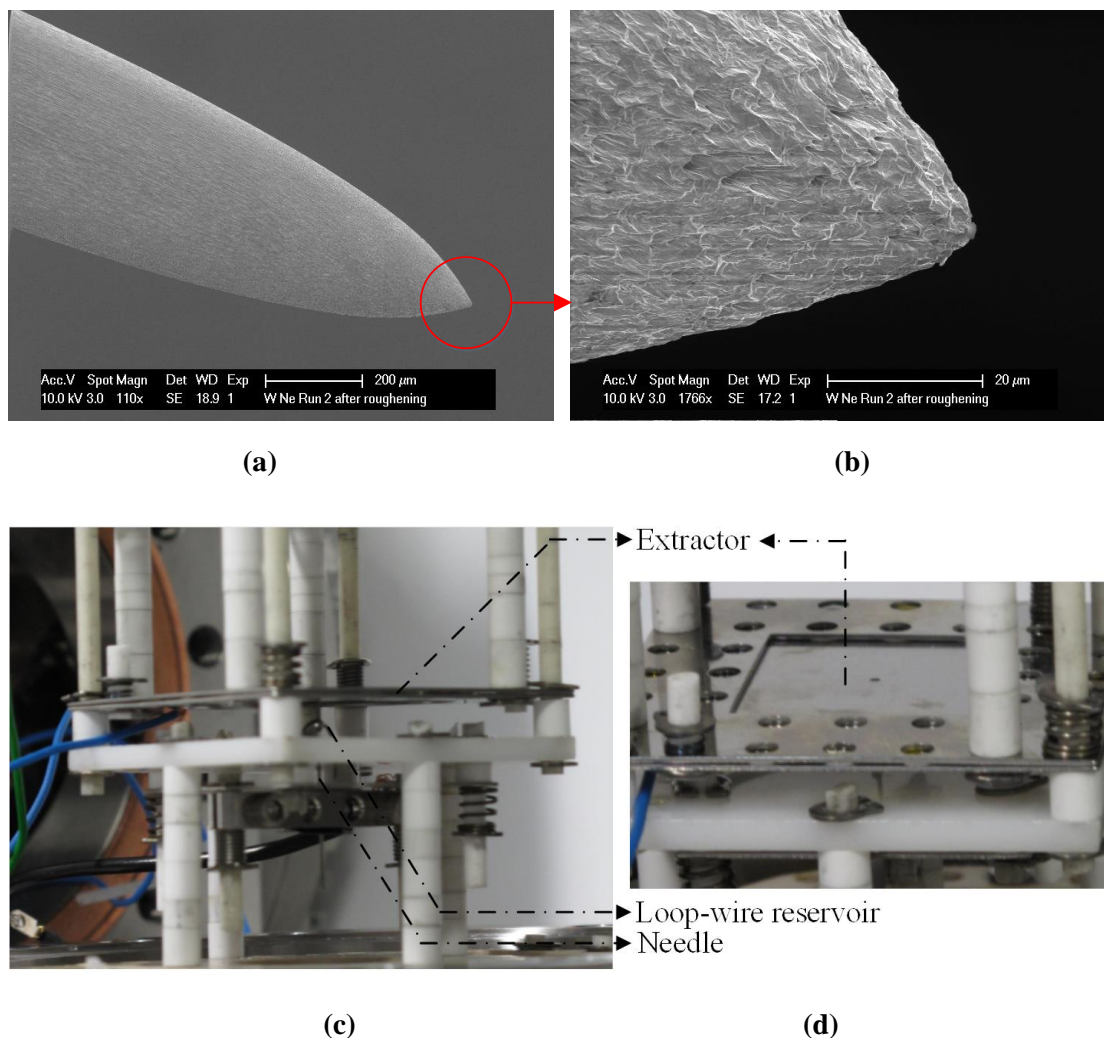
Figure 3.13: (a) SEM image of an electrochemically etched tungsten emitter. In (b), a zoomed image of the tip-section is shown. (c) The assembly for electrospray emission from tungsten emitter. A 1 mm diameter aperture in a stainless steel plate is used as the extractor aperture.

3.4.2. The ion-guide

As described in section 3.2.2, the ion-guide is manufactured from commercially available eV parts from KimballPhysics [166]. In Figure 3.15 (a) an image of the ToF-MS setup and in (b) an image of the ion-guide are shown. Alignment of the parts of the ion-guide is achieved using alumina tubing going through the 2.54 mm diameter holes in the plates used for the electrodes. The parts of the high voltage electrodes are joined using H20S electrically conductive two-part epoxy [172]. The electrospray source is mounted directly on the right side of the ion-guide and a Faraday cup FC-72A is mounted on the left side. The entire ion-guide with the Faraday cup and the electrospray source slides into the flight tube from the

opposite side of the cubical six-way cross as described in section 3.2.2. In this process, the ion-guide is coarsely aligned with the flight tube axis without sagging. The free-end of the in-guide consisting of the electrospray device is nearly at the centre of the cubical six-way cross and this side sags a little, making the electrospray axis slightly misaligned with the axis of the tube; but due to strong guiding capability of the ion-guide along its axis, it is expected that the emitted charges will be guided along the axis of the guide to the detector. The edges of the square plates for the high voltage electrodes of the ion-guide are chamfered by 5 mm in order to avoid electrical contact with the body of the tube while the plates for the grounded electrodes rest on the tube through their corners.
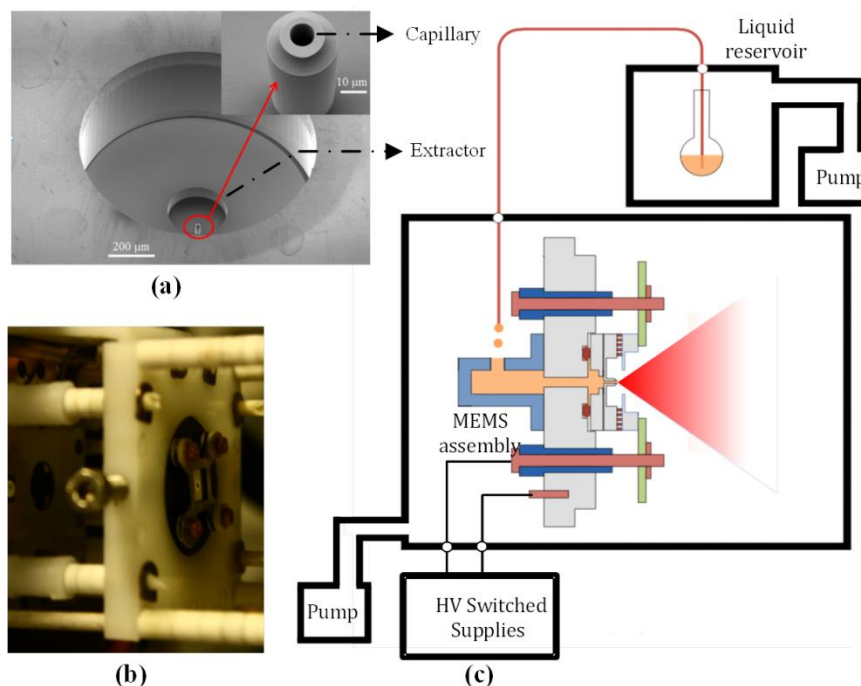
Figure 3.14: (a) SEM image of a microfabricated capillary electrospray source. The capillary emitter is shown in the inset. (b) The mounting assembly for the capillary device for electrospray application. (c) A schematic of the experimental setup.
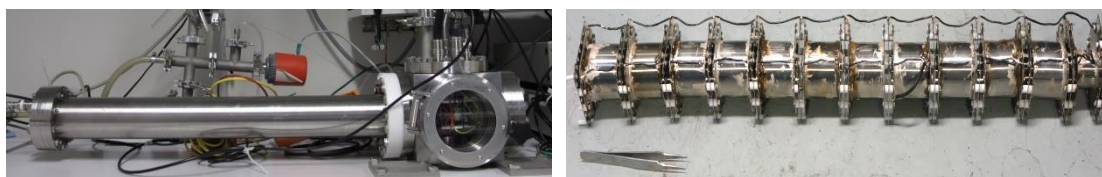
Figure 3.15: (a) An image of the ToF-MS setup. (b) An image of the ion-guide. The ion-guide slides into the flight tube from right side of the cubical vacuum chamber in the ToF-MS setup. The emitter is mounted directly on the ion-guide from the right side of the ion-guide and the Faraday cup is mounted on the left side.

Another metallic plate, with a 25 mm diameter aperture and a grid with 85% optical transparency, is placed between the first ground electrode of the ion-guide and the electrospray source so that the gate signal can be applied to it for ToF measurement. In the present case, the gate electrode consists of only one plate with a grid, unlike the three-electrode assembly or the comb-type configuration described in section 2.1.1. In the present

case, the gate is normally closed, repelling all the emitted charges opposite to the direction of emission and opens within a very short with a very short fall time of the gate signal for ToF measurement of the charges allowed to enter the flight tube. The ratio of detected current to the emitted current is multiplied by the 1.18 during experiments in Chapter 4 in section 4.1.2 and section 4.2.3 for tungsten emitter and capillary emitter respectively to take into account the 85% transparency of the gate grid.

3.4.3. The electronic setup

The electronic signals required for the ToF-MS to operate in bipolar spray operation are summarized in Table T1 and a schematic of the electronic setup is shown in Figure A1 in Appendix A. For positive and negative emission polarities, high voltage positive and negative power supplies are implemented using EMCO CA20P and CA20N high voltage regulated DC-DC converters [173]. These devices operate by 12 V DC power supply and produce up to 2 kV and −2 kV outputs respectively proportional to a 0−5 V control signal with 0.001% ripple. For the ion-guide and the gate power supplies, EMCO H30P and H30N DC-DC converters are used [173] which can produce up to 3 kV and −3 kV output. The six high voltage DC-DC converters are mounted on a high voltage power supply printed circuit board (PCB) as shown in Figure 3.16 (a) and (b).

(a)   **(b)**
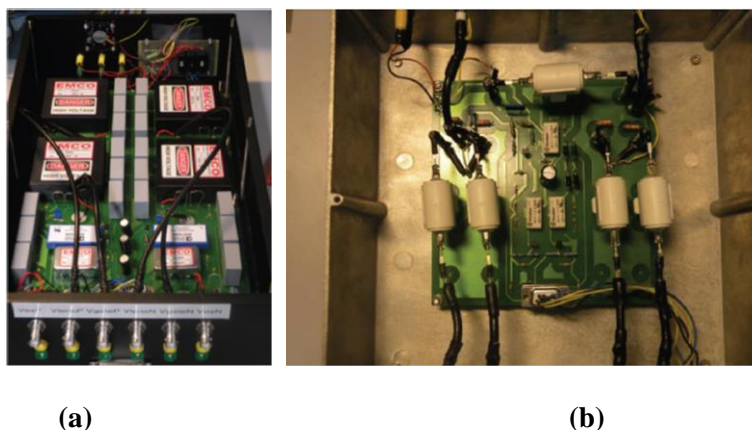
Figure 3.16: (a) High voltage power supply PCB consisting of 6 high voltage DC-DC converters for bipolar power supplies for the emitter, ion-guide and the gate, and a pair of isolation amplifiers for emitter current monitor. (b) The high voltage relay PCB which can change polarity of applied potential to the emitter and the ion-guide. Another relay in the PCB is used for changing from emitter voltage monitor mode to emitter current monitor mode.

Two AD210 isolation amplifiers [174] with selectable gain settings are also assembled on the same PCB to measure the emitter currents from the two emitter power supplies separately. For switching the polarity of applied voltages to the emitter and the ion-guide, high voltage relays are used in a configuration similar to that reported in [35] and as shown in Figure 3.16 (b). For fast switching of the gate signal, a PVX-4140 high-speed pulse generator [175] is used with one EMCO H30P and one EMCO H30N DC-DC converter. This pulse generator can produce gate pulses up to ± 3.5 kV within 100 ns rise/fall time.

In order to monitor the high voltage power supply outputs, monitor signals from the DC-DC converters are recorded. The actual bipolar power supplies delivered to the emitter and the ion-guide are monitored with a 1000:1 resistive potential divider circuit. However, an additional switching circuit is implemented to switch between emitter bipolar power supply monitor and emitter current monitor mode in order to avoid drawing significant current by the potential divider while electrospraying. In each polarity of emission, the voltage monitor mode is turned on only for a fraction of the emission duration and is cut-off for the rest of the duration monitoring the emission current. During the voltage monitoring duration, the emitter current is offset from the electrospraying current due to current drawn by the resistor in the potential divider. A detailed timing diagram of the emitter current monitor can be found in Figure 4.8 in Chapter 4 while describing the experimental results from the microfabricated electrospray device.

The pulsating gate signal is monitored from the PVX-4140 pulse generator monitor output and is used as the trigger for the oscilloscope such that ToF traces can be measured with respect to the rising or falling edge of the gate trigger signal. The detector current output from the Faraday cup is connected to the FEMTO DHPCA-100 transimpedance amplifier with selectable gain settings and the output of the amplifier is used as ToF trace. A Tektronix DPO2014 digital phosphor oscilloscope is used for measuring the flight times.

All the monitor signals are recorded with 16-channel analog input device NI-USB-6210 [176]. All the control signals for the power supplies and switching are generated using NI-9264 16-channel analog output system [177]. The signal generation and data acquisition are automated for continuous bipolar operation using Matlab (version 7.9).

3.4.4. The beam-shape measurement setup

Apart from ToF and charge collection fraction measurement, the experimental setup is also adapted for measuring the spray divergence from the electrospray device. In order to find the spray current density distribution in the emission cross-section, two different types of detectors, each consisting of 19 collector plates, have been manufactured on FR-4 PCB. The 19-hex plate consists of nineteen identical hexagonal plates as shown in Figure 3.17 (a) and the 19-annular plate consists of nineteen concentric annular plates as shown in Figure 3.17 (b). While the 19-hex plate can be used for spray-symmetry measurements, the 19-annular configuration is useful for measurement of angular distribution of current density with a higher angular resolution.

In Figure 3.18 (a) the schematic of the beam-shape measurement configuration is shown. A switching mechanism has been made in another PCB that can be attached with any of the nineteen plate configurations shown in Figure 3.17. The PCB consists of nineteen Reed relays [178] each of which can select one of the nineteen plates and the current received from the plume on the plate can be readout across a 1 MΩ resistor using an analog input channel of NI-USB-6210 analog input system. A de-multiplexer and five analog output channels of the NI-9264 analog output system are used to sequentially select each of the nineteen relays during emission and the current in the nineteen plates are readout serially.

The ToF-MS setup thus features the capabilities of flight time measurement from electrospray propulsion sources and also can be adapted for measurement of their spray angle divergence.

The detailed experimental results with two different types of electrospray sources are discussed in Chapter 4.

<center>(a)</center> <center>(b)</center>
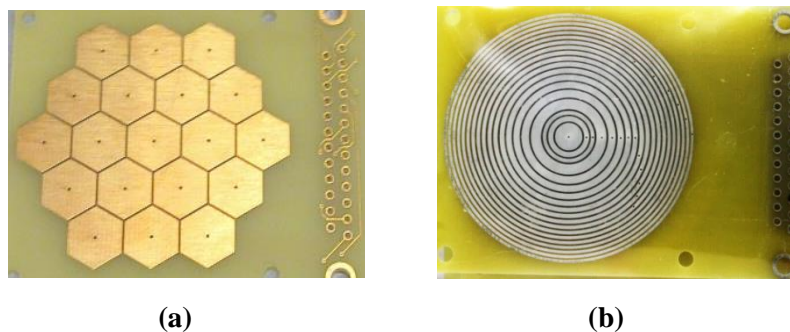
Figure 3.17: (a) 19-hex detector plate. It consists of nineteen identical regular hexagonal plates with each side of length 5 mm. The gap between neighbouring plates is 0.5 mm and the area of each plate is 65 mm^2. (b) 19-annular detector plate. It consists of nineteen annular detectors. The first three have an area 22 mm^2 each and the rest have an area 66 mm^2 each.

<center>(a)</center> <center>(b)</center>
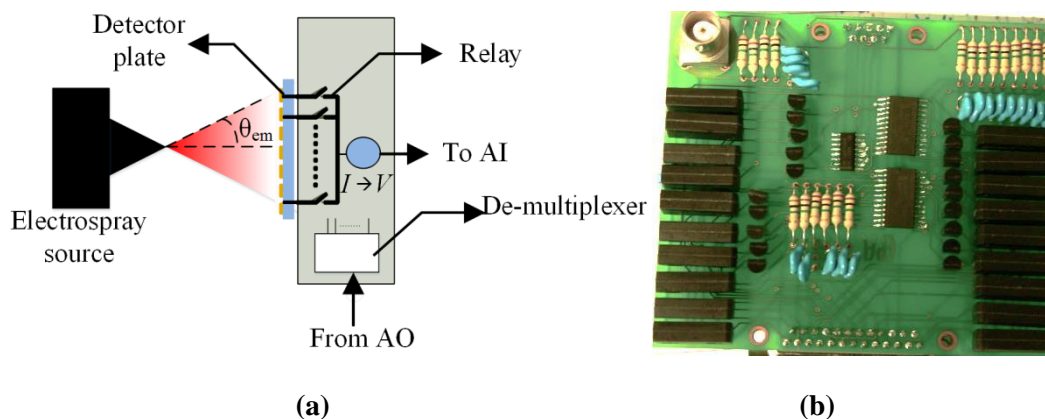
Figure 3.18: (a) Schematic of the beam-shape measurement setup. The multiplexed detector plates are placed in front of the emitted plume and the current on each plate is measured sequentially. The distance between the emitter tip and the plane of the plates, and the size and position of the plates relative to the assumed axis of emission determines the angular distribution of the plume. (b) The plate switching and detector PCB. It consists of nineteen Reed relays which are enables sequentially to record the current on each plate. Five analog output channels of NI-9264 analog output system and a de-multiplexer are used to enable the relays and detecting the current in the selected plate.

3.5. Summary

In this chapter, the design and experimental setup for a ToF-MS system with an electrostatic ion-guide has been discussed. The ion-guide consists of 13 stages of cascaded symmetric Einzel lenses all along the length of a 65 cm flight tube to guide charges emitted from electrospray propulsion sources on a small Faraday cup detector of radius 5.64 mm. Simulations show that the ion guide can collect all mono-energetic charges with up to 23° emission half-angle for a given potential applied to the ion-guide and thus increases the fraction of collected current on the detector for a given emitter current. From an emission

half-angle of 15$^\mathrm{o}$, typical of externally wetted tungsten emitters, nearly 30% energy spread in the emitted charged species can be collected with a given deflecting potential applied on the ion-guide. The accommodation of large fraction of the emission for mass spectrometric analysis allows the gain and speed requirement of a transimpedance amplifier to be greatly relaxed. Unlike ToF-MS setup with a large detector plate used for electrospray propulsion devices, a small Faraday cup and hence a much smaller diameter flight tube can be used. Also, the ion-guide enables mass analysis from a large fraction of the emission at once, thus can be useful for analysis from rapidly changing spray composition in real time instead of scanning over the entire beam cross-section.

However, due to accommodation of higher angular spread and hence different flight path lengths of the emitted particles, a significant spread in the flight times for a given q/m is expected which is a drawback of the ion-guide that limits its application in resolving masses with high resolution. However, for emission from electrospray devices concentrated closer to the axis of emission, the effect of the spreading can be small and high transmission and better mass resolution both should be possible.

In Chapter 4, the use of the ion-guide in measuring charge collection fraction and flight times from two types of ionic liquid electrospray devices are discussed. The charge collection fraction and spread in the flight times are discussed in light of angular spread and fragmentation in different sections of the flight path of the emitted particles.

4 Ion-guide characterization

In this chapter, characterization results of the ion-guide is discussed. In section 3.3 in Chapter 3, it has been shown by simulation that, for a given deflecting potential V_{lens} applied to the ion-guide, the designed 65 cm long ion-guide can potentially focus all emitted mono-energetic charges with kinetic energy $1.05 \times qV_{\text{lens}}$ within 23° half-angle about the axis of the ion-guide on a small Faraday cup detector of 1 cm^2 circular area placed at the end of the ion-guide. Therefore, for emission from externally wetted tungsten emitters, typically within a 15° emission half-angle, all emitted charges can be detected with the small detector. For uniformly distributed mono-energetic charges over 40° half-angle, 34% of the charges are within the 23° emission half-angle and the maximum charge collection efficiency is expected to be 34% and more than 20% even from an energy spread about 30%. Due to repeated deceleration and acceleration of the particles in the electrostatic field of the ion-guide, the flight time of the charges is expected to be higher than their otherwise unaltered flight times and significant spreading in the flight times are expected due to accommodation of wide angular spread.

The purpose of the experiments in this chapter is to characterize the ion-guide for its charge collection fraction measurement and its use in flight time measurement from electrospray sources. This has been done in this chapter with two types of electrospray sources as described in Table 3.1 in Chapter 3. It is seen in section 4.1.2 that the ion-guide shows nearly 80% charge collection from the externally wetted tungsten emitters. The experimental results have been compared with simulation results discussed in section 3.3.1 in Chapter 3 and possible sources leading to the differences, such as angular divergence and fragmentation have been addressed. Measurement of flight times from emission of these emitters has shown in section 4.1.3 that the increase in flight times with lens voltage follows the simulated increase very closely. Measurement of charge collection fraction with the micro-fabricated internally wetted capillaries has also shown more than 30% maximum charge collection fraction in section 4.2.3 despite nearly 40° emission half-angle measured in section 4.2.2. The ion-guide characterization results discussed in this Chapter along with the design and simulation results shown in Chapter 3 are published in the following article.

4.1. Ion-guide characterization with tungsten emitter

The characterization metric for the ion-guide with the tungsten emitters has been summarized in Table 4.1. First, emitted current I_{em} vs. emitter voltage V_{em} measurements are shown to find a stable operating voltage region. Then, at a given set of V_{em} the charge collection fraction is

measured and compared with the simulation results shown in section 3.3.1 in Chapter 3. Finally measurement of flight times of the observed monomers and dimers in the emission is discussed.

Table 4.1: Characterization metric for the ion-guide with tungsten emitters

Experiment	Section
I_{em} vs. V_{em}	4.1.1
Charge collection fraction by varying V_{lens}	4.1.2
Flight time measurement with varying V_{lens}	4.1.3

The tungsten emitters are fabricated using an electrochemical process described in [44]. The experimental setup for the measurements has been discussed in section 3.4 in Chapter 3. The fabricated tungsten emitter is wetted with ionic liquid EMI-BF$_4$ and is aligned with an extractor electrode with 1 mm diameter aperture as shown in Figure 3.13 (c) and (d). The emitter voltage is applied with high voltage DC-DC converters (EMCO CA20P and CA20N) and emitter current is monitored using an isolation amplifier (AD210) on the emitter power supply. The current on the Faraday cup detector is monitored using DHPCA-100 transimpedance amplifier for charge collection fraction and flight time measurement.

4.1.1. I-V characteristics

First, I_{em} vs. V_{em} characteristics of a fabricated tungsten emitter (Emitter 1) are experimentally obtained to find onset of emission and stable operation voltages. V_{em}, applied between the emitter and the grounded extractor is increased from 1000 V to 2000 V at 5 V steps in positive and negative emission polarities separately. The ion-guide and the gate electrode both are grounded. At each step, hundred samples of I_{em} are recorded with an analog input channel with 20 ms sampling time and the average $|I_{em}|$ is plotted as a function of $|V_{em}|$ in Figure 4.1 in both polarities. The standard deviation of the measured current is shown on the average reading as error-bar.

Figure 4.1 shows that, emission sets in at around $|V_{em}| \geq 1.1$ kV in both polarities. The emitter current $|I_{em}|$ reaches around 95 nA and 63 nA in positive and negative polarities respectively as $|V_{em}|$ is increased to 2 kV. At close to onset voltage, the current increases sharply with relatively high instability. This region is possibly due to emission from a Taylor cone building up and annihilating in an unstable way. The inflexion around at 40 nA in positive polarity and 20 nA in negative polarity indicates beginning of stable emission which is limited by the transport of the ionic liquid to the tip of the Taylor cone [167], [171]. With increasing electric field, clear jumps in the emission current is visible for positive polarity, which are most likely indicative of formation of multiple Taylor cones [15], [65]. Above $|V_{em}| = 1.4$ kV, the standard deviation of the current is typically less than 10%. Therefore, for ion-guide charge collection fraction experiments in section 4.1.2, the emitter voltage is set to $|V_{em}| \geq 1.4$ kV for stable emission.
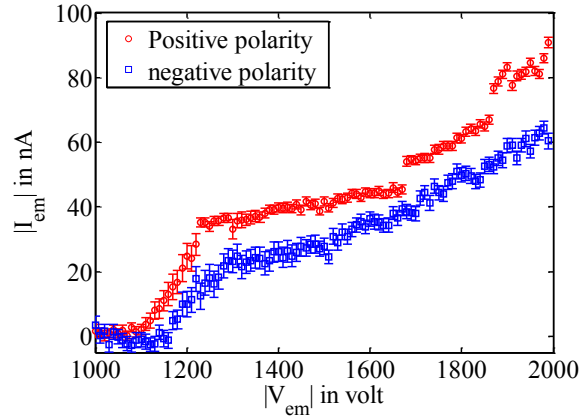
Figure 4.1: Emission current vs. emission voltage plot of tungsten emitters (Emitter 1) in positive and negative polarities. The average of hundred samples at each emission voltage is plotted and the standard deviation is shown as error-bar. In both polarities, emission sets in at around $|V_{em}| \geq 1.1$ kV.

4.1.2. Ion-guide charge collection fraction

Since stable emission is achieved beyond ± 1.4 kV in both polarities for Emitter 1, measurement of the ion-guide charge collection fraction has been performed for emitter voltages higher than this value. The gate electrode is grounded and the emitter voltage V_{em} is set to different fixed values and the voltage to the ion guide, V_{lens}, is varied from 0 to $1.1 \times V_{em}$ in 51 steps for each V_{em}. At each step, the emitted I_{em} and the detected current I_{det} are recorded with NI-USB-6210 analog input system for 1 s with 100 samples/s sampling rate and averaged. The collection fraction is defined in terms of the average emitted current and detected current as

$$\eta = 1.18 \times \frac{I_{det}}{I_{em}} \tag{4.1}$$

where the factor 1.18 is included to take into account the 85% transparency of the gate grid. In Figure 4.2 (a) and (b), η is plotted against V_{lens}/V_{em} at three different emitter voltages in positive and negative polarities respectively. For comparison with the simulation results, the simulated charge collection fraction with the beam-shape reported in [44] for the tungsten emitter is reproduced from Figure 3.10, Case 2 on the same figure. The details of the simulations with the beam-shape are discussed already in section 3.3.1 in Chapter 3.

The measured fraction of detected current reaches a maximum of 80% at $V_{em} = 1450$ V and above 60% for $V_{em} = 1650$ V and 1850 V when the focusing voltage is around $V_{lens} \approx 0.6 \times V_{em}$. In negative polarity, maximum collection fraction reaches 90% for $V_{em} = -1450$ V with $V_{lens} \approx 0.8 \times V_{em}$. For $V_{em} = -1650$ V and -1850 V, the maximum values of η are nearly 80% and 55%, at $V_{lens} = 0.6 \times V_{em}$ and $0.5 \times V_{em}$ respectively. The collection fraction is above 40% with V_{lens}/V_{em} between 0.5 and 1.0 except for $V_{em} = -1850$ V. The maximum collection fraction is in the similar range as obtained in [83], [179] using large metallic plate to collect current, and nearly seven times higher than that obtained in [39] with a single-stage lens within similar angular spread which shows that the ion-guide can enable collection of a large fraction of emitted current on a small detector by guiding the charges along its axis.

However, comparison with the simulated plots on the same figures shows that, although high, the measured collection fraction does not reach the simulated 100%. The broad maxima is wider than the simulated range of V_{lens}/V_{em} and is also shifted by nearly $V_{lens}/V_{em} \approx 0.15$ from the simulation results.

(a) **(b)**
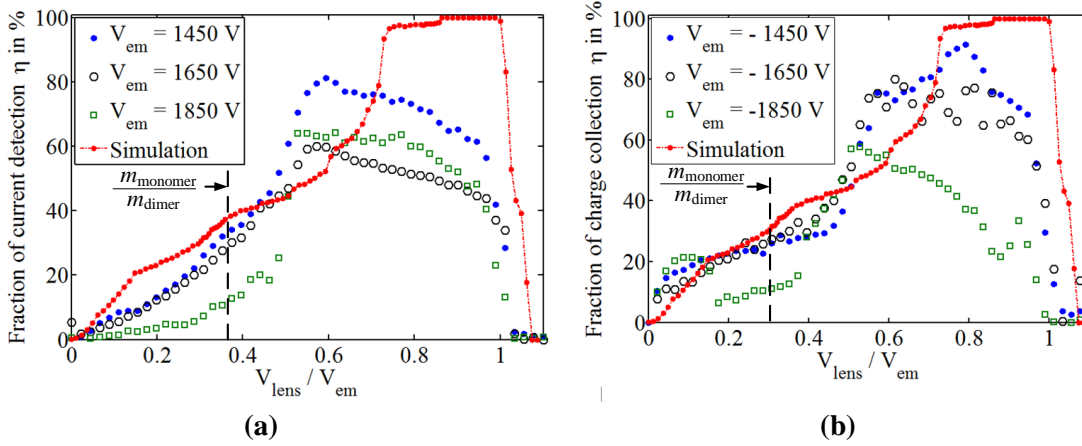
Figure 4.2: Plot of measured fraction of current collected from the tungsten emitter (Emitter 1) vs. V_{lens}/V_{em}. Up to 80% of the emitted beam is collected at the end of the 65-cm long flight tube. The simulation values have also been plotted for comparison. The simulations were performed assuming mono-energetic emission with kinetic energy = qV_{em} and the beam-shape reported in [44]. The dotted black vertical lines correspond to the ratio of mass of a monomer, $m_{monomer}$ to the mass of a dimer, m_{dimer} for emission in respective polarities.

One possible explanation to the left-shift of the apparent broad maxima of the collection fraction may be a beam shape different from that has been assumed in the simulations. In the simulations, the beam shape similar to that reported in [44] has been assumed, which is limited to approximately 15° with a nearly parabolic profile later described in [167], [171]. In [44], a 1.4 mm diameter extractor aperture is used and the emitter tip is in the same plane with the inner plane of the extractor as opposed to 1 mm extractor aperture diameter in the configuration used for the source here. In [171] a 1.6 mm aperture is used with different distances from the extractor and a 10° half-angle is reported for emission voltages between 2.3 kV and 2.95 kV. It can be seen from Figure 3.10 that, as the charges are concentrated closer to the axis of emission, for a given V_{lens}/V_{em} the simulated charge collection fraction is higher, i.e. η(Case 2) > η(Case 1) > η(Case 4) > η(Case 3). If the emitted beam from the used tungsten emitter is concentrated more towards the axis of emission and/or has lower emission half-angle than the assumed beam shape (Case 2), it is expected to have higher charge collection for a given V_{lens}/V_{em}, thus shifting the maxima towards left and broadening the range of V_{lens}/V_{em} that corresponds to 100% collection. However, this should also make possible 100% charge collection which is not obtained in the measurements.

The kinetic energy deficit in the ions may lead to slight left-shift seen in the Figure 4.2 as well. In the simulations, it is assumed that the kinetic energy of the charges is qV_{em} when V_{em} is applied to the tungsten emitter. It has been observed in experimental studies of emission from these emitters that 1% to 3% deficit depending on the type of ionic liquid is possible. In [41], kinetic energy deficit in the emission from EMI-Tf$_2$N less than 7 eV is obtained with 7–8 eV FWHM spread, when emitter voltage is $V_{em} = \pm900$ V to ±1200 V. In [46], less than 15 eV deficit has been observed with BMI-I while operating between ±1.5 kV and ±1.7 kV.

With EMI-BF$_4$, Lozano and Martínez-Sánchez observed less than 2.8% deficit operating at $V_{em} = \pm 1.7$ kV [44]. Therefore, similar fraction of emitted charges is expected to be collected with nearly 1–3% less V_{lens} than those shown in simulation in Figure 4.2, although the observed left shift is nearly 15%.

Another possible explanation to the relatively large left shift may be associated with fragmentation of the emitted charge species. It will be seen in section 4.1.3 that the emission from the tungsten emitter primarily seems to consist of monomers and dimers and the dimers can fragment into monomers. In this following discussion, only monomers and dimers along the axis of the ion-guide are considered. It can be noted that non-zero initial angles of charges, which are also collected (up to 23° as per simulation in Figure 3.9) using the ion-guide, may produce energy spread as well [39]. With increasing concentration at lower kinetic energies than qV_{em} left-shift in the charge collection profile in Figure 4.2 is expected.

Three possible regions of fragmentation can be considered as shown in Figure 4.3.
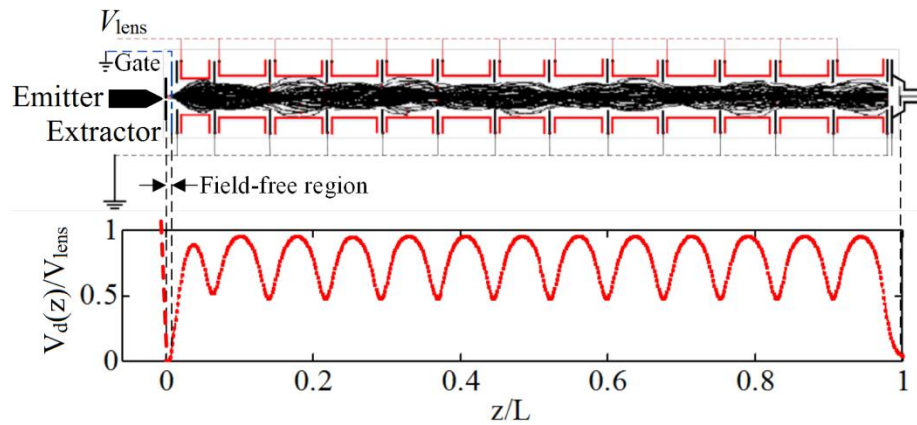
Figure 4.3: (Top) Schematic of the ion-guide with gate electrode grounded. (Bottom) The potential distribution along the axis of the ion-guide for an applied V_{lens}. The field-free region is the region between the extractor electrode of the emitter and the grounded electrode. The red dotted line on the left of the shallow field-free region represents schematically the un-simulated potential distribution inside the accelerating region of the ion species. The right side of the field-free region is the simulated potential distribution inside the ion-guide (between gate electrode and the detection plane of the Faraday cup).

1. In the accelerating region between the tip of the Taylor cone on the emission site and the extractor: In the potential profile at the bottom of Figure 4.3, this is shown as an un-simulated dotted red line at $z/L \leq 0$, but limited to only slightly inside the emitter depending on the electric field distribution between the emitter tip and the extractor.

2. In the field-free region between the extractor electrode and the gate electrode: It can be noted that the extractor and the gate electrode, both, are grounded for charge collection fraction measurements and provides a field free region in between. The electric field from the ion-guide penetrates into the region between the gate grid and the first ground electrode of the ion-guide, however is screened by the gate grid producing a field-free region between the extractor and the gate grid. This is the shallow region on the right side of $z/L = 0$ line.

3. Inside the ion-guide: On the right side of the shallow field-free region, i.e. inside the ion-gudie, the electric field is a nearly periodic function of the distance from the entrance of the ion-guide. In Figure 4.3, the SIMION-simulated normalized (by V_{lens}) electric potential inside the ion-guide is shown. It can be seen that the potential inside the ion-guide periodically oscillates between $0.95 \times V_{lens}$ and $0.48 \times V_{lens}$ except for the first stage and inside the Faraday cup detector.

If a dimer of mass m_{dimer} breaks into a monomer of mass $m_{monomer}$ and a neutral inside the accelerating region, say, at a point where the potential is V_{im}, the kinetic energy of the dimer immediately before break-up is $q(V_{em} - V_{im})$ as the emitter is at a potential V_{em}. The kinetic energy of the fragmented monomer immediately after break up is

$$(K.E.)_{im} = q \frac{m_{monomer}}{m_{dimer}} (V_{em} - V_{im}) \tag{4.2}$$

Just before entering the field-free region, the monomer is further accelerated to gain additional energy qV_{im} and its final kinetic energy at the entrance of the field-free region is

$$(K.E.)_2 = q \frac{m_{monomer}}{m_{dimer}} (V_{em} - V_{im}) + qV_{im} = qV_{em} \left[\frac{m_{monomer}}{m_{dimer}} \left(1 - \frac{V_{im}}{V_{em}} \right) + \frac{V_{im}}{V_{em}} \right] \tag{4.3}$$

where qV_{em} is the ideal kinetic energy of any un-fragmented ion emitted if no other energy loss mechanisms are present [44]. Considering all theoretically possible break-up situations inside the accelerating region, $0 \leq V_{im} \leq V_{em}$ and hence

$$qV_{em} \geq (K.E.)_2 \geq q \frac{m_{monomer}}{m_{dimer}} V_{em} \tag{4.4}$$

The fragmented monomer with kinetic energy in the range given in (4.4) and the un-fragmented monomers and dimers with kinetic energy qV_{em} can therefore be emitted for an applied emitter voltage V_{em}.

The un-fragmented dimers after emission with kinetic energy qV_{em} can also break-up in the field-free region to generate monomers with kinetic energy given by

$$(K.E.)_2 = q \frac{m_{monomer}}{m_{dimer}} V_{em} \tag{4.5}$$

which is same as the lower limit of $(K.E.)_2$ in the relation (4.4). Therefore, if fragmentation occurs before entering the ion-guide field region, the emitted species may possess kinetic energy in the range given by (4.4) even if the emitter voltage is set to V_{em}. In [41], measurements of energy spectra from EMI-Tf$_2$N with a single-grid RPA placed close to the emitter has shown peaks at much lower retarding voltages than the emission voltage V_{em} corresponding to fragmentation of dimers and trimers into smaller ions corresponding to $V_{im}/V_{em} \approx 0$, i.e. field free region. By placing a high resolution RPA grid at the end of a flight tube they also observed secondary peak corresponding to fragmentation in the acceleration region spreading by around 50 eV below the primary peak corresponding to the un-fragmented ions. In [171], similar secondary peaks spreading by around 300 eV below the primary peak has been observed with BMI-Im ionic liquid. With EMI-I, secondary peaks

corresponding to fragmentation of dimers and trimers in the field-free region with full beam capture and around 50 eV spread of the secondary peak corresponding to fragmentation in acceleration region has been observed in [46]. These fragmented ions with lower kinetic energies than qV_{em} are expected to be registered at lower V_{lens}/V_{em} while sweeping V_{lens}. As a result, left-shift of the broad peak of the observed charge collection fraction results shown in Figure 4.2 is expected. Also fragmentation of the emitted particles originally at energy qV_{em} increases population of charges at lower kinetic energies by reducing the number of particles at qV_{em}, resulting in lowering of the charge collection fraction peak value.

Although the wide-spread kinetic energies in the emission due to fragmentation seems a plausible explanation to the observed differences with the simulated profile in Figure 4.2, no prominent peak corresponding to $m_{monomer}/m_{dimer} \times qV_{em}$ in Figure 4.2 are observable when V_{lens} is low enough to collect these charges. It can be noted that the operation of the ion-guide is somewhat similar to a wide-band energy analyzer that allows a wide range of kinetic energies of the ions through the guide for a given applied V_{lens}. Therefore, a distinct kinetic energy peak at $m_{monomer}/m_{dimer} \times qV_{em}$ is expected to be fully transmitted for a broad range of values of V_{lens}, hence flattening the peak that would have been observed with an otherwise high resolution single-grid or multiple-grid RPA analyser such as in [41], [46]. Also, further broadening of the kinetic energy distribution among the emitted ions is expected due to possible fragmentation of in-flight un-fragmented ions inside the ion-guide where they are repeatedly decelerated and accelerated due to the electric field distribution of the ion-guide. The un-fragmented dimers entering the ion-guide may break-up inside an arbitrary stage, n, of the ion-guide at a distance z_0 from the entrance of the ion-guide where the potential is $V_d(z_0)$ shown in Figure 4.3 after losing energy $qV_d(z_0)$. In that case, the kinetic energy of the monomer immediately after fragmentation can be written as

$$(K.E.)_2 = q \frac{m_{monomer}}{m_{dimer}} \left[V_{em} - V_d(z_0) \right] \tag{4.6}$$

Since $0.48 \times V_{lens} \leq V_d(z_0) \leq 0.95 \times V_{lens}$, in almost all the stages in the ion-guide, depending on where fragmentation took place, the kinetic energy of the monomer can be in the range

$$q \frac{m_{monomer}}{m_{dimer}} V_{em} \left(1 - 0.48 \frac{V_{lens}}{V_{em}} \right) \geq (K.E.)_2 \geq q \frac{m_{monomer}}{m_{dimer}} V_{em} \left(1 - 0.95 \frac{V_{lens}}{V_{em}} \right) \tag{4.7}$$

or in the range

$$q \frac{m_{monomer}}{m_{dimer}} V_{em} \geq (K.E.)_2 \geq q \frac{m_{monomer}}{m_{dimer}} V_{em} \left(1 - 0.95 \frac{V_{lens}}{V_{em}} \right) \tag{4.8}$$

considering the region close to entrance or exit of the ion-guide where $V_d(z)/V_{lens} \approx 0$. This relation shows that, depending on the ratio of applied deflection potential V_{lens} to the emitter voltage V_{em}, and depending on where inside the dimer fragments, a considerable range of kinetic energies below $m_{monomer}/m_{dimer} \times qV_{em}$ are also possible for the fragmented monomer. Un-fragmented ions emitted from the accelerating region of the emitter, are more likely to fragment in the long ion-guide under decelerating electric field than in the shallow field-free region due to their much longer residence time in the ion-guide and hence the fragmented ions are expected to have a range of kinetic energies below $m_{monomer}/m_{dimer} \times qV_{em}$. These ions are

collected for lower values of V_{lens} than that required to collect the ions fragmented in the field-free region.

This above discussion can be summarized below in terms of the kinetic energies of fragmented ions in the three regions:

1. Fragmentation in the accelerating region:

$$qV_{em} \geq (K.E.)_2 \geq q\frac{m_{monomer}}{m_{dimer}}V_{em} \qquad (4.4)$$

2. Fragmentation in the field-free region:

$$(K.E.)_2 = q\frac{m_{monomer}}{m_{dimer}}V_{em} \qquad (4.5)$$

3. Fragmentation inside the ion-guide

$$q\frac{m_{monomer}}{m_{dimer}}V_{em} \geq (K.E.)_2 \geq q\frac{m_{monomer}}{m_{dimer}}V_{em}\left(1 - 0.95\frac{V_{lens}}{V_{em}}\right) \qquad (4.8)$$

It can be mentioned here that, these ranges are only for axially directed ions and considering fragmentation of dimers into monomers only, pertinent to the case of emission comprising of only monomers and dimers as will be seen from flight time measurement in section 4.1.3 for the tungsten emitters under use. For mixed ion-droplet emission and emission of higher solvated ions discussed in section 4.2 from capillary emitters, many different mass-ratios are possible before and after fragmentation.

Maximum collection lower than expected 100% on the detector may also be caused by practical imperfections of the entire system, such as misalignment of the parts of the ion-guide, or, of the axis of the emitter with respect to the axis of the ion-guide. It has been mentioned in section 3.4.2 that the source-end of the ion-guide sags a little inside the vacuum chamber, introducing angular offset of the axis of the emitter with the axis of the ion-guide. The emitter itself may be slightly tilted with respect to the normal to the extractor or the sharp tip of the emitter may have angular inclination. This may result in part of the emission not entering the ion-guide and reducing the collection fraction on the detector. It is also possible that, as in [15], [65], emission may occur from Taylor cones away from the tip of the emitter at a non-zero angle to the ion guide axis, or, from multiple emission sites having angular offset among themselves, resulting in fraction of the emission physically blocked by the grounded gate electrode or the first ground electrode of the ion-guide.

It is seen in Figure 4.2 that at different emission voltages, the charge collection fraction results are different for a given V_{lens}/V_{em}. At $|V_{em}| = 1450$ V, highest collection is achieved. It can be mentioned here that the tests are performed by continuously operating at a single V_{em} and varying V_{lens} from 0 to $1.1 \times V_{em}$ in 51 steps. The total duration of continuous emission at a given V_{em} is nearly 1 minute. Measurement sequence in terms of V_{em} is: 1450 V, then -1450 V, then 1650 V, then -1650 V, then 1850 V and then -1850 V. During continuous spray for about one minute at each polarity, the electrochemical reactions on the emitter may continuously degrade the emitter and the ionic liquid [43]. Also, in [65], results of in-situ transmission electron microscopy (TEM) observation of Taylor cone formation during unipolar electrospray from tungsten emitters with ionic liquid OMIM-BF$_4$ have shown

multiple Taylor cones and growth of solidified dendritic structures from Taylor cones with time. Such geometric and chemical changes in long-duration emission may lead to non-repeatable emission characteristics over time and emission from a particular emission site in a particular direction may not be ensured in the entire duration of the measurements shown in Figure 4.2.

The non-repeatability of charge collection fraction from a single emitter has been observed by electrospraying from the same emitter, Emitter 1, at same emission voltage in successive measurements. Also, from emitter to emitter, the charge collection fraction results are found to be different. Figure 4.4 (a) shows the charge collection fraction results for Emitter 1 at V_{em} = 1650 V performed three successive times after the measurements shown in Figure 4.2. In Figure 4.4 (b), the results for another emitter, Emitter 2, are shown. The results for Emitter 2 show that only up to around 35% of the emission could be collected as opposed to more than 80% for the Emitter 1. The maxima in η for both the emitters lie in the same range of V_{lens}/V_{em}, typically around at 0.6 ± 0.1 indicating that the kinetic energy of emitted ions are similar in both the emitters. However, much lower collection fraction for Emitter 2 may be due to majorly off-axis emission.

(a) **(b)**
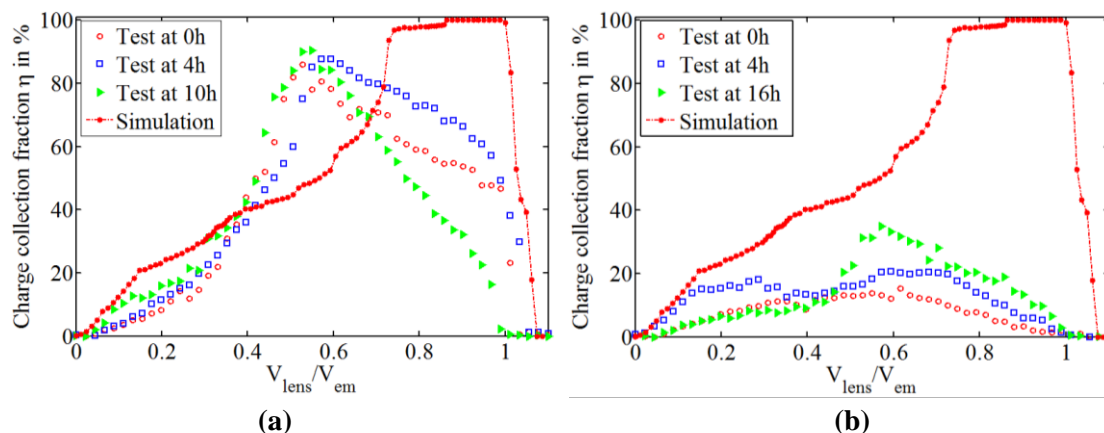
Figure 4.4: Plot of measured fraction of current collected versus V_{lens}/V_{em} from two different tungsten electrospray emitter, Emitter 1 (a) and Emitter 2 (b). The successive experiments on the same emitter do not show identical profile. Different emitters show different charge collection fraction.

4.1.3. Flight time measurement

In section 3.3.2 in Chapter 3 it was mentioned that the flight time of the charges increases with increase in deflecting potential V_{lens} for a given emitter voltage V_{em}. A ToF correction factor is defined in Eqn. (3.5) as a function of V_{lens}/V_{em} which is independent of q/m and from Figure 3.11 (b) it is seen that for different initial angles of the ions, the ToF correction factor is different, leading to spreading in the flight times even for the same q/m and same initial kinetic energy.

The flight time of the ions are recorded at three different values of V_{em} in both polarities of operation from Emitter 1 while varying the lens voltage V_{lens}. The gate signal V_{gate} is triggered at time $t = 0$ with a fall-time less than 100 ns using pulse generator PVX-4140 [175] to allow the emitted ions through the ion-guide. No averaging over traces has been performed on the ToF traces.

In Figure 4.5, the ToF traces at two different ion-guide potentials V_{lens} but at the same emitter voltage of $V_{em} = 1650$ V are shown. The traces are rather noisy; however, with averaging over samples on the oscilloscope, this can be reduced. From the non-averaged traces in Figure 4.5, it can be clearly seen that monomers and dimers exist in the emission. At different V_{lens}, the flight times of the emitted monomers and dimers are different, both increasing with V_{lens} for a given V_{em}.
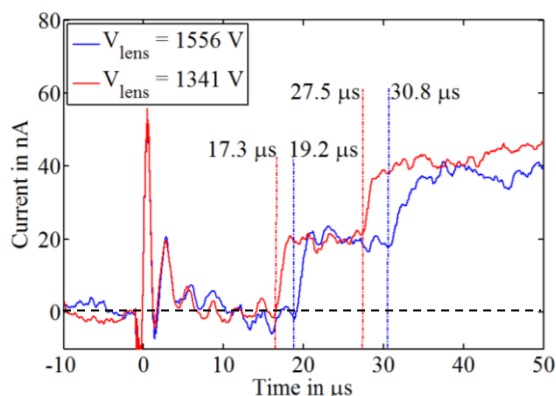
Figure 4.5: Time of flight traces at two different ion-guide potentials from the tungsten emitter, Emitter 1, at $V_{em} = $ 1650 V. Existance of monomers and dimers in the traces are visible. With increase in ion-guide potential V_{lens}, the flight time of the same ions increases.

The non-infinite slope in the traces at times corresponding to the flight times of the monomers and dimers indicate spreading of the flight times by around 1 μs for monomers and 2−3 μs for dimers. It can be remembered here section 3.3.2 in Chapter 3 that the maximum spread in flight times for ions with same q/m and initial kinetic energy can be as high as 36% between the ions travelling along the axis of the ion-guide and ions having an initial angle of 23°, i.e. at the limit of acceptance angle of the ion-guide. The observed spread in the flight times is hence smaller than the estimated spread. This is most likely because most of the emitted ions are closer to the axis in the nearly parabolic beam shape of the emission. Apart from different initial angle of the ions, possible spread in kinetic energy due to fragmentation may also contribute to spreading in flight times. If the dimers fragment inside the field-free region of the ToF setup, after gaining a kinetic energy close to qV_{em}, (the gate electrode is grounded when measuring flight times) as described in section 4.1.2 and in Figure 4.3, the monomers immediately after fragmentation are expected to have the kinetic energy $(K.E.)_2$ given by Eqn. (4.5) and a speed equal to the speed of the original dimer. Unlike a field-free flight tube, where these monomers travel the flight length to register on the detector with the same flight time as the original dimer would have, the ion-guide may or may not allow the fragmented monomer through the flight tube depending on $qV_{lens}/(K.E.)_2$. It can be seen from Figure 3.9 (b) in Chapter 3 that if the kinetic energy of the ion is less than $qV_{lens}/1.2$, they are not transmitted through the ion-guide at all. If V_{lens} is high, such as, in the range $0.6 \times V_{em}$ to $0.9 \times V_{em}$, the fragmented monomer with kinetic energy $(K.E.)_2$ much lower than qV_{em} may not be allowed together with the un-fragmented ions with energy qV_{em} whereas at lower V_{lens} only a small fraction of un-fragmented ions at qV_{em} very close to the axis may pass through the ion-guide. If the fragmented ion is transmitted, they would take longer time than an originally generated monomer and shorter time than an un-fragmented dimer because of dependence of the ToF correction factor on V_{lens} and hence would lead to finite slope of the ToF traces.

Dimers fragmented in the acceleration region, such that the kinetic energy of the fragmented monomer is less than, but close to, qV_{em} [41], [46], [171], may pass through the ion-guide along with the un-fragmented ions at energy qV_{em} given the width of the pass-band of the ion-guide. For monomers generated due to fragmentation inside the ion-guide, kinetic energy is even less than those fragmented in the field-free region and hence would be allowed to be detected only for very low V_{lens}/V_{em}.

Therefore, while at low V_{lens}/V_{em}, mainly fragmented ions in the field-free region and in the ion-guide, and only un-fragmented ions emitted very close to the axis of the ion-guide are registered for flight time measurement, at higher V_{lens}/V_{em}, mostly un-fragmented ions and ions fragmented in the accelerating region over a wide angle are registered. In both situations, the fragmented ions are expected to produce spreading in the flight times of the otherwise un-fragmented monomers, smaller at high V_{lens}/V_{em} and higher at low V_{lens}/V_{em}.

(a)

(b)
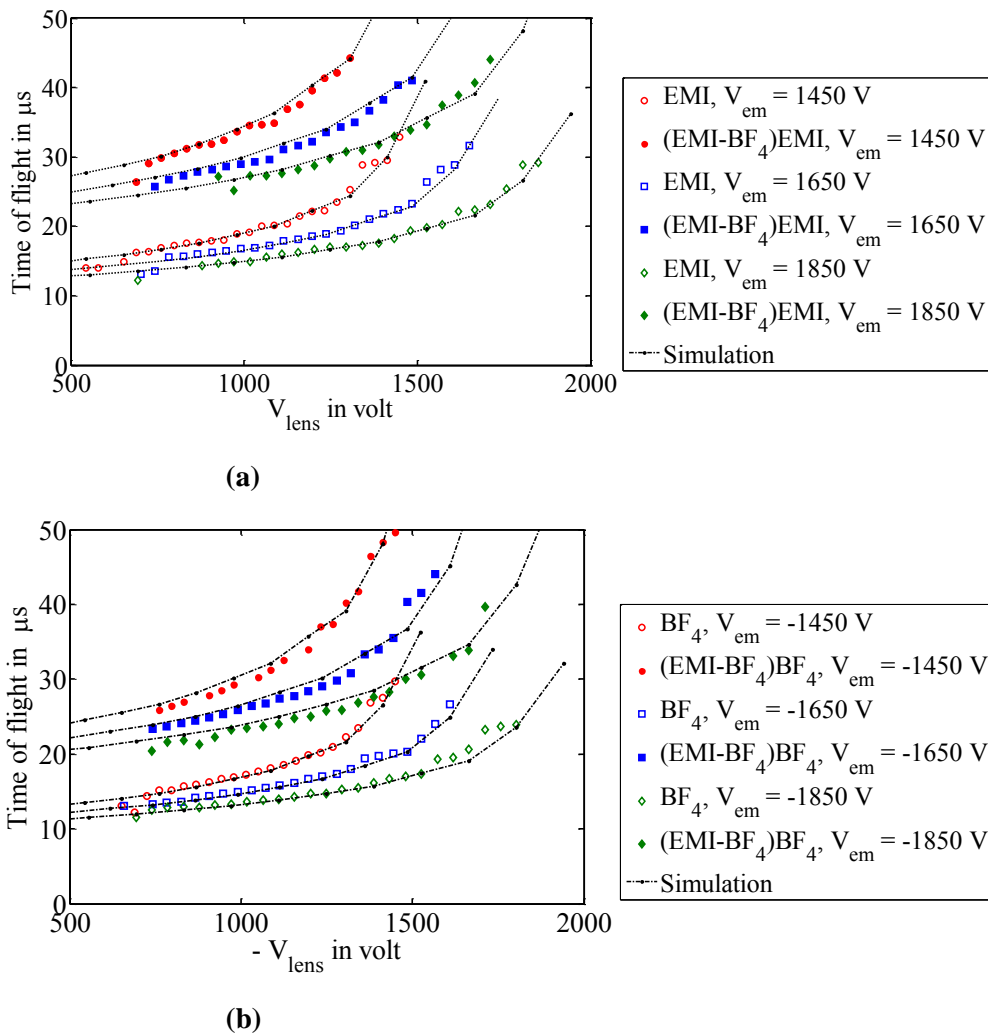
Figure 4.6: Plot of measured flight times of monomers and dimers from tungsten electrospray emitters versus lens voltages at three emitter voltages in both positive (a) and negative (b) polarity of emission, showing the increase in flight time with lens voltage. The simulated values are also shown in the same figure for comparison. The change of the ToF with V_{lens} for the different species very closely follows the simulation results.

In Figure 4.6 (a) and (b), the experimentally observed variation of the flight times of the

observed monomers and dimers with V_{lens} at different emission voltages is shown for both polarities of emission. Since fragmented ions and initial angular spread in the emission, both, lead to spreading in the flight times, the flight times in Figure 4.6 (a) and (b) are taken to be the value corresponding to the beginning of the rise of the current trace where the current steps up. This instant of time in the ToF traces correspond to the flight time of only un-fragmented charges emitted along the axis of the ion-guide, i.e. the fastest ones reaching the detector. The simulation results, based on the ToF correction factor shown in Figure 3.11 (b) for the corresponding situations with $\theta_{em} = 0°$, are also shown on the same figures for comparison. At lower $|V_{lens}|$ than 500 V, the charge collection fraction is very low and flight time measurements at these values are not performed. Also, at lower $|V_{lens}|$, ions generated due to fragmentation in the field-free region and in the ion-guide are expected to be collected with almost arbitrary flight times leading to ambiguity in the flight times of the un-fragmented ion species. In the range of V_{lens} shown in Figure 4.6, the maximum difference between the measured flight times and the simulated flight times is around 2 μs and the flight times follow the simulated variation within ±2 μs. The closeness of simulated flight times at $\theta_{em} = 0^o$ with the measured values indicate that, in the range of V_{lens} used, mostly un-fragmented ions and fragmented ions in the accelerating region with kinetic energy close to that of the un-fragmented ions are collected on the detector, given that experimental error in determining the flight time from the slope also contributes to the 2 μs error.

4.2. Ion-guide characterization with capillary emitter

The ion-guide has also been characterized with internally wetted micro-fabricated single capillary emitter, typical properties of which have been displayed in Table 3.1 in Chapter 3. Retarding potential analysis (RPA) of these devices has previously shown that the kinetic energy of emission can have nearly 10% deficit from the applied emitter potential V_{em} [5], [57], [35] and secondary peaks corresponding to fragmentation. The emission typically comprises of mixture of ions and droplets [5], [57], [35], [61]–[63] unlike the externally wetted tungsten emitters discussed in section 4.1. It will be seen in section 4.2.2 that the beam-half angle from these devices is nearly 40°. Therefore, charge collection fraction from these emitters may be widely different from the tungsten emitters.

To characterize the ion-guide with these devices, first the emitter current I_{em} vs. emitter voltage V_{em} measurements are performed. Simultaneously, beam-shape measurement of the emission has also been performed. Finally charge collection fraction measurements and flight time measurements have been performed at stable emission region. A summary of the characterization metric can be listed in Table 4.2.

Table 4.2: Characterization metric for the ion-guide with capillary emitters

Experiment	Section
I_{em} vs. V_{em}	4.2.1
Beam shape measurement	4.2.2
Charge collection fraction by varying V_{lens}	4.2.3
Flight time measurement with varying V_{em}	4.2.4

4.2.1. I-V characteristics

First, the setup has been prepared for beam-half-angle measurement. Emitter current vs. emitter voltage plots are obtained with beam-shape plots simultaneously. The multiplexed annular detection plate, as discussed in section 3.4.4 in Chapter 3 has been placed at 2.5 cm from the emitter and emitter current, extractor current and the current on the nineteen detector plates are recorded in both polarities of emission. No additional measure has been taken to suppress secondary emission from the detector when the emitted charged particles hit the plate at high velocity. Emitter current is monitored using isolation amplifiers from the emitter power supply as described in section 3.4.3. In Figure 4.7, the average emitter current and extractor current in both polarities of emission for a capillary emitter with 150 μm extractor diameter and 10 μm emitter capillary inner diameter are shown by sweeping the emitter voltage from ±600 V to ±850 V. At each step of applied $|V_{em}|$, the emitter current and extractor current are recorded for 5 sec with $+ V_{em}$ and then another 5 sec with $-V_{em}$ with analog input channel at a sampling speed 500 samples/sec. Since at each V_{em} current on the nineteen detectors are to be recorded serially with the beam-shape measurement setup, the frequency of the bipolar emission operation is set to a low value, 0.1 Hz, such that current on the nineteen plates can be recorded within 5 sec in each polarity. This slow bipolar operation is not optimal for ionic liquid electrospray for suppressing electrochemical reactions [43], but provided nearly 250 ms for selecting a detector plate using the relays in the beam-shape measurement setup and read the current. The standard deviation of the measured emitter current and extractor current at each emitter voltage is shown as an error bar on the corresponding mean values in Figure 4.7. The beam-shape results are discussed in the next sub-section.

It can be seen from Figure 4.7 that emission sets in at around $|V_{em}| = 700$ V in both polarities and increases to above 1.5 μA as the emitter voltage in increased. At the same time, nearly 3% of the emitted current is either blocked by the extractor while emitting from the capillary or is retraced back to the extractor after hitting on the detector plates. Secondary electrons emitted from the detector and intercepted by the extractor may decrease the magnitude of extractor current in positive polarity of emission and increase in negative polarity of emission. Since the extractor current is nearly same in both polarities and much smaller than the emitter current, the secondary electron current is neglected here.
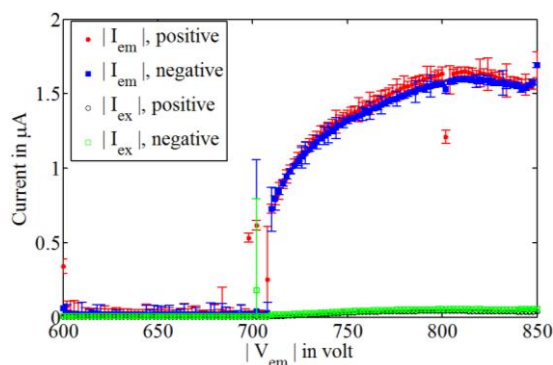
Figure 4.7: Current vs. voltage plots from a capillary electrospray emitter. The emitter inner diameter is 10 μm and extractor diameter is 150 μm. The average emitter and extractor currents are plotted against the emitter voltage in both polarities.

4.2.2. Beam-shape measurement

In each polarity of emission, during the 5 sec time, the current in the 19 detectors in the multiplexed detector plate are recorded serially for 200 ms duration each allowing nearly 50 ms for selecting a plate using the relays and eliminating the transients. In Figure 4.8, the monitor signals and the detector plate signal from the same capillary emitter discussed above are shown. At each $|V_{em}|$, the emitter current I^+_{em} and I^-_{em}, from the two high voltage power supplies for $+V_{em}$ and $-V_{em}$ are monitored separately. The emitter voltage supplies are set to $+V_{em}$ and $-V_{em}$ and the voltage to the emitter is switched at the instant $t = 5.3$ sec from $+V_{em}$ to $-V_{em}$. The bipolar emitter voltage between $+V_{em}$ and $-V_{em}$ is actually measured only during the small pulses shown in the corresponding trace in Figure 4.8 ($V_{em(mon)}$) and during monitoring the emitter voltage, there is corresponding offset in the emitter current monitor signals as the voltage monitor circuit draws current from the emitter power supplies in addition to the actual emitter current in the capillary. The detector current trace at the bottom of Figure 4.8 during each half of the entire trace is a serial readout from the 19 detector plates and the steps in the current correspond to currents read at different detector plates.
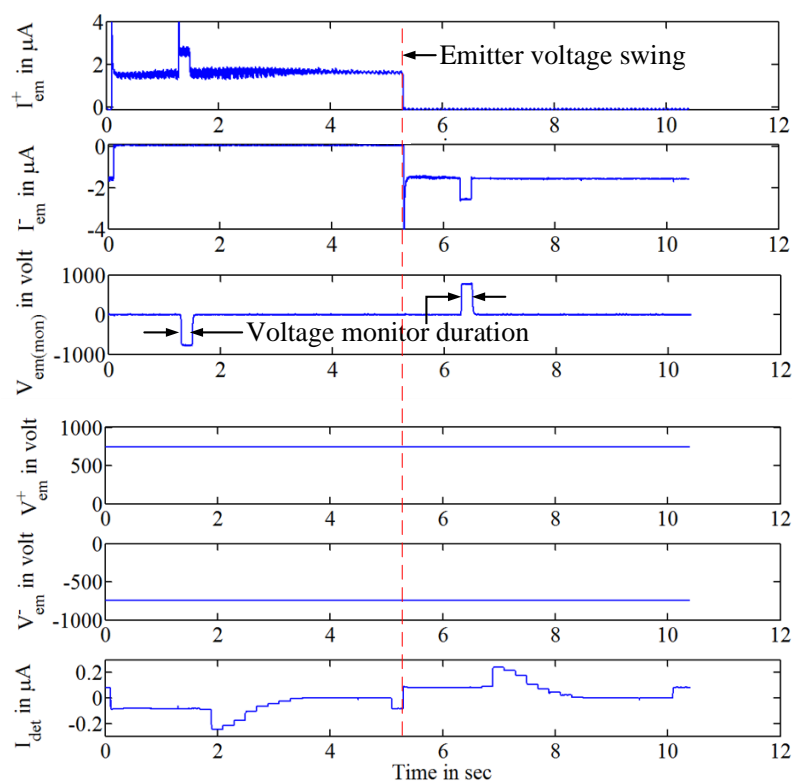
Figure 4.8: Typical traces recorded during beam-shape measurement with a multiplexed detector plate. In the top two traces, the current from the positive and negative emitter supplies are monitored. In each polarity, only during 300 ms, the actual switched emitter potential is monitored by changing from the emitter current monitor mode to emitter voltage monitor mode. However, the power supply voltages directly from the two emitter supplies are continuously monitored during the entire operation. The current in the 19 detector plates are serially monitored in both polarities.

First, the 19-hex detector plate has been used to find the axial symmetry of emitted current in the spray cross-section. In Figure 4.9, the currents at each plate normalized to the total current

detected in all plates at $V_{em} = -740$ V are shown for the same capillary device. The colour-bar represents the current fraction in each plate. The spray current is axis-symmetric with maximum differences in the detected current in the six plates in the first annular ring within 14% and 16% in the twelve plates in the second annular ring.

With the annular ring detector plate, as discussed in section 3.4.4 in Chapter 3, the radial or angular current density distribution is obtained with higher angular resolution assuming an axis-symmetric spray. If IR_n and OR_n are the inner and outer radii of the nth ring detector in the 19-annular plate shown in Figure 3.17 (b) and I_n is the current detected by the nth plate, an average current density J_n can be defined, with certain degree of approximation, at the mean radius $R_n = (IR_n + OR_n)/2$ ($n \geq 0$) with $IR_0 = 0$ (for the central circular detector plate) such that
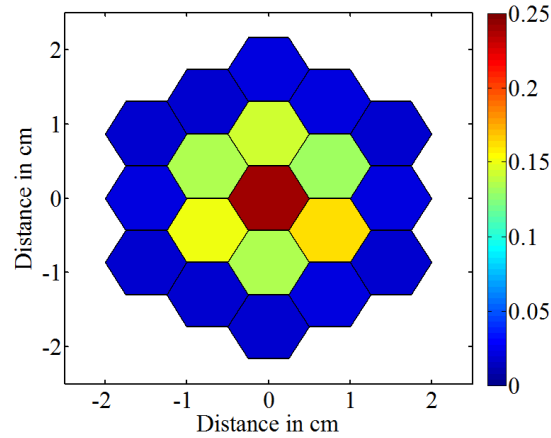
Figure 4.9: Current distribution in the 19-hex multiplexed detector plates at −740 V emitter voltage. The colour in each hexagonal area corresponds to the fraction of the total current detected in each plate. The current distribution in the emission cross-section shows nearly axis-symmetric emission.
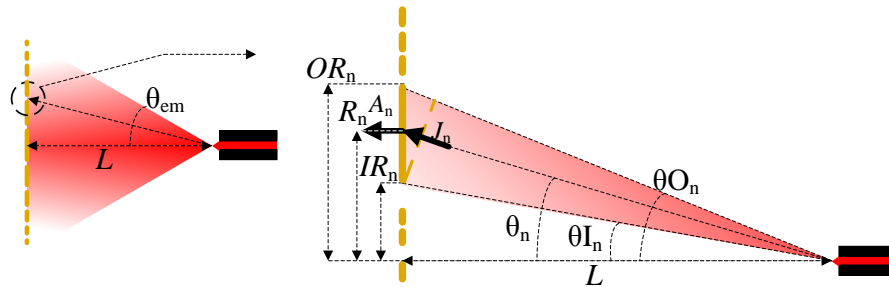
Figure 4.10: Beam-shape measurement schematic. The annular multiplexed detector plate is placed at a distance L from the emitter head. The Current density in each plate is defined at the mean radius of each annular detector.

$$I_n = \vec{J}_n . \vec{A}_n = \pi(OR_n^2 - IR_n^2)\cos\theta_n J_n \tag{4.9}$$

at an angle θ_n given by

$$\tan\theta_n = \frac{R_n}{L} \tag{4.10}$$

where L is the distance between the capillary and the plates as shown in Figure 4.10.

In Figure 4.11 (a) and (b), the current density vs. angle plot at different positive and negative emitter voltages are shown for the same capillary device. The results show that the current density is distributed over an overall half-angle of between 30° and 40°, increasing as $|V_{em}|$ increases. The calculated current density from the measured current is found to have an off-axis maxima, approximately at around 10°–15°.

(a)   (b)
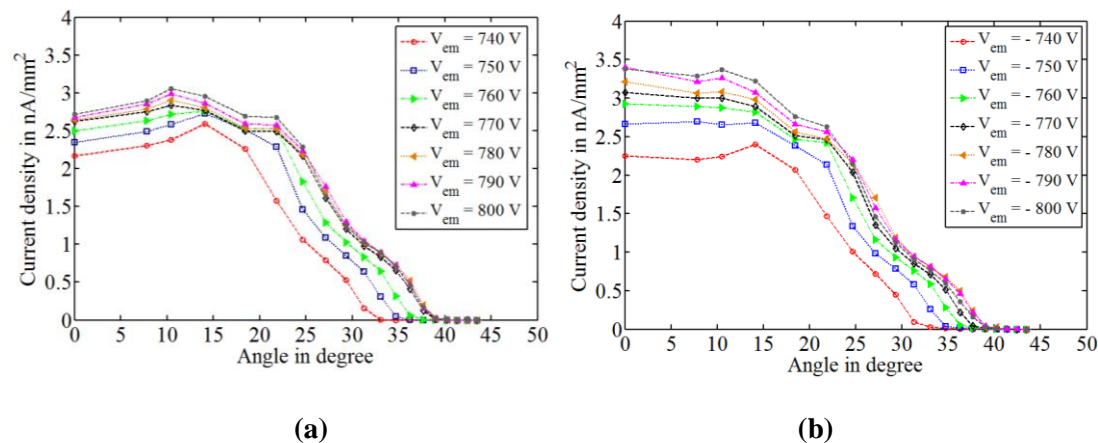
Figure 4.11: Measured current density vs. emission half-angle at different positive (a) and negative (b) emission voltages from the capillary emitter. The emitted current is distributed typically within a half-angle of 30°–40°.

Beam-angle measurments have been performed on single capillary emitters with150 μm, 200 μm, 250 μm and 300 μm extractor diameters and the similar trend in beam shape has been observed. This angular spread in the internally fed capillary device is wider than that reported for externaly wetted tungsten emitters [44], [171]. Also, the apparent off-axis peak in the current density is not observed from the externally wetted tungsten emitters which has a nearly parabolic beam-shape [44], [171]. On the other hand, in [59], measurements with metallic capillary emitter has shown nearly 35° half-angle spread and a peak current density at around 20° with almost no current close to the axis. In [87], angular spread in droplet emission from capillary emitters is found to be around 30° with two very distinct regions of high population of charge species: lower q/m closer to the axis and higher q/m away. Possibility of formation of a cone-jet structure on the ionic liquid during emission in mixed ion-droplet mode has already been discussed in section 1.4.2 and Figure 1.7 in Chapter 1 based on Ref. [41], [109] in which, droplets are expected to be emitted close to the axis of the emitter and ions at larger angles from the axis. The wide emission half-angle and the off-axis peak in the observed beam shape in Figure 4.11 for the capillary devices is indicative of a superposition of droplet emission close to the axis and ionic emission away from the axis.

4.2.3. Ion-guide charge collection fraction

For ion-guide charge collection fraction measurements, the beam-shape measureent setup is removed and the current is detected on the Faraday cup at the end of the ion-guide. Similar to section 4.1.2, the gate electrode is grounded. In Figure 4.12, the measured fraction of current collected for different positive and negative emitter voltages using Eqn. (4.1) are shown for the same capillary emitter used in section 4.2.1 and 4.2.2. The experimental configuration is

identical to the that for the tungsten emitters, but the positive and negative polarities of operation are performed in a bipolar mode, where the polarities of emission voltage and the ion-guide voltages are alternated at at 1 Hz. At each emitter voltage the ion-guide potential is increased from 0 to $1.1 \times V_{em}$ and ratio η is found out as a function of V_{lens}/V_{em}.
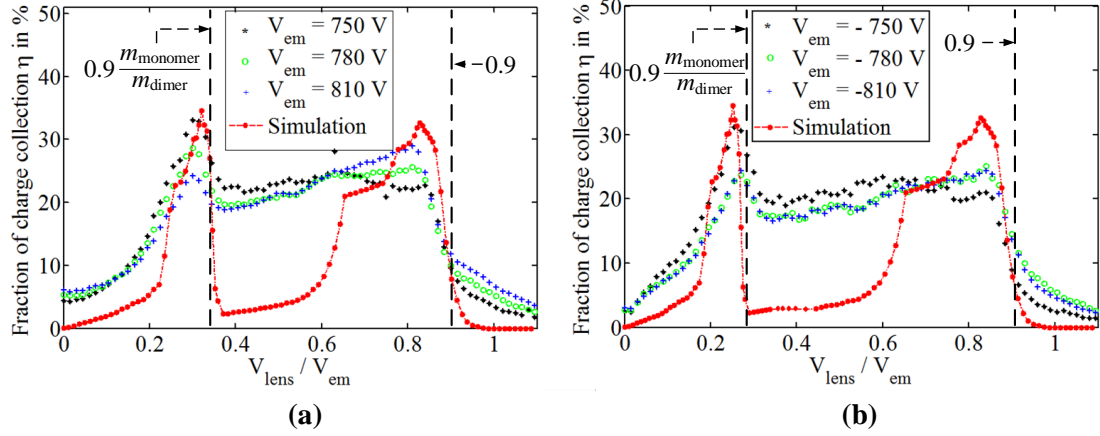
Figure 4.12: Plot of the fraction of current detected from the microfabricated electrospray emitters versus V_{lens}/V_{em} in (a) positive and (b) negative polarity if emission. The simulation results assuming a beam-shape as shown in Figure 4.11 (b) for $V_{em} = -740$ V and two kinetic energies given by (3.3) and (3.4) with equal intensities are also shown in the same figures for qualitative comparison.

It can be seen in Figure 4.12 that the experimentally obtained η is above 20% over a wide range of V_{lens}/V_{em} between 0.25 and 0.9, reaching a maximum of around 35%. Particularly interesting is the significant peak at around $V_{lens}/V_{em} = 0.3$ in positive polarity and $V_{lens}/V_{em} = 0.25$ in negative polarity. It is mentioned from Ref. [5], [57], [35] at the beginning of section 4.2 that the primary peak kinetic energy of the emitted species from micro-fabricated capillary devices is approximately at $0.9 \times qV_{em}$ when emission voltage is set to V_{em}. The emission spectra of the full-beam also comprises of secondary peaks associated with fragmentation. Therefore, for comparison, the vertical dotted lines at $V_{lens}/V_{em} = 0.9$ and $V_{lens}/V_{em} = 0.9 \times m_{monomer}/m_{dimer}$ are shown in Figure 4.12 (a) and (b) assuming only the simplest case of fragmentation of a dimer at $0.9 \times qV_{em}$ into monomer in a field-free region. Also, on the same figures, the simulated charge collection fractions are plotted for emission only at these two kinetic energies with equal intensities and both species following a beam-shape identical to the case $V_{em} = -740$V shown in Figure 4.11 (b). It can be remembered that this simulation configuration is the Case 5 in Figure 3.10 and more details of the simulation is available in section 3.3.1 in Chapter 3.

It can be inferred from comparison of the simulation and measurement results in Figure 4.12 that the peak close to $V_{lens}/V_{em} = 0.3$ in positive polarity and $V_{lens}/V_{em} = 0.25$ in negative polarity indeed correspond to break-up of dimers into monomers in the field-free region or very close to the extractor plane in the accelerating region of the emitter, after gaining a kinetic energy close to $0.9 \times qV_{em}$. The collection fraction for the un-fragmented particles, on the other hand, show a broad peak nearly coinciding with the simulated peak close to $V_{lens}/V_{em} = 0.8$. However, it will be seen in Figure 4.13 and in section 4.2.4 that the emission shows evidence of possible emission of trimers and droplets as well. When a droplet or a trimer breaks into a smaller droplet or ion, the mass ratio and hence the kinetic energy of the

fragmented charges may cover a wide range. The break-up of higher solvated ions (trimers or droplets) are expected to take place quicker, before entering the ion-guide [41]. If they fragment into a monomer in the field-free region, the monomers have kinetic energy on the left side of the vertical line at $0.9 \times m_{monomer}/m_{dimer}$ due to lower mass ratio. If they fragment in the accelerating region before the extractor, the monomer can have from extremely low kinetic energy up to $0.9 \times qV_{em}$ depending on mass ratio and V_{im} in Eqn. (4.3), i.e. which charge species fragmented into which smaller charge species and where inside the accelerating region it took place. The measured large collection fraction in the wide range of V_{lens}/V_{em} between the two peaks is most likely due to fragmentation of various types of solvated ions into smaller ones taking place anywhere between the emitter tip and the detector. The 5–15% collection fraction below $V_{lens}/V_{em} = 0.2$, may, for example, be contributed by three types of species:

1. Un-fragmented charges with kinetic energy close to $0.9 \times qV_{em}$ but directed axially which are guided even at low V_{lens}.

2. Trimers and droplets fragmenting into smaller ions with a mass ratio smaller than $m_{monomer}/m_{dimer}$ in the field-free region, producing kinetic energy equal to or slightly higher than the qV_{lens} applied by the ion-guide for collecting them.

3. Any type of fragmentation inside the ion-guide that produces kinetic energy after fragmentation lower than $0.9 \times m_{monomer}/m_{dimer} \times qV_{em}$.

Also, as discussed for tungsten emitters in section 4.1.2, angular spread of the emission, misalignment of the emission axis with the axis of the ion-guide also may lead broadening of the η vs. V_{lens}/V_{em} profiles for the capillary devices.

4.2.4. Flight time measurement

It has already been established in section 4.1.3 and with the help of Figure 4.6 that the increase in flight times of the charge species follows the ToF correction factor defined in Eqn. (3.5) and in Figure 3.11 (b) in Chapter 3 quite accurately. Hence, flight time measurements are performed on the capillary emitters for different V_{em} with $V_{lens} = 0.7 \times V_{em}$ to ensure high fraction of charge collection of kinetic energies close to that of un-fragmented charges, instead of varying V_{lens} at constant V_{em} collecting all possible kinetic energies up to qV_{em}. At $V_{lens} = 0.7 \times V_{em}$, it is expected that mostly un-fragmented charge species at $0.9 \times qV_{em}$ and those fragmented to produce kinetic energies smaller than, but close to, $0.9 \times qV_{em}$ are collected for ToF measurement. Fragmented ions having kinetic energies widely away from the acceptable range of the ion-guide at the given V_{lens} are expected to be blocked by the ion-guide.

Setting $V_{lens} = 0.7 \times V_{em}$ leads to a ToF correction factor of 1.5 for the axially aligned beams from Figure 3.11 in Chapter 3. In Figure 4.13 (a), the ToF trace from the capillary emitter at an emission voltage $V_{em} = -770$ V is shown. The existence of monomer and dimer in the ToF trace is visible; however, the spreading in the flight time is also clearly seen. A transition from dimers currents to higher m/q current is also visible in the trace indicating existence of trimers or droplets although the current is much lower than that corresponding to the monomer and dimer.

There is approximately a 2 μs spread, around 10%, in the flight time of the monomers, partly attributable to the wide acceptance angle of the ion-guide and partly to fragmentation of

solvated ions inside the accelerating region of the emitter. It can be noted that, this value is less than the estimated 36% based on nearly 40° emission half angle as given in Eqn. (3.6a) in Chapter 3. Apart from the angular spread, the relatively large spread in the trace corresponding to an un-fragmented dimer may be caused, in general, by a dimer or a monomer generated by fragmentation of larger charge species. For example:

1. Dimer breaking into monomer inside the accelerating region of the emitter and the resulting monomer having kinetic energy in the acceptable range of the ion-guide at its entrance and travelling faster than the original dimer through the ion-guide, but slower than an originally emitted monomer. These ions, depending on their kinetic energy at the entrance of the ion-guide, contribute to both, spreading of flight times of the un-fragmented monomer shown by the red dotted line at 24.8 µs in Figure 4.13 (a) and increase the current levels close to the beginning of the dimer trace.

2. Trimers or droplets breaking into dimers inside accelerating region of the emitter such that the kinetic energy is in the acceptable range of the ion-guide. These dimers travel slower than an originally emitted dimer but faster than the larger mother-charge species, leading to spreading in the flight time corresponding to an un-fragmented dimer shown as the red dotted line at 47.4 µs in Figure 4.13 (a).

3. Dimers or larger charge species breaking into a monomer inside the field-free region produces too low kinetic energy to be allowed through the ion-guide at $V_{lens} = 0.7 \times V_{em}$; however, fragmentation inside the ion-guide may produce flight times of the monomers or dimers in the range of that of the un-fragmented dimer.

The flight time of the dimers observed in Figure 4.13 (a) is therefore ambiguous resultant of many possible events.

(a) (b)
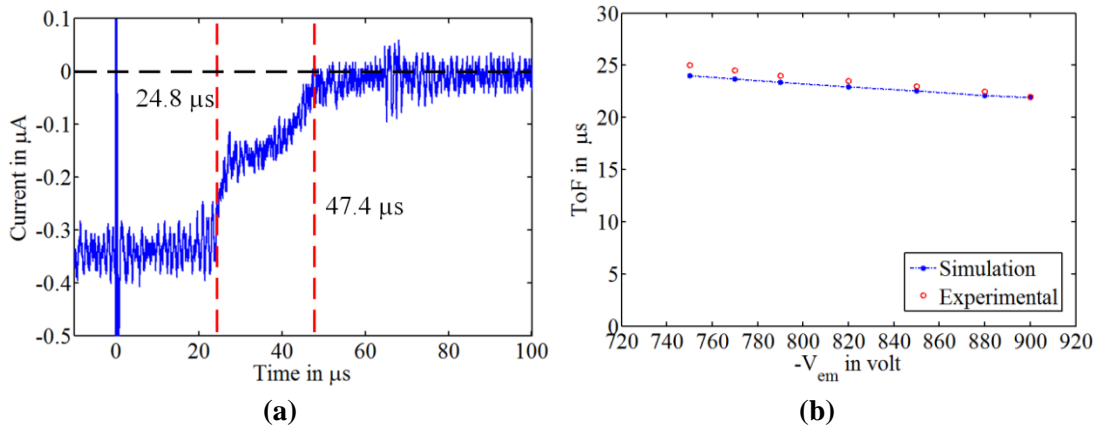
Figure 4.13: (a) ToF trace from a capillary emitter at emission voltage $V_{em} = -770$ V. The oscilloscope is triggered at time $t = 0$ using the monitor signal for the gate electrode. No averaging over traces are performed on the trace. Ion guide potential is set to $0.7 \times V_{em}$. (b) Variation of the experimental and simulated ToF with the emitter voltage V_{em}. The ion-guide potential is set to $0.7 \times V_{em}$ for all V_{em} and a ToF correction factor 1.5 is applied in the simulation results. Also a 10% deficit in the kinetic energy is assumed in the simulation results from the applied energy qV_{em}. The simulation results are within 4.5% of the experimentally obtained values.

In Figure 4.13 (b), the measured ToF of BF_4^- ions, noted from the beginning of the monomer current trace is plotted against V_{em} for $V_{lens} = 0.7 \times V_{em}$. The simulated ToF values at $\theta_{em} = 0^o$, based on ToF correction factor = 1.5 and kinetic energy= $(K.E)_1 = 0.9 \times qV_{em}$ for this case are also shown in the same figure. The results match within 4.5%. The difference may be due to uncertainty of measurement from the spreading ToF traces and energy deficit of the emitted species different from 10% assumed in the simulation. It can be noted that the flight times corresponding to the beginning of the monomer trace corresponds to originally emitted monomers only along the axis of the ion-guide. However, the large spread in the flight time corresponding to the dimer, as seen in Figure 4.13 (a) can be due to many possible fragmentation situations anywhere in the flight path and hence cannot be unambiguously explained from the measurements.

4.3.   Conclusion

In this chapter, the characterization results of the ToF-MS with the ion-guide have been discussed with the help of two different types of electrospray emitters. The ion guide allows collecting at the Faraday cup, at the end of a 65 cm long flight tube, charges from the electrospray sources that emit with large beam half-angles and with wide energy spread. The fraction of charge collection of the electrostatic ion guide with nearly mono-energetic ion beams from the tungsten emitters show that a maximum of nearly 80% of the emitted charges can be detected for ToF measurements which is otherwise possible with a large detector in a wide flight tube. From microfabricated capillary emitters, with emission half-angle nearly 40°, maximum of around 30% of the emission was collected, which is nearly 4 times larger than that reported in [55] in a 40 cm long flight tube without any electrostatic focusing. This allows characterizing the spray behaviour over a large emission divergence of the emitted charges and is, thus, potentially capable of providing spray information from a large fraction of the emission. The measured beam half-angle of around 40° from the capillary devices has been used in Chapter 5 as a constraint for designing the thrust stand. ToF measurements have been performed on pure ion beams as well as on mixed ion-droplet electrospray (ions/droplet emission) and in both cases the measured ToF matched the predicted dependence on the focusing voltage closely, showing the ion guide allows for ToF timing acquisition, while collecting many times more current than could be possible with or without an Einzel lens. This means (1) the gain requirements of the trans-impedance amplifier can be greatly relaxed, (2) a smaller Faraday cup and, hence, much smaller diameter flight tube can be used, and (3) a wider part of the beam can be collected, allowing a more complete characterization of the emitted species (not just the centre of the beam).

While the wide acceptance angle of the ion-guide allows high detectability of current, it also leads to spreading in the flight times of the charges even with the same kinetic energy, but emitted at different angles. Also fragmentation of emitted charges in different sections of the ion-trajectory leads to further spreading in the flight times due to spreading in the kinetic energies. In a field-free flight tube, fragmented species generated in the large field-free region, are not discriminated from otherwise un-fragmented mother-species and take the same flight time to reach the detector. However, the electric field inside the ion-guide affects the fragmented charges differently than the mother-species and hence their flight times differ, leading to ambiguity in the flight time measurement. If fragmentation takes place only in the accelerating region of the emitter, and the fragmented charge species gain sufficiently high kinetic energy during further acceleration to be allowed through the ion-guide, the ion-guide

behaves similar to a single-stage Einzel lens allowing the narrow energy spread. Particularly for wider kinetic energy spread around qV_{em}, such as the case of the internally wetted capillaries, the ion-guide can accommodate more of spread for detection than a single-stage lens. But this wide band can be a drawback for post-acceleration fragmentation, especially from mixed ion-droplet emission, where kinetic energies in the wider pass-band after fragmentation may result in ambiguity in flight time measurements. Since estimation of thrust from flight time measurement is sensitive to longer flight times, large error in the estimate can be anticipated if large number of post-acceleration fragmentation takes place, while field-free drift tubes are benign to this.

5   Development of a nN thrust stand

It has been pointed out in section 2.2 in Chapter 2 that measurement of thrusts down to μN with sub-100 nN resolution is a primary challenge in characterizing microthrusters. Particularly for electrospray thrusters, measurement of thrust from flight time measurement of the emitted species has been the conventional means. A direct measurement of thrust is desirable for more reliable characterization of microthrusters of any type, including thrusters that emit neutral particles as well. Direct nN thrust measurements have been possible for last few years despite some generic challenges. State-of-the-art nN thrust stands are generally challenged by the following problems which are discussed in section 2.2.3 in Chapter 2.

- Drift in thrust measurements, limiting accuracy.

- Facility vibration and resulting noise and resolution issues.

- Adaptability to different types of microthrusters.

- Large size and vacuum facility requirement.

- Electrical, mechanical and propellant feed-through going to the thruster mounted on the thrust stand.

In this chapter, development of a nN thrust stand that attempts to provide immunity over these issues has been discussed. The thrust stand works on the principle of intercepting the emitted plume from a micro-thruster with a suspended plate and measuring the force on the plate with a force sensor. The advantage of the method is its compactness, high natural frequency and complete isolation from the thruster; however, since measurement is done on the impingement force on the plate rather than thrust on the thruster like a direct thrust stand, accuracy of the correlation of the impingement force and the thrust directly affects the accuracy of the measured thrust. Measurements of thrust from a sub-sonic cold-gas ejector and from an electrospray source are discussed in Chapter 6 and Chapter 7 respectively where these correlations have been attempted to address.

In this chapter, first a trade-off and constraints study has been performed among different possible techniques and components in section 5.1 for the designing the thrust stand. The operating principle and the design of the thrust stand have been discussed in section 5.2. In section 5.3, an analytical method for designing the particle intercepting plate followed by finite element simulation has been presented and the expected performance of the plate has been analysed in section 5.4. The plate manufacturing process has been detailed in section 5.5 and characterization of the plate to compare with its simulated performance has been provided in section 5.6.

5.1.   Trade-off study of nN thrust stand

The design objective of the thrust stand is summarized in Table 5.1. In a direct thrust stand, as

discussed in section 2.2 in Chapter 2, the thruster is mounted on the thrust stand, typically on a torsional arm, to measure thrust. The electrical and propellant feed-through to the thruster are a major challenge when thrust in the order of sub-100 nN is to be resolved as any movement of the feed-throughs can contribute to significant drift in measurement of such small thrusts. Most thrust stands are designed and adapted for a particular type of thruster where the design is optimized for minimizing the effect of these external disturbances.

Table 5.1: Objectives of the thrust stand design

Property	Value
Thrust range to measure	$\geq 100\ \mu N$
Desired thrust resolution	≤ 10 nN
Thruster type to adapt to	Adaptable to various types

In the designed thrust stand in this chapter, adaptability to different types of thrusters is taken as the first trade-off. To achieve this, the thrust stand is conceived as a stand-alone instrument, mechanically and electrically isolated from the thruster itself and measuring thrust by intercepting the ejected particles. In this way, any type of thruster, with any thrust to weight ratio, can be placed in front of a particle-intercepting device of the thrust stand and by measuring the force on the device, thrust can be obtained. However, the force on the particle intercepting device would depend on the beam shape of the emission and interaction of the ejected particles with it and hence a prior knowledge of the interaction type must be known for estimating the thrust from the measured force. This issue is discussed in Chapter 6 and Chapter 7 for a cold-gas ejecting capillary and an electrospray thruster respectively. However, in this chapter, only the measurement of the force on the particle intercepting device has been considered.

The other fundamental resource-level constraints that need to be satisfied for the development of the thrust stand are listed below.
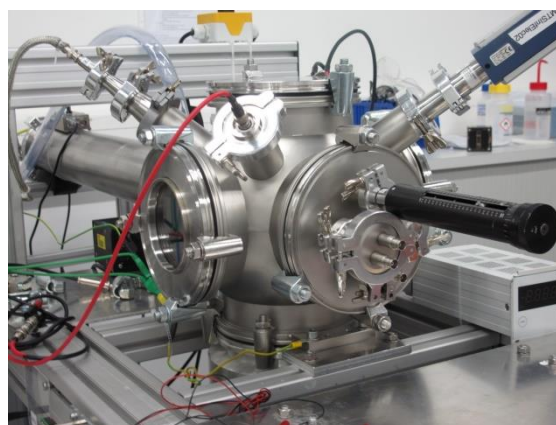
Figure 5.1: The vacuum chamber for microthruster characterization in Microsystems for Space Technologies Laboratory (LMTS), EPFL.

- The thrust stand should fit inside the vacuum chamber installed in LMTS-EPFL, at Microcity, Neuchatel, for electrospray microthruster characterization. The vacuum

chamber is a ISO160 six-way cross directly attached to a turbomolecular pump (Varian Turbo-V 551, 550l/s) [35] as shown in Figure 5.1. This calls for a compact thrust stand within limited volume, leaving space for a mounting a thruster inside the vacuum chamber from certain distance from the particle intercepting device. The thrust stand should be mounted on one of the ISO 160 flanges to fit inside the vacuum chamber and therefore a foot-print and height should be chosen appropriately small for the purpose.

- The thrust stand should be low-cost.

- The development time should be small, within 18 months.

Apart from these fundamental constraints, the following scientific constraints on the thrust measurement system can be drawn.

- The thrust stand should be able to measure up to 100 μN thrust with a resolution 10 nN. This constraint is driven by the need of measurement of thrust from microthrusters particularly desired for todays and future space missions discussed in the Chapter 1.

- The thrust-stand should be able to measure force from both, charged and uncharged emitted particles. For cold-gas or chemical thrusters, the emitted particles are essentially neutral in nature, whereas for electric microthrusters such as electrospray emitters, the emitted particles are predominantly electrically charged in nature although they may also contain neutrals.

- The thrust stand should be immune to facility vibrations. This means, the thrust stand should be able to measure thrust with the desired resolution amidst up to a few 10s of Hz vibrating platform. Building vibrations typically range from deep sub-Hz to 10s of Hz and the r.m.s. velocity vibration can be in the range of 100 μm/s [180]. The thrust stand should either be able to isolate the platform vibration from the measurement or damp the vibration to achieve the desired performance. Therefore, either a proper damping mechanism should be implemented as discussed in section 2.2 in Chapter 2 or a high natural frequency of the setup should be ensured. Additional damping mechanism adds complexity to the system; therefore a high natural frequency is chosen as a design parameter for the thrust stand for system-level simplicity.
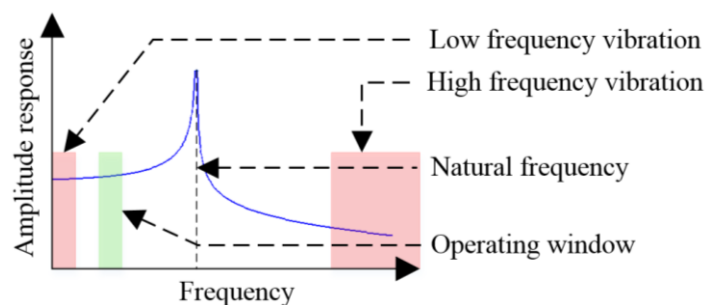
Figure 5.2: Schematic of frequency response of a general under-damped second order system applicable to the operation of the thrust stand. The natural frequency should ideally be in between the low frequency and high frequency disturbance regions. For AC measurement, the operating frequency range should be much lower than the natural frequency but high enough to avoid low frequency disturbances.

The thrust stand can be considered as a second order vibrating system with amplitude response as shown in Figure 5.2. The natural frequency should be high enough so that the low-frequency facility vibrations do not excite resonance in the structure. On the other hand, the turbomolecular pump may generate vibrations in the range of a few 100s' of Hz and the natural frequency should be either much larger than this range or optimally chosen in between the low frequency and high frequency range of external disturbances. As it is discussed in section 5.3, a high natural frequency in the range of several 100s' of Hz above even the vibration frequencies from the pump, although desirable, is difficult to achieve due to requirement of a low spring constant of the particle intercepting device. A natural frequency in the range [50 Hz, 100 Hz] is chosen for the thrust stand as a trade-off in between the low frequency and high frequency disturbance range. Also, as it is discussed in section 6.3 in Chapter 6, measurement of thrust at a reference frequency using a lock-in amplifier is the desired mode of operation for the thrust stand due to large drift of measured force in otherwise steady-state measurement. Therefore, an optimal operating frequency range should avoid the low frequency vibration range and yet much lower than the natural frequency in order not to excite resonance. This has been schematically shown in Figure 5.2.

- The particle intercepting device should be able to capture the entire spatial distribution of the emitted particles from the thruster from a safe distance. Either it should capture the entire emission cross-section at once or it should be able to raster the emission cross-section and map the force. For electrospray microthrusters, it has been seen in section 4.2.2 in Chapter 4 that the emission half-angle can be as high as 40°. In the thrust stand, a particle intercepting plate, large enough to capture the entire emitted plume, is designed. Smaller the distance between the emitter and the plate, smaller is the area of the plate required. However, in order not to affect the emission process, the plate should be placed at a safe distance.

(a)   **(b)**
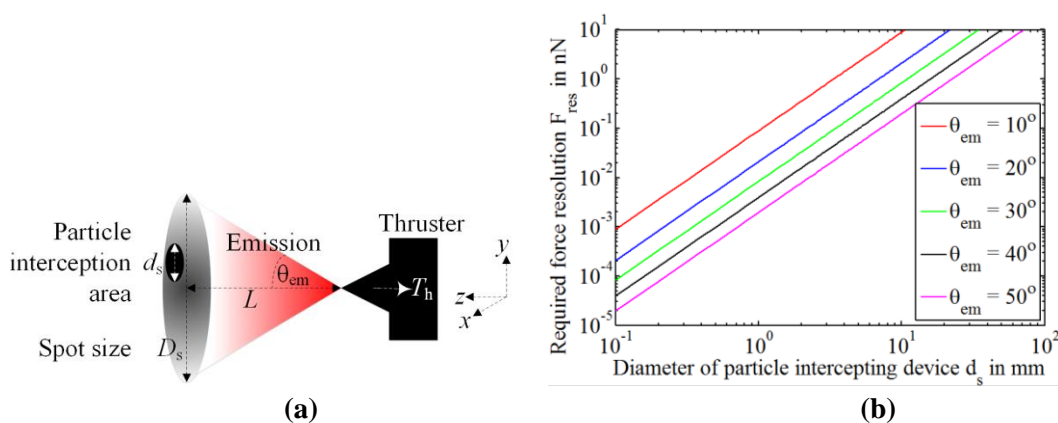
Figure 5.3: (a) Schematic of the force measurement from a distance from the thruster head. To capture the entire plume, the particle intercepting device should either cover the entire spot-size or raster the whole spot size in steps. (b) Relation between required device level force resolution and diameter of a particle intercepting device for measuring force over the entire spot size with a system level resolution 10 nN from a distance 3 cm. For larger emission half-angles, the higher resolution is required.

For beam-shape measurement from the capillary ionic liquid electrospray devices in section 4.2.2 in Chapter 4, the nineteen plate detector was placed at a distance 2.5 cm.

In [44], for beam-shape measurement, and in [171] for RPA analysis, the detector to emitter distance was set to 3 cm with tungsten externally wetted emitters. In the design of the thrust stand, the distance between the thruster and the plate is considered to be $L = 3$ cm. At 3 cm distance, with $\theta_{em} = 40^{o}$ emission half-angle, the emission cross-section covers a diameter of $D_s = 42$ mm. So the thrust stand should capture emission from a 42 mm or larger diameter at once or raster over this area to cover the entire cross-section as shown in Figure 5.3 (a). In Figure 5.3 (b), the relation between the required device level force resolution, F_{res}, of a circular-area force measurement device to its diameter, d_s, is plotted for measuring an overall 10 nN force distributed uniformly over different emission half-angles from a distance 3 cm. For a smaller intercepting area, the device level force resolution needs to be higher so that an overall 10 nN system level resolution can be achieved over the entire emission cross-section.

- Reading current from the thrust intercepting device may be optional, but a desirable feature. This would be particularly useful for emission of charged particles from electrospray thrusters and compare the thrust measured with its relation to emitted current. This necessitates the thrust intercepting device to be electrically conductive and coupled to a current monitor.

- The thrust stand should feature both static and homodyne measurement capabilities as discussed in the previous page. In homodyne detection technique, the force needs to be exerted on the intercepting device in synchronism to a reference signal and measured with a lock-in amplifier. This can be implemented by blocking and opening an aperture between the thruster and the intercepting device without affecting the thruster operation. For example, in measuring thrust from electrospray devices, an electrostatic gate, as used for flight time measurement in Chapter 4, can be used. However, such switched operation should therefore be a part of the thrust stand.

- The components of the thrust stand should be high vacuum compatible ($\sim 10^{-6}$ mBar) in order to operate inside the vacuum chamber.

Some possible force measurement schemes from the intercepted particles have been traded off as discussed below. In all these possible schemes, it is assumed that the emitted particles would be intercepted to measure thrust; the thruster would not be mounted on the thrust stand directly.

The thrust estimation by means of current measurement or retarding potential measurement or ToF measurement has their intrinsic limitations as pointed out in Chapter 2. These schemes do not work with neutral particle emission. To measure thrust from charged as well as neutral particles, the velocity of the emitted particles parallel to the emission axis can be converted into a displacement of a particle intercepting device and the displacement can be a measure of the thrust.

Displacement due to impact of the emitted particles can be measured in many ways. An accelerometer or a pressure sensor is primarily a force transducer that can measure deflection due to the force exerted by the particles on its proof-mass or the membrane respectively. If a force F is applied perpendicular to their sensitive direction of motion, it can be related to the acceleration, a_c, for the accelerometer by

$$F = m_p a_c \tag{5.1}$$

where m_p is the suspended proof-mass for the accelerometer.

High-resolution accelerometers are based on MEMS technology, typically with a suspended proof-mass size in the sub-mm to mm range and thickness in the μm to 100s' of μm range [181]. Accelerometers with sensitive direction of motion perpendicular to the surface of the proof-mass (out-of-plane) will offer higher area to the particles than those moving laterally (in-plane). In Table 5.2, some of the out-of-plane accelerometers and their calculated force resolution based on mass and acceleration resolution are given.

Table 5.2: Out-of-plane accelerometers and their calculated force resolutions

Accelerometer type	Proof-mass (mg)	Proof-mass size (mm×mm)	Acc. resolution (μm/s^2)	Calculated force resolution (nN)
Capacitive [182]	0.001	0.5 × 0.5	25000	25
Capacitive [183]	14.7	4 × 4	10	0.15
Capacitive [184]	0.0005	0.4 × 0.4	113000	0.06
Interferrometric [185]	30	5.6 × 5.6	1	0.03
Tunnelling [186]	180	10 × 10	0.1	0.018

It can be seen from Table 5.2 that the accelerometers can resolve forces in the pN–nN ranges. However, this has to be traded off against the surface area of the proof-mass as shown in Figure 5.3 (b). Surface micro-machined accelerometers are typically in the proof-mass range of μg to mg and surface area in the order of 100 μm × 100 μm, providing 10–100 μm/s^2 acceleration resolution [181] with a force resolution down to pN. However, the extremely small surface area necessitates a very long experimental time or a large number of identical accelerometers to cover the entire spot size. The tunnelling accelerometer in Ref. [186], can potentially capture particles in an area 1 cm^2 with a required force resolution of the order of 0.4 nN to measure an overall 10 nN force over a 42 mm diameter spot-size. However, the capturing of charged particles from the thruster may damage or degrade the performance of the accelerometers while measuring thrust. Also, most of the commercial accelerometers are hermetically packaged without access to the proof-mass. Therefore, development time and cost of an accelerometer with the desired area and force resolution trade-off and finally the charge handling capability and 2-axis rastering scheme to cover the entire emission cross-section will be large. Pressure sensors, on the other hand, provide direct access to the membrane to capture particles. However, similar to the accelerometers, they may also not be immune to the impinging charges with possibility of damaging the sensor.

An alternative to the use of accelerometer or pressure sensor can be using a spring-loaded plate and measuring its displacement under the exerted force by a displacement sensor as shown in Figure 5.4 (a). From the knowledge of the spring constant of the suspended plate and measuring the displacement, the force can be obtained. In principle, this is not different from the accelerometer or the pressure sensors, but this gives the flexibility of designing a plate and displacement sensing mechanism suitable for the present purpose. The plate can be made electrically conductive and shunted to ground to avoid charging. Also, this scheme

allows the possibility of capturing the full plume and measure thrust at once instead of the raster-based scheme mentioned above. To cover the 100 μN thrust range with 10 nN resolution, a dynamic range of 10000:1 would be required for a linear displacement sensor.

Displacement of a plate can be measured using electromagnetic, optical interferrometric technique or capacitive technique as discussed in section 2.2 in Chapter 2. A list of displacement transducers with their minimum measurable displacement and dynamic range is provided in Table 5.3.

Table 5.3: Some displacement sensors and their resolution

Displacement transducer type	Manufacturer	Model	Range (mm)	Minimum displace-ment (nm)	Dynamic range
LVDT	Macro Sensors [187]	BBP 315-040	1	150	6667:1
DVRT	Microstrain [188]	NANO-DVRT-0.5	0.5	125	2000:1
Fibre Optic displacement sensor	Philtec [189]	DMS-RC25	0.76	50	15200:1
		D20	0.02	7	2847:1
		D12	0.05	5	10000:1
Capacitive	MTI [190]	Accumeasure 500	12.5	200	62500:1
	Lion Precision [191]	CPL490	0.01	0.05	200000:1
Atomic Force Microscopy (AFM)	IBM/Stanford [192]	--	--	0.1	--
Atomic Force Microscopy (AFM)	Digital Instruments [193]	Dimensions 3100	0.006	0.1	65536:1

(a)   (b)
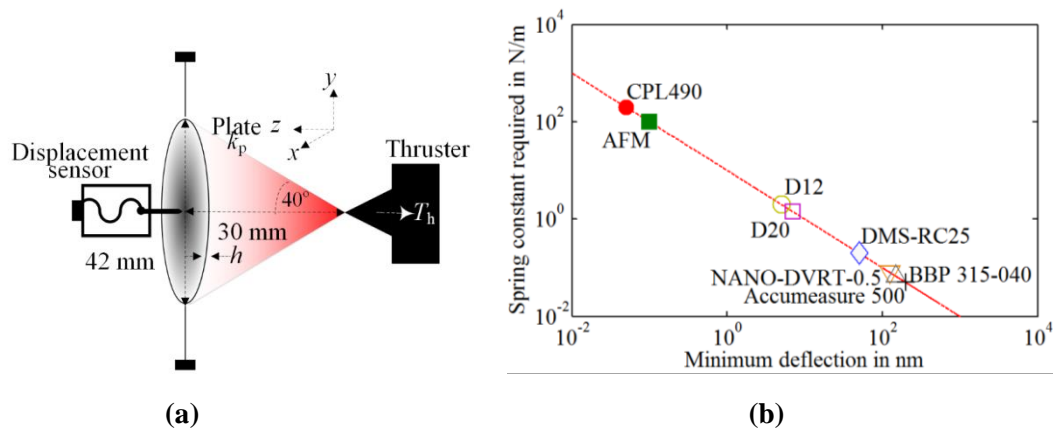
Figure 5.4: (a) Schematic of thrust measurement scheme with a particle intercepting plate and a displacement sensor. It is assumed that the plate with diameter 42 mm is placed at 3 cm distance from the plate to cover all charges within 40° emission half-angle (b) Plot of required spring constant of the plate against the minimum deflection that can be measured with a displacement transducer to achieve a resolution 10 nN. The corresponding requirements for the displacement sensors listed in Table 5.2 are also marked on the same plot.

Most of the displacement transducers can cover the full dynamic range required for the thrust stand. However, depending on the resolution, the displacement sensor requires a minimum spring constant of the suspended plate in order to measure down to 10 nN force on the plate. If it is assumed that the plate captures the entire plume, a 10 nN force on the plate should produce displacement above the minimum displacement d_{min} that can be measured by the displacement sensor. In Figure 5.4 (b) the required minimum spring constant of the plate to produce minimum displacement d_{min} under a 10 nN force is shown. The corresponding values for the displacement sensors in Table 5.3 are also marked on the same plots.

The displacement sensors with larger minimum displacement require below 1 N/m spring constant of the plate. Displacement sensors have been used earlier in direct thrust measurement applications as discussed in detail in Chapter 2. However, the low spring constant requirements in these applications led to very low natural frequencies, typically below 1 Hz. In order to achieve a natural frequency above 50 Hz, displacement sensor with much smaller minimum detectable displacement is required so that the plate can have much higher spring constant. Capacitive transducers manufactured by Lion Precision [191] or AFM probes [192], on the other hand, require much higher spring constants due to sub-nm displacement resolution. Laser interferrometric displacement sensing mechanisms also can measure sub-nm displacements [194].

While sub-nm displacement sensors are potential candidates for the nN thrust stand, another alternative for the present application can be using a force sensor. In this case, the plate can be mounted on the force sensor or can be suspended like the previously discussed scheme. If the plate is mounted on the force sensor, the entire force on the plate is measured by the force sensor. If, on the other hand, the plate is suspended with a spring, part of the force is balanced by the reaction force of the plate and the rest is measured by the force sensor. Therefore, in Table 5.4, some of the force sensors, and their resolution and range are listed. Atomic force microscopic probes can once again resolve pN forces and are used in many applications including bio-mechanical [195], [196], Casimir force [197] measurement. However, typically the force range of AFM probes is limited within a few μN and thus cannot cover the entire thrust range. Therefore, the plate has to be small to capture a fraction of the thrust and raster across the whole spot-size of the emitted particles. Also, the AFM tips are very sharp, typically within 10 nm radius [198]. Therefore, surface-roughness of the plate can be a very strong source of artefact, especially when the suspended plate vibrates or moves under the applied force and the movement is monitored from a few nm distances.

Looking at the other force sensors in Table 5.4, FT-S100 force sensor can be seen to meet the desired thrust range and resolution. The probe tip is 50 μm × 50 μm in size [199], much larger than a standard AFM tip. In principle, a very simple thrust measurement scheme can therefore be thought of with this sensor. Direct force reading can be extracted from the sensor output [199] unlike an optical interferometric arrangement with large part counts and very precise alignment requirements of the parts. The sensor probe can be left electrically floating [199] and current can be readout from the plate by shunting it to ground through a resistor and thus there is minimal risk of charging up the sensor and affecting its performance or safety. The force-range is appropriate for intercepting the entire plume at once with a plate, thus eliminating need of rastering the plate and the sensor across the plume cross-section. Therefore, with proper design of the plate ensuring high natural frequency, a thrust stand can be designed which meets the desired resolution, range and overall performance criteria. The

sensor can be used in air and is also suitable for in-vacuum thrust measurement [199]. A diagram of the FT-S100 force sensor is given in Figure 5.5

Table 5.4: List of μN–mN range force sensors

Force sensor	Manufacturer	Range (μN)	Resolution (nN)
F329UF00A0 [200]	NovaTech	100000	25×10^3
FT-S100000 [199]	Femtotools	100000	5×10^3
FT-S10000 [199]	Femtotools	10000	500
FS-2000 [201]	Xidex	2000	400
FT-S1000 [199]	Femtotools	1000	50
FS-180 [201]	Xidex	180	50
FT-S100 [199]	Femtotools	100	5
Cell-mechanics force sensor [195]	UIUC	--	0.5
Bio-MEMS force sensor [196]	UIUC	1	0.05
Intermolecular force sensor [198]	Agilent/Stanford	--	0.2

(a)   (b)
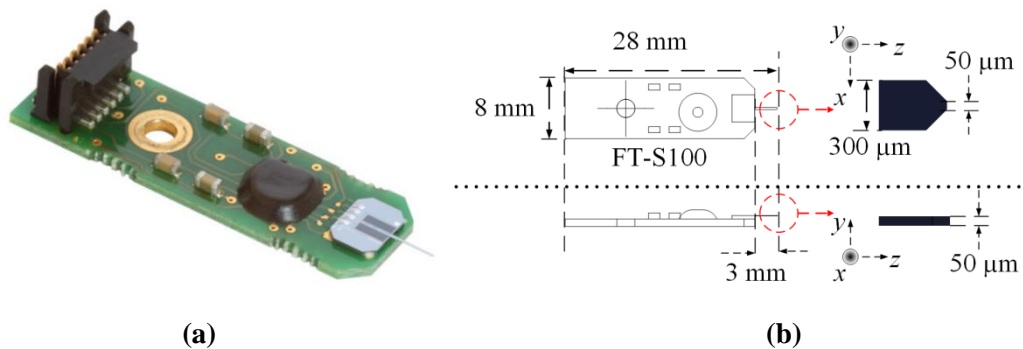
Figure 5.5: (a) Picture of a FT-S100 probe [199]. (b) Dimensions of FT-S100 sensor [199]. The sensor tip is 3 mm long and tapered at the tip to 50 μm width.

Based on the above discussion, it can be summarized that many different techniques of transducing the force on the plate due to the impinging particles from the thruster can be utilized to make the thrust stand within the desired range and resolution specifications. The plate can either capture the entire plume at once or can be smaller in size to raster across the spot-size of the particle plume in the detection plane. However, capturing at once makes an easy and fast choice, which can detect instantaneous overall thrust and does not need 2-axis long-range translational motion of the plate and the sensor inside the vacuum chamber. The FT-S100 force sensor deems an ideal choice for full-plume thrust measurement with the desired resolution and force range for simplicity of operation and compatibility to vacuum applications. With this force sensor, the design of the thrust stand, therefore, completely boils down to the design of the plate and the rest of the thrust stand. A summary of the constraints, therefore, can be listed in the Table 5.5 for ready reference.

Table 5.5: Summary of the trade-off study and choices

Property	Value	Comment
Distance between plate and thruster	3 cm	For safe operation
Emission half-angle to capture	$\leq 40^o$	Colloid thruster
Size of plate	$\geq$ (42 mm × 42 mm)	Minimum size to capture 40°
Plate natural frequency	$\geq$ 50 Hz	For immunity over facility vibrations
Entire plume or fraction?	Entire plume	For simple, fast operation
Charged particle or neutral	Both	Plate should not charge up
Thrust range	$\geq$ 100 μN	--
Thrust resolution	$\leq$ 10 nN	--
Force detection using	FT-S100 [199]	Force probe, capable of 5 nN resolution and 100 μN range
Conceptual design of the thrust stand		
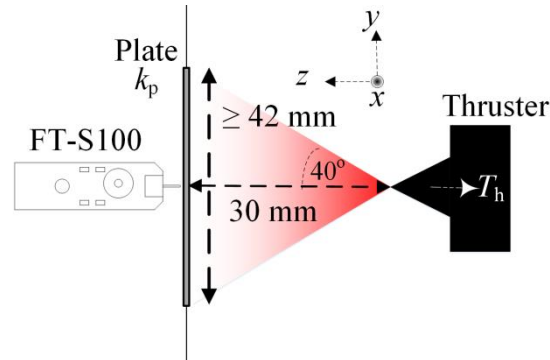
Figure 5.6: Schematic of the thrust stand with the FT-S100 sensor and a plate

5.2.   Design of the nN thrust stand

As discussed in the previous section and summarized in the Table 5.4, FT-S100 force probe is chosen as the primary force transducing element in the thrust stand. In this section, the operating principle of the thrust stand, the design methodology, and the sub-systems of the thrust stand are discussed.

5.2.1. Operating principle

The FT-S100 force sensor is a MEMS capacitive transducer with a very soft micro-machined sensor and probe, details of which are discussed in section 5.2.2.1. However, it is not possible to attach a plate on the sensor probe without risking the safety of the sensor. Therefore, the plate has to be suspended with a spring. Hence, part of the force exerted on the plate by the impinging particles is balanced by the plate and the rest is measured. In Figure 5.7, the schematic of the operating principle is shown.

If the force sensor is moved with a translation stage until the probe pushes on the plate, the reaction force from the springs attached to the plate will be exerted on the force sensor once contact is achieved. If an additional force is applied on the plate by the emitted particles from the thruster, part of the force is balanced by the spring attached to the plate and the rest will be exerted on the force sensor, leading to an increase in the measured force. The increase in the force measured by the force sensor is a measure of the applied force due to the thruster.

Let us say, the force sensor is moved forward to push the plate at its centre by an amount z_p from its initial position. If k_p is the spring constant of the plate due to the springs, the reaction force on the force sensor probe is

$$F_{OFF} = k_p z_p \tag{5.2}$$

(a)   **(b)**   **(c)**
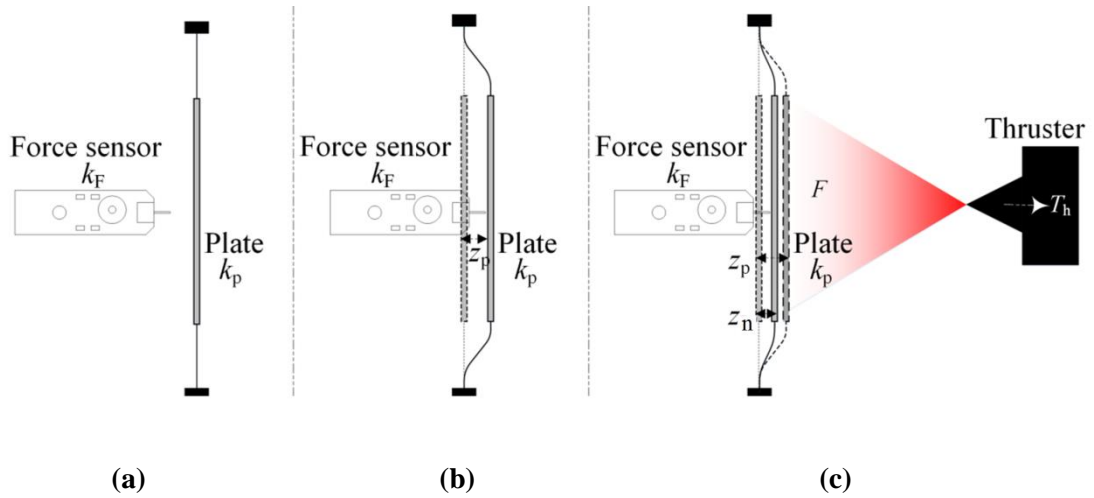
Figure 5.7: The schematic of the thrust measurement scheme. (a) The force sensor just in contact with the suspended plate. No force on the sensor. (b) The force sensor is moved forward to push the plate so that the plate moves from its initial position by z_p. The reaction force of the suspended plate due to deflection z_p causes deflection z_f of the force sensor (not shown in the figure). (c) The applied external force on the plate causes an additional force on the force sensor as the plate moves towards left in the figure by $(z_p–z_n)$.

This force is exerted on the force sensor and pushes the spring of the force sensor to deflect by an amount z_f. If the spring constant of the force sensor is k_f, then

$$F_{OFF} = k_p z_p = k_f z_f \tag{5.3}$$

Now, if an additional force F is applied at the centre of the plate to push it towards left in the Figure 5.7, the new position of the centre of the plate with respect to its initial position (z_n) and the new deflection of the force sensor spring (z_F) can be related to

$$F + k_p z_n = k_f z_F = F_{meas} \tag{5.4}$$

where F_{meas} is the new measured force by the force sensor. Since,

$$z_p - z_n = z_F - z_f \tag{5.5}$$

replacing z_n from Eqn. (5.5) in Eqn. (5.4)

$$F_{meas} - F = k_p\left(z_p - z_F + z_f\right) = k_p\left(\frac{F_{OFF}}{k_p} - \frac{F_{meas}}{k_f} + \frac{F_{OFF}}{k_f}\right)$$ (5.6)

Rearranging the terms, it can be shown that

$$F = \left(1 + \frac{k_p}{k_f}\right)\left(F_{meas} - F_{OFF}\right)$$ (5.7)

Thus, if the spring constant of the force sensor and that of the suspended plate are known, the force exerted on the plate can be found out from the force sensor readout and the offset force when no external force was applied. If the force sensor has a resolution of F_Δ, i.e. if it can differentiate a force difference F_Δ, the theoretical resolution of the thrust stand can be derived to be

$$F_{res} = \left(1 + \frac{k_p}{k_f}\right)F_\Delta$$ (5.8)

The range of force measurement can be written as

$$F_{max} = \left(1 + \frac{k_p}{k_f}\right)\left(F_{s,max} - F_{OFF}\right)$$ (5.9)

where $F_{s,max}$ is the maximum force that can be measured by the sensor. Therefore, depending on the offset force F_{OFF} and the ratio of spring constant of the plate to that of the force sensor, the range can be adjusted up to $(1 + k_p/k_f) \times F_{s,max}$. In order to achieve 10 nN resolution, the resolution of the force sensor has to be better than 10 nN and k_p/k_f has to be low. On the other hand, as discussed in section 5.1, and summarized in Table 5.5, a natural frequency in the range [50 Hz, 100 Hz] is desired. These two requirements contradict with each other and an optimal design of the plate is required to meet both these requirements which is discussed in detail in section 5.3. Also, the plate has to be sufficiently large, at least 42 mm × 42 mm, to be able to capture the entire emitted beam from the thruster over a maximum 40° half-angle from a distance chosen to be 3 cm. Additionally, the spring constant of the plate has to be fairly constant over the variation of the spot size and position of the captured beam on the plate. These issues would lead to a critical plate design aspect which are discussed later in this chapter. A summary of the requirements of the plate is listed in Table 5.7 later.

In the following section, the components of the thrust stand are discussed.

5.2.2. Components of the thrust stand

The thrust stand consists of the following main components as shown in Figure 5.8.

1. The force sensor FT-S100.

2. Translation stage.

3. The particle intercepting plate.

4. Mechanical supporting components.

5. Electrical components.
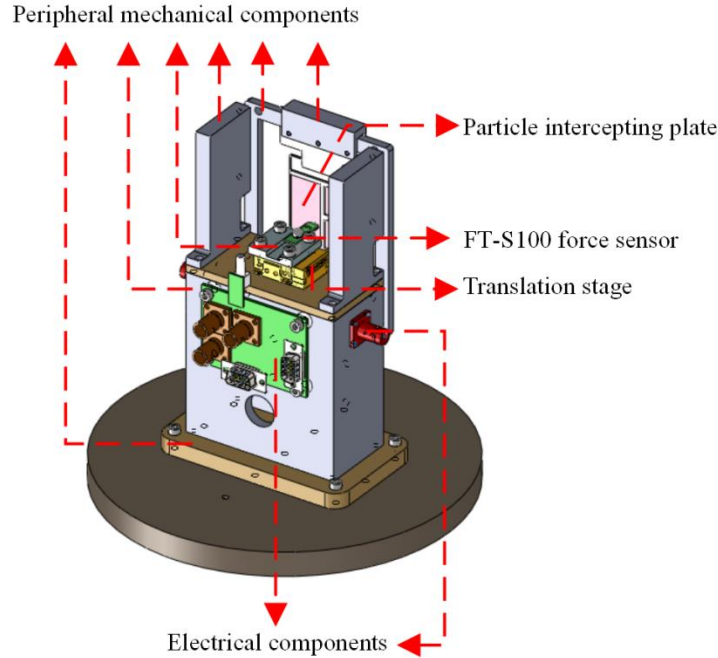
Figure 5.8: A schematic of the thrust stand comprising of the force sensor, the translation stage, the particle intercepting plate and associated mechanical and electrical components. These components will be discussed in section 5.2.2.

5.2.2.1. The force sensor

In the Table 5.6, the properties of the force sensor FT-S100 are listed. The sensor can measure both tensile and compressive forces along the axis of the probe, details of which can be found in Ref. [202]. When a compressive force is applied, the output voltage decreases from V_{NL} with the sensitivity S_F. For a 100 μN compressive force on the probe, the output voltage reduces by approximately 2 V from V_{NL} with 100 μV for every 5 nN force, slightly different from device to device based on the individually calibrated sensitivity values. The dimensions of the probe have already been discussed in section 5.1. The 28 mm long device has 6-pin connectors, four of which are used for the power supply, ground, output signal and probe potential. The natural frequency of the probe is 1.1 kHz. A 2.4 mm diameter mounting hole on the device can be used for mounting the sensor using M2 screws.

5.2.2.2. The thrust intercepting plate

The thrust intercepting plate has to meet the following criteria based on previous discussions.

- It should capture the entire plume from the microthruster from not below 3 cm distance from the thruster. The plate is to be designed to capture up to 40° emission half-angle. Therefore, for a square-shape, the sides of the plume capturing plate

should be above 42 mm. The plate dimensions are hence taken to be 45 mm × 45 mm keeping a 3 mm tolerance on all sides.

Table 5.6: Properties of the FT-S100 force sensor

Property	Value	Image
Model	FT-S100	
Manufacturer	FemtoTools [199]	
Force range	± 100 µN	
Force resolution F_Δ	5 nN	
Spring constant	50 N/m[#]	
Natural frequency	1.1 kHz[#]	
Mass of the sensor	1 mg[#]	**(a)** **(b)**
Sensitivity, S_F	50 µN/V[*]	**Figure 5.9: (a) Picture of the FT-S100 probe. (b) 3-D model of the capacitive sensor [202]**
No-load voltage, V_{NL}	2.25 V	
Power supply	5 V	

[*] Individual calibration of sensitivity is provided with the sensors.
[#] Obtained from discussion with Application Engineer in FemtoTools.

- The plate should be electrically conductive and current on the plate should be monitored so that capturing charged particles do not charge up the plate.

- In order to ensure a vibration-immune design, the plate should have a high natural frequency. A 50 Hz or above natural frequency is desired.

- In order to achieve the thrust resolution of $F_{res} = 10$ nN or better, the spring constant of the plate should be low. For FT-S100 force sensor to be used, $k_f = 50$ N/m. Therefore, from Eqn. (5.8), the required spring constant of the plate suspension structure can be obtained to be

$$k_p \leq \left(\frac{F_{res}}{F_\Delta} - 1 \right) k_f = 50 \quad \text{N/m} \tag{5.10}$$

- To ensure reasonable constancy of the stiffness of the plate irrespective of the spot-size and particle density distribution across the plume cross-section, the capturing plate area should be at least 100 times stiffer than the suspension springs, so that bending occurs in the spring, not in the plate region.

- To minimize damages in the soft and fragile plate, the plate should be always clamped on a support frame such that, the plate can be manufactured and then mounted on the thrust stand always along with the support frame.

The plate is the most critical sub-system of the thrust stand and the design specifications are stringent. Comprehensive detail of the analytical and simulation-based design approach for the plate is therefore is provided in the section 5.3.1 separately. The support frame will be discussed in the context of plate manufacturing process in section 5.3.2. The design specifications based on the above-discussion can, however, be summarized in the Table 5.7.

Table 5.7: Desired properties of the particle intercepting plate

	Property name	Property value
Electrical	Conductivity	High (metallic)
Mechanical	Plate shape	Square
	Plate dimensions ($L_\text{p} \times L_\text{p}$)	45 mm $\times$ 45 mm
	Plate natural frequency f_p (Hz)	≥ 50
	Plate suspension spring constant k_p (N/m)	≤ 50
	Plate to spring stiffness ratio	≥ 100

5.2.2.3. Translation stage

In order to move forward the force sensor to push on the plate and backward to release and bring to safe distance for diagnostics purposes, a translation stage is required. The following criteria should be met by the translation stage.

- The translation stage should be motorized and remote operated. This feature is required to ensure movement of the force sensor without affecting the vacuum when operating in the vacuum chamber. The translation stage can be operated manually before turning on the pump to bring the force sensor in contact with the plate, however, during pumping down the pressure level in the vacuum chamber, the parts can move while the flange is rigidly tightened on the sealant O-ring due to pressure different across it. This might damage the force sensor if it already in contact with the plate. Hence, the force sensor should be approached forward to achieve contact only after the vacuum chamber is closed and pumped down.

- The translation stage should be vacuum compatible. The parts of the stage and the cable to the stage should be specially designed for high vacuum ($\sim 10^{-6}$ mBar) applications and the grease used as lubricant should have very low vapor pressure.

- The range of motion of the translation stage should be no less than 5 mm so that it can be retracted back to a safe distance from the plate during debugging.

- The minimum incremental motion of the stage should be 200 nm or less. This necessity is driven by the safety requirement of the FT-S100 force sensor which can deflect only by 2 μm for a maximum $F_\text{max} = 100$ μN force. If the force sensor is moved towards a rigid plate with infinitely large spring constant, the translation stage can be only moved by 2 μm after immediate contact and before the force sensor output saturates. There should be at least 10 steps in between to ensure safety of the force sensor and choose an offset force. Therefore, from Eqn. (5.3), the minimum incremental motion of the stage should be

$$\delta \leq \frac{F_\text{max}}{10k_\text{f}} = 200 \quad \text{nm} \tag{5.11}$$

- The foot-print of the translation stage must be within 100 mm $\times$ 100 mm in order to fit inside the vacuum chamber.

A list of some of the vacuum compatible motorized translation stages, meeting the desired travel range and minimum incremental step specifications, is given in Table 5.8.

Table 5.8: List of some vacuum compatible translation stages

Translation stage	Manufacturer	Foot-print (mm × mm)	Range (mm)	Min. incremental motion (nm)
8MT173V-10DCE [203]	Standa	128 × 30	10	100
NLS4-2-16V [204]	Newmark	250 × 99	50	30
AG-LS25-27V6 [205]	Newport	35 × 50	27	100
AG-LS25V6 [205]	Newport	35 × 26	12	50
ECS3040 [206]	Attocube	30 × 40	25	1
ECS3030 [206]	Attocube	30 × 30	20	1

The stages that can match the foot-print requirement are the Newport Agilis series and Attocube ECS series translation stages. These translation stages travel by Piezo drives [205], [206]. However, the Newport stages are cheaper than the Attocube ones and for the thrust stand, Newport AG-LS25V6 translation stage has been selected. This translation stage is made of stainless steel, occupies a volume of 35 mm × 26 mm × 13 mm and can support up to 3 N normal load [207]. The travel range and the minimum incremental step are 12 mm and 50 nm respectively. However, individual steps are not 100% repeatable and external feedback is necessary to sense the absolute motion [207]. It is notable from Eqn. (5.9) that the force measurement does not need prior information about the position of the force sensor and hence in application of the translation stage in the thrust stand, no external feedback is required. This model comes with AG-UC2 controller which can be remote controlled using serial port commands through USB port. The cables between the controller and the stage is also vacuum compatible, however, the mini-DIN connector is not; therefore, for application inside the vacuum chamber, the mini-DIN connector needs to be replaced with a high vacuum compatible connector. A summary of the specifications of the chosen translation stage can be listed in Table 5.9.

The FT-S100 force sensor can be mounted on the translation stage with a base plate as shown in Figure 5.10 (a). The base plate is manufactured in Mechanical Workshop in Microcity, Neuchatel, from 5 mm thick aluminium plate. The base plate is clamped to the top of the translation stage with M3 stainless steel screws and the force sensor is mounted on the translation stage with the base plate using a M2 stainless steel screw as shown in Figure 5.10 (b).

5.2.2.4. The stand

The stand is the structure as shown in Figure 5.11 where all the parts of the thrust stand are mounted. The stand is 105 mm tall and is made from 101.6 mm × 50.8 mm rectangular tube of wall thickness 6.25 mm. The stand is mounted on the ISO-160 flange using a 10 mm thick base plate and vented socket head cap-screws. A 20 mm diameter hole is made on the wall to allow air to vent out when the stand is placed inside vacuum. On the other side, threaded holes are created to mount the particle intercepting plate along with its support frame. The

AG-LS25V6 translation stage with the FT-S100 probe is mounted on the stand using a 5 mm plate.

Table 5.9: List of properties of the AG-LS25V6 motorized translation stage [207]
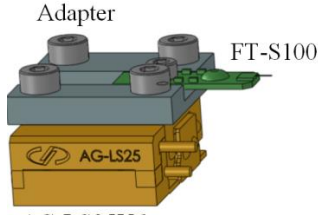
Property	Value	Image
Model number	AG-LS25V6	
Manufacturer	Newport	
Vacuum rating (mBar)	10^{-6}	
Foot-print (mm × mm)	35×26	
Material	Stainless steel	
Height (mm)	13	**(a)**
Mass (g)	70	
Travel mechanism	Piezo-motor	
Travel range (mm)	12	
Min. incremental step (nm)	50	
Absolute position accuracy (μm)	100	
Max. normal load capacity (N)	3	**(b)**
Axial load capacity (N)	2	**Figure 5.10: (a) Image of the AG-LS25V6 translation stage [207]. (b) Mounting the FT-S100 probe on the stage.**
Motor controller	AG-UC2 Piezo controller	
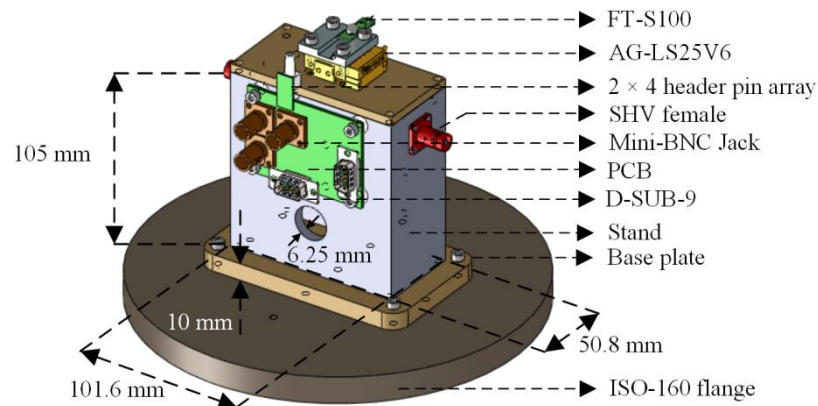
Figure 5.11: The thrust stand with the force sensor and the PCB on the aluminium stand. The particle intercepting plate is not shown in this figure. See Figure 5.39 for reference.

5.2.2.5. The electrical connections and PCB

The electrical connections required for the thrust stand can be summarized in the Table 5.10. As discussed before, the thrust stand should be fitted inside the vacuum chamber and it should be a complete stand-alone instrument. Therefore, all connections to and from the thrust stand

should be connectable and detachable in a way so that adaptability to different vacuum chambers can be maximized. In order to achieve this, a PCB is made as an interface between the external connections to the thrust stand as shown in Figure 5.11. The power supply and ground for the FT-S100 sensor and the four wires for the translation stage are connected to the PCB using ultra high vacuum (UHV) DSUB-9 connector from Lewvac [208] and then divided to one 2×4 header pin array for the FT-S100 sensor and another UHV DSUB-9 connector for the translation stage. The force sensor output is extracted from the PCB using a mini-BNC jack connector soldered on the PCB. Two other mini-BNC jack are soldered for monitoring the current at the particle intercepting plate such that a coaxial cable from the plate is connected to one of them and the cable to the current monitor instrument comes out from the other one.

Table 5.10: Electrical connections for the thrust stand

Connection from	Connection to	Property
5 V power supply	FT-S100 power pin	Power supply to force sensor
FT-S100 signal pin	Multimeter/Lock-in amplifier	Measurement of thrust
AG-UC2	Translation stage	4 pins to the translation stage
Thrust intercepting plate	Current monitor	Measurement of current intercepted by the plate
High voltage switched power supply	Electrostatic gate	For electrostatic switching of the force on the plate in synchronism with a reference signal
Ground	Ground electrodes, Translation stage, FT-S100 ground pin	All grounds should be a common reference for voltage

Apart from the PCB, two more SHV female connectors are mounted on the stand as shown in Figure 5.11. It has been mentioned before that the thrust stand should be capable of synchronous detection so that the force on the particle intercepting plate can be pulsated at a reference frequency without affecting the emission from the thruster. For different types of thruster, this can be different. For electrospray thruster, this can be done by applying high voltage pulsating signal to an electrostatic gate placed between the thruster and the plate. The gate assembly is discussed in Chapter 7 while using the thrust stand with electrospray microthrusters. The purpose of the SHV connections is to provide the pulsating signal to the gate for electrospray thruster. The two connectors are connected through inside the stand. One of the connectors is connected to the gate electrode and the other is connected to the signal input through coax cables.

All the connections are designed in such a way that by disconnecting the coaxial cables between the stand and the feed-through of the vacuum chamber, the thrust stand can be completely isolated without affecting the internal connections to the force sensor, the translation stage and the gate. The thrust stand can be plugged in for operation or taken out of the vacuum chamber for debugging with minimum connections to make inside the thrust stand.

The coaxial cables, and the connectors and the wires for the DSUB-9 are chosen with high vacuum compatibility. The insulation material in the wires and the connectors are PTFE based and the coaxial cable is ultra-high vacuum rated kapton insulated from Lewvac [208]. The body of the connectors are nickel-finished and the pins are gold-coated. The PCB is attached to the stand using ceramic stand-offs. However, the PCB is made from FR4 and has gold-finished ground plane to cover most of it. The 2×4 array header pins and the cable from the PCB to the force sensor provided by the manufacturer are not high vacuum rated.

5.3. Design of the thrust intercepting plate

As it has been pointed out before, the thrust intercepting plate is the most crucial sub-system of the thrust stand and needs to be custom-manufactured to meet a set of specifications mentioned in Table 5.7.

5.3.1. Design of the plate

In this section, the details of the design, manufacturing and characterization of the thrust intercepting plate will be discussed and finally the expected performance of the thrust stand based on the experimentally obtained properties of the plate will be discussed in section 5.6.

5.3.1.1. Material selection

As pointed out in Table 5.7, the plate needs to have high electrical conductivity, σ. Therefore, metal sheets are the best choice for making the plate. Also, the plate region needs to be much stiffer than the spring section. If the plate is divided into two sub-sections, the spring with spring constant k_{sp} and the particle intercepting plate section with spring constant k_{pl}, the overall spring constant of the entire plate can be written as

$$k_{p} = \frac{k_{pl}k_{sp}}{(k_{pl} + k_{sp})} \qquad (5.12)$$

Here, spring constant of the plate section is defined in terms of force applied and its deflection at its centre and spring constant of the spring section is defined in terms of the force applied and its deflection at the plate section end. Therefore, the design should ensure that

$$k_{pl} \geq 100\,k_{sp} \qquad (5.13)$$

so that,

$$k_{p} \approx k_{sp} \qquad (5.14)$$

For a given shape and size and of a mechanical structure, the spring constant is directly proportional to its Young's modulus, E, and the natural frequency is directly proportional to the square root of specific stiffness, i.e. square root of the ratio of Young's modulus E and density ρ. Therefore, in order to achieve low spring constant ($k_{p} \leq 50$ N/m) and high natural frequency ($f_{p} \geq 50$ Hz) for the entire particle intercepting plate, the Young's modulus E of the spring section has to be low but specific stiffness E/ρ has to be high. At the same time, the plate region needs to be 100 times stiffer than the spring section, requiring high E. The density of the plate section ρ has to be low, so that mass of the plate section is low, providing

high natural frequency. Therefore, the spring and the plate section can be made of two different metals; the spring with low E, high E/ρ and plate section with high E and low mass. Stiffness of the plate region can also be increased with relatively lower increase in mass by using higher thickness. However, it is convenient to cut the spring and the plate section from a single metal sheet so that they do not need to be attached separately with risks of damaging the sub-sections and misalignment. Therefore, for the entire plate, a single metal sheet, with constant thickness should be chosen and the plate section can be hardened by tweaking the design. Hence, metal with moderate to low E and high E/ρ can be a potentially good solution.

In Table 5.11, a list of metals usable in vacuum conditions with their E, E/ρ and σ is given from Ref. [209] unless otherwise mentioned. Aluminium stands out as the ideal choice for high E/ρ and low E application. For example, a plate made of stainless steel will have almost the same natural frequency, but almost three times higher spring constant than an identical plate made of aluminium. Also, aluminium plate is easy to machine and aluminium plates of wide range of thicknesses are available [210], [211]. Therefore, aluminium is chosen as the metal for manufacturing the plate.

Table 5.11: List of metals and their properties [209]

Material	Young's modulus E (GPa)	Specific stiffness E/ρ (GPa.m^3/kg)	Electrical conductivity σ (MS/m)
Aluminium	70	0.028	35.5
Copper	110	0.012	69.6
Stainless steel[*]	193–200	0.024–0.025	13.9
Titanium	116	0.026	23.8
Molybdenum	329	0.032	18.7
Tungsten	400	0.021	17.9
Beryllium	287	0.016	27.8
Nickel	200	0.002	14.3
Platinum	168	0.008	9.4
Gold	79	0.004	41.0
Zirconium	88	0.013	2.3

[*] AISI Type 304 Stainless Steel. Taken from Ref. [212]

5.3.1.2. Analytical plate design approach

First an analytical approach has been considered for designing the plate based on the constraints and then finite element method (FEM) in COMSOL is used to simulate and compare the results for the final design. The analytical method is based on a spring-mass model of the suspended plate and hence many assumptions are made in the approach which are discussed in course of the design methodology.

Preliminary design considerations

If it is assumed that the plate is much stiffer and heavier than the spring, for translation motion of the plate, the natural frequency f_p and spring constant k_p of the system can be related as

$$f_p^2 = \frac{1}{2\pi} \frac{k_p}{M_{pl}}$$

(5.15)

where M_{pl} is the mass of the plate. If the entire plate is made of the same metal with size $L_p \times L_p$ and thickness h, the mass of the square plate is given by

$$M_{pl} = \rho L_p^2 h$$

(5.16)

In order to keep $f_p \geq 50$ Hz and $k_p \leq 50$ N/m as mentioned in Table 5.5, the ratio $k_p/f_p^2 \leq 20$ g is required. Therefore, with $L_p = 45$ mm as discussed in Table 5.7, a limit on the thickness h can be derived from Eqn. (5.15) and (5.16) as

$$h \leq h_{max} = \frac{1}{4\pi\rho L_p^2} \frac{k_p}{f_p^2} = 92 \ \mu m$$

(5.17)

for the chosen material aluminium, with $\rho = 2700$ kg/m^3. At this point, two different geometries for the suspension system can be considered as described in Table 5.12. For both these configurations, the plate can be considered, with a certain degree of assumption, as another spring clamped on both side. The moment of inertia and the spring constant of the plate region can be written under this assumption as [213]

$$I_{pl} = \frac{L_p h^3}{12}$$

(5.18)

and

$$k_{pl} = \frac{16 E h^3}{L_p^2}$$

(5.19)

As long as its stiffness is much higher than that of the springs, the translational motion of the system under external force can be considered similar to that of a double-side clamped spring system with a central proof-mass. If once again, the mass of the springs is negligible compared to that of the plate region, the spring constant and translational natural frequency of the two configurations can be expressed in terms of the length L_s, width b and thickness h of the springs as given in Table 5.12. The quad-beam configuration is intrinsically less susceptible to torsional vibration than the dual-beam configuration. For the dual-beam case, the torsional natural frequency can be expressed as [213]

$$f_{trd2} = \frac{1}{2\pi} \sqrt{\frac{24 G K b h^2}{\rho L_s L_p^2}}$$

(5.20)

where G is shear modulus of the material (26 GPa for Al) and K is a function of the ratio b/h

given by

$$K = \frac{1}{3}\left(1 - \frac{192}{\pi^5}\frac{h}{b}\sum_{n=1,3,5\ldots}^{\infty}\frac{1}{n^5}\tanh\frac{n\pi b}{2h}\right)$$ (5.21)

Therefore, for the dual-beam configuration, the dominant mode of vibration is whichever is lower between f_{spd2} and f_{trd2}, in Table 5.12, i.e.

$$f_{d2} = min[f_{spd2} \quad f_{trd2}]$$ (5.22)

where $min[w_1 \; w_2]$ represents the lower between two values w_1 and w_2.

In order to ensure $k_{sp} \leq k_{pl}/100$, as described above, a minimum value, L_{min}, can be obtained for the spring length L_s from the expressions of k_{sp} and k_{pl} in Table 5.12 and for the two different types, the expressions for L_{min} are also listed in the Table 5.12. For all the configurations, the maximum thickness of the plate to keep $k_p/f_p^2 \leq 20$ g is given by relation (5.17) and the minimum length of the spring is given in Table 5.12. For $h \geq h_{max}$ (Eqn. 5.17), desired $k_p \leq 50$ N/m and $f_p \geq 50$ Hz cannot be achieved. For $L_s \leq L_{min}$ the condition $k_{sp} \leq k_{pl}/100$ cannot be satisfied.

It can be seen from Table 5.12 that $f_p/k_p \propto b^{-1/2}$ for a given L_s and h. Therefore, width b of the spring should be as low as possible to keep a high f_p and low k_p. However, minimum b depends on the minimum width of a strip that can be cut from the plate. From initial experiments on laser machining aluminium plate, it has been observed that smooth edges could be achieved on thin aluminium strips where the cut-width was between 40 μm and 50 μm as shown in Figure 5.14. Therefore, if the width of the designed spring is less than 500 μm, the uncertainty in the width of the manufactured spring will be more than 10%. So, the minimum width of the spring is considered as 500 μm.

In Figure 5.15, the analytically obtained variation of the fundamental natural frequency, f_p, with the spring constant, k_p, is shown by increasing the length of the spring, L_s from corresponding L_{min} to $10 \times L_{min}$. The different thicknesses of the plate up to a maximum 100 μm are chosen from the plate thicknesses available from Alfa Aeser [210] and McMaster [211]. The width, $b = 500$ μm for the springs is chosen for all the four cases.

It is observed that, in none of the two configurations, the desired f_p-k_p combination can be achieved. The abrupt change in the curves for the dual-beam configuration represents a transition from torsional fundamental mode to a translational fundamental mode as the length L_s is increased. It must be noted that the maximum f_p-k_p values in Figure 5.15 correspond to the condition $L_s = L_{min}$. Further reduction in the length of the spring violates the condition $k_{sp} \leq k_{pl}/100$. Increasing the width b only flattens the curves for a given thickness. Therefore, it is concluded that, with a plate ($L_p \times L_p$) completely made from aluminium, the desired f_p-k_p combinations cannot be achieved.

Table 5.12: Summary of design parameters and expressions for two plate configurations

Property	Double spring	Quad spring
Schematic	**(a)****(b)** **Figure 5.12: Schematic of a dual-beam plate configuration. (a) top view. (b) cross-section**	**(a)****(b)** **Figure 5.13: Schematic of a quad-beam plate configuration. (a) top view. (b) cross-section**
Spring constant of the spring (k_{sp})	$k_{spd2} = \dfrac{2Ebh^3}{L_s^3}$	$k_{spd4} = \dfrac{4Ebh^3}{L_s^3}$
Spring constant of the plate (k_{pl})	$k_{pld2} = \dfrac{16Eh^3}{L_p^2}$	$k_{pld4} = \dfrac{16Eh^3}{L_p^2}$
Overall spring constant (k_p) for $L_s \geq L_{min}$	$k_{d2} \approx k_{spd2}$	$k_{d4} \approx k_{spd4}$
Natural frequency (Translation)	$f_{spd2} = \dfrac{1}{2\pi}\sqrt{\dfrac{2Ebh^3}{L_s^3 M_p}}$	$f_{spd4} = \dfrac{1}{2\pi}\sqrt{\dfrac{4Ebh^3}{L_s^3 M_p}}$
Natural frequency (Torsion)	$f_{trd2} = \dfrac{1}{2\pi}\sqrt{\dfrac{24GKbh^2}{\rho L_s L_p^2}}$	--
Dominant mode frequency (f_p)	$f_{d2} = \min[\; f_{spd2} \quad f_{trd2}\;]$	$f_{d4} = f_{spd4}$
Minimum length of the spring (L_{min})	$L_{min\_d2} = \left(\dfrac{25}{2}bL_p^2\right)^{1/3}$	$L_{min\_d4} = \left(25bL_p^2\right)^{1/3}$
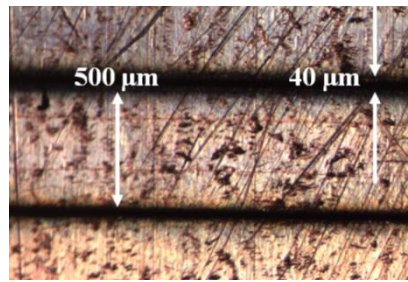
Figure 5.14: Image of laser cutting aluminium plate at Reconfigurable Robotics Lab, EPFL, Lausanne (rrl.epfl.ch). Laser power 95%, marking speed 0.4 m/s and number of cuts 150. A typical 40 μm width of the cut-line is observed.

(a)   (b)
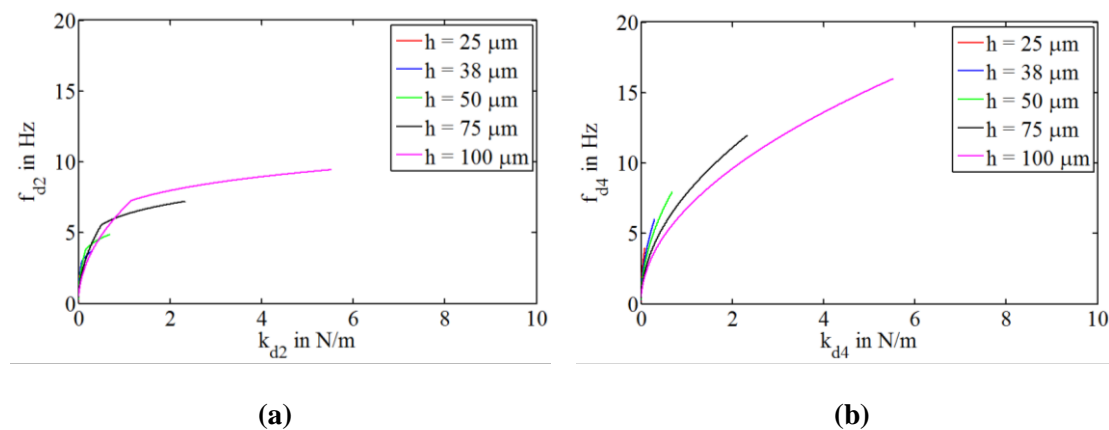
Figure 5.15: Analytically obtained plot of variation of dominant mode frequency with the spring constant for (a) dual-beam and (b) quad-beam aluminium plate configuration obtained by increasing the length of the spring from the corresponding L_{min} to $10 \times L_{min}$ for different available thicknesses. The width of the spring is 500 μm.

Design modification approach

A modified design can be thought of to reduce the mass of the thrust intercepting plate region without compromising its spring constant. This will increase the natural frequency for a given spring constant, shifting the f_p-k_p plots upwards. However, the frame will have same thickness h as the springs and hence it will need to be stiffened elsewise to keep the plate region much stiffer than the spring region. This can be done by modifying the square plate region into a frame as shown in Figure 5.16 (a) and placing an electrically conducting membrane to fill-up the particle capturing area.

Initially two different stiffening schemes have been considered by bending the plate as shown in Figure 5.16 (b) and (c). The 'L' shaped indent in the 1st scheme can be manufactured by first cutting the plate and then plastically bending the long narrow strips using a punch. However, during bending, the plate may move laterally as one side of the section is free. This scheme has been therefore discarded.

The 2nd scheme is based on first bending the plate using a punch in an ideally semi-circular shape and then cutting the frame. In this scheme, both the sides of the section to bend are part of the plate and hence can be rigidly fixed while bending, eliminating chances of lateral movement causing misalignment. Therefore, the 2nd scheme has been pursued for modifying the plate design. In Figure 5.17 (a), a schematic of the process is shown. However, the

problem with plastically bending plates is that on removal of the punch, the plate suffers spring back effect and retracts to increase the radius of curvature as shown in Figure 5.17 (b).
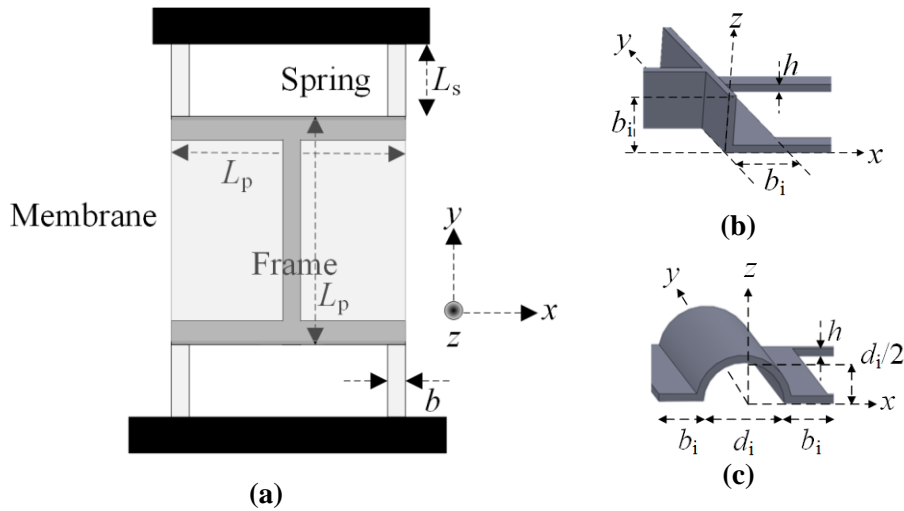
Figure 5.16: (a) Schematic of the modified plate. The particle intercepting area is modified into a frame and covered with an electrically conducting membrane. Stiffening of the frame can be achieved by bending the arms of the frame in (b) 'L' shape or (c) circular indent.

If the radius of curvature at the bending junction before and after removal of the punch are R_i and R_f respectively, an estimate of the spring back can be found from the relation [214]

$$\frac{R_i}{R_f} = 4\left(\frac{R_i Y}{Eh}\right)^3 - 3\left(\frac{R_i Y}{Eh}\right) + 1 \tag{5.23}$$
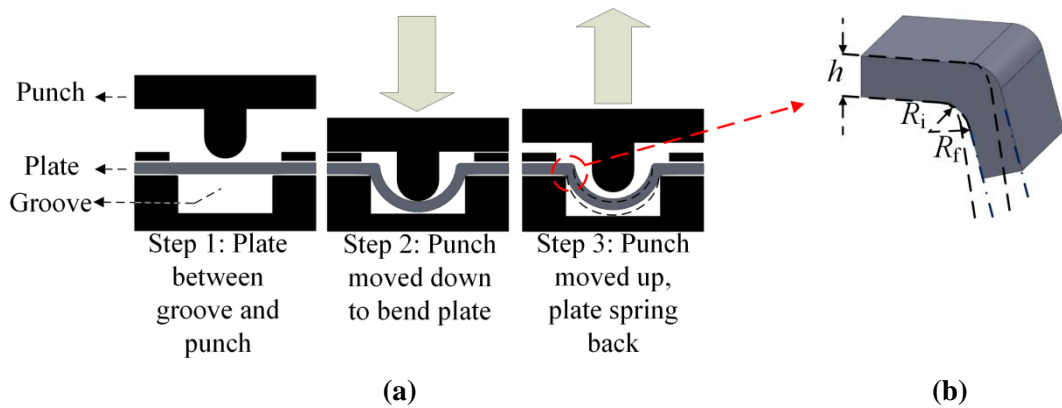
Figure 5.17: (a) Schematic of the bending process for the plate. The Punch pushes the plate into a groove to plastically deform it. On removal of the punch, the plate suffers spring back effect to retract. (b) Spring back effect at the bent radius. The radius of curvature increases when the punch is removed.

where Y is yield strength of the metal. Spring back effect will be small if Y/E is small and R_i/h at the bending junction is small. For aluminium, $Y = 20$ MPa and $E = 70$ GPa, giving a ratio $Y/E = 0.03\%$. As a result, aluminium is expected to have very low spring back and can be deformed into the desired shape if proper forming methods are used [214]. The method of bending the aluminium plate is discussed in detail in section 5.5. However, in the present case, the desired radius of curvature at the bending junction can be considered to be zero

before and after removing the punch, so that a semi-circular indent can be considered as shown in Figure 5.18.

In the stiffened frame, as shown in Figure 5.16 (c), all the three arms of the frame can be considered as doubly clamped cantilevers with force applied at their centres when an external force is applied at the centre of the plate. If I_{arm} is the second moment of inertia of each arm, the moment of inertia and the spring constant of the entire frame can be written as [213]

$$I_{fr} = \frac{I_{arm}}{3} \qquad (5.24)$$

and

$$k_{fr} = \frac{192\,EI_{fr}}{L_p^3} = \frac{64\,EI_{arm}}{L_p^3} \qquad (5.25)$$

respectively. k_{fr} can be increased by increasing I_{arm}. The value of I_{arm} depends on the cross-sectional shape of the indent which in-turn depends on how well the plate can be bent. Essentially, bending can be performed by using a punch to deform the plate into a groove and the semi-circular shape can be a good approximation for the best bent shape. However, some part of the frame should be left flat on both sides of the indent in order to attach a membrane to it. Also, bending of the plate is to be performed with a punch as shown schematically in Figure 5.17. In practice, the semi-circular shape may not be achieved, although this shape is assumed for the analysis. The diameter of the indented semi-circle should be large enough to allow the punch to properly bend it. On the other hand, a wider indent may deviate largely from the desired semi-circular shape. Therefore, the following assumptions have been made in the shape of the indent.

Table 5.13: Assumptions for the semi-circular indent in the arms of the frame
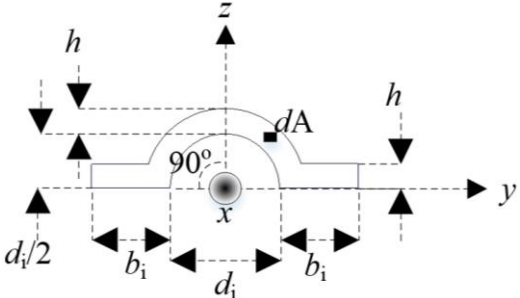
Property	Value
Shape of indent	Semi-circular
Inner diameter of the indent (d_i)	$2h \le d_i \le 20h$
Space left on both sides of the indent (b_i)	500 μm
Schematic	

Figure 5.18: Schematic of the assumed semi-circular indent shape for the arms of the frame

It must be noted that the condition on h_{max} as obtained in relation (5.17) does not apply here as

the frame is of comparable mass with the spring. However, to keep $k_{sp} \leq k_{fr}/100$, a minimum length can once again be derived as

$$L_s \leq L_{min} = \left(\frac{25}{4} \frac{bh^3}{I_{arm}} L_p^3 \right)^{1/3} \tag{5.26}$$

To find I_{arm}, the position of the neutral axis for the arms of the frame from the bottom plane of the plate can be written as

$$z_N = \frac{\int\limits_{z=0}^{h+d_i/2} z \, dA}{\int\limits_{z=0}^{h+d_i/2} dA} \tag{5.27}$$

where dA is an elementary area in the cross-section of the indent at a height z as shown in Figure 5.18. The second moment of inertia of the arms of the frame can be written as

$$I_{arm} = \int\limits_{z=-z_N}^{h+d_i 2/2 - z_N} z^2 \, dA \tag{5.28}$$

The mass of the frame can be written as

$$M_{fr} = 6\rho L_p \int\limits_{z=-z_N}^{h+d_i 2/2 - z_N} dA \tag{5.29}$$

A comparison of the moment of inertia and mass of the frame and that of the full-plate configuration in Figure 5.13 is shown in Figure 5.19 (a). In this figure, I_{fr}/I_{pl} is plotted against M_{fr}/M_{pl} by varying the diameter d_i of the semi-circular indent from $2 \times h$ to $20 \times h$ at different available thicknesses of aluminium plates from Alfa Aeser [210] and McMaster [211]. I_{fr} and M_{fr} have been obtained by numerically solving Eqn. (5.28) and (5.29) respectively. The plots show that, significant mass reduction and increase in the moment of inertia can be achieved with the indented frame compared to the full-frame case. In Figure 5.19 (b), the corresponding f_p-k_p relation is plotted for the same range of d_i as the length of the spring is kept at the corresponding minimum defined by Eqn. (5.26). The width of the springs is once again kept at the practical minimum of 500 μm. The shaded rectangle in the figure represents the desired f_p-k_p range. It is observed that, with $L_s = L_{min}$, the desired f_p-k_p relation can be achieved for thickness ≥ 38 μm. The f_p corresponding to a given k_p however decreases as the thickness is increased. However, for $h = 38$ μm, the f_p-k_p relation enters the desired region only marginally for $L_s = L_{min}$ and increasing L_s above L_{min} may lead to undesirably low f_p. Practical manufacturing deviations from this simplistic analytical approach may also lead to undesirably low f_p for $L_s \geq L_{min}$.

A more detailed design perspective into the f_p-k_p relations can be found by looking at the relation of f_p and k_p with d_i separately as shown in Figure 5.20 (a) and (b) respectively. It is seen that for $h \leq 50$ μm, f_p can enter the desired region only for $d_i > 20 \times h$ (outside the range of the plot) for $h = 25$ μm. On the other hand, for $d_i \leq 10 \times h$, desired high f_p can be achieved at the expense of undesired high k_p for $h \geq 75$ μm. If a practical ratio $d_i/h = 10$ is assumed for

designing and manufacturing the plates, it can be seen that $h = 75$ μm and $h = 100$ μm can reach the desired f_p and k_p values at $L_s = L_{min}$. With $h = 130$ μm and $h = 200$ μm $k_p = 92.99$ N/m and $k_p = 466.23$ N/m respectively are obtained, although both the cases produce $f_p > 50$ Hz. However, if L_s is allowed to increase beyond L_{min} to reduce k_p, all the four cases with $h \geq 75$ μm can be considered as long as $f_p \geq 50$ Hz.

(a)	(b)
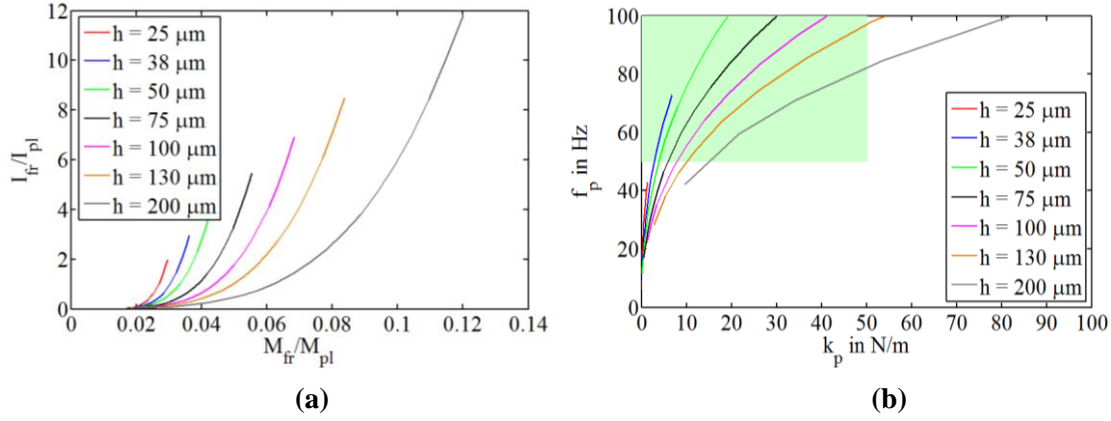
Figure 5.19: (a) Analytically obtained plot of moment of inertia ratio against mass ratio of the semi-circular indented frame in Figure 5.16 to the full-plate (Figure 5.13) structure as the diameter of the semi-circular indent is increased from $2h$ to $20h$. Thicknesses are taken from those available commercially. (b) Plot of fundamental mode frequency against the spring constant of suspended frame shown in Figure 5.16 as the diameter d_i of the semi-circular indent is increased from $2h$ to $20h$. Width of the spring is kept as 500 μm and length of the spring at the corresponding L_{min} derived in relation (5.26). The shaded rectangle is the desired range of f_p and k_p.

In Figure 5.21 (a) and (b), the f_p-L_s and k_p-L_s relations for the four different available thicknesses with $h \geq 75$ μm are shown while varying L_s from L_{min} to $10{\times}L_{min}$ and keeping $d_i = 10{\times}h$ in the analytical model. Width of the spring b is once again kept at the practical minimum value 500 μm. It can be seen from the plots that the desired f_p-k_p can be achieved with these thicknesses. Although k_p is in the desired range for $h = 75$ μm with all $L_s \geq L_{min}$ f_p is in the desired range only between 16.7 mm $\leq L_s \leq$ 20.1 mm. On the other hand, 32.1 mm $\geq L_s \geq$ 28.2 mm is required for $h = 200$ μm to keep both k_p and f_p in the desired range. The cases $h = 100$ μm and $h = 130$ μm require a range 15.5 mm $\leq L_s \leq$ 23.8 and 18.1 mm $\leq L_s \leq$ 26.5 mm respectively. Both these thicknesses can be chosen. Alternatively, ratio d_i/h other than 10 can also be chosen. In the present case, $h = 130$ μm and $d_i/h = 10$ is chosen for further analysis.

In order to compare these results with FEM simulations, the structures have been constructed in COMSOL multiphysics simulator (version 4.4) as shown in Figure 5.22. Spring constant has been evaluated by applying a force at the centre of the frame and finding the displacement at the centre, which is identical to the definition of spring constant in the analytical model as well. The simulated f_p and k_p values for $h = 100$ μm and $h = 130$ μm are shown in the corresponding analytical plots in Figure 5.21 (a) and (b) for comparison. The simulation results show that the results for a given k_p, the required lengths obtained from the simple analytical method are within 25% of the corresponding FEM results. In the FEM simulation, the length of the springs is not limited to L_{min}, rather allowed shorter L_s as well, between 5 mm and 20 mm. However, the condition $k_{sp} \leq k_{fr}/100$ does not apply in those cases where $L_s \leq L_{min}$.
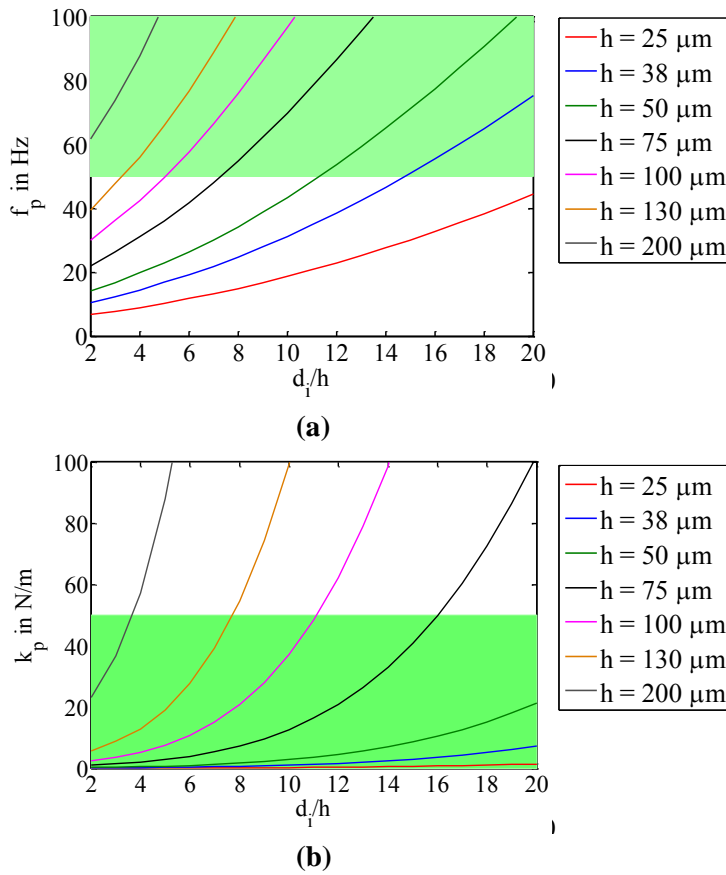
Figure 5.20: (a) Analytically obtained plot of natural frequency and (b) spring constant of the suspended frame shown in Figure 5.16 as the diameter of the semi-circular indent is increased from $2h$ to $20 \times h$. Width of the spring is kept as 500 µm and length of the spring at the corresponding L_{min} derived in relation (5.26). The shaded rectangles are the desired range of f_p and k_p. The shaded rectangles are the desired range of f_p and k_p.
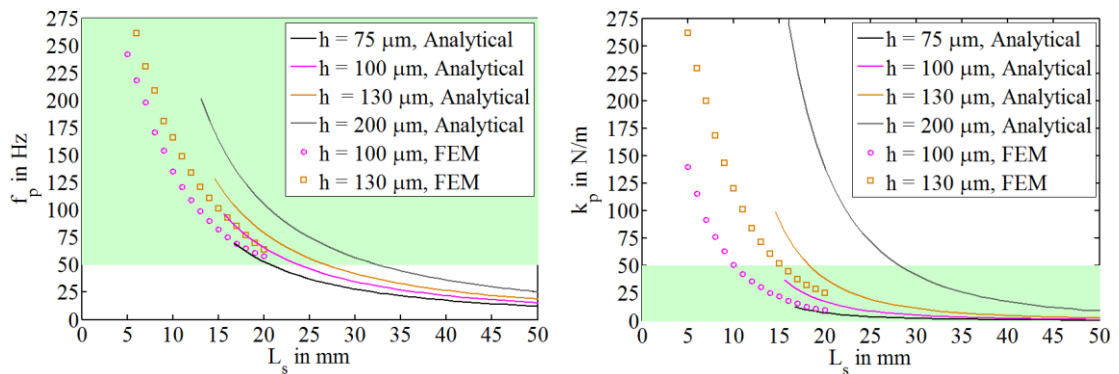
Figure 5.21: (a) Analytically and FEM simulated plot of natural frequency and (b) spring constant of the suspended frame shown in Figure 5.16 as the length L_s of the spring is increased from L_{min} to $10 \times L_{min}$. Width of the spring is kept as 500 µm and diameter of the semi-circular indent at $d_i = 10 \times h$. The shaded rectangles are the desired range of f_p and k_p.

The differences between the simulation and analytical results might have originated from the intrinsic assumptions in the analytical approach. The analytical approach is based on the lumped spring-mass model of the entire structure. The arms of the frame have been considered as lumped spring elements with individually defined spring constants. Also, the moment of inertia estimation of the arms of the frame has been obtained about their own neutral axes in the analysis; coincidence of the neutral axis of the frame section with the spring section has not been considered. Therefore, the overall deflection profile of the particle intercepting plate, obtained from this analytical approach, may be different from the finite element approach in the more accurate multiphysics simulator platform. Therefore, for further analysis, the simulated results are accepted rather than the analytical approach, while analytical approach led us to a simple way to reach towards an optimal design.

(a)   (b)
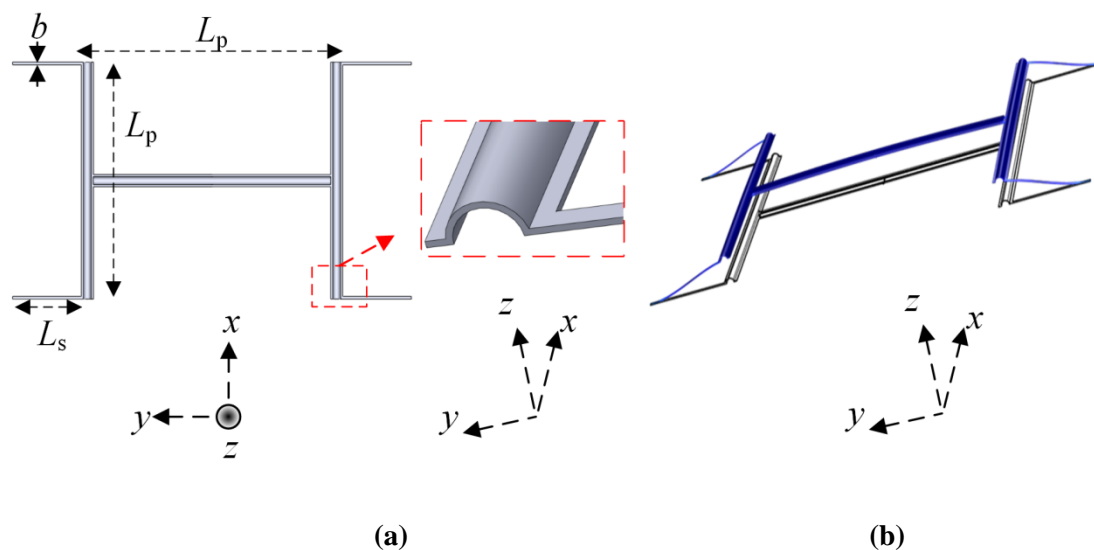
Figure 5.22: (a) 3-D model of the frame for FEM simulation. A zoomed in view of the semi-circular indent is in the inset. (b) Displacement of the frame under force at the centre. The structures with different h and L_s are generates in Solidworks (version 2010) and exported to COMSOL.

A further modification in the design, with an eye to practical situation is made before finalizing the dimensions of the frame and spring structures. The manufactured plate may not be flat due to an initially bent mother-plate or during laser machining or due to mishandling. When the plate is attached to a stiff frame, the residual stress concentrated at the rigidly clamped end might affect the spring constant and natural frequency of the structure. In order to minimize the stresses at the ends of the springs, additional torsion beam can be added to them so that by torsional deflection of these beams, initial flatness of the actual plate region can be improved. In this case, L_s does not need to be constrained above L_{min} since the combined spring constant of the added beam and the original spring now provides deflection of the frame and the overall spring constant of the combination of two beams in all the four quadrants needs to maintain its upper limit to $k_{fr}/100$. Since the frame is not changed in the modification approach, this condition will be met if $k_p \leq 50$ N/m can be achieved.
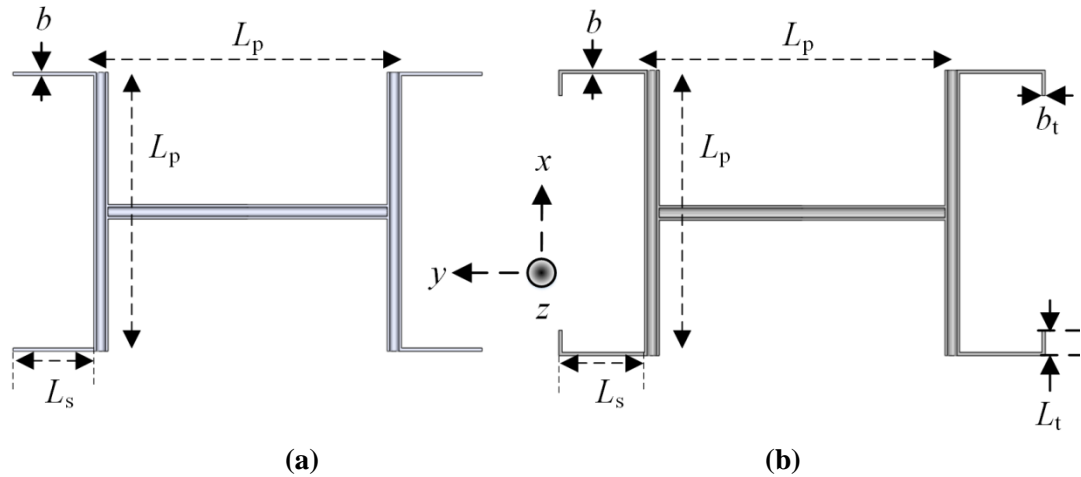
Figure 5.23: Schematic of the frame (a) without and (b) with torsion beams

In order to keep the stiffness of the additional beams very low, once again, width b_t is kept to the practical minimum value 500 μm. In Figure 5.24 (a) and (b), the f_p-L_t and k_p-L_t relations for different fixed L_s are plotted for h = 130 μm from COMSOL simulation results. In Figure 5.24 (c) the corresponding f_p-k_p relation is shown. From the simulation results, a range of L_s and L_t can be obtained within this range of L_s and L_t used in Figure 5.24 (a) and (b) that can satisfy the relation $f_p \geq 50$ Hz and $k_p \leq 50$ N/m as shown in Figure 5.24 (d). It must be noted that the desired area can extend in the right side more, however, these dimensions have not been considered in the simulation. Also, the accurate shape of the area depends on the steps in the lengths chosen for simulation within the range. It can also be noted that L_s and L_t both are defined as the external lengths of the two beams in each quadrant of the particle intercepting plate, and hence L_t = 0 in Figure 5.24 (a), (b) and (c) correspond to (L_s + b_t) in Figure 5.21(a) and (b) with b_t = 0.5 mm.

In Figure 5.24 (d) it can be seen that the final lengths chosen for the spring section of the particle intercepting plate correspond to the minimum L_t and L_s that produces $k_p \leq 50$ N/m and $f_p \geq 50$ Hz. This is because of two reasons:

1. In practice, the frame is to be bent from an initially flat plate and it is expected that the punched indent may not be the ideal semi-circular shape chosen for the simulations. Therefore, it is expected that in practice, k_p and f_p both will be lower than expected for a given L_s and L_t.

2. Addition of membrane will further reduce the natural frequency of the structure by increasing mass of the plate section.

Since a minimum acceptable L_s and L_t in Figure 5.24 (d) corresponds to the maximum natural frequency satisfying $k_p \leq 50$ N/m, for the final dimensions, this pair of L_s and L_t is chosen such that practical manufacturing imperfections leading to lowering of k_p and f_p still ensures $f_p \geq 50$ Hz and $k_p \leq 50$ N/m.

The final dimensions of the springs have been summarized later in Table 5.14 along with the membrane configuration at the end of the section. However, the design of the springs based on the discussion in section 5.3.1 can be summarized here as L_s = 10 mm, L_t = 6 mm, both defined as the outer lengths, $b = b_t = 500$ μm, h = 130 μm and $d_i = 10 \times h$. The spring constant

and natural frequency of the structure are obtained to be k_p = 50.23 N/m (0.46% above the desired maximum value) and f_p = 93.45 Hz respectively. In Figure 5.25 the deflection of the suspended frame is shown from COMSOL simulation platform. The relative deflection of the centre of the frame region from the end of the spring is found 0.81% of the deflection of the end of the spring from its rigid end. This corresponds to a k_{fr}/k_{sp} ratio of 123.5, higher than the desired ratio of 100.

(a)   **(b)**

(c)   **(d)**
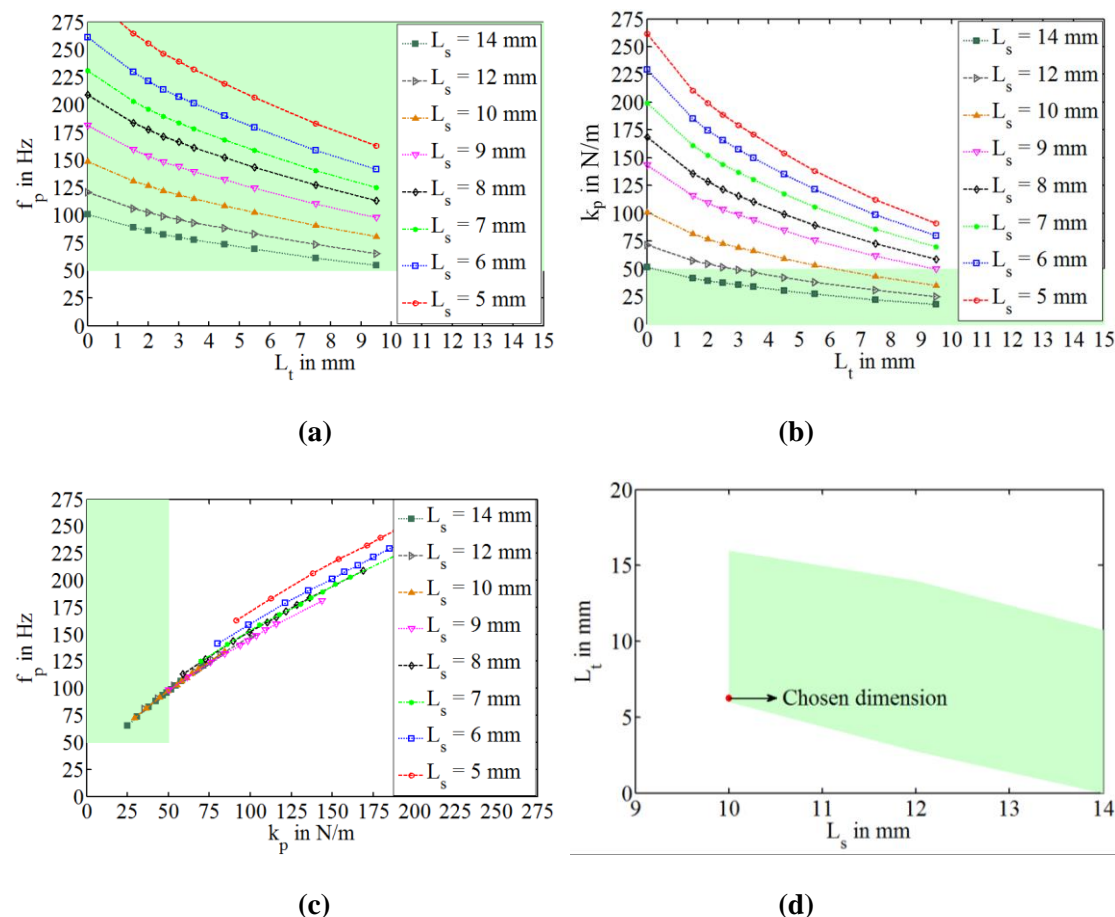
Figure 5.24: FEM simulated plot of (a) natural frequency and (b) spring constant of the suspended frame shown in Figure 5.23 (b) with the length L_t of the additional beam. Width is kept as 500 μm. Thickness h = 130 μm. The shaded rectangles are the desired range of f_p and k_p. (c) Corresponding f_p-k_p relation shows that 10 mm $\leq L_s \leq$ 14 mm can reach the desired range. The corresponding range of L_s and L_t is shown in the shaded polygon in (d). The acute shape of the polygon, however, depends on the values of L_s and L_t chosen within the simulated range. The final dimension chosen for the plate is marked with a red dot at L_s = 10 mm, L_t = 6 mm. The shaded rectangles are the desired range of f_p and k_p.

5.3.2.   The membrane

Addition of membrane to the frame increases the mass of the frame section and as a result, it is expected to reduce the natural frequency further. Therefore, the membrane and the adhesive layer have to be very thin, so that the membrane adds very small mass. Also, the membrane needs to be electrically conductive and it should be electrically shorted to the frame. For adhesive, ARclear® 8154 [215] is chosen. It has a 25 μm thick adhesive layer between

polyester liners on both sides which can be deposited on the aluminium plate and cut with the laser cutter along with the aluminium. Mylar film of 2 μm thickness and metalized with aluminium [216] is chosen for the membrane. For electrical connection between the metalized side of Mylar film and the aluminium frame, a small area on one side of the middle arm of the frame is created with 3 mm × 3 mm area and the adhesive layer has an aperture of 2 mm diameter at the centre of the area as shown in Figure 5.26. Finally, two-part electrically conductive epoxy EPO-TEK® H20S [172] is chosen to make electrical contact between the Mylar film and the aluminium frame through the aperture.
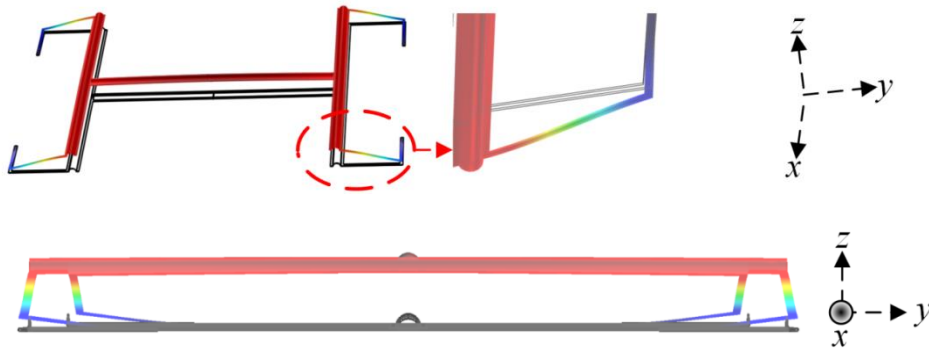
Figure 5.25: Deflection of the final frame under a force at the centre. The deflection of the frame region is negligible compared to the deflection of the combined spring section

(a)

(b)
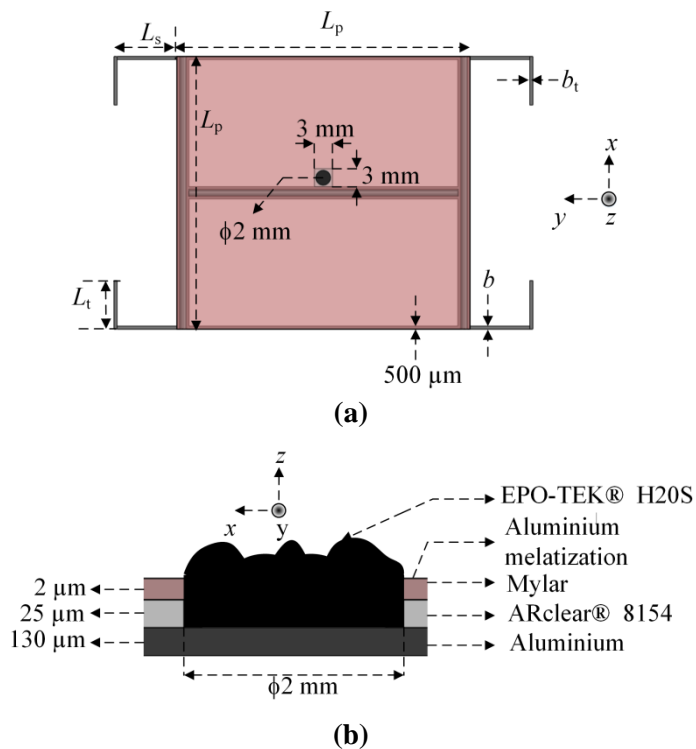
Figure 5.26: (a) Final design schematic of the particle intercepting plate with Mylar membrane, 2 additional arms of 500 μm width in the frame and the 3 mm × 3 mm area on the central arm for electrical contact. (b) Schematic cross-section of the electrical contact at the 2 mm diameter aperture on the 3 mm × 3 mm square area. Thicknesses are not scaled in the diagram. H20S conductive epoxy to make contact between metalized side of Mylar and aluminium frame.

Another modification, based on initial experiments on Mylar attachment, has been made in the design and two additional beams of 500 μm width have been added to the initially free sides of the square frame region as shown in the final design of the plate in Figure 5.26. The Mylar should be pre-stretched during attachment, so that the membrane responds to thrust with low response time. The method of attaching pre-stretched Mylar on the frame is discussed in section 5.5. Initial experiments on attaching pre-stretched Mylar on pre-cut PMMA frame show that the free sides of the membrane shrink towards their original unstretched shape and buckle as shown in Figure 5.27. Depending on the spring constant of the arms of the frame in the shown y direction, the stress in the Mylar may bend the arms and the overall membrane section may buckle. The additional beams are added to the design as stiffeners so that when stuck to them, it does not allow bending of the arms of the frame.

Based on the mass of the additional arms of the frame, the contact area, mass of the adhesive membrane and epoxy, the natural frequency is expected to fall from the values obtained without them. The reduction in natural frequency based on these masses is calculated in Table 5.15 to estimate the final natural frequency of the structure. For initial experiments with the plate, EPO-TEK® H20S is not used to make the contact, so expected natural frequency without and with epoxy are calculated separately.

Figure 5.27: Initial experiments on attaching pre-stretched Mylar on a prototype PMMA frame. The free ends of the pre-stretched membrane buckle as shown.

5.4. Expected performance of the particle intercepting plate

The designed plate has a spring constant 50.23 N/m when a force is applied at the centre of the plate to move it in the z direction. The final natural frequency with addition of the membrane is expected to be 81.77 Hz. It is expected that the plate with this natural frequency can avoid resonance due to external disturbances. The expected force resolution can be evaluated from Eqn. (5.8) to be $F_{res} = 10.02$ nN if FT-S100 probe with spring constant $k_f = 50.00$ N/m is used with a resolution $F_\Delta = 5$ nN.

However, the spring constant k_p has been evaluated under the assumption that a point force is applied at the centre of the plate and deflection is measured at the centre. The relation $k_{fr} \gg k_{sp}$ is satisfied in the design to keep k_p reasonably constant over the location and spot size of the particle plume on the plate. The variation in k_p with the location and spot size directly relates to the uncertainty in the force measured.

In order find the dependence of the measured force at the centre of the plate on the position and spot size of the particle plume, a cantilever beam with spring constant 50.00 N/m and a tip of area 100 μm × 100 μm in contact with the centre of the frame is simulated in COMSOL to emulate the force sensor. When a force is applied on the plate with arbitrary location and spot-size, the deflection of the cantilever tip is the measure of the force that the FT-S100 sensor would sense.

Table 5.14: Final dimensions of the particle intercepting plate

Part	Property	Value
Frame + spring	Material	Aluminium
	Material of membrane	Metalized Mylar
	Thickness (h)	130 μm
	Frame size ($L_p \times L_p$)	45 mm × 45 mm
	Shape of indent	Semi-circular
	Indent diameter (d_i)	1.3 mm
	Adhesion space (b_i)	500 μm
	Length of spring (L_s)	10 mm
	Width of spring (b)	500 μm
	Length of torsion beam (L_t)	6 mm
	Width of torsion beam (b_t)	500 μm
	Width of additional arms	500 μm
	Square shape for electrical contact	3 mm × 3 mm
Adhesive	Material	ARclear® 8154
	Thickness	25 μm
	Covering	On the arms of the frame
	Aperture for contact	2 mm diameter
Membrane	Material	Metalized Mylar
	Metallization	Aluminium
	Size	45 mm × 45 mm
	Thickness	2 μm
	Condition	Pre-stretched
	Covering	Entire frame
	Aperture for contact	2 mm diameter
Electrical contact	Material	EPO-TEK® H20S
	Location	At the aperture in Mylar

To apply simulated force at different locations and with different spot sizes, a membrane is created on the frame similar to the Mylar membrane. However, over the large lateral size of the plate, a 2 μm thick membrane requires extremely fine mesh for FEM simulations and extremely long time for a convergent output. Therefore, a membrane of arbitrary material with thickness 100 μm, Young's modulus 40 kPa and density 28 gm/m^3 has been created on the frame. The choices are driven by the desire to keep the overall mass and stiffness of the membrane same as the actual Mylar film.

Two different conditions are simulated.

1. A constant point force is applied at a position (x, y) on the plate and force $F(x, y)$ is evaluated from the deflection of the cantilever as shown in Figure 5.28 (a).

2. A constant force distributed uniformly over a circular spot-size of radius r about the centre of the plate is applied and force $F(r)$ is evaluated from the deflection of the cantilever as shown in Figure 5.28 (b).

In Figure 5.28 (c) and (d), the map of $F(x, y)/F(0, 0)$ and $F(r)/F(0)$ on the entire plate are plotted respectively. The results show that the difference of the measured force at the centre for a given applied force is within 5% over the different spot sizes and location of the applied force. Therefore, it can be inferred that the maximum inaccuracy in the measured thrust due to misalignment of the thruster with respect to the centre of the plate and due to non-zero spot size is within 5%. Placing the thruster closer to the plate reduces the inaccuracy due to smaller spot size for a given emission half-angle, however, this might be detrimental for the thruster operation.

Table 5.15: Properties of the designed particle intercepting plate and estimation of reduction of natural frequency due to attachment extra mass to the frame

Property	Value
Natural frequency of the frame without membrane (Hz)	93.45
Spring constant of the frame, k_p (N/m)	50.23
Mass of the frame used in simulations, M_{fr} (mg)	144.1
Mass of the springs (mg)	11.2
Mass of additional contact area in the frame (mg)	3.2
Mass of the additional stiffening beams (mg)	15.8
Mass of ARclear® 8154[*]	9.0
Mass of Mylar film[#]	5.6
Mass of EPO-TEK® H20S[@]	2.4
Increase in mass of frame without epoxy δM (mg)	33.7
Fractional increase in mass without epoxy, $\delta M/M_{fr}$	0.233
Fractional decrease in natural frequency, $0.5 \times \delta M/M_{fr}$	0.117
Total increase in mass of frame with epoxy, ΔM (mg)	36.1
Fractional increase in mass with epoxy, $\Delta M/M_{fr}$	0.250
Fractional decrease in natural frequency, $0.5 \times \Delta M/M_{fr}$	0.125
Expected natural frequency without epoxy (Hz)	82.56
Expected final natural frequency with epoxy f_p (Hz)	81.77

[*] Density of ARclear® 8154 is taken to be 1.02 kg/m^3 from e-mail communication
[#] Mass of Mylar does not include the metallization mass [216]
[@] 1:1 combination of the two-part epoxy [172], assuming 1 mm^3 volume
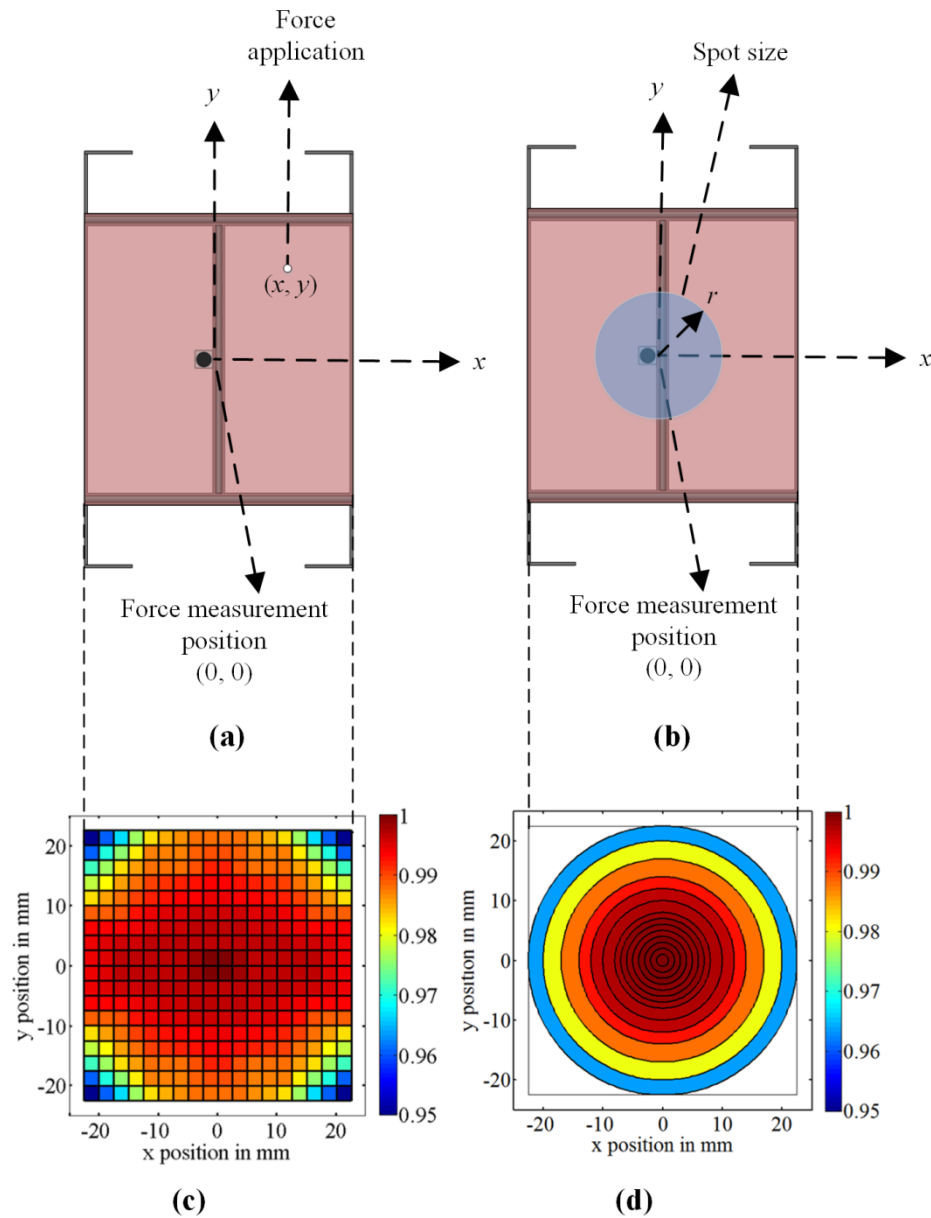
Figure 5.28: Schematic of simulation of force map on the plate with (a) a point force applied on the plate and (b) a uniformly distributed force over a circular spot size applied on the plate. In both cases, force measured at the centre is simulated from the deflection of the cantilever used as the dummy force sensor. (c) FEM simulation results showing the force measured at the centre with a constant force applied at (x, y) normalized to force measured at the centre with the force applied also applied at the centre. (d) FEM simulation results showing the force measured at the centre with a distributed force with spot radius r normalized to the force measured at the centre with the force with $r = 0$ applied at the centre. The global variation of the force in both cases is within 5%.

Therefore, the expected performance of the plate and hence the thrust stand can be summarized in Table 5.16. It must be noted that the accuracy mentioned here is only based on the spot size and location of the particle plume on the plate and does not consider the experimental effects. As mentioned before, the force on the plate is related to the generated

thrust at the thruster head depending on the type of interaction of the particles with the plate. For example, if the particles suffer perfectly elastic collision with the plate, the force on the plate is twice as great as the thrust on the thruster. For electrospray thrusters, depending on the type of charged particle, the collision might be different and based on how accurately the collision type for the individual type of particles can be determined, the accuracy may be lower. These issues is discussed in the Chapter 6 and Chapter 7 in more detail.

Table 5.16: Expected performance metrics of the thrust stand

Property	Value
Expected natural frequency, f_p (Hz)	81.77
Spring constant of the plate, k_p (N/m)	50.23
Force resolution, F_{res} (nN)	10.02
Force range F_{max} (μN)	100.23[*]
Accuracy from the spot size and location of applied force	95%

[*] Assuming a 50% offset force on the force sensor in Eqn. 5.9

5.5. Plate manufacturing process

The plate manufacturing process essentially can be divided into three parts. First, the aluminium plate needs to be bent in the desired shape of the indents. Then Mylar film will be attached to it. Finally, electrical contact will be established between the Mylar film and the metal plate. In the entire process, certain constraints are to be satisfied.

- During the plate manufacturing process, the plate should never be removed from the manufacturing setup. The plate should be rigidly clamped on a frame, and after completion of the process, the manufactured plate should be directly mounted on the thrust stand without removing from the frame. This is to eliminate chances of mishandling and deformation in the fragile plate.

- The process should be reproducible so that multiple plates can be manufactured with identical settings to produce similar spring constant and natural frequency parameters.

- Minimum transportation of the plate should be ensured during the manufacturing process, especially after attaching the Mylar film. This is to ensure safety of the fragile Mylar membrane along with the frame and springs. So, the manufacturing process should be performed within the facility at one or two locations with minimum transportation between them.

- Bending of the plate should ensure minimal spring back so that the shape of the indent close to the assumed shape can be achieved without uncertainty due to spring back. A review of low spring back metal sheet bending process indicates that a process can be used in which the plate is sandwiched between a die and a pressure load while a punch deforms the plate [214] into the desired indent shape.

- Mylar should be pre-stretched during attachment on the plate, so that the applied thrust from the impinging particles during thrust measurement does not lead to plastic deformation of the very soft membrane and all the force is exerted on the spring.

Also, unstretched Mylar may respond to the applied force with a large and unpredictable response time which is undesirable.

5.5.1. The parts for plate manufacture

The plate manufacturing process starts with a flat aluminium mother-plate of size 125 mm × 50 mm and 130 μm thickness available from Alfa Aeser [210]. The following parts have been manufactured for making the plate.

Plate bending jig

To machine the suspended plate from this mother-plate, a plate bending jig is manufactured from 10 mm thick aluminium in mechanical workshop in Lausanne as shown in Figure 5.29. This jig has a 5 mm deep groove 5 mm inside its boundaries, where a 5 mm thick support frame can be placed and bolted with M4 screws. There is a 2 mm deep groove in the middle of the jig such that a punch can bend the aluminium plate into this groove for the three arms of the frame. Since the chosen plate is 130 μm thick and the desired shape of the indent is a semicircle with inner diameter 1.3 mm, the width of the groove is kept 1.5 mm. Four dowel pins of diameter 6.25 mm and height 25 mm are press-fitted in four holes in the jig so that the punch can be aligned within 10 μm accuracy to the grooves. Also, four sharp 90° corners have been bored for precise alignment of the plate-cutting drawing to the plate.
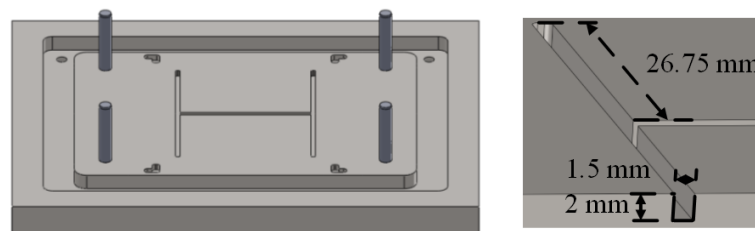
Figure 5.29: The plate bending jig with the grooves for placing a support frame along the boundary, the groove for bending the plate in, the dowel pins and the 90° alignment corners. On the right side, a cross-section of the bending groove is shown. It is 2 mm deep, 1.5 mm wide and 55 mm long on the two side arms of the frame to be made and 45 mm long for the central arm.

The support frame

The purpose of the support frame, as shown in Figure 5.30, is to fit into the corresponding groove in the bottom jig and attach the plate to it for cutting. Once attached, the plate is not detached from it unless the plate is damaged. The manufactured plate is mounted on the thrust stand with this frame itself to reduce handling the fragile plate after manufacture. Therefore, multiple identical support frames have been manufactured to manufacture multiple number of working plates.

The punch guide

The punch guide jig is a 15 mm thick aluminium jig with precisely cut openings to allow the punching process as shown in Figure 5.31. This jig fits on the bending jig with precise alignment through the four dowel pins on the bending jig. When the plate is sandwiched between the bending jig and the punch guide, the pressure load of the guide helps reducing the spring back of the aluminium plate during bending. The openings in the guide jig are 600

µm wide to allow a 500 µm wide punching blade. The staircase-shaped boundary of the opening in the guide allows the punch to remain straight.
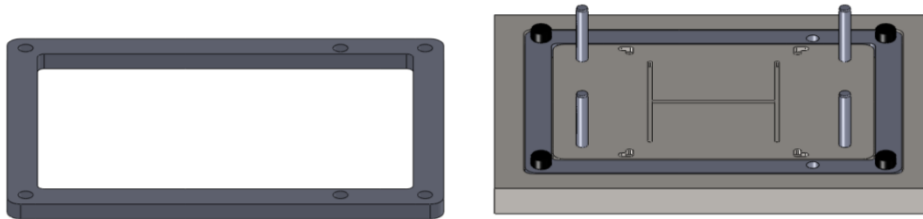
Figure 5.30: The support frame to fit into the border groove in the bending jig. The support frame can be placed on the bending jig and bolted as shown on the right side of the figure. The mother-plate can be stuck to the support frame and after machining the plate, the support frame along with the plate can be directly mounted on the thrust stand.
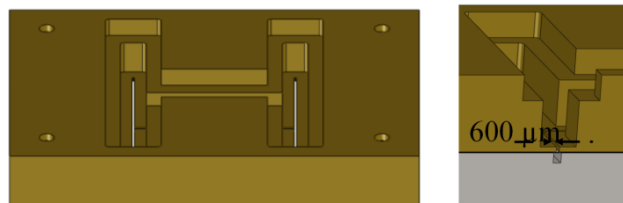
Figure 5.31: The punch guide. This jig can be aligned with the four dowel pins on the bending jig so that the openings in the guide are precisely aligned with the grooves in the bending jig for punching the plate.

The punch

The punch consists of three parts, a stainless steel blade of width 500 µm held between two aluminium pieces with three M2 set screws as shown in Figure 5.32. The aluminium pieces allow keeping the blade straight inside the opening of the guide jig and pressing the blade to bend the plate as shown in the middle and right side part of Figure 5.32. The edges of the blades are chamfered and smoothened so that the punching process does not break or cut the plate. The height of the blade protruding from the aluminium pieces is 2 mm and while pressing the blade the punch guide provides hard stop for the blade as the blade moves more than 0.8 mm. The plate needs an indent close to 0.65 mm inner radius, however, the extra 0.15 mm height of the blade is to produce a bending depth more than 0.65 mm so that even after spring back, the indent depth is ≥ 0.65 mm.

Two different punches are manufactured, one of length 44 mm for the middle arm of the frame in the plate and another of length 52 mm for the two other arms of the frame.

The vacuum chuck for attaching ARClear® 8154

A vacuum chuck has been manufactured from 5 mm thick PMMA plate to hold the ARclear® 8154 adhesive for attaching to the plate as shown in Figure 5.33. The chuck has matching holes so that it can be aligned with the plate on the bending jig using the dowel pins and transfer the adhesive by holding and releasing vacuum exactly on the frame.

(a)   (b)   (c)
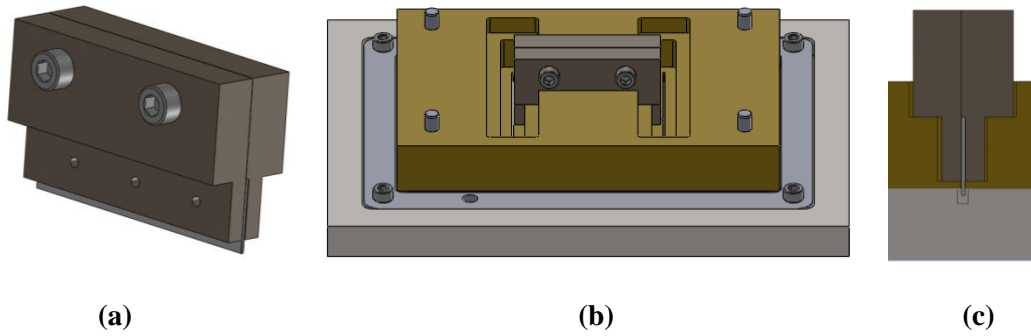
Figure 5.32: (a)The punch. It consists of three parts, a stainless steel blade of width 500 μm held between two aluminium pieces. The aluminium pieces keep the blade vertical and provides a punch-stop while bending the plate as shown in (b) and (c).
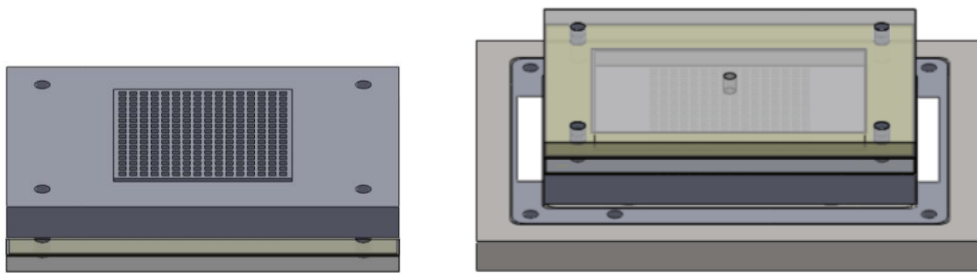
Figure 5.33: The vacuum chuck made of PMMA for placing ARclear® 8154 adhesive on the frame region of the mother plate. The alignment to the frame region is achieved by using the dowel pins in the bending jig to align the chuck.

(a)   (b)

| Piston | Bending jig | Support frame | Piston guide | Mylar | Aluminium |

(c)   (d)
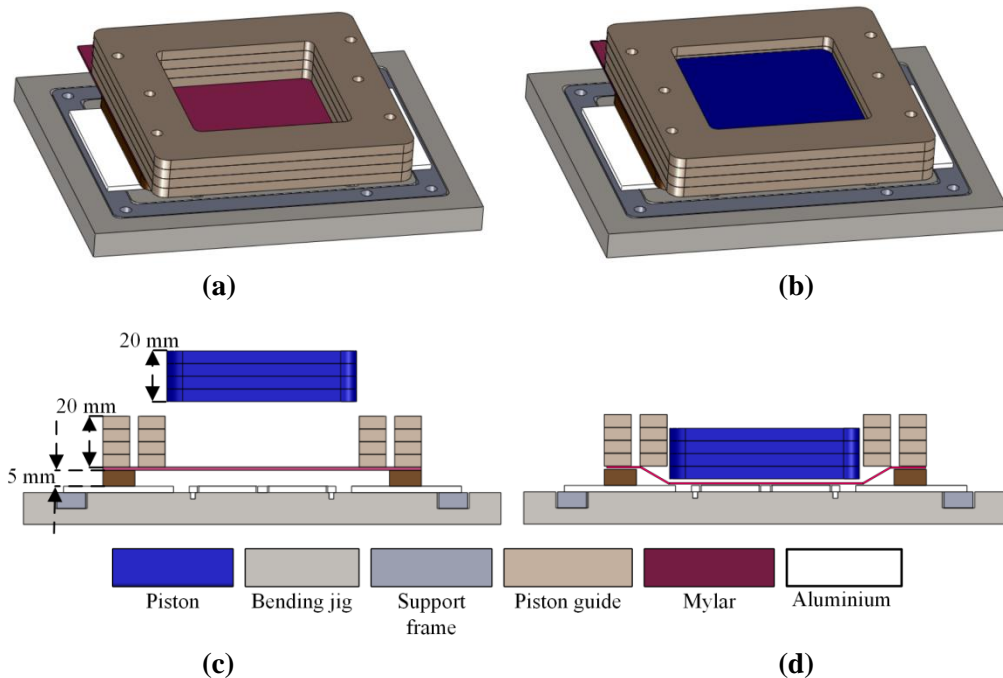
Figure 5.34: Mylar placement jigs and process. The thickness of aluminium plate and Mylar film are scaled up for visualization. (a) Placement of the piston guide and the Mylar attachment frame on the bending jig. (b) Piston is guided and pushed though the guide jig to stretch Mylar and attach to the aluminium plate. (c) and (d) Cross-section of the processes.

Parts for attaching pre-stretched Mylar

As mentioned in the beginning of section 5.5, Mylar attachment needs critical attention to keep it pre-stretched during attachment. To do this, first, the same vacuum chuck is used to hold Mylar and manually keep it as flat as possible. Then, this flat Mylar membrane is transferred and stuck to a rectangular frame using kapton tape along its border. This frame has matching holes to align with the dowel pins in the bending jig through which the Mylar film is kept at a height 5 mm from the plate as shown in Figure 5.34 (a) and (c). To attach Mylar on the plate, a piston is made by stacking four pieces of 5 mm thick PMMA plates which can push the Mylar down and attach it to the ARclear® 8154 adhesive on the plate. Since the edges of the Mylar film are stuck to the 5 mm thick frame, this process stretches Mylar while attaching. Initial experiments had been performed with different thicknesses of this frame between 2 mm and 5 mm and the 5 mm initial gap between the plate and the Mylar film is observed to produce best pre-stretched Mylar attachment. However, in order to keep the piston vertical during pushing Mylar down, another guide is made with PMMA plate such that the opening in the guide allows only vertical movement of the piston as shown in Figure 5.34 (b) and (d).

5.5.2.   Plate manufacturing steps

1. The plate manufacturing process starts with clamping the support frame on the bending jig with screws and placing the aluminium mother-plate on the jig. The aluminium plate is stuck to the support frame using conductive tape and to the bending jig using kapton tape as shown in Figure 5.35 (a). The location of the kapton tape between the plate and the bottom-jig is such that after cutting the plate, the cut out plate can be released from the bottom jig while attached on the support frame and the extra material remains on the bottom-jig.

2. Then using the guide jig and the punches the plate is bent into the grooves in the bending jig as shown in Figure 5.35 (b) and (c). The punch is pressed using a punching press and the guide jig provides hard stop for the punch once the depth of 0.8 mm is achieved.

3. Then using the vacuum chuck as described in section 5.5.1, ARclear® 8154 adhesive is transferred to the frame region that is bent. A pre-cut ARclear®8154 piece of size 50 mm × 50 mm with the contact aperture is held with the vacuum chuck and using the dowel pins as aligner, it is transferred to the plate as shown in Figure 5.35 (d).

4. The next step is to cut the plate using a laser cutter. In Figure 5.35 (e), the CAD-drawing for cutting the aluminium plate is shown. It is to be noted that the cutting takes place on aluminium on the spring regions and on aluminium and ARclear® 8154 layer on the frame region. There are four 90° corners in the drawing to align it with the four 90° sharp corners drilled in the bending jig. The small 2 mm × 2 mm region near the centre is also aligned with the centre of the 2 mm diameter hole in the ARclear®8154 so that conducting surface of aluminium is accessible through this hole. The top protective layer of ARclear® 8154 is removed before cutting the plate, because after cutting the thin arms of the frame, the removal of ARclear® 8154 without damaging the arms is difficult. As discussed before, the laser cutting process ablates the aluminium with approximately 40 μm cut-width; the CAD-drawing has

been modified accordingly to compensate for this error to reduce uncertainty in the widths of different sections of the manufactured plate.

5. After completion of the cutting, the extra aluminium and ARclear® 8154 is easily removed by removing the kapton tape from the bending jig. As a result, only the cut frame with the springs is left on the jig, attached to the support frame with conductive tape.

6. The next step is to attach Mylar film on the frame. First, using the vacuum chuck, Mylar is transferred to a pre-stretching frame as discussed before and then using the piston guide and the piston as shown in Figure 5.35 (b) and (d), Mylar is pushed down to stick to the adhesive. After attachment, the piston guide is removed keeping the piston in place and the edges of the attached Mylar film is cut as shown in Figure 5.35 (g). The Mylar film stays attached to the frame and is thus released from the pre-stretching jig.

7. Finally, another laser cut for Mylar gives it the square shape on the frame with a 2 mm diameter circular aperture aligned with the aperture in ARclear® 8154. A small drop of EPO-TEK® H20S (Two parts mixed 1:1) is used at the aperture to make electrical contact between the metalized side of Mylar film and the aluminium frame and cured at 80°C for 90 minutes [172]. Finally the support frame is unbolted from the bending jig to release the plate with the support frame as shown in Figure 5.35 (h). However, for initial characterization of the plates, the epoxy has not been applied. The epoxy application is done on the plates only when a conductive plate is required for intercepting charged particles, such as in Chapter 7 for electrospray propulsion device.

The first plate was manufactured at Reconfigurable Robotics Lab, EPFL, Lausanne (rrl.epfl.ch) with the help of Amir Firouzeh for checking feasibility of the process steps. Later on, rest of the plates have been manufactured at He-Arc at La Chaux-de-Fonds, Neuchatel, (http://www.he-arc.ch).

In Figure 5.36 (a), an image of the Plate 2 after bending in the jig and applying ARclear® 8154 but before cutting is shown. The small circle close to its centre is the aperture for electrical contact. In Figure 5.36 (b), the image of a manufactured plate with Mylar attachment is shown. In Figure 5.36 (c), microscopic image of one of the indents in Plate 2 is shown. For comparison with the expected semi-circular shape, a circle is drawn on the figure with a radius five times the thickness of the plate. The shape of the indent shows that the edges of the indent do not have the perfect zero radius of curvature as expected; but the depth of the indent is nearly 50 μm more than the assumed value of $5h$. This is because the height of the punch to bend the plate was 0.8 mm, 0.15 mm more than the $5h$ value to account for spring back. The non-zero radius of curvature at the indent edges is expected to reduce the stiffness of the frame from the simulated and analysed values; on the other hand the increase in indent depth is expected to increase the stiffness, as more material is located away from the neutral axis of the plate. It is also observed that the fine structures in the plate are slightly bent during laser cutting process and the overall plate is slightly buckled. Therefore, characterization of the plate is essential to find its natural frequency and spring constant in order to estimate its performance as the particle intercepting plate.

(a)

(b)

(c)

(d)

(e)

(f)

(g)

(h)
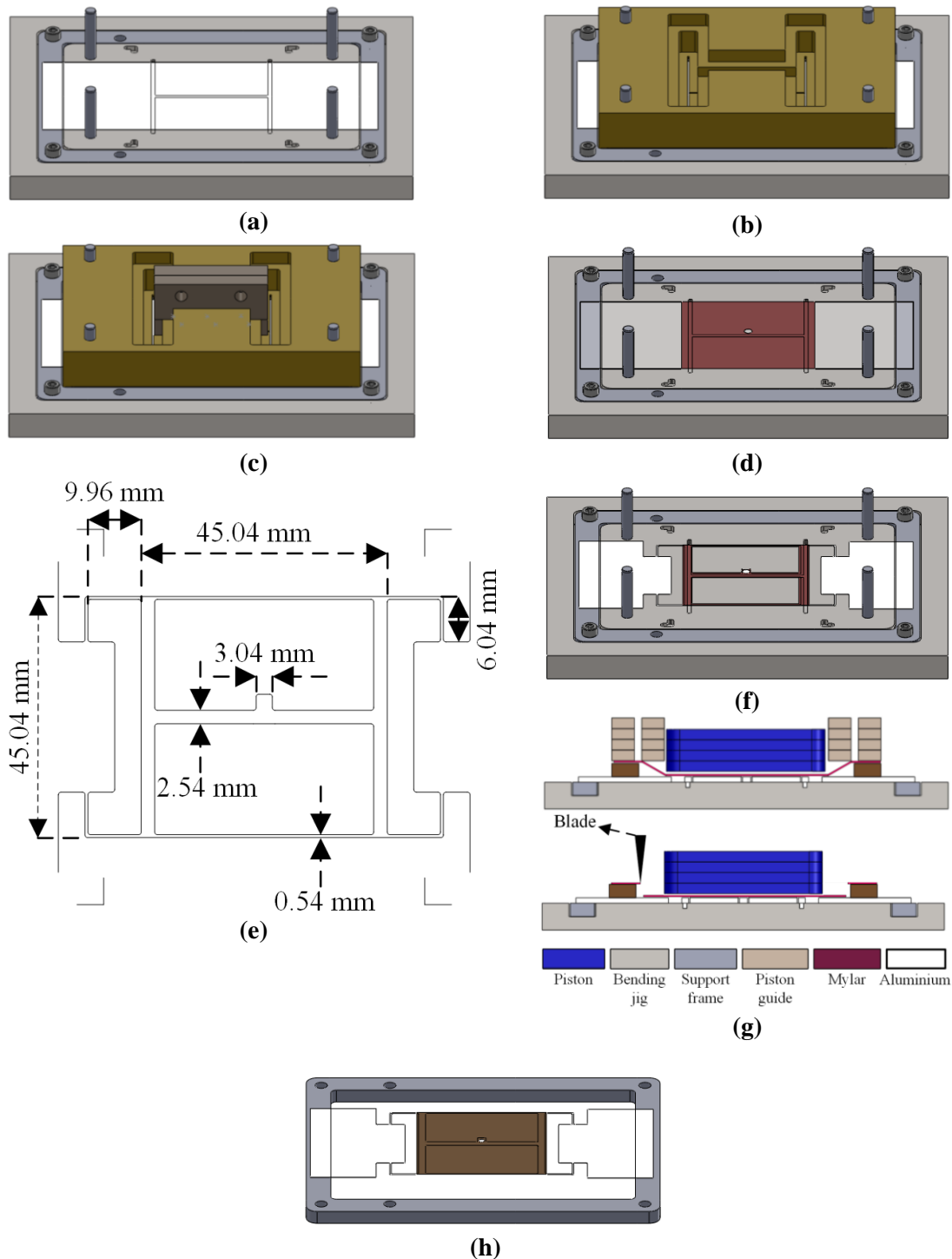
Figure 5.35: Plate manufacturing process steps. (a) Aluminium mother plate stuck on the bending jig and the support frame. (b) Punch guide jig aligned with the dowel pins to sandwich the plate in between. (c) The punching process. The punch is pressed using a punching press. (d) Pre-cut ARclear® 8154 transferred to the plate using the vacuum chuck. Alignment achieved using th dowel pins. (e) The CAD-drawing for cutting aluminium plate. (f) After cutting, the extra aluminium stuck on the bending jig are removed. (g) Mylar attached on the frame and and cut with a blade to release it. (h) Another laser cut for Mylar to keep it only on the frame region and then releasing the final plate inercepting plate from the bending jig.

(a)   (b)   (c)
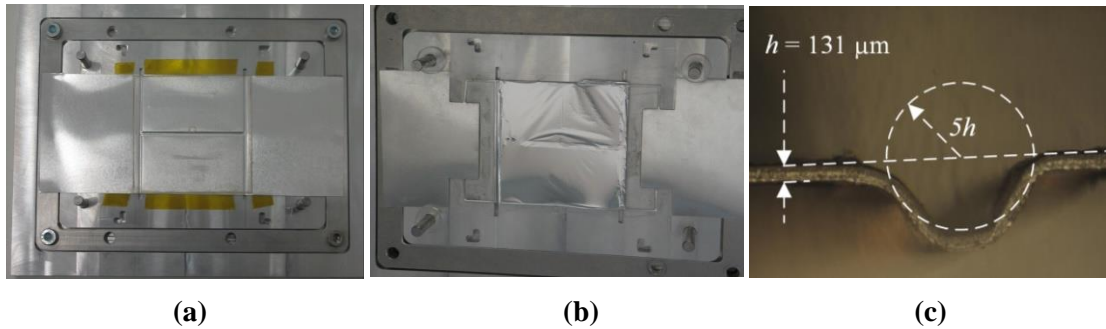
Figure 5.36: (a) Photograph of the plate with ARclear ® 8154 before cutting. (b)Photograph of the plate after cutting and applying Mylar. (c) Microscopic image of the indent in one of the arms of the frame in Plate 2, the second manufactured plate.

5.6.   Plate characterization

Five plates have been manufactured for performing experiments on thrust measurement. The following metrics are defined for characterizing the plate.

- **Spring constant:** The expected spring constant of the designed plate is 50.23 N/m when external force is applied at the centre of the plate. The spring constant along with the force resolution of the FT-S100 sensor gives the resolution of the thrust stand and the measurement of force. Therefore, spring constant measurement of the plate is an essential characterization metric.

- **Natural frequency:** The natural frequency of the plate is expected to be 82.56 Hz without epoxy EPO-TEK® H20S and 81.77 Hz with the epoxy. It must be noted that natural frequency measurements have been performed without the epoxy.

5.6.1.   Spring constant measurement

The spring constant measurement essentially involves either applying a force at the centre of the plate and measuring its deflection at the centre, or deflecting the plate by a known distance and measuring the reaction by a force sensor. One possible way to do this is to use the FT-S100 force sensor and the AG-LS25V6 translation stage to record the force vs. deflection. However, as mentioned before, the individual steps of the translation stage are not 100% repeatable and hence deflection of the plate cannot be accurately set using this. Therefore, translation stage with known steps should be used. With the available manual translation stages, a 10 μm minimum known step can be ensured. However, for a 10 μm deflection of the plate, the reaction force on the force sensor will be 502.3 μN if the plate has the desired spring constant of 50.23 N/m. This is beyond the range of the force sensor FT-S100.

Therefore, to measure spring constant of the plates, manual translation stage with a LRF-400 load cell from Futek [217] has been used. This load cell has a range of 10 mN and hence can accommodate larger deflection of the plate. The spring constant measurement setup is shown in Figure 5.37 (a) and (b) and the force vs. deflection of the plate has been measured for the five plates and plotted in Figure 5.37 (c). The calibration factor for the load cell has been included in the force measurement from its output voltage measured using Keithley 2000 multimeter in slow mode.
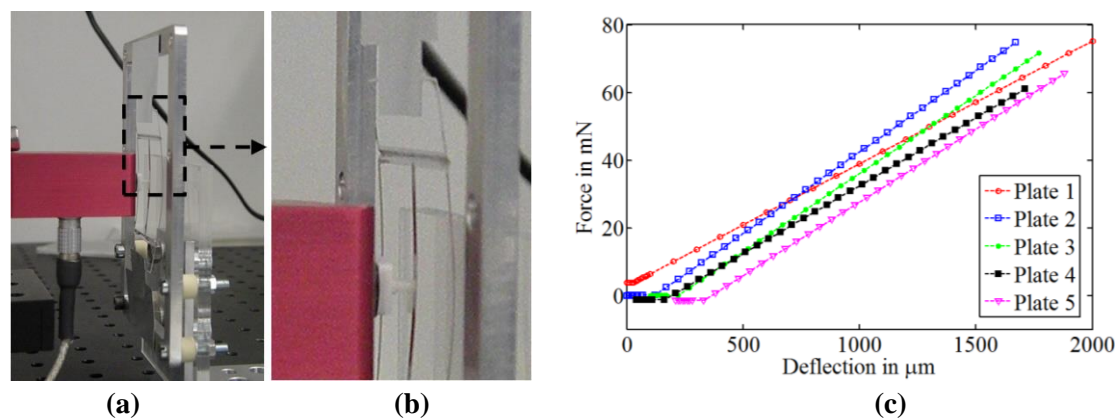
Figure 5.37: (a) Setup for measurement of spring constant of the plate with LRF-400 load cell. (b) Zoomed in view of a section of the deflected plate showing the deflection of the spring section and the frame section. (c) The force vs. deflection curves of the five plates. Spring constant is obtained from the slope of the curves.

The spring constant has been found out from the linear force vs. deflection curves using a linear fit in Matlab curve fitting tool with 95% confidence bounds. In Table 5.17, the spring constant results for the five plates are given. Based on the measured spring constants, the force resolution of the thrust stand can also be estimated from Eqn. (5.8) as tabulated.

Table 5.17: Simulated and Experimentally obtained spring constant of the manufactured plates

Simulated k_p (N/m)	Experimental		
	Plate	k_p (N/m)	**Expected F_{res} (nN)**
50.23	Plate 1	36.23 ± 0.01	8.62
	Plate 2	48.21 ± 0.01	9.82
	Plate 3	46.21 ± 0.01	9.62
	Plate 4	40.02 ± 0.01	9.00
	Plate 5	43.22 ± 0.01	9.32

It is found that the measured spring constant of the plates are within 20% of the expected spring constants for Plate 2 to Plate 5, although for the Plate 1, the value is nearly 30% less. The first plate, manufactured for checking feasibility of the manufacturing steps, was later abandoned for measuring thrust.

5.6.2.   Natural frequency measurement

Natural frequency measurement has been performed by measuring the step response of the plate using laser displacement sensor LK-H022 from Keyence [218]. The plate is dropped from 6 mm height after lifting its one side and the step response of the centre of the plate has been recorded using the laser displacement sensor with 10 μs sampling time for 2 s. The

displacement accuracy of measurement is 1 μm. From the transient displacement the oscillatory part $y(t)$ has been fitted as a function of time t to the following expression of damped oscillation using Matlab curve fitting tool with 95% confidence bounds.

$$y(t) = B + Ae^{-2\pi\gamma f_p t} \sin\left[2\pi f_p \sqrt{(1-\gamma^2)}t + \Phi\right] \qquad (5.30)$$

where A, γ and Φ are the amplitude of vibration, damping ratio and phase respectively and B is the final displacement read by the displacement sensor as the plate comes to a steady state. In Figure 5.38 (a), the experimental setup for the measurement is shown. The height of the laser head is adjusted to keep the displacement of the centre of the plate within the ± 3 mm range of the laser displacement sensor. In Figure 5.38 (b), the oscillation $y(t)$ derived from the step response and the curve-fitted plot are shown. The actual transient response over 2 s is shown in the inset of Figure 5.38 (b).

For the Plate 2, natural frequency is measured before and after attaching Mylar, however, for the other plates, natural frequency has been measured with Mylar.
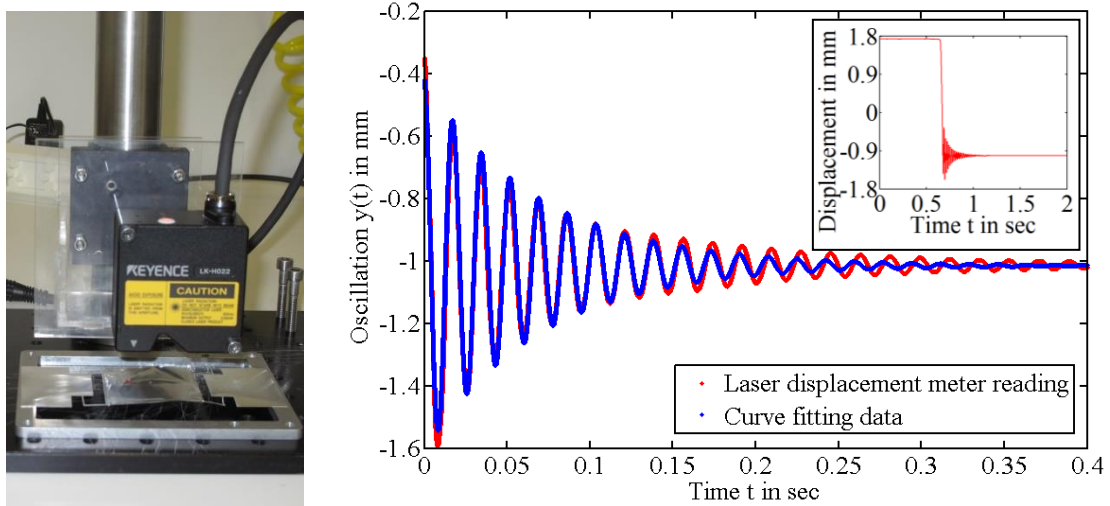
Figure 5.38: (a) Setup for natural frequency measurement of the manufactured plates. (b) Oscillatory part of the step response of the plate recorded by the laser displacement meter to find the natural frequency using curve-fitting. The transient response over 2 s recording time is shown in the inset of (b)

In Table 5.18, the obtained values of f_p and γ are listed for the five plates. The uncertainties over the mean f_p and γ in Table 5.18 are obtained from the standard deviation in three successive measurements for each plate. It is observed that the natural frequency of the plates with Mylar is within 50−60 Hz which is in the desired range. For the Plate 2, natural frequency has been measured without and with Mylar and Mylar attachment reduced the natural frequency by 26% for Plate 2 although the expected reduction was 12% from Table 5.16. It can be seen in Table 5.16 that the expected fractional decrease in natural frequency is estimated as $0.5 \times \delta M/M_{fr}$ in Table 5.16, i.e. from the fractional increase in mass of the frame due to the springs, ARclear® 8154 adhesive, Mylar, and the two additional stiffening beams on the frame. Metallization on the Mylar film has not been considered in the calculation of mass of the Mylar film, which is only 16.6% of the total change in mass; however, from the sheet resistance of the metalized Mylar film, the thickness of the aluminium film can be

calculated to be 20 nm and inclusion of the mass of the aluminium metallization increases ratio $\delta M/M_{fr}$ only by 0.1%. The damping ratio increases by nearly an order of magnitude due to attachment of Mylar as seen in Table 5.18 for Plate 2, which is due to large area for air damping; however, this one order of magnitude increase in damping ratio reduces the natural frequency only by 0.5%. The most significant contribution to $\delta M/M_{fr}$ is due to the mass of the aluminium springs and the two additional stiffening arms. The discrepancy between measured fractional change in natural frequency with $0.5 \times \delta M/M_{fr}$ is most likely due to inaccuracy in the assumed fractional frequency change as $0.5 \times \delta M/M_{fr}$. It can be noticed that the springs of the particle intercepting plate are a combination of a translational spring and an orthogonally placed torsional spring and the natural frequency may not scale as $M^{-1/2}$ where M is the total mass of the particle intercepting plate including the springs.

However, the experimentally measured natural frequency is in the desired range for the plates except the Plate 1 and hence the plate, Plate 2, has been initially assembled in the thrust stand for characterization of the thrust stand, which is discussed in Chapter 6.

Table 5.18: Simulated and experimentally obtained natural frequency of the manufactured plates

Expected		Experimental			
Mylar	f_p **(Hz)**	**Plate**	**Mylar**	f_p **(Hz)**	γ
		Plate 1	Yes	47.71 ± 0.02	$(4.12 \pm 0.08)\times10^{-2}$
No	93.45	Plate 2	No	79.63 ± 0.05	$(4.43 \pm 0.02)\times10^{-3}$
Yes[*]	82.56		Yes	58.21 ± 0.03	$(9.83 \pm 0.03)\times10^{-2}$
		Plate 3	Yes	57.54 ± 0.03	$(11.11 \pm 0.02)\times10^{-2}$
		Plate 4	Yes	51.24 ± 0.04	$(16.22 \pm 0.06)\times10^{-2}$
		Plate 5	Yes	56.67 ± 0.06	$(8.73 \pm 0.03)\times10^{-2}$

[*] Expected natural frequency without epoxy, as displayed in Table 5.16

5.7. The thrust stand assembly

After manufacturing and characterization of the plates, Plate 2 is directly mounted on the thrust stand along with the support frame. The Figure 5.39 shows the schematic (a) and picture (b) of the thrust stand without the gate electrodes.

As current measurement on the plate is desired, 4 mm long ceramic stand-offs have been used between the support frame and the stand in order to avoid electrical contact. Since the plate is attached to the support frame only with conductive tape, a pair of aluminium frame-clamps, as shown in the figure, is used to further clamp the plate into the support frame using M2 set screws. To rigidly clamp the support frame to the stand, additional aluminium side walls have been manufactured and placed as shown.

(a)   (b)
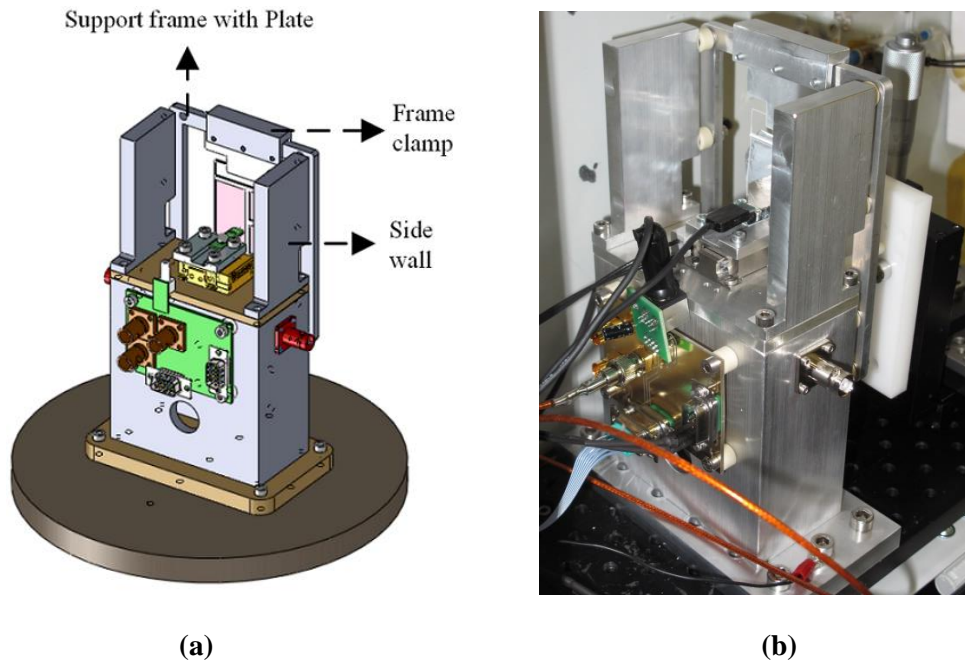
Figure 5.39: (a) 3-D drawing of the thrust stand with the plate placed in front of the force sensor. The gate electrode assembly for synchronous detection of thrust from electrospray thrusters is not shown in this diagram as they will be discussed in Chapter 7. The rest of the components are explained in Figure 5.11. (b) The picture of the working thrust stand.

5.8. Summary

The thrust stand described in this chapter works on the principle of measuring force on a suspended plate due to impact of emitted particles from a microthruster by a force sensor. The square shaped particle intercepting plate of size 45 mm $\times$ 45 mm can intercept up to 40° emission half-angle of the plume if placed 3 cm away from the thruster. The design methodology and fabrication method of the plate has been explained and the parts of the thrust stand have been discussed. Detailed design approach for the particle intercepting plate has been provided in this chapter to achieve a spring constant less than 50 N/m and natural frequency above 50 Hz. Depending on the measured spring constant of the manufactured plates, it can be concluded that the thrust stand can potentially resolve ~ 10 nN differences in force on the plate for up to more than 100 μN range. The natural frequency of the manufactured plates is experimentally obtained to be above 50 Hz, and hence the operation of the thrust stand is expected to be benign to external disturbances. Based on the simulation results, the expected accuracy of the thrust stand is estimated to be 95% depending on the location of the thruster and spot size of the plume on the plate as long as the entire plume is captured on the plate. The thrust stand can potentially adapt to different types of microthrusters as the thruster is not directly mounted on the thrust stand. The thrust range can be easily scaled up simply by replacing the FT-S100 force sensor by FT-S1000, FT-S10000 or FT-S100000 force sensors with higher force ranges from the same manufacturer with identical mechanical structure and interfaces, but, at the cost of lower resolution [202].

However, the main drawback of the thrust stand is that accurate estimate of the thrust depends on knowledge of the impingement force on the plate by the emitted particles and the thrust on the thruster, which depends on the emission characteristics. Therefore, uncertainty in the

relation will lead to increased inaccuracy in the thrust measurement. These issues will be discussed in Chapter 6 and Chapter 7 while characterizing the thrust stand for two different types of thrust generating devices, 1. A sub-sonic cold-gas ejecting capillary in Chapter 6 and 2. An ionic liquid electrospray propulsion device in Chapter 7.

6 Atmospheric characterization of the thrust stand with a cold-gas ejector

In this chapter, the characterization results on the performance of the thrust stand are discussed. It has been described in the previous chapter that the thrust stand can potentially resolve 10 nN thrust within the range 0–100 µN or above (depending on F_{OFF}, Eqn. 5.9) by intercepting the emitted particles from a microthruster. The natural frequency of the plate is slightly above 50 Hz which is expected to be safe in order not to excite resonance under facility vibrations. Depending on the spot-size and the location of the spot of the emitted particles on the plate, the inaccuracy of measurement can be around 5% as discussed in section 5.4. In this chapter, the performance of the thrust stand is experimentally verified with the help of a cold-air emitter made from silica capillary which is discussed in detail in section 6.1.2. The force on the plate has been measured in air by changing its inlet air-pressure. It has been shown that although a large drift in the measured thrust over time is observed in steady state measurement in section 6.2.2, by homodyne detection scheme with a lock-in amplifier, a 10 nN thrust resolution is achieved which is described in section 6.4. The spot-size and location related inaccuracy in the measurements has been estimated by changing the lateral position and distance of the capillary-head with respect to the centre of the plate in section 6.4.5 and the inaccuracy has been estimated to be around 11% which limits the accuracy of thrust measurement of the thrust stand. Finally, the force on the plate has been compared to direct thrust measurement by mounting an air-ejector on a load-cell in section 6.5.

6.1. Thrust stand characterization setup

For atmospheric characterization of the thrust stand with a cold-gas ejecting capillary a few modifications have been made on the thrust stand first from an otherwise designed setup for using it inside the vacuum chamber discussed in section 5.2 in Chapter 5.

6.1.1. Adjustments in the thrust stand for atmospheric characterization

In Figure 6.1 an image of the thrust-stand in the atmospheric characterization setup is shown. A schematic of the setup is shown in Figure 6.1 (b) showing the mechanical and electrical feed-through.

- Instead of mounting the thrust stand on the ISO-160 flange for vacuum chamber as discussed in section 5.2 in Chapter 5, it is mounted on an optical breadboard using an aluminium base-plate. The aluminium stand of the thrust stand with the PCB is mounted on the base-plate using M4 screws underneath the stand and the base-plate is then bolted on the optical breadboard.

- A plastic box has been modified to enclose the thrust stand. The purpose of the box is to avoid undesired air-flow on the plate. Holes have been made in the box in order to

provide electrical feed-through into the box from outside to connect to the thrust stand. The lid of the box is optically transparent and facing sidewise so that visual observation is possible during the experiments as shown in Figure 6.1 (a) and 6.1 (b). The box is 600 mm long, 400 mm wide and 220 mm high.

- In order to avoid mechanical coupling between the large box and the thrust stand, four additional holes have been made on the shorter wall of the box and four 10 cm long optical posts have been connected to the optical breadboard through these holes without direct physical contact with the box as shown in Figure 6.1 (b). The box and the thrust stand inside it are thus mounted on different posts without any direct mechanical contact.

- In order to avoid movement of the cables and feed-through to the thrust stand, all the cables coming out of the thrust stand are clamped in two stages before connecting to the instruments such that any movement on the instrument end of the cables do not induce motion in the thrust stand ends. A small plastic box is mounted on the wall of the box to assemble the feed-through to the force sensor and the translation stage as shown in Figure 6.1 (b).

- Finally, the entire setup is assembled on an Accurion Halcyonics micro series [219] vibration isolation table which provides good vertical and horizontal vibration isolation from as low as 0.6 Hz. This enables comparison of the noise floor in the measurements with and without vibration isolation from the environment.
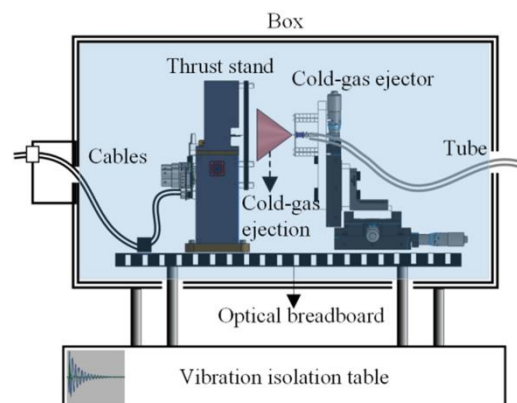
| (a) | (b) |

Figure 6.1: (a) Image of the thrust stand for atmospheric characterization. The thrust stand is installed inside a plastic box on a vibration isolation table. Later, the thrust stand has been isolated from the box using another four posts. The four posts for separating the thrust stand from the box are not shown in this figure. (b) A schematic of the atmospheric characterization setup showing the thrust stand and the capillary cold-gas ejector. The thrust stand is mounted on an optical breadboard which is mechanically isolated from the box. For electrical and air feed-though, holes have been made on the box.

6.1.2. Capillary cold-gas ejector setup

The cold-gas ejector is a 150 μm inner diameter and 360 μm outer diameter fused silica capillary emitting nitrogen at room temperature as shown in Figure 6.2 (a) and (b). Several

capillaries of length (18.0 ± 0.1) mm have been cut from a long capillary using Shortix capillary column cutter [220]. This is the minimum length that can be cut using the capillary cutter with repeatable length by looking through a microscope. The capillary is attached with a 1 mm inner diameter and 3 mm outer diameter soft tube using nano-port assembly as shown in Figure 6.3 (a), (b) and (c). The soft-tubing is connected to the output channel of a Fluigent MFCS-8C microfluidic controller [221] as shown in Figure 6.3 (c). The pressure controller can produce 0−1000 mBar positive pressure from ambient with feedback-control with less than 1 sec settling time. A schematic of the assembly is shown in Figure 6.3 (d). The pressure output from the pressure controller can be set to a desired value and the measured pressure can be monitored either from the dedicated software interface for the instrument, or by using the Fluigent Matlab toolkit which can be linked with instrument control and automation scripts for other measurement setups.

(a)   (b)
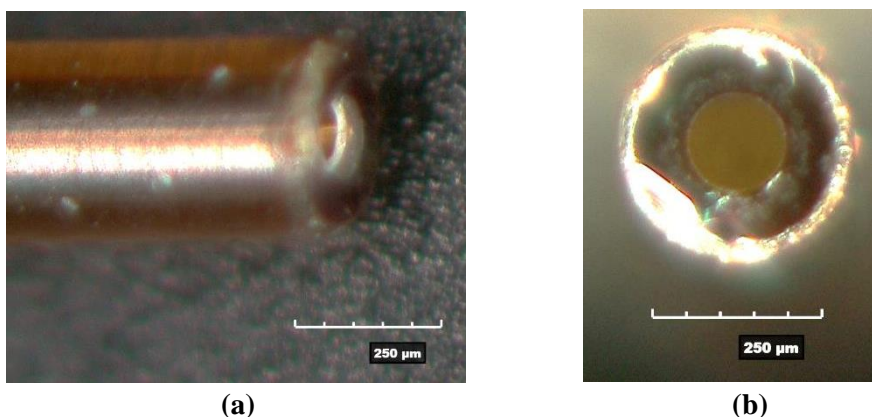
Figure 6.2: Fused silica capillary used as cold-gas ejector for atmospheric characterization of the thrust-stand. Inner diameter 150 μm and outer diameter 360 μm.

6.1.3. Expected thrust from the capillary cold-gas ejector

The capillary cold-gas ejector in principle is an un-optimized cold-gas thruster that generates thrust by ejecting cold nitrogen fed to its inlet. Thrust analysis of the cold-gas ejecting capillary is beyond the scope of the thesis and the capillary is not an optimized cold-gas thruster which usually consists of a converging-diverging nozzle [222], [223]. However, a simple analytical approach towards understanding the thrust generated by the capillary under applied inlet pressure is presented in this section followed by an approximate relation between the thrust on the capillary and the force on the particle intercepting plate due to the impinging jet.

The jet emitted from the capillary has been theoretically and experimentally analyzed in many research articles before [224]–[229]. In Figure 6.4, a schematic of the impinging jet and the different zones of the flow are shown from Ref. [227]. The impinging jet consists of a developing flow-zone of the jet, typically of a height of six nozzle diameters [227], [228], where air from the surrounding is entrained into the jet and the centre-line jet velocity equals the nozzle exit velocity. Further away from the emission plane, the axial velocity of the jet approaches a uniform value due to spreading of the jet. In the vicinity of the impingement plane, typically within one to two nozzle diameter distances from the plane, the jet loses axial velocity rapidly with corresponding increase in static pressure. Within this wall-jet region, the jet flow is predominantly transverse.

(a)

(b)

(c)

(d)
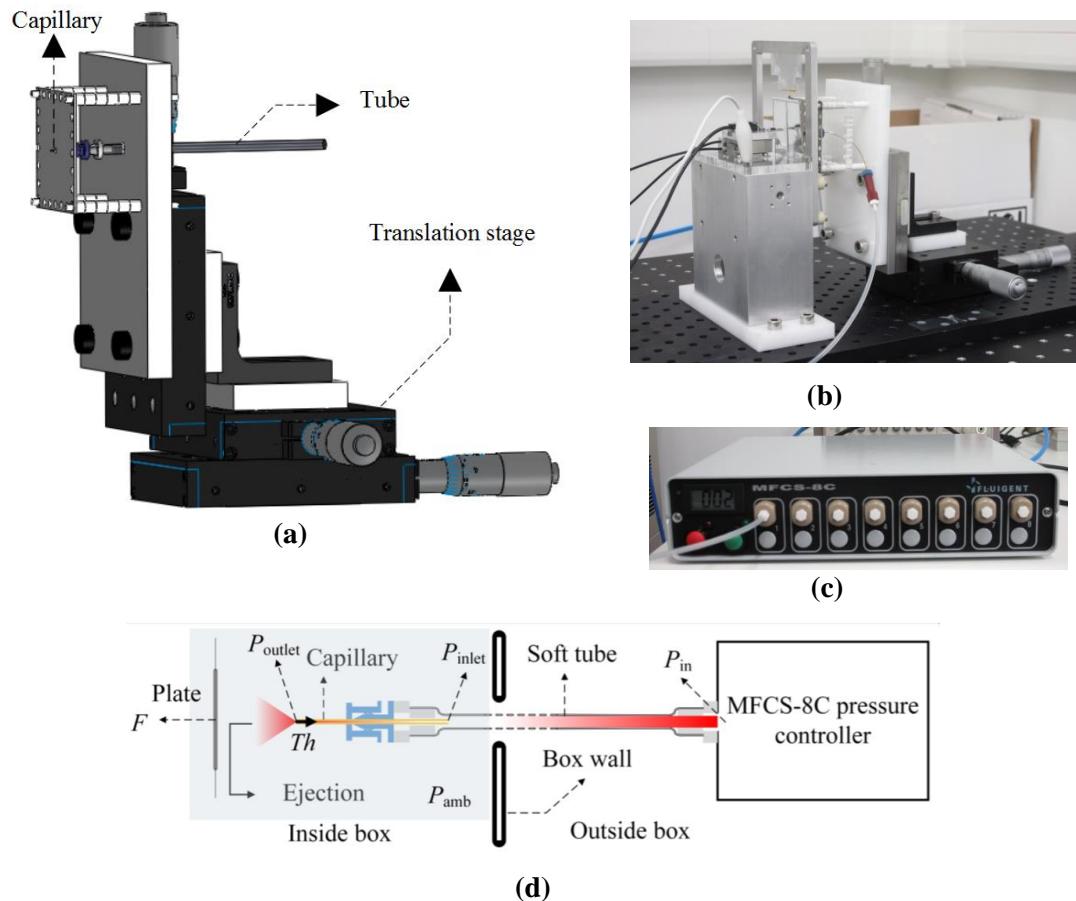
Figure 6.3: (a) Schematic of the cold-gas ejector assembly. It consists of a fused silica capillary and a soft tube that is connected to a pressure controller MFCS-8C. The assembly is mounted on three translation stages for three-axis movement of the capillary ejector with respect to the particle intercepting plate. (b) An image of the cold-gas ejector in front of the particle intercepting plate in the thrust stand. (c) An image of the pressure controller. Soft tube attached to the channel applies pressure to the inlet of the fused silica capillary. (d) A schematic of the tubing connection. The soft tube from the pressure controller enters the plastic box through a hole made in it and is attached to the capillary ejecting cold-gas.
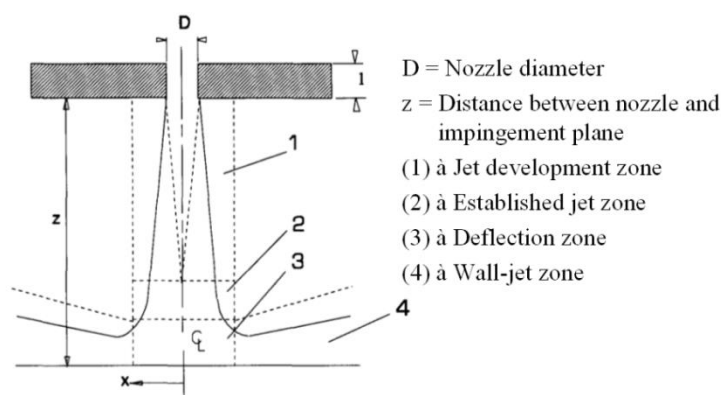
Figure 6.4: Schematic of the flow regions of an impinging jet taken from Ref. [226]. The impinging plane is the plane of the plane of the particle intercepting plate of the thrust stand, and the jet exit point is the capillary head ejecting cold-gas.

In the present case, the set pressure, P_{in}, at the pressure controller creates the jet of room-temperature nitrogen at the capillary outlet. Since the capillary cross-sectional area A_{cap} is much smaller than the inner cross-sectional area of the soft tube, it can be assumed that the soft tube provides much lower fluidic impedance in the flow of the gas than the glass capillary and pressure drop takes place in the capillary tube only due to viscous effects. If P_{inlet} and P_{outlet} are the pressures at the inlet and outlet of the capillary,

$$P_{inlet} \approx P_{in} \tag{6.1}$$

Pressure drop through the capillary is therefore

$$\Delta P = (P_{inlet} - P_{outlet}) = (P_{in} - P_{outlet}) \tag{6.2}$$

If the flow-velocity at the outlet of the capillary is v, the thrust generated can be written in most general form as [222]

$$Th = \dot{m}v + (P_{outlet} - P_0)A_{cap} \tag{6.3}$$

where $\dot{m}$ is the mass flow rate at the outlet, P_0 is the absolute ambient pressure. Under the condition, $P_{inlet} \approx P_{in}$, the Mach number, M_{inlet} at the inlet of the capillary can be found to be $M_{inlet}^2 << 1$ from analysis of isentropic flow of compressible fluid, details of which can be obtained in Ref. [230]. Under this condition, it can be shown that the flow through the capillary can be approximated as an incompressible flow [230] with a constant density ρ_0 and the pressure difference ΔP can be written in terms of a volume flow rate Q as

$$\Delta P = R_h Q \tag{6.4}$$

where R_h is defined as the hydraulic impedance of the capillary, and is a function of the dynamic viscosity of the cold-gas through the capillary, the distribution of velocity components in the capillary and the geometry of the capillary, and Q is related to the mass flow rate $\dot{m}$, density ρ_0, exit velocity v and area of the capillary A_{cap} as

$$Q = \frac{\dot{m}}{\rho_0} = A_{cap} v \tag{6.5}$$

Combining (6.4) and (6.5) it can be shown that

$$Th = \rho_0 A_{cap} v^2 + (P_{outlet} - P_0)A_{cap} = \left(\frac{\rho_0}{A_{cap} R_h^2}\right)(P_{in} - P_{outlet})^2 + (P_{outlet} - P_0)A_{cap} \tag{6.6}$$

This simplistic approach discussed above is based on many assumptions discussed during deriving the thrust expression. A more complete expression for the thrust can be obtained from Ref. [139] using Navier-Stokes equation as

$$Th = \int_{r=0}^{r_{cap}} \left[\rho v_z^2 + P - P_0 - \frac{4}{3}\mu \frac{\partial v_z}{\partial z} + \frac{2}{3}\frac{\mu}{r}\frac{\partial(rv_r)}{\partial r} \right] 2\pi r \, dr \tag{6.7}$$

where $v_z(r, z)$ and $v_r(r, z)$ are the axial and radial components of the local velocity of the fluid through the capillary, $P(r, z)$ is the local pressure, ρ and μ are density and dynamic viscosity

of the fluid and r_{cap} is the radius of the circular cross-section capillary, the integration being taken over the circular cross-section of the capillary at its tip. It can be noted that (6.7) reduces to the simple expression (6.6) derived here under the conditions that the flow of the cold-gas through the capillary is incompressible and unidirectional, i.e., $\rho = \rho_0$, constant density of the cold nitrogen, $v_z = v$, constant, and $v_r = 0$ and $P = P_{outlet}$ does not have a distribution across the radial direction at the capillary tip, the assumptions already made in deriving (6.6). In general, these conditions may or may not be valid in particularly the present problem and details of the validity of these assumptions are beyond the scope of the thesis. As a consequence, comparison of the calculated thrust from the capillary and experimentally obtained value in this chapter is not attempted by evaluating R_h. However, for sub-sonic flow, since there are no shocks or expansion waves, it can be assumed that $P_{outlet} = P_0$ [229] and hence,

$$Th = \frac{\rho_0}{A_{cap} R_h^2} (P_{in} - P_0)^2 \tag{6.8}$$

The relation in (6.8) indicates that the thrust on the capillary head is expected to follow a parabolic variation with the pressure difference across the capillary.

A comparison has been made in [139] between thrust at the thruster-head and impingement force on a plate due to the ejected jet. It has been shown that, under certain conditions, which may or may not be valid in general, the thrust at the thruster-head and the force on a plate intercepting the emitted particles are same. The thrust at the capillary tip and the force on the plate have been computed numerically in Ref. [139] and it has been found that for cold nitrogen emission in atmospheric conditions, the two produce the same value. Experimental results in [139] show that the impinging force measured on the plate is constant over a distance approximately from 10−150 times the throat diameter of the thruster. Comparison of the impinging force and generated thrust has been performed in [140] as well, in which collision of the impinging particles with the plate has been considered for measuring thrust with a plate. Experimental results with cold xenon and cold argon emission at room temperature have shown very good agreement between the calculated generated thrust and the thrust measured on the plate. In [231], comparisons of thrust and impingement force have been performed at sea-level for different Mach numbers of emission from helium and air and it has been shown that for sub-sonic Mach numbers, the ratio is close to unity.

In [231], the relation between thrust Th and the impingement force F has been written in terms of the coefficient of restitution $_|K_|$ as

$$Th = \frac{1}{(1 + _|K_|)} F \tag{6.9}$$

by considering collision of the impinging particles on the plate, where $0 \leq {}_|K_| \leq 1$. For a sub-sonic jet impinging on the particle intercepting plate and transforming into a lateral wall-jet, the normal component of the jet velocity in the wall-jet region can be negligible, leading to $_|K_|$ ≈ 0 which is congruent with the experimental observations described in the last paragraph. From all these observations, it can be concluded that under the experimental conditions in the present setup, the force on the plate, F and the thrust generated at the capillary head, Th, are same, i.e.,

$$F = Th \tag{6.10}$$

6.2. Initial experiments

In this section, initial experiments on characterization of the thrust stand using the capillary cold-gas ejector are presented. First, force measurement on the plate has been performed without any applied pressure at the capillary and by measuring the force sensor output under the different conditions as discussed below. At this point, the expression of thrust measured by the force sensor can be recalled from Chapter 5 for quick reference.

$$Th = F = \left(1 + \frac{k_p}{k_f}\right)(F_{meas} - F_{OFF}) = \left(1 + \frac{k_p}{k_f}\right)S_F V_\Delta \tag{5.7}$$

where S_F is the sensitivity of the force sensor FT-S100, defined in Table 5.6. V_Δ is the differential output corresponding to the applied force F on the plate, i.e. the output voltage difference between two conditions:

1. The force sensor is pushing on the plate and no external thrust is applied

2. The thrust is applied on the plate while the sensor pushes on the plate.

If V_{NL} is the no-load voltage output of the force sensor, i.e. the output with no force is applied on the horizontally mounted sensor and V_{OFF} is the voltage output when the force sensor is in contact with the plate with a force F_{OFF},

$$F_{OFF} = S_F(V_{NL} - V_{OFF}) \tag{6.11}$$

When an additional force F, corresponding to the thrust Th is applied on the plate, the force sensor output is V_{meas} given by

$$F_{meas} = S_F(V_{NL} - V_{meas}) \tag{6.12}$$

Therefore the differential force can be written as

$$F_d = S_F(V_{OFF} - V_{meas}) = S_F V_\Delta \tag{6.13}$$

And hence

$$F = \left(1 + \frac{k_p}{k_f}\right)F_d \tag{6.14}$$

These equations can be easily looked upon by referring to section 5.2.1; however, for quick reference to the measurement, these expressions have been listed here. Here, k_p and k_f are the spring constants of the particle intercepting plate and the force sensor FT-S100 respectively. S_F is typically 50 µN/V [199], however, individual force sensors are calibrated by the manufacturer and the actual value of the sensitivity of the particular devices purchased for the thrust stand development are provided in Table 6.1. The measured spring constant k_p of five manufactured plates have been listed in Table 5.17 in Chapter 5. The spring constant of the force sensor FT-S100 is $k_f = 50$ N/m.

Table 6.1: List of FT-S100 force sensors and their sensitivity values provided by the manufacturer

FT-S100 manufacturer ID	FT-S100 lab-ID used for the thrust stand	Sensitivity S_F (μN/V)[*]
S100-140123 30	FEMTO-1	49.85
S100-140123 20	FEMTO-2	51.47
S100-140123 21	FEMTO-3	49.52
S100-140123 24	FEMTO-4	49.36
S100-140123 27	FEMTO-5	49.92

[*]Typical value as per datasheet = 50 μN/V. Individual device calibrated by the manufacturer.

Table 6.2: List of default parameters used for the atmospheric characterization of the thrust stand unless otherwise specified

	Property	Value
Force sensor	Lab ID	FEMTO-1
	Manufacturer ID	S100-140123 30
	Spring constant k_f	50 N/m[*]
	Sensitivity S_F	49.85 μN/V
Particle intercepting plate[@]	Plate ID	Plate 2
	Spring constant k_p	48.21 N/m
	Natural frequency f_p	58.21 Hz
	Vibration isolation	Enabled
	Box lid open/closed	Closed
	Laboratory environment	Normal[#]

[*] Value assumed for all the force sensors based on email communication.
[@] Refer to section 5.6 for details.
[#] A laminar flow-hood usually operating. A turbomolecular pump and a backing pump usually turned on for the vacuum chamber. Normal lab activities unrestricted.

For initial experiments, the sensor FEMTO-1 has been used and in the entire chapter, the lab-ID of the sensor is used instead of the manufacturer ID. The plate used for the experiments is Plate 2 unless otherwise mentioned specifically in this chapter, properties of which have been listed in Table 5.17 and 5.18. The vibration isolation is also enabled during the experiments unless otherwise mentioned. A summary of the default conditions mentioned above has been summarized in Table 6.2. The output voltage of the force sensor is monitored with Keithley 2000 multimeter [232]. A schematic of the initial experimental setup is shown in Figure 6.5. Another Keithley 2000 multimeter has been initially used for monitoring the power supply voltage for the force sensor. The force sensor output and the power supply have also been

monitored with two analog input channels of the NI-USB-6210 analog input system as well for later use. Additionally the force sensor output is also monitored using an oscilloscope (Lecroy wavesurfer 424 [233]). A signal generator Agilent 33220A [234] is also setup for optional use.
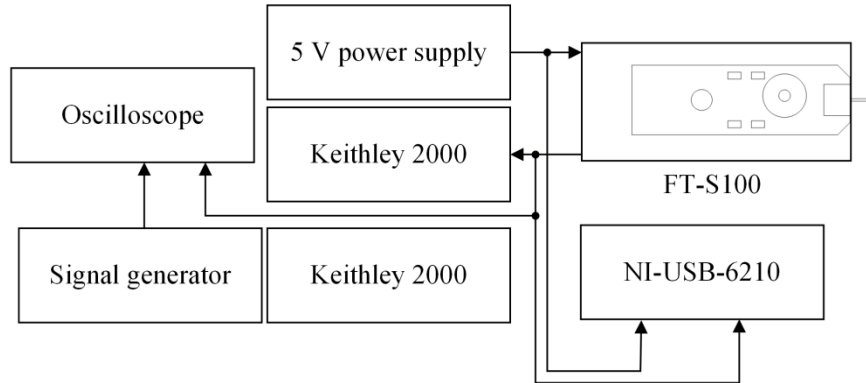
Figure 6.5: Schematic of the initial experimental setup for the thrust stand characterization. The FT-S100 probe is powered by a 5 V lab power supply. The output of the sensor and the power supply voltages are monitored with Keithley 2000 multimeters and two channels of NI-ISB-6210 analog input system. An oscilloscope is also connected to the output of the force sensor.

6.2.1. Force sensor output stability under constant force

Based on this initial setup, some general experiments on the stability of the force sensor output under constant force have been performed and conclusions have been drawn first, as listed below.

1. The force sensor's no-load voltage V_{NL} corresponding to $F_{OFF} = 0$ does not change by more than ± 200 µV over a duration of 1 hour if the power supply voltage fluctuation is within ± 1 mV.

2. The force sensor output does not change by more than ± 10 nN over 1 hour under constant force of around ± 10µN applied to it. For a constant force to be applied on the force sensor, the force sensor is mounted looking vertically upward and downward so that the weight of the force probe provides constant compressive and tensile force on the force sensor as shown in Figure 6.6.

The discussed results are summarized in Figure 6.7 (a) and 6.7 (b). The power supply voltage is typically stable within 1 mV. The response of the force sensor under a constant force suggests that the force measurement with the thrust stand by a continuously applied constant thrust can have around ± 10 nN noise floor peak to peak. Therefore, when an external force is applied on the plate and the multiplying factor $(1 + k_p/k_f)$ is incorporated in measurement of the applied force, the uncertainty in the force measurement can be $\sim \pm 20$ nN between successive samples as $k_p = 48.21$ N/m for Plate 2 and $k_f = 50$ N/m respectively. This uncertainty is twice as great as the resolution targeted to achieve, which was 10 nN.
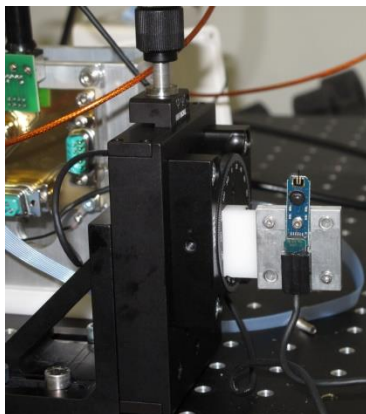
Figure 6.6: A picture of the FT-S100 force sensor (FEMTO-1) on a rotary stage for mounting the sensor looking vertically upward or downward. The weight of the sensor probe provides constant compressive or tensile force on the sensor to evaluate stability of the sensor output.
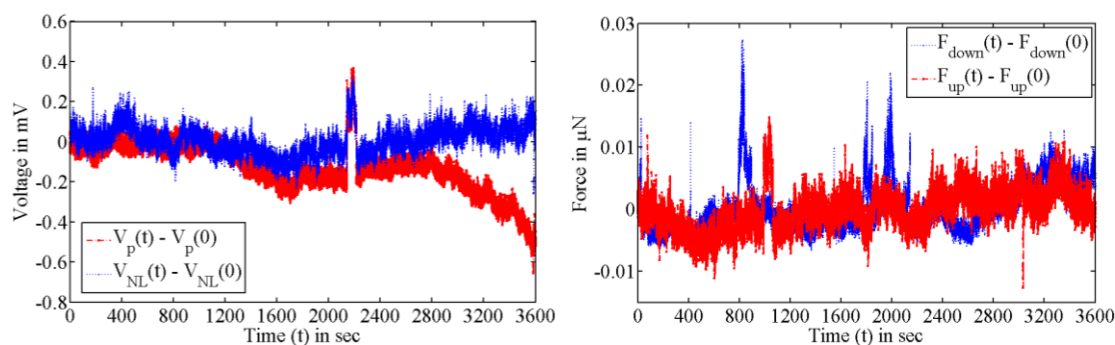
Figure 6.7: (a) Variation of the power supply voltage V_P and no load voltage V_{NL} with time by mounting the FEMTO-1 force sensor horizontally. The power supply and the output voltage are stable within ± 1 mV and ±200 µV typically. (b) Variation of the measured constant forces F_{up} and F_{down} with time for the force sensor FEMTO-1. These two forces are produced by placing the force sensor looking upward and downward respectively and using the weight of the sensor probe itself as compressive and tensile forces of the order of ±10 µN on the sensor.

6.2.2. Force sensor output with F_{OFF} from the plate

While the sensor output under a constant force is stable within ±10 nN, the force output from the sensor is seen to drift much more significantly while the spring force of the particle intercepting plate, F_{OFF}, is measured with it. For these experiments, the force sensor is approached towards the plate horizontally with the translation stage AG-LS25V6 and the output voltage of the sensor is monitored with the Keithley 2000 multimeter at each step until the force sensor output indicates that contact with the plate has been achieved and the force due to deflection of the plate is around between 30 µN and 60 µN. At this point, the translation is stopped and the force sensor output is monitored for 1 hour. The procedure is automated in Matlab (version 7.9) by reading the force sensor output from Keithley 2000 multimeter and commanding the translation stage to move one step with the minimum incremental motion until the measured output represents a force above 30 µN.

In Figure 6.8 the offset force measured using the Keithley 2000 multimeter in slow mode (200 ms integration time) for 1 hour duration is shown from two different experiments. It can

be seen that the measured force drifts by more than 10 μN over the duration of the experiments. Since the drift under a constant force has already been seen to be within ±10 nN, the origin of the large drift is attributable the rest of the mechanical and electrical assembly. Several experiments have been performed in order to find the reason and possibly eliminate the drift, and the conclusions are summarized below.
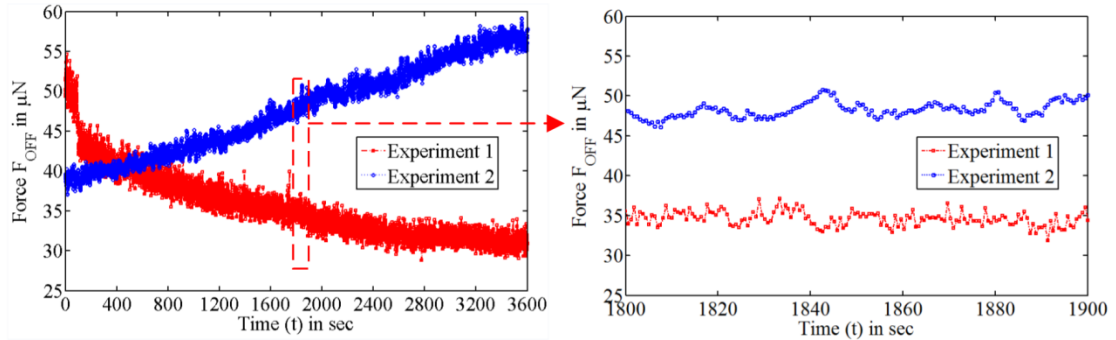
Figure 6.8: (a) Drift of the measured force F_{OFF} by the force sensor FEMTO-1 while pushing on the plate, Plate 2. Over 10 μN drift has been observed. (b) A zoomed-time detail of (a) shows sub-Hz noise in the measured output.

(a)   (b)
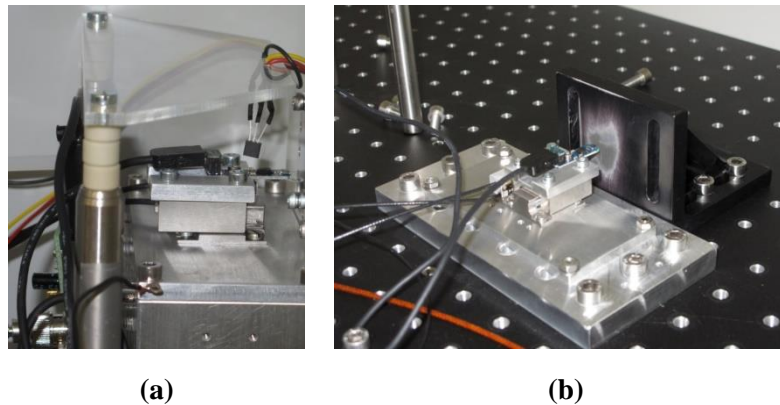
Figure 6.9: (a) A picture of the setup for monitoring the temperature in the vicinity of the force sensor while pushing on a plate. Linear temperature sensor MCP9700 [235] has been used for monitoring the change in temperature in tandem with the force sensor output. (b) A picture of the setup for measuring drift of the offset force by pushing on a rigid wall. In this setup, the possibility of air-flow as a source of drift can be ignored. However, large drifts have been observed in this setup as well, leading to the conclusion that non-ideal mechanical stiffness of the thrust stand is the most plausible reason for the drifts in the force sensor output.

1. The power supply fluctuations during the experiments are observed to be within 1 mV during all the experiments. In section 6.2.1 it is seen that the no-load voltage drift is less than ± 200 μV for up to 1 mV fluctuation in the power supply. It can be inferred that power supply voltage is not the source of the drift observed in F_{OFF}.

2. The temperature changes due to mechanical contact between the plate and the force sensor tip has been monitored in the vicinity of the force sensor using a MCP9700 linear temperature sensor [235] as shown in Figure 6.9 (a). The temperature change during the experiments has been found to be within 0.1 ^{o}C, which is common in the laboratory environment and no

significant contribution from heating the force sensor is observed. However, this does not conclusively provide information about local heating at the force sensor, if any.

3. The force sensor output is monitored with two different Keithley 2000 multimeters simultaneously in order to eliminate the intrinsic drift of the multimeter, if any, as a source of the measured drift. However, the outputs from the two multimeters are not different by more than 10 μV during the experiments and this is eliminated as a source of the large drift in the measured F_{OFF}, since 5 nN force corresponds to 100 μV output.

4. Offset force on the plate has been monitored with the vibration isolation enabled and locked. In general, with vibration isolation locked, the force output is observed to have ripples with amplitude in the range of a few μN at sub-Hz frequencies while with vibration isolation enabled, the amplitudes are nearly an order of magnitude lower. However, in both cases, typically around or above 10 μN drift of force over 1 hr is observed. The vibration isolation reduces coupling of the facility vibrations with the thrust stand, however, the slow drifts in the measured force is either not generated due to coupling of facility vibrations to the plate or, if they are, are not completely isolated from the thrust stand due to higher transmissibility at lower frequencies [219].

5. Offset force measurement has also been performed with the lid of the plastic box open and closed. While the results shown in Figure 6.8 are with the lid closed, with the lid open, the force sensor output either saturates or returns to no-load voltage within typically 5−10 minutes irrespective of the vibration isolation conditions, drifting much quicker than when the lid is closed. Also air-flow due to movements in the lab, opening and closing of doors are seen to produce large fluctuations in the measured force. Therefore, for the rest of the experiments, the lid is kept closed to eliminate influence of the ambient disturbances.

Although the conclusions on the thermal drift discussed above are not exclusively definite, there might be other reasons such as mechanical movement of the parts of the thrust stand that are expected to produce drift in the force sensor output. The thrust stand comprises of several mechanical parts discussed in Chapter 5 and they are connected using screws. The particle intercepting plate is also attached to the support frame using conductive tape and frame-clamps as shown in Figure 5.39 in Chapter 5. During experiments, the plate can move relative to the tip of the force sensor in contact due to vibrations of the building, undesired air-flow inside the plastic box covering the thrust stand from environment. It can be noted that the electrical cables for the thrust stand in the atmospheric characterization setup are clamped so that the movement of the cables minimally affect the measurements. The entire setup is installed on a vibration isolation table and the results are obtained with vibration isolation enabled. However, as small as 100 nm movement of the plate relative to its initial contact point on the plate can produce 5 μN change of force since the force sensor has a spring constant $k_f = 49.85$ N/m.

The translation stage AG-LS25V6 is expected to operate at up to 2 N axial loads [207] and hence is expected to be stable under the range of force measured in the present case. The force sensor measuring offset force by pushing on a rigidly fixed metallic wall is shown in Figure 6.9 (b), where the effect of air-flow on the measured force can be avoided and ignored. However, the drift of the offset force F_{OFF} is found to be of the order of 10 μN in this setup as well, over repeated experiments for 1 hour. Therefore, the rigidity of the atmospheric characterization setup is suspected to be the possible reason for the drift, along with possibility of movement of the membrane of the plate under airflow.

One way the drift can be eliminated is to pass it the force sensor output through a high-pass filter or a band-pass filter that removes the low-frequency components in the measured force; however, in that case, the thrust must be pulsed at a frequency in the pass band of the filter, details of which are discussed later in this section. In Figure 6.10 (a), the amplitude spectrum corresponding to the measured $F_{OFF}(t)$ in Experiment 1 in Figure 6.8 is shown by taking discrete Fourier transform, and in the inset, the frequency axis is zoomed-in to illuminate the average of the force measured over 1 hour corresponding to frequency $f = 0$. The signal was sampled at an interval of 0.5 sec from the Keithley 2000 multimeter in slow mode (200 ms integration time) and hence the frequency range in the spectrum is limited to 1 Hz. The plot shows very strong signal amplitude at frequencies bellow 0.2 Hz whereas the amplitudes at higher frequencies up to 1 Hz are less. In all experiments for finding the drift of $F_{OFF}(t)$, the low-frequency band is found to be limited to below 0.3 Hz whereas at higher frequencies the amplitude reduces to below 0.01 µN.

Higher frequencies in the response F_{OFF} of the force sensor is extracted from the oscilloscope traces recorded over a 1 sec time duration with a sampling speed 250 kS/s. In Figure 6.10 (b), the frequency domain response of the offset force $F_{OFF}(t)$ by taking discrete Fourier transform of the signal measured by the oscilloscope is shown. The time domain traces of the force sensor output, $F_{OFF}(t)$ is shown in the inset. A TTL output signal from the signal generator Agilent 33220A at 2 Hz is used as a trigger signal at $t = 0$ for averaging the traces on the oscilloscope. It can be seen that the spectrum of the offset force consists of strong amplitudes in the range 50 Hz to 150 Hz and above. On averaging for 100 times on the oscilloscope traces, the amplitude of the signal is reduced to roughly 20 nN in the range.

(a)   (b)
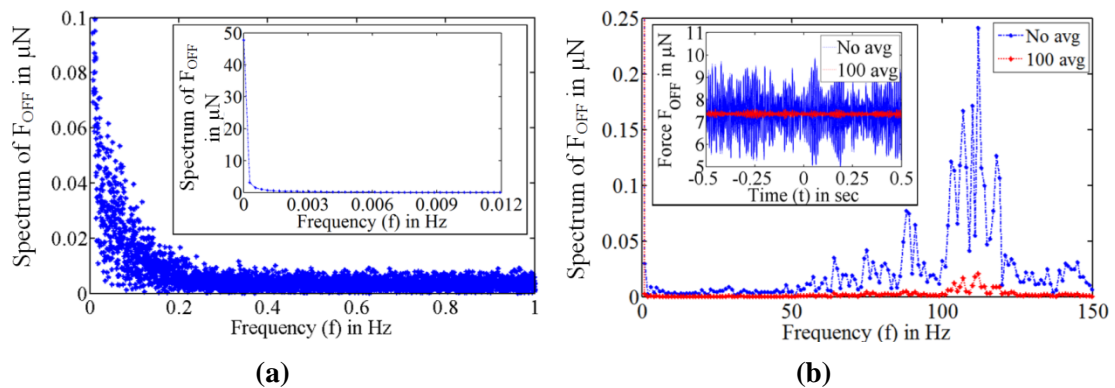
Figure 6.10: (a) Amplitude spectrum of the offset force F_{OFF} measured Experiment 1 in Figure 6.8 in the low frequency domain. Discrete Fourier transform has been taken on the reading of Keithley 2000 multimeter sampled at 0.5 sec interval. Low frequency noise up to 0.2 Hz (where the amplitude falls to below 10 nN) is observed while measuring steady state force around 50 µN corresponding to frequency $f = 0$. (b) Higher frequency amplitude response of the offset force. Discrete Fourier transform has been taken over oscilloscope traces sampled at 250 kS/s. On-screen averaging has been performed by using a 2 Hz TTL signal as the trigger signal. High frequency amplitudes above 50 Hz are observed where the amplitude exceeds 10 nN.

Referring to Table 5.18 in Chapter 5, the natural frequency of the suspended plate, Plate 2, is obtained to be $f_p = 58.21$ Hz by measuring its step response. However, the traces of the measured force, $F_{OFF}(t)$, which is a reflection of the motion of the plate, suggests a frequency range 50 Hz to 150 Hz and beyond, with the maxima at around 110 Hz. It must be noted that

during these experiments, the force sensor is in contact with the plate at its centre and the plate is deflected by the force sensor and hence the natural frequency is expected to be higher than its characteristic value listed in Table 5.18 because the force sensor adds a constraint on the motion of the plate. Also, the typical 50 Hz line frequency may be coupled with the natural frequency of the plate's response.

Looking at Figure 6.10 (a) and 6.10 (b), it can be inferred that, if a constant external force F is applied on the plate, the slow integration time of the multimeter can eliminate the high frequency ripples in the output, however, the low frequency drifts affect the accuracy of the measured force. The low frequency drifts and the high frequency vibrational response can be eliminated by band-pass filtering the output of the force sensor, but in that case, the external force F should be operated in pulsed mode at a frequency which is in the pass-band of the high pass filter, but away from the low and high frequency peaks in the spectrum of F_{OFF} observed in Figure 6.10. Also, it will be seen in section 6.4.2 that the high frequency modes, although average out under DC conditions, are excited by the pulses of force applied and even on averaging over several samples of the pulses, they contribute significant ripples in the pulsed output. In other words, the high frequency ripples are not completely asynchronous with the pulsating signal.

Therefore, for atmospheric characterization of the thrust stand, the continuous DC mode of operation has been rejected and pulsed mode operation at an optimally chosen frequency of excitation f_{ref} is pursued. The force can be measured by homodyne detection scheme using a lock-in amplifier. In homodyne detection, a pulsed output is AC coupled to the lock-in amplifier and detection is done only in a very narrow band around a chosen harmonic of the pulsed output at f_{ref} by shifting the harmonic frequency to DC, details of which is discussed below.

6.3.　　Thrust measurement by homodyne detection scheme

The homodyne detection scheme is very useful for measuring a low signal from a noisy environment. In this section, first the homodyne detection scheme with a lock-in amplifier is discussed. Then the modification to the test-setup for homodyne detection of thrust from the cold-gas ejector is discussed. Finally in the next section, the detailed experimental results on thrust measurement are shown. It is shown that thrust measurement down to 10 nN with a resolution better than 10 nN can be achieved with the homodyne detection method using a lock-in amplifier.

6.3.1.　Homodyne detection technique

In homodyne detection method, the signal to be measured is modulated with a periodic signal, typically with sinusoidal or square wave signal, and the measurements are performed to extract the harmonic amplitude and phase where the signal to noise ratio is much improved from a steady-state measurement. In the present case, the signal to be measured is F, given in Eqn. (5.7). Although the actual signal to be measured is the force sensor output voltage, in the present analysis, the notation of force is used instead, keeping in mind that there is a constant multiplication factor $S_F = 49.85$ μN/V. Now if the applied force is switched on and off in a square wave shape, the force measured by the sensor at any time instant t_1 during off time can be written as

$$F_1(t_1) = F_{OFF}(t_1) \tag{6.15}$$

When the external constant force F is applied in the next half of the switching period, the force measured at a time instant t_2 in that half-cycle can be written as

$$F_2(t_2) = F_{OFF}(t_2) + \frac{F}{\left(1 + \dfrac{k_p}{k_f}\right)} = F_{OFF}(t_2) + F_d \tag{6.16}$$

Therefore, the output force measured by the force sensor pulsates with a peak-to-peak value F_d over a time dependent base value $F_{OFF}(t)$. If this output of the force sensor is applied to the input of a lock-in amplifier synchronized at the same frequency f_{ref}, the input to the lock-in amplifier can be written as

$$F_{in}(t) = F_{OFF}(t) + F_d G(t) \tag{6.17}$$

where $G(t)$ is the switching square wave signal at the reference frequency f_{ref} of excitation and can be written as

$$G(t) = \begin{cases} 1, & 0 \le t < \dfrac{1}{2 f_{ref}} \\ 0, & \dfrac{1}{2 f_{ref}} \le t < \dfrac{1}{f_{ref}} \end{cases} \tag{6.18}$$

within one period of $1/f_{ref}$. Using complex Fourier series expansion, the switching signal can be written as

$$G(t) = \sum_{n=-\infty}^{\infty} C_n e^{j 2 n \pi f_{ref} t} \tag{6.19}$$

with the coefficients C_n defined by

$$C_n = \begin{cases} \dfrac{1}{2} & n = 0 \\ \dfrac{1}{j\pi n} & n = \text{Odd} \\ 0 & n = \text{Even} \end{cases} \tag{6.20}$$

Here $j = \sqrt{(-1)}$. Using (6.19) in the expression of $F_{in}(t)$ one can write $F_{in}(t)$ in time domain and frequency domain as

$$F_{in}(t) = F_{OFF}(t) + \sum_{n=-\infty}^{\infty} F_d C_n e^{j 2 n \pi f_{ref} t} \tag{6.21}$$

and

$$\Phi_{in}(f) = \sum_{n=-\infty}^{\infty} F_d C_n \delta(f - n f_{ref}) + \Phi_{OFF}(f) \tag{6.22}$$

respectively, where $\Phi_{in}(f)$ and $\Phi_{OFF}(f)$ are Fourier transforms of $F_{in}(t)$ and $F_{OFF}(t)$ respectively, $\delta(f)$ is unit impulse function. It can be noted here that $\Phi_{OFF}(f)$ represents the frequency domain response represented in Figure 6.10.

Now if the modulated signal $F_{in}(t)$ is multiplied by a sinusoidal signal of amplitude S and frequency f_{ref}, same as the switching signal repetition frequency, the signal output of the multiplier can be written in time domain and frequency domain as

$$F_{out}(t) = S\,F_{OFF}(t)\,e^{j(2\pi f_{ref}\,t+\varphi)} + \sum_{n=-\infty}^{\infty} S\,F_d\,C_n\,e^{j(2n\pi f_{ref}\,t+\varphi)} \tag{6.23}$$

and

$$\Phi_{out}(f) = \left[\Phi_{OFF}(f - f_{ref}) + \sum_{n=-\infty}^{\infty} F_d C_n\,\delta(f - n\,f_{ref} - f_{ref})\right]Se^{j\varphi} \tag{6.24}$$

respectively, where φ is the phase difference between the sinusoidal reference signal and the switching square wave signal. It can be seen that

$$\Phi_{out}(0) = \left[\Phi_{OFF}(-f_{ref}) + \sum_{n=-\infty}^{\infty} F_d C_n\,\delta[-(n+1)\,f_{ref}]\right]Se^{j\varphi}$$

$$= \left[\Phi_{OFF}(-f_{ref}) + C_{-1}F_d\right]Se^{j\varphi} \tag{6.25}$$

It can be seen from (6.24) that the spectrum $\Phi_{out}(f)$ consists of distinct frequencies at multiple of f_{ref} and the spectrum of $F_{OFF}(t)$ shifted to by $-f_{ref}$. Therefore, if the output signal $F_{out}(t)$ is passed through a sharp low-pass filter that can reject all the harmonics of $\Phi_{out}(f)$ and selects only $\Phi_{out}(0)$, the output of the low-pass filter consists of the DC value proportional to F_d and the values of $\Phi_{OFF}(f)$ within the narrow pass band around f_{ref}. If therefore, the reference frequency f_{ref} is chosen in a region of minimum amplitude in Figure 6.10 and the low-pass filter bandwidth is sharp, the contribution of $\Phi_{OFF}(f)$ on the output DC value can be made very small. For an ideal square wave modulation of the signal, the even harmonics in the spectrum of $F_{in}(t)$ do not exist and hence the contribution of the next harmonic ($|n| \geq 3$) are further reduced. If the input signal is AC coupled before multiplying with the sinusoidal signal, the contribution of $\Phi_{OFF}(f)$ and C_0 on the measured DC value are further reduced. Therefore, this scheme can produce very high signal to noise ratio by proper choice of f_{ref} and the low-pass filter.

In this analysis, it has been assumed that the sinusoidal signal frequency is 'exactly' same as the switching square signal frequency. A sinusoidal signal can be generated using a phase locked loop (PLL) that takes the square wave signal as input and generates a sinusoidal signal with frequency locked to the repetition frequency of the switching signal. Also, the output of the low pass filter depends on the phase difference of the sinusoidal signal with the modulated signal as seen in Eqn. (6.25). Therefore, reading the signal value and its phase from the output of the low-pass filter is necessary to actually know the original signal F_d. Conversely, the modulated signal can be multiplied by a sine and a cosine signals separately, both at the same reference frequency, f_{ref}, and at a phase difference 90°, and the amplitude $C_{-1}F_d S$ can be

extracted without the phase term from the two outputs, $C_{-1}F_dS\times\cos(\varphi)$ and $F_{-1}F_dS\times\sin(\varphi)$. All these processing can be done using a dual lock-in amplifier, such as model SR850 [236].

6.3.2. Lock-in amplifier

A functional block diagram of the dual lock-in amplifier, SR850 can be found in Ref. [236]. It consists of an internal square wave and a sinusoidal wave signal generator which can be used to modulate the signal to be measured and the same reference internally generated frequency can be used for demodulating the signal. Conversely, an external signal generator with arbitrary periodic signal can be used for modulating the signal and the external periodic signal can be used as a reference input for a PLL inside the lock-in amplifier to lock the internal reference generator to that frequency for demodulation. In both cases, it generates an internal sine and cosine signal at the locked frequency to demodulate the signal in quadrature and separates the phase term and the amplitude term. The signal $F_{in}(t)$ can be AC coupled to reject low frequency components in the signal up to 160 mHz [236]. The r.m.s. voltage output of the lock-in amplifier, R_{out} corresponding to force F_{out} can be converted to the actual peak-to-peak signal to be detected, F_d by

$$F_d = \frac{1}{\sqrt{2}}\left|C_{-1}\right|^{-1}F_{out} = \frac{\pi}{\sqrt{2}}F_{out} = 2.221F_{out} = 2.221S_F R_{out} \tag{6.26}$$

and hence, the force F applied by the intercepted particles on the plate is

$$Th = F = 2.221 \times \left(1 + \frac{k_p}{k_f}\right)S_F R_{out} \tag{6.27}$$

which is overlapped by noise contributions from the spectrum of $F_{out}(t)$ within the pass-band of the low-pass filter.

6.3.3. Choice of f_{ref} and low-pass filter

It can be concluded from the spectrum of $F_{OFF}(t)$ and the above discussion that f_{ref} can be chosen far from the frequencies at which $F_{OFF}(t)$ comprises of significant amplitudes. Looking at Figure 6.10, it can be therefore inferred that a choice of f_{ref} can be made in the range where the amplitude of $\Phi_{OFF}(f)$ is below 10 nN and hence

$$1\,\mathrm{Hz} \le f_{ref} \le 50\,\mathrm{Hz} \tag{6.28}$$

However, to excite $F_{in}(t)$ in a near-perfect square wave shape, the excitation period should be much higher than the characteristic response time of the suspended plate. In Table 5.18, the damping ratio and natural frequency of the Plate 2 have been evaluated to be $\gamma = 9.83\times10^{-2}$ and $f_p = 58.21$ Hz respectively in air under step response when the force sensor is not in contact with the plate. If the force F_d is applied to the plate and the force sensor is in contact, for a critically damped response of the plate, the time constant can be estimated to be $\sim 1/f_p \sim$ 17.2 ms. It is shown in section 6.4.2 that the response of the plate is under-damped and vibrations at frequencies between 50–150 Hz are excited when the force is applied periodically on the plate. Therefore, with the estimated damping ratio, the time to reach the first overshoot amplitude is $\sim 1/(4f_p) \sim$ 1.4–4.3 ms. To keep this time to at least 10 times

smaller than the half-period of the excitation signal, the reference frequency should be limited to

$$1\,\mathrm{Hz} \le f_{\mathrm{ref}} \le 5.8\,\mathrm{Hz} \tag{6.29}$$

In section 6.4.2, an error estimation associate with the response time of the plate is provided for frequencies between 1 Hz to 10 Hz. It can be seen that the lock-in amplifier output R_{out} reduces as the frequency f_{ref} is increased. This is because, for the same non-zero rise and fall time of the pulses, the pulse shape deviates more from the ideal square-wave shape as the repetition frequency increases.

The low-pass filter in SR850 lock-in amplifier can be with up to 24 dB/oct roll-off after a 3-dB cut-off frequency $f_{\mathrm{3\text{-}dB}}$ [236]. If the time constant of the low-pass filter is T_{c} and a 100 dB reduction in transfer function magnitude is desired at f_{ref}, the time constant of the low-pass filter should be set within the range

$$2^4 f_{\mathrm{3\text{-}dB}} = \frac{2^4}{2\pi T_{\mathrm{c}}} \le f_{\mathrm{ref}}$$

or $\qquad T_{\mathrm{c}} \ge \dfrac{8}{\pi f_{\mathrm{ref}}}$ $\hfill$ (6.30)

Under this condition, the transfer function magnitude of the low-pass filter is -3 dB at $f_{\mathrm{3\text{-}dB}}$ and -99 dB at f_{ref}. This implies that a $\Phi_{\mathrm{OFF}}(0) = 100$ µN contributes less than 10 nN at R_{out} of the lock-in amplifier.

6.3.4.   Experimental setup for homodyne measurement of thrust

In order to excite the thrust at a reference frequency for homodyne detection, a 3-way pressure switch V114 from SMC [237] has been used as shown in Figure 6.11. In Figure 6.12, a picture of the setup is shown during use in the characterization setup. In this arrangement, the 3-way pressure switch is installed between the input pressure line P_{in} and ambient pressure P_0. By using a 0–24 V switching signal at f_{ref}, the pressure at the outlet of the switch can be pulsated between P_0 and P_{in}. The TTL signal output from the lock-in amplifier is used to generate the switching signal at f_{ref} by using a simple bipolar junction transistor-based (BJT) amplifier. The switching frequency for the 3-way switch can be varied up to 20 Hz [237] and hence the desired frequency range can be achieved. A dead-volume of nitrogen is created in a sealed plastic box at the P_{in} inlet as a reservoir so that during switching the pressure, the inlet pressure or the pressure read at the pressure controller does not fluctuate. This arrangement does not affect the operation of the capillary ejector, but allows reading a stable pressure P_{in} at the pressure controller while pulsating the inlet pressure to the capillary between P_{in} and P_0. The output of the force sensor is connected to the input of the lock-in amplifier and to the oscilloscope as well. For safety of the force sensor, the output is also monitored with the analog input channel of NI-USB-6210. A schematic of the entire test setup is shown in Figure 6.13.

In this case, the pulsation of the pressure takes place at the frequency at which the switch is operated, however, vibration of the 3-way switch during switching is found to be small and is isolated from the thrust stand by mounting the switch on the plastic covering box, without

direct mechanical contact with the thrust stand except though the vibration isolation table and the soft tube.
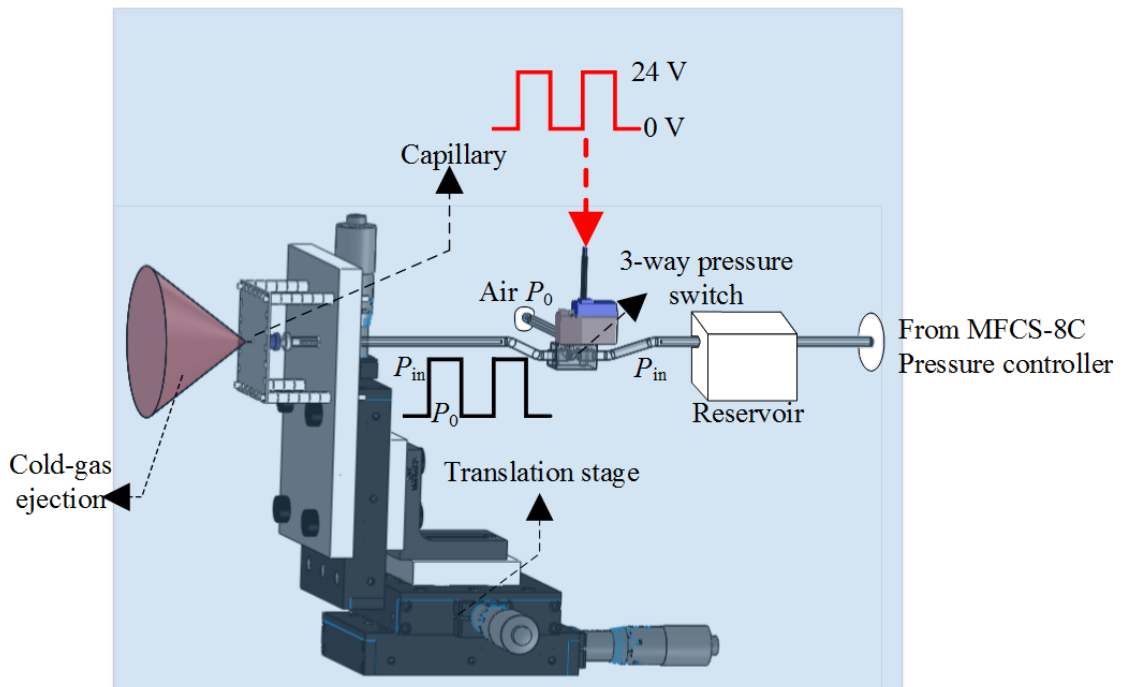
Figure 6.11: Schematic of the force excitation setup using a 3-way pressure switch. This scheme has been used for homodyne detection of thrust from the cold-gas ejector for characterization of the thrust stand. The pressure switch output is pulsated between the set pressure at the pressure controller and ambient pressure. A reservoir is created in the pressure input line P_{in} to maintain steady value of the set pressure during switching pressure. The shaded region represents parts inside the plastic box covering the thrust stand.
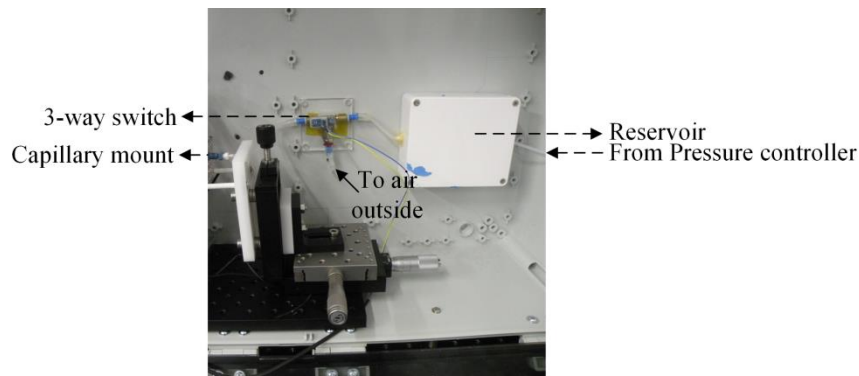
Figure 6.12: A picture of the pulsed pressure input to the capillary cold-gas ejector. The particle intercepting plate (not shown here) is on the left side of the picture. The 3-way switch and the reservoir are shown.
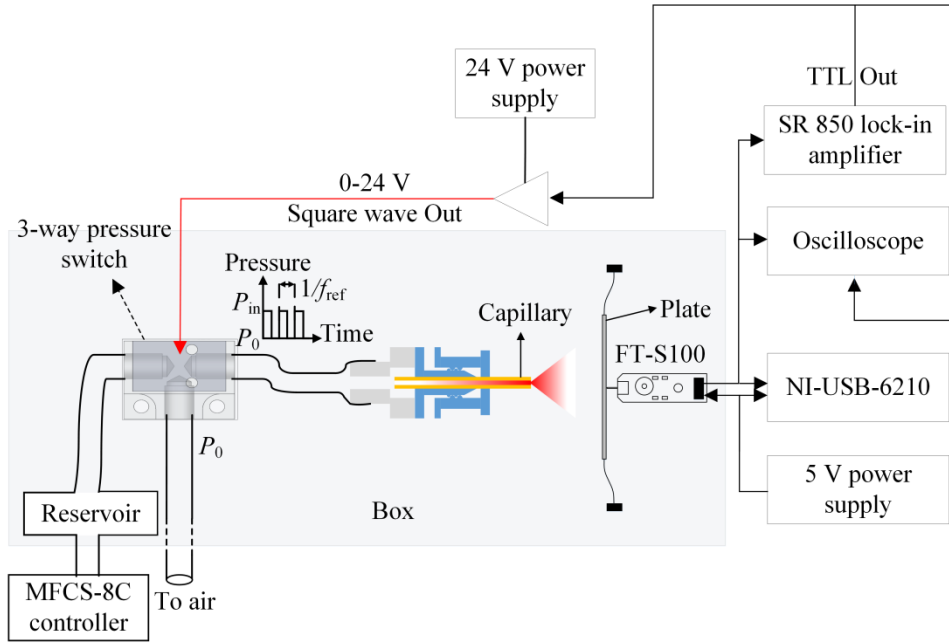
Figure 6.13: Schematic of the test setup for homodyne detection of thrust from a capillary cold-gas ejector for atmospheric characterization of the thrust stand. The TTL signal output from the lock-in amplifier is used to generate the switching signal at f_{ref} by using a BJT amplifier. A dead-volume of nitrogen is created in a sealed plastic box at the Pin inlet as a reservoir so that during switching the pressure. The output of the force sensor is connected to the input of the lock-in amplifier and to the oscilloscope as well. For safety of the force sensor, the output is also monitored with the analog input channel of NI-USB-6210. The shaded region represents parts inside the plastic box covering the thrust stand.

6.4.   Thrust stand characterization using lock-in amplifier

In this section, thrust stand characterization results are presented in terms of the force measured by the force sensor in the homodyne detection scheme instead of the voltage output from the lock-in amplifier, defined by Eqn. (6.26). The sensitivity of the force sensor FEMTO-1, S_F = 49.85 μN/V, spring constant k_f = 50.00 N/m and spring constant of the plate Plate 2, k_p = 48.21 are used in Eqn. (6.27) to convert R_{out} to F_{out}.

First the noise floor of the thrust stand is determined and then thrust measurement results are discussed for resolution, repeatability and accuracy estimation.

6.4.1. Noise floor measurement

Noise floor in the thrust stand has been measured without any applied pressure at the inlet, i.e. $P_{in} = P_0$ and $F_d = 0$ so that the output R_{out} comprises of the spectrum of $F_{OFF}(t)$ only, shifted by f_{ref}. For these measurements, the force sensor is brought in contact with the plate using the translation stage and then the switching signal is excited at f_{ref} with $P_{in} = P_0$. The reference frequency f_{ref} is varied from 1 Hz to 10 Hz for these experiments and the time constant is set to T_c = 3 sec for all the frequencies to satisfy the condition (6.29), which requires $T_c \geq 2.5$ sec for f_{ref} = 1 Hz and lower than 2.5 sec for higher f_{ref}. A list of configurations used for the experiments is described in Table 6.3. The dynamic reserve of the lock-in amplifier is set to

'Auto' [236] and sensitivity is set by monitoring the 'output overload bit' and increasing the sensitivity by one step starting from 1 µV f.s. [236] up to the point when, corresponding to the output signal level, the output does not overload after the excitation signal is applied. The r.m.s. output R_{out} and phase output φ are both recorded for 100 seconds with a 1 second interval. The entire test procedure is automated in Matlab (version 7.9).

Table 6.3: Summary of configuration for the lock-in amplifier

Property	Value
Sensitivity	Based on output overload bit
Dynamic reserve	Auto
Reference frequency f_{ref}	1 Hz–10 Hz
Reference signal type	TTL internal
Time constant T_c	3 sec
Input coupling	AC
Low-pass filter	24 dB/oct
Harmonic	1st
Measure	R_{out}, φ
Conversion factor	$2.221 \times (1 + k_p/k_f) \times S_F$ *
Synchronous detector	OFF

* $k_p = 48.21$ N/m, $k_f = 50.00$ N/m, $S_F = 49.85$ µN/V

In Figure 6.14 (a), the averages of 100 samples measured from the lock-in output at different frequencies have been shown. The standard deviations of the 100 samples at each frequency have been shown as error bar on the average values. The experiment has been performed with vibration isolation enabled and vibration isolation table locked while the box covering the thrust stand is always closed.

It can be seen that the standard deviation of the measured force is below 10 nN for frequencies $f_{ref} > 3$ Hz in both cases. A comparison of this noise floor can be made with the steady state measurement in Figure 6.8, where in the same duration of 100 seconds, the drift of the offset force is around 300 nN. The offset value in Figure 6.14 corresponds to the minimum detectable signal level [236] and is always positive by definition irrespective of $X_{out} = R_{out}\cos(\varphi)$ and $Y_{out} = R_{out}\sin(\varphi)$ changing sign [236] which are directly measured by the lock-in amplifier and R_{out} and φ are internally calculated from these two signals.

In Figure 6.14 (b), the measured 100 samples of X_{out}, Y_{out} and R_{out} are plotted (after converting into force units) against time for the case $f_{ref} = 1$ Hz and vibration isolation locked. It can be seen that X_{out} and Y_{out}, both fluctuate with amplitude around 10 nN or less at a rate in the order of 20 mHz. It can be remembered that $T_c = 3$ sec. time constant of the low-pass filter at the output of the lock-in amplifier corresponds to a 3-dB bandwidth of $f_{3\text{-dB}} = 53$ mHz and it is expected to pass all signal components in the spectrum of $F_{OFF}(t)$ shown in Figure 6.10 in the range $f_{ref} \pm f_{3\text{-dB}} = (1 \pm 0.053)$ Hz while beyond the range, the roll-off of the low-pass filter attenuates the signals. The non-zero, but less than, 2.5 nN average of the X_{out} and Y_{out} outputs indicates

1. The low-pass filter has small, but non-zero transfer function value at $f_{ref} = 1$ Hz and passing small, but non-zero fraction of $|\Phi_{OFF}(0)|$.

2. The 100 sec duration comprises of only 2–3 full cycles at around 20 mHz, and averaging over more number of cycles may produce lower mean value.

3. Coupling of vibrations generated by the three-way switch at the same frequency as f_{ref}.

The R_{out} output, which is calculated inside the lock-in amplifier as $R_{out} = |(X_{out}^2 + Y_{out}^2)^{1/2}|$, is always positive as seen in Figure 6.14 (b) and hence is expected to have larger mean than X_{out} and Y_{out} individually but lower standard deviation. Fluctuations in X_{out} and Y_{out} are related with the amplitude of noise passed through the low-pass filter and its random phase difference with the internally generated sinusoidal signal, but R_{out} is only sensitive to the amplitude of the noise. When an actual signal at frequency f_{ref} is excited, the fluctuations in phase difference reduce. Signal levels with r.m.s. value higher than the non-zero offset in R_{out} can be measured and the standard deviation over the offset value represents the noise in the signal.

(a)   (b)
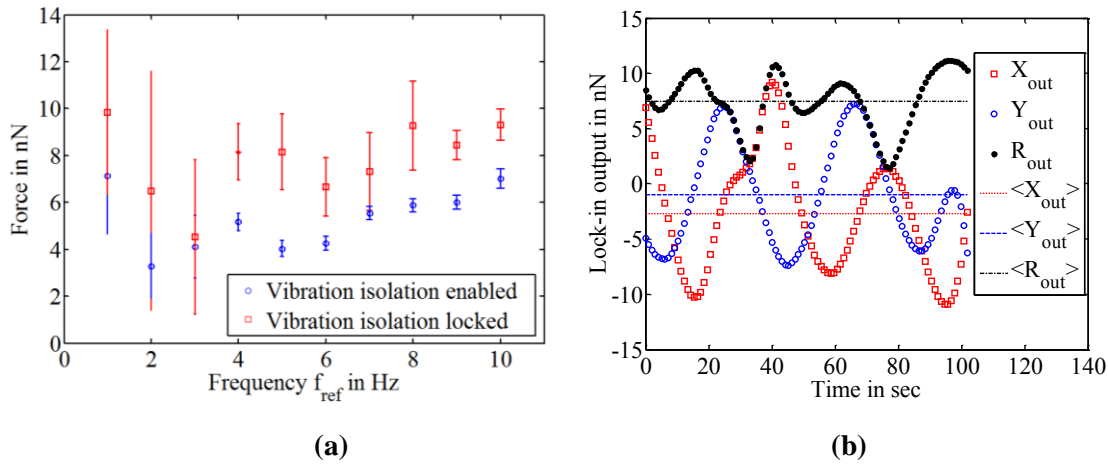
Figure 6.14: (a) Noise floor of the thrust stand vs. reference frequency f_{ref}, measured without applying any thrust from the capillary cold-gas ejector on the particle intercepting plate. The noise floor, which is the standard deviation over the offset values at different frequencies, is well below 10 nN when the vibration isolation in enabled. Without any vibration isolation and in normal lab environment, the noise floor is still below 10 nN for frequencies higher than 3 Hz. (b) Plot of measured X_{out}, Y_{out}, and R_{out} from the lock-in amplifier converted into force units. The corresponding average values of the 100 readings for each signal, $\langle X_{out} \rangle$, $\langle Y_{out} \rangle$ and $\langle R_{out} \rangle$ are also shown as straight lines in the same figure.

6.4.2. Thrust measurement with the lock-in amplifier

It has been observed in Figure 6.14 (a) that the offset and the standard deviation of the offset force measured without any jet on the particle intercepting plate is below 10 nN for frequency $f_{ref} > 3$ Hz. Therefore, for initial experiments, the reference frequency is set to $f_{ref} = 4$ Hz with $T_c = 3$ sec. The force sensor is first brought in contact with the plate to produce around 15 μN offset force. The pressure at the pressure controller is increased in steps from 0 to 400 mBar above ambient pressure in steps of 100 mBar. At each pressure, 100 samples of the pressure from MFCS-8C, R_{out} and φ from lock-in amplifier with an interval of 1 second between samples are recorded. After increasing the pressure P_{in} from the previous value to the present value, a pause of 100 sec is provided so that the output of the low-pass filter settles to the

final value. It can be noted that for the time constant T_c = 3 sec, a typical 15−20 sec time is required for the output to reflect the input as the low pass filter takes about 5 time constants to settle to its final value [236]. During each measurement, the force sensor output voltage is monitored to ensure that the force sensor is in contact with the plate and that the force sensor output has not reached the saturation and in any of the two cases, the translation stage can be moved backward and the experiment can be restarted. The entire test program is automated in Matlab. For all these experiments, the conditions listed in Table 6.2 are valid; in addition, the capillary is placed at a distance Z = 8 mm from the plane of the plate along the axis through the centre of the plate, i.e. $X = Y = 0$ unless otherwise mentioned.

In Figure 6.15, the pressure difference read in the MFCS-8C pressure controller and the thrust calculated from the measured output R_{out} of the lock-in amplifier are plotted together against the recording time. The dotted regions in the plots represent the pause of 100 seconds during which the pressure in increased from the previous value to the present value and the lock-in amplifier output is allowed to settle. At each pressure the pressure and thrust are measured 100 times.
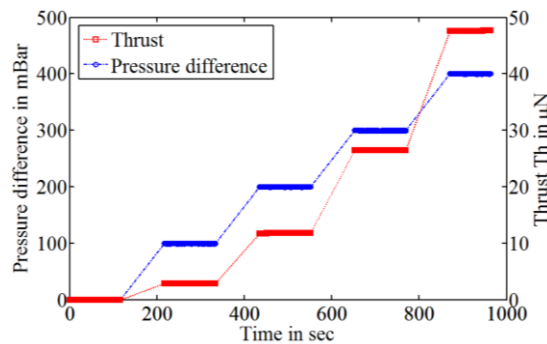
Figure 6.15: Plot of measured pressure and thrust against time of recording. The pressure in increased in step of 100 mBar and in each step, 100 samples of pressure and thrust are recorded. After changing pressure from previous value to present value, a settling time of 100 seconds is given so that the pressure and the lock-in amplifier output can reach the stable values. Here f_{ref} = 4 Hz and T_c = 3 sec. Vibration isolation is enabled. At 400 mbar, the thrust output is (47.616 ±0.015) µN.

It can be found that for pressure difference 400 mBar, the measured thrust is (47.616 ±0.015) µN where the uncertainty in the value represents the standard deviation of the 100 samples measured at 400 mBar. Since the thrust stand is designed for up to 100 µN range, the pressure can be further increased, however, for all the experiments, the pressure is limited to 400 mBar. The resolution of thrust measurement will be looked into in greater detail later in this section.

In Figure 6.16 (a) and (b) the traces of the oscilloscope channel reading the force sensor output are shown at two different reference frequencies f_{ref} = 1 Hz and f_{ref} = 4 Hz. The voltage outputs of the traces are converted to the corresponding forces using the sensitivity S_F of the force sensor FEMTO-1 and the spring constant of the plate Plate 2. The pressure difference in both cases is 400 mBar and the TTL output providing f_{ref} is used as a trigger signal at time t = 0 for averaging 100 traces on the oscilloscope. The traces clearly show the offset force F_{OFF} and the force F_{meas} corresponding to the switching of the pressure, where the applied force is

$F = (1 + k_p/k_f) \times (F_{meas} - F_{OFF})$. It can be seen that at each transition, the high frequency oscillations are triggered in the force output. For the case of $f_{ref} = 1$ Hz, the oscillations die out during 0.5 sec pulse-width whereas for the case of $f_{ref} = 4$ Hz, the pulse width of 125 ms is not sufficient for the under-damped oscillations to die out. Recalling Figure 5.36 (b) it can be seen that the vibrational motion of the plate lasts more than the pulse width of the square wave signal at $f_{ref} = 4$ Hz.
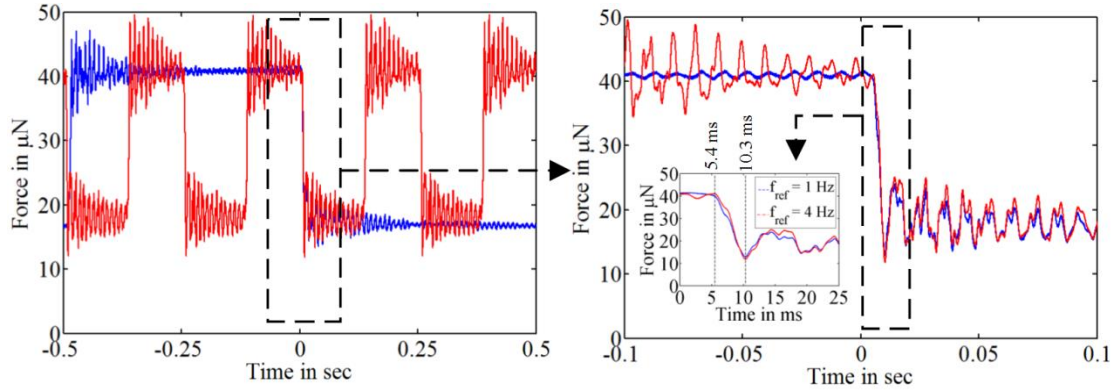
Figure 6.16: (a) Oscilloscope traces of the force output from the force sensor with $f_{ref} = 1$ Hz in blue and $f_{ref} = 4$ Hz in red after 100 averages. The transient high frequency oscillations can be seen in the traces excited at the transition of the forces. (b) A zoomed-in view of the traces around the triggering time $t = 0$. A 5.4 ms delay and another 4.9 sec time up to the first overshoot amplitude is seen. The transient response is almost identical for both the frequencies.

Although the high frequency oscillations excited by the triggering of the pulses are not expected to affect the homodyne measurement at f_{ref} as long as f_{ref} is much smaller than the oscillation frequency, as discussed in section 6.3, the non-zero rise time and fall time of the force pulses are seen to be a significant parameter affecting the thrust measurement. Time-zoomed views of the oscilloscope traces at $f_{ref} = 1$ Hz and $f_{ref} = 4$ Hz in Figure 6.16 (b) and in the inset show that at both the frequencies, the transient response during switching is almost identical. There is a delay of approximately 5.4 ms from the edge of the TTL triggering signal to the start of the pulse of force on the force sensor and the force takes approximately another 4.9 ms up to the peak of the first overshoot amplitude of oscillation. The first 5.4 ms delay is due to the response time of the 3-way pressure switch [237], however, the 4.9 second required for the thrust to build up to the first oscillation amplitude can be partly attributed to the plates response time and the time required for the pressure to build up to the set value at the capillary inlet after the 3-way switch is turned on. It can be noted from section 6.3.3 that the expected maximum time for the plate's vibration to reach the first oscillation amplitude is 1.4–4.3 ms for a vibration frequency range 50–150 Hz observed in Figure 6.10 under identical conditions, but without any applied pressure.

This observed non-zero rise time changes the shape of an otherwise perfect square wave pulse and hence the amplitude of the first harmonic of the force signal, which is to be measured by homodyne detection technique in the lock-in amplifier. For higher reference frequencies, the reduction in the first harmonic amplitude is expected to be higher due to increased ratio of the rise time to pulse width. In Figure 6.17, the frequency response, obtained by discrete Fourier transform of the traces shown in Figure 6.16 at $f_{ref} = 1$ Hz and $f_{ref} = 4$ Hz are shown. By

definition, this is the Fourier transform of $F_{in}(t)$ at the input of the lock-in amplifier. From Figure 6.19, it can be seen that the high frequency response of the plate corresponding to the ripples in Figure 6.18 are concentrated at around 100–110 Hz. The odd harmonics of the signal $F_{in}(t)$ at two different f_{ref} are visible, however, it can be seen that the even harmonics especially for f_{ref} = 4 Hz are prominent as well, resulting from distortion of the otherwise square wave signal having no even harmonic.
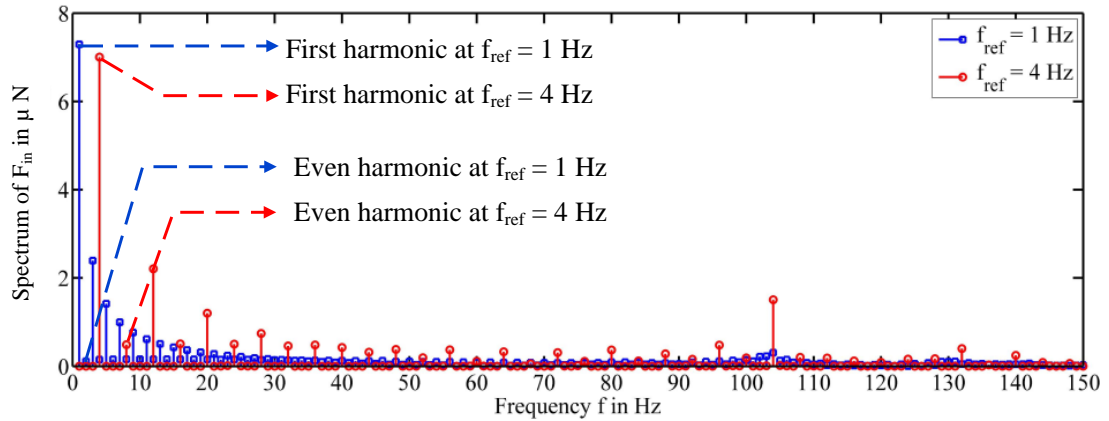
Figure 6.17: Amplitude spectrum of the pulsed force traces at f_{ref} = 1 Hz and f_{ref} = 4 Hz shown in Figure 6.18. In the insets, the frequency scales are zoomed in in the low frequency and high frequency range. The prominent odd harmonics correspond to the square wave shape of the signals. However, the finite rise time of the signals produce prominent, but much less significant even harmonics as well. The amplitude of the 1st harmonic for the case f_{ref} = 1 Hz is larger than that at f_{ref} = 4 Hz.

It can be seen from Figure 6.17 that the amplitude of the first harmonic for f_{ref} = 4Hz is smaller than that for f_{ref} = 1 Hz as discussed in the previous paragraph although for an ideal square wave the amplitude of the harmonics are independent of the frequency. Since the lock-in amplifier operates at the first harmonic, a comparison can be made between the measured thrust by the lock-in amplifier and thrust obtained from the amplitude of the first harmonic in the oscilloscope traces. In Figure 6.18, these two are plotted for different reference frequencies. The r.m.s. output of the lock-in amplifier is converted to thrust Th using the conversion factor given in Table 6.3 and the average of the 100 samples taken with 1 sec interval is plotted. The 100 times averaged traces from the oscilloscope in a 1 sec time-scale are discrete Fourier transformed to find the first harmonic amplitude and then the amplitude is converted to thrust using Eqn. (6.28). If the peak-to-peak value of the force pulses at f_{ref} = 1 Hz from the oscilloscope trace in Figure 6.18 is taken as the force F_d within the resolution limit of the oscilloscope traces, the thrust Th that should be measured by the force sensor can also be plotted in the same figure for comparison, which is independent of the frequency f_{ref}. For 400 mbar pressure difference in this case, the height of the pulse obtained from the oscilloscope trace is 487 mV which corresponds to 47.58 µN using the sensitivity and spring constant of FEMTO-1 and Plate 2. For comparison, all the thrust values are normalized to this value.

If can be readily seen from Figure 6.18 that with increasing the reference frequency f_{ref} reduces the thrust measured by both, the lock-in amplifier and the oscilloscope. There is nearly a 1% difference between the values obtained from the oscilloscope trace and that

obtained from the lock-in amplifier which might arise from the vertical sensitivity of the oscilloscope. It can be noted that the traces on the oscilloscope used for calculating the thrust pulsate between around 1.82 V and 1.33 V for a pressure difference 400 mBar with 1 V/div vertical scale. The vertical gain accuracy of the oscilloscope is around 1.5% of the full-scale [233] and a few mV errors in the values are expected leading to the difference with the lock-in amplifier results.

It can be seen from Figure 6.18 that at lower reference frequencies, the thrust measured by the lock-in amplifier is closer to the expected value. At higher f_{ref} up to 10 Hz, a 12% reduction in the measured thrust is expected which leads to higher uncertainty in the measurement as well. For $f_{ref} < 3$ Hz, the noise floor is higher as seen in Figure 6.14. Therefore, a compromise has been made in f_{ref} between the noise floor and accuracy and for the subsequent experiments the reference frequency is kept at the initially chosen $f_{ref} = 4$ Hz with $T_c = 3$ sec with an expected uncertainty of 4% and noise well less than 10 nN over 100 sec experimental duration.
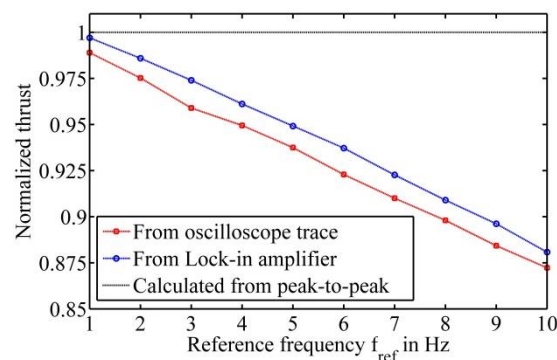
Figure 6.18: Comparison of the thrust measured at a pressure difference 400 mBar at different reference frequencies from the first harmonic of the oscilloscope traces and from the Lock-in amplifier operating at the first harmonic. The blue horizontal line represents the actual thrust calculated from the height of the pulses which is used to normalize all the thrust values.

In Figure 6.19 (a) measured thrust up to a pressure difference of 400 mBar with a step of 10 mBar is shown. The experimental conditions are identical to that for Figure 6.15 with $f_{ref} = 4$ Hz and $T_c = 3$ sec. At every pressure step, 100 samples of pressure difference, R_{out} and φ are recorded with a 1 sec interval between samples. The average of the 100 samples at each pressure is plotted and the standard deviation of the measured thrust is shown as error bar and also in the inset.

In Figure 6.19 (b), the corresponding phase difference φ between the reference sinusoidal signal internally generated by the lock-in amplifier and the pulsed input signal is shown. It can be seen that the phase is also very stable during the entire range of thrust. The stability of the phase φ rather than the exact value of φ bear significance here because the initial phase of the sinusoidal reference signal is never forced to an initial value, say 0, at the beginning of measurement. The phase reading is important if instead of R_{out} signal, X_{out} and/or Y_{out} signal output were recorded from the lock-in amplifier, details of which can be found in Ref. [236].

The non-linear variation of thrust with the pressure difference can be compared with the relation in Eqn. (6.8). In Figure 6.22, the measured average thrust is normalized to the

maximum measured thrust at 400 mbar and is plotted against the pressure difference normalized to the maximum pressure difference 400 mBar. It can be noted from Eqn. (6.8) that the thrust for a given P_{in} follow $||Th|| = ||(P_{in} - P_0)||^2$ where $||w||$ represents w normalized to the maximum value of w. In the same figure, Figure 6.20, expected parabolic relation between $||Th||$ and $||(P_{in} - P_0)||$ is also plotted. It can be easily seen that the measured thrust follows the expected parabolic profile very closely.
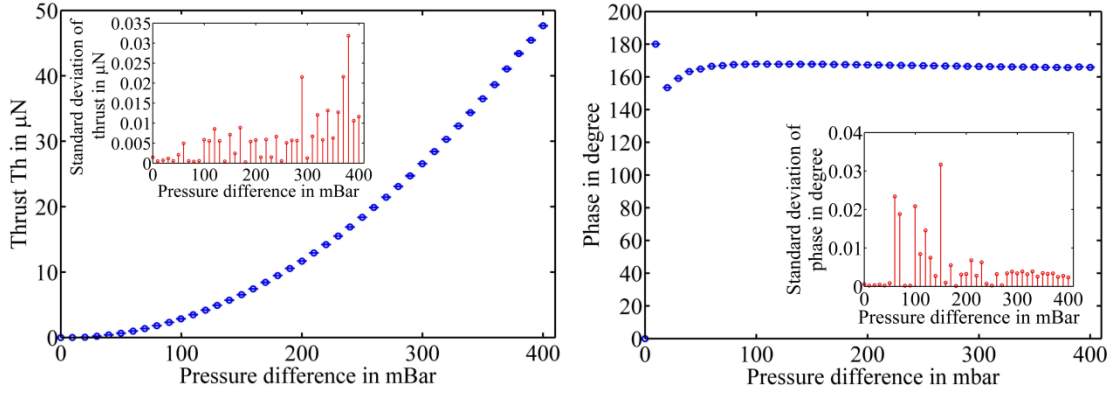
Figure 6.19: (a) Plot of measured thrust vs. applied pressure difference up to 400 mBar in 10 mBar step. The average of 100 samples taken at each pressure with 1 sec interval between is plotted and the standard deviation of the measured thrust is shown as error-bar and also in the inset. (b) The corresponding plot of phase measured from the lock-in amplifier against the pressure difference and the standard deviation shown as error-bar and also in the inset.
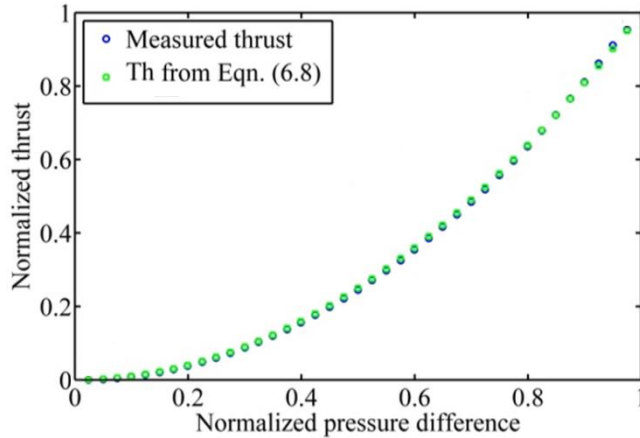
Figure 6.20. Plot of normalized thrust to normalized pressure difference obtained from Figure 6.19 (a). In the same figure the normalized thrust obtained from Eqn. (6.8) is also plotted for comparison. It can be readily seen that the measured normalized thrust follows the profile of $||Th||$ from Eqn. (6.8) very closely.

It can be seen from Figure 6.19 (a) that the standard deviation exceeds 10 nN only for higher thrust levels, above 30 µN. The parabolic variation of thrust with pressure difference suggests that

$$\frac{\Delta Th}{Th} = 2 \frac{\Delta(P_{in} - P_0)}{(P_{in} - P_0)} \tag{6.31}$$

or

$$\Delta Th = 2 \frac{\rho_0}{A_{cap} R_h^2} (P_{in} - P_0) \times \Delta(P_{in} - P_0) \tag{6.32}$$

using Eqn. (6.8), where Δw represents error in the value of w. Apart from the noise floor of the measurements, stability of $(P_{in} - P_0)$ also leads to error in Th. The pressure controller is typically stable within 1 mBar [221] and there can also be local fluctuations of ambient pressure P_0 inside the plastic box. At low $(P_{in} - P_0)$ the proportional error in $(P_{in} - P_0)$ is high and decreases with increasing $(P_{in} - P_0)$. Therefore, proportional error in Th is expected to reduce with increasing $(P_{in} - P_0)$, but uncertainty of measured Th is expected to increase as $(P_{in} - P_0)$ increases.

6.4.3. Thrust resolution

It has been observed in Figure 6.14 that the noise floor at $f_{ref} = 4$ Hz and $T_c = 3$ sec is below 10 nN and in Figure 6.19, thrust measurement up to 400 mBar has shown that for below 30 µN thrusts, the standard deviation of the measured thrust is below 10 nN. In order to verify the minimum thrust that can be detected and minimum resolvable thrust difference, the pressure steps are set to 1 mBar and range up to 40 mBar. Once again, 100 samples at each pressure are recorded in identical settings discussed above. In Figure 6.21, the thrust vs. pressure difference results up to 40 mbar with 1 mbar step are shown.

It can be seen that thrusts as low as 10 nN can be resolved with the thrust stand and minimum thrust lower than 10 nN can also be detected. From the results in Figure 6.21 and those in Figure 6.21, it can be concluded that the thrust stand has a resolution better than 10 nN for sub-µN thrust ranges. For higher thrust ranges, typically above 30 µN, the noise over the measured value can be conservatively defined to be 20 nN.

6.4.4. Thrust repeatability

Repeatability of the measured thrust has been verified by repeating the thrust measurement experiments several times and with three different plates at pressure differences 100 mBar to 400 mBar in steps of 100 mbar. In each experiment, the conditions are identical to the experimental conditions described in the section 6.4.2 and 6.4.3, i.e. $f_{ref} = 4$ Hz, $T_c = 3$ sec., and rest of the settings for the lock-in amplifier as described in Table 6.3. In Table 6.4, the thrust measurement results are listed for different experiments. Experiment 3 with Plate 2 has been performed after dismantling the capillary cold-gas ejector setup and then once again bringing it to the same position used for all the previous experiments, i.e. $X = 0$, $Y = 0$ and $Z = 8$ mm from the centre of the plate.

It can be noted from Table 6.4 that the thrust results for the same plate are repeatable within 0.15% at the maximum thrust measured from the cold-gas ejector. For different plates, with slightly different spring constants, the repeatability of the results is within 1.7% measured at the maximum thrust level. This may be partly contributed by uncertainty in different spring constant of the different plates, possible difference in rigidity of the plate section relative to the spring section due to manufacturing defects, the state of the Mylar film during attaching to the frame and error associated with the process of removing a plate and assembling another plate in the thrust stand.
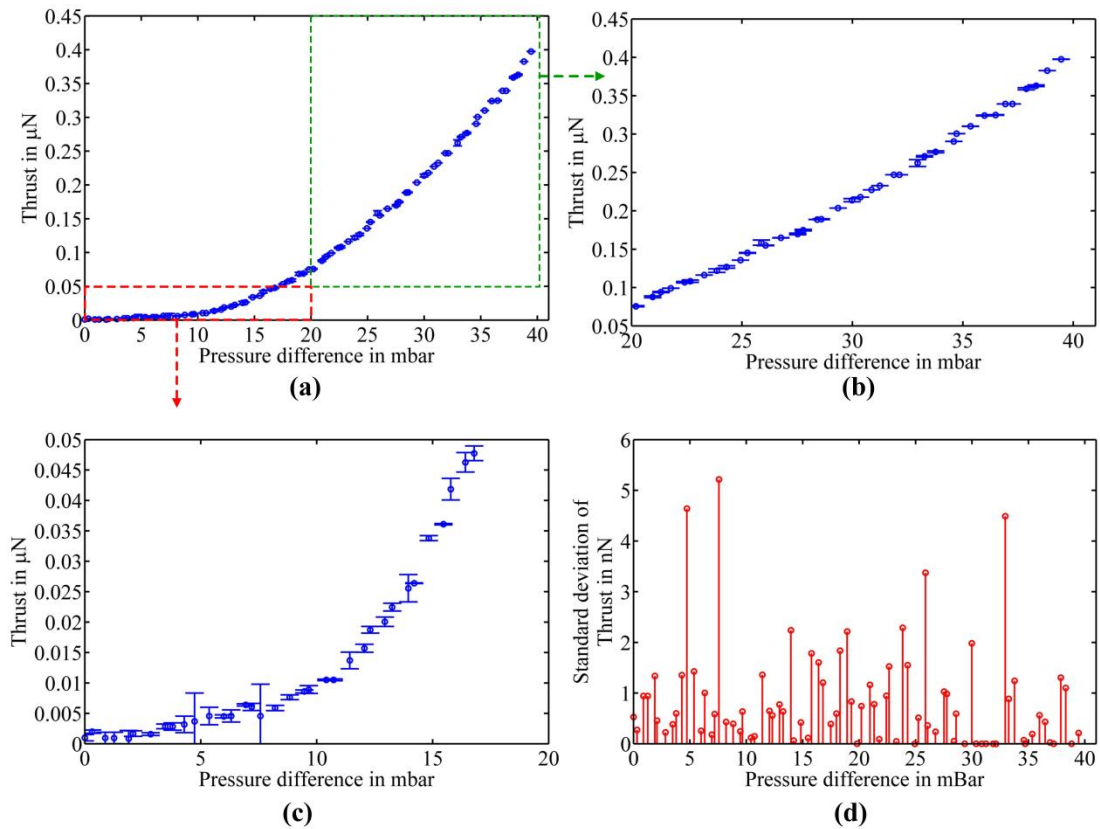
Figure 6.21: (a) Plot of measured thrust up to 40 mbar with 1 mBar step. The higher pressure region and the lower pressure region in the range are zoomed in in (b) and (c) respectively. (d) Plot of the standard deviation of 100 samples taken in 100 seconds at each pressure. The thrust noise is well below 10 nN.

6.4.5. Thrust accuracy

The accuracy of thrust measurement is partly dictated by the four issues.

1. Validity of the relation $F = Th$ i.e. the measured thrust by intercepting the emitted particles is equal to the thrust on the capillary.

2. Errors due to the rise time of the plate.

3. The constancy of the measured thrust due to impingement of particles over a large spot size on the plate or impingement away from the centre of the plate.

4. Angular misalignment of the force sensor w.r.t. the normal to the plate.

The first condition mentioned here has been already discussed in section 6.1.3 and from survey of analytical and experimental results discussed in [139], [140], [231], and within around 10% uncertainty limit, the equality $F = Th$ can be assumed. This issue is linked with the validity of the correlation of the two forces and can be separated from the rest of the inaccuracy issues which are part of the thrust stand itself. The first condition is verified in section 6.5 by direct measurement of thrust on the capillary using a load-cell; however, the resolution of the load-cell limits the conclusion of the equality to approximately 10%.

Table 6.4: Summary of repeatability tests of thrust measurement

Plate	Spring constant k_p (N/m)[*]	Experiment no.	Pressure difference (mBar)	Thrust (µN)
Plate 2	48.21	1	100 200 300 400	2.858 ± 0.005 11.677 ± 0.009 26.566 ± 0.012 47.653 ± 0.019
		2	100 200 300 400	2.843 ± 0.007 11.657 ± 0.009 26.531 ± 0.008 47.625 ± 0.017
		3[#]	400 400	47.682 ± 0.017 47.670 ± 0.011
Plate 3	46.21	4	400	47.379 ± 0.005
Plate 4	40.02	5	400	46.841 ± 0.008

[*]Spring constants are listed in Table 5.17.

[#] Repeated after re-assembling the capillary ejector and bringing it to the previous position, i.e. $X = Y = 0$, $Z = 8$ mm w.r.t to the centre of the plate

The uncertainty due to rise time of the plate is already discussed in section 6.4.2 and it has been seen that for $f_{ref} = 4$ Hz the measured thrust is nearly 4% lower than expected. This parameter is dictated by the choice of reference frequency particular to the thruster to be examined and the plate used for intercepting the emission, and can be corrected for by calibrating the thrust stand as shown in Figure 6.18.

The angular misalignment of the force sensor with the normal to the plate can produce error in thrust measurement. In the thrust stand, the direction of the force sensor is guided by the adapter placed between the force sensor and the translation stage as shown in Figure 5.10 and 5.11 in Chapter 5. The overall maximum angular offset between the axis of the force sensor and the normal to the plate is expected to be only a couple of degrees, leading to less than 0.1% error in the normal force measured by the force sensor.

In this following sub-sections, the inaccuracy of the measured thrust due to spreading of the emitted jet is verified. It can be noted that in the section 6.4 so far, all the experiments have been performed with $X = 0$, $Y = 0$ and $Z = 8$ mm, i.e. the capillary tip was at a distance 8 mm from the plane of the particle intercepting plate on the normal axis through the centre of the plate. It has also been discussed that this distance is safe to avoid having the capillary tip in the deflection zone of the jet around the plate, where the axial velocity of the jet transforms into lateral velocity.

6.4.5.1. Thrust accuracy estimation by varying distance of the capillary

In Figure 6.22, the thrust measured from three distances $Z = 8$ mm, 16 mm and 24 mm and at pressure differences 100 mBar to 400 mBar in 100 mBar steps are shown. These

measurements have also been performed with Plate 2 and in the conditions identical to those used in the rest of the section 6.4.

It can be seen that for $Z = 8$ mm to $Z = 24$ mm, the measured thrust reduces by nearly 1%. At this point, reference to the simulation results shown in Figure 5.28 (c) and (d) in Chapter 5 can be drawn which show that with increasing spot size of the impinging jet or position of the spot on the plate, the inaccuracy of measurement can be a maximum of 5% as long as the entire jet is intercepted by the plate. For an assumed circular cross-section uniform jet perpendicular to the plane of the plate, the results in Figure 5.28 (d) show a 3% reduction of force measured by the force sensor when the radius of the spot size on the plate increases from 0 mm to 22.5 mm. The results in Figure 6.22 suggest that up to at least 24 mm distance, the plate intercepts all the emitted particles, i.e. the spot size on the plate is well within the size of the plate. The nearly unchanged (~ 1%) measured thrust from $Z = 8$ mm to $Z = 24$ mm in Figure 6.22 is congruent with experimental observations and simulation results in [139] for sub-sonic jet. At shorter distance, the spot size on the plate is smaller and it increases as the distance Z increases with more of the jet impinging away from the centre of the plate. It is seen in section 6.4.5.2 that by changing the lateral position of the capillary w.r.t. the centre of the plate reduces measured thrust by 5–10%, as long as the plate can capture the full jet. Much less change of measured force by changing the distance Z in this section and in Figure 6.22 is due to less contribution of the off-axis fraction of jet to the normal force on the plate measured by the force sensor. Since inclined impingement reduces normal force on the plate, normal force per unit area is expected to reduce with increasing distance from the centre while in simulation in Figure 5.28 (d), the normal force is assumed constant over the entire spot size. Therefore, a practical jet emitted from the capillary is expected to produce less change in measured force due to increasing spot-size than the 3% observed in simulation in Figure 5.28 (d).
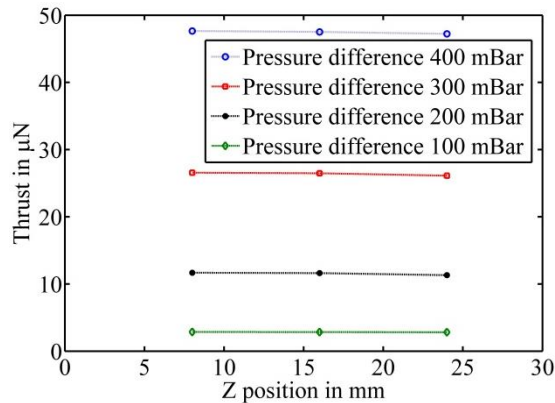
Figure 6.22: Plot of measured average thrust vs. distance of the capillary from the plate. An approximately 1% reduction in measured thrust is observed by changing the Z position from 8 mm to 24 mm, i.e. $Z/d_{cap} = 53$ to 160 where $d_{cap} = 150$ µm is the capillary inner diameter.

6.4.5.2.   Thrust accuracy estimation by varying lateral position of the capillary

In Figure 6.23, the measured average thrust at 400 mBar by changing the X position of the capillary in one direction is shown where $X = 0$ represents the centre of the plate and $X = 22.5$ defines the boundary of the plate. Here, $Y = 0$ and $Z = 8$ mm. It can be seen that the thrust measured by the force sensor at the centre of the plate sharply falls to zero from $X = 17$ mm to

$X = 30$ mm. For $X \leq 17$ mm, the measured thrust is within 5% of that measured at $X = 0$. From the plot, an estimate of the spot diameter can be estimated roughly to be $D_s = 13$ mm for $Z = 8$ mm. This gives a rough estimate of the angular divergence of the jet and the half-angle can be estimated to be 39°.
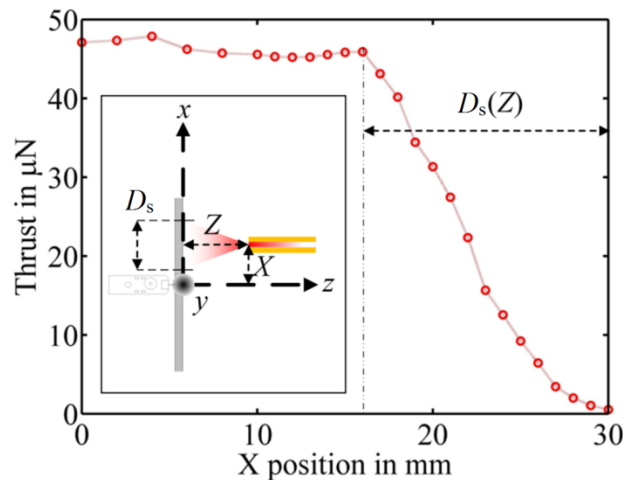
Figure 6.23: Measured thrust vs. X position of the capillary head from the central axis normal to the plate. The distance between the plate and the capillary head is $Z = 8$ mm with $Y = 0$. In the schematic in the inset, the coordinate and position definitions are recalled from Chapter 5. The spot-size of the jet is estimated by moving the capillary w.r.t. the centre of the plate in x direction and finding the range of X where the measured thrust drops from an approximately constant value to 0 with distinguishable slope. The angular divergence can be estimated from the D_s and hence the angular spreading. In this case, with $Z = 8$ mm, D_s is 13 mm.

In Figure 6.24, the average thrust measured by changing the X and Y position of the capillary head across the area of the plate from a distance $Z = 8$ mm are shown for Plate 2, Plate 3 and Plate 4 respectively, where the colour in the circles represent the thrust normalized to the thrust measured with $X = Y = 0$. The diameter of the circles represent the approximate spot size of 13 mm from the distance $Z = 8$ mm. The FEM simulated results shown in Figure 5.28 (c) assuming point force are redrawn in Figure 6.24 (a) for comparison, which shows that up to 5% difference of the measured force by the force sensor is expected.

It can be seen that for Plate 2, the maximum difference of the measured thrust due to misalignment of the capillary head w.r.t the central axis of the plate is 13% for the Plate 2. For Plate 3 and Plate 4, the maximum difference of the measured force is within 10% of the thrust measured with $X = Y = 0$. These values exceed the simulated inaccuracy results. The difference of the results between the plates and asymmetry of the measured thrust on the same plate is due to manufacturing imperfection of the individual plates. Therefore, depending on the plate, the maximum inaccuracy of the measured thrust can be different, but close to 10%. However, this scenario represents an extremely offset thruster head and in practice, the thruster head is expected to be aligned to the central axis of the plate and the inaccuracy is expected to be smaller. For example, if the axis of the thruster is within 10 mm radius from the centre of the plate, the inaccuracy is given by the five circles closest to the centre of the plate in Figure 6.24 (b), (c) and (d) which is less than 7%, 3% and 3% for Plate 2, plate 3 and Plate 4 respectively.
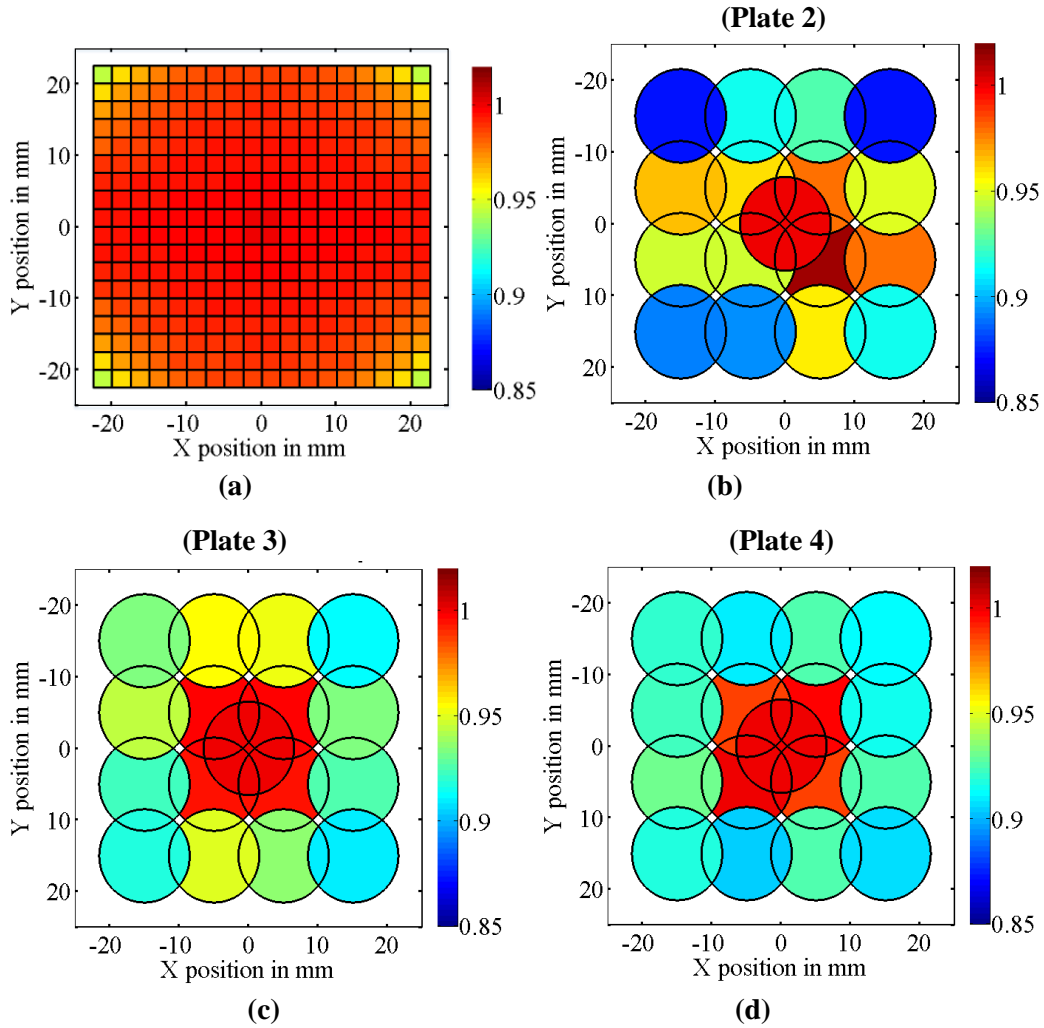
Figure 6.24: (a) Simulated normalized force measured by the force sensor at the center of the plate as a function of position of point force applied at the corners of the square boxes. This figure is identical to Figure 5.28 (c) in Chapter 5. Thrust measured by the force sensor at the centre of the plate by placing the capillary at position (*X*, *Y*) and at distance *Z* = 8 mm are shown for Plate 2 (b), Plate 3 (c) and Plate 4 (d). The diameter of the circles represent the approximate diameter of the spot of jet while emitting from a distance *Z* = 8 mm. The measured thrust is normalized by the thrust measured with *X* = *Y* = 0. The colour bar in each figure represents the normalized thrust.

Uncertainty in the values of k_p and k_f, the spring constant of the plate and that of the force sensor, also contributes to small uncertainty in the measured force. In Table 5.17 in Chapter 5, measurement of spring constant of the plates suggests around 0.2% uncertainty in k_p. For the force sensor, k_f = 50.00 N/m is assumed for all measurements in this chapter, however, uncertainty values in k_f are not available. Calibration plots provided by the manufacturer [199] shows very good linearity between applied force and voltage output and the standard deviation of the calibration data with linear fit is in part contributed by the uncertainty in k_f. If the uncertainty in k_p and k_f both are considered to be around 0.2%, their contribution to uncertainty in measured force can be calculated from Eqn. (6.14) as

$$\frac{(k_p / k_f)}{(1 + k_p / k_f)}\left(\frac{\Delta k_p}{k_p} + \frac{\Delta k_f}{k_f}\right) \approx 0.2\% \tag{6.33}$$

167

assuming $k_p = k_f$. Here, Δw represents maximum uncertainty in the value of w.

Therefore, it can be summarized here that

1. A maximum 10% uncertainty in the measured thrust is expected from the position of the thruster relative to the central axis of the plate.

2. Around 2% uncertainty in the measured force is expected among different plates.

3. Around 1% uncertainty in the measured force is expected from the distance of the thruster head from the plane of the plate as long as the entire jet is intercepted by the plate.

4. Around 0.2% uncertainty is expected in the measured thrust over repeated measurements with the same plate.

5. Around 0.1% uncertainty due to misalignment of the force sensor to the normal to the plate.

6. Around 4% reduction in measured force is expected due to non-zero response time of the plate, according to Figure 6.18 (This has been measured only for Plate 2).

Hence, an overall maximum uncertainty of 11% in the measured impingement force with the particle intercepting plate can be defined using the different relatively independent possible sources of uncertainties. However, the major contribution in the error coming from the position related uncertainty in practice may be much lower because the thruster is expected to be aligned with the central axis of the plate. The 4% uncertainty due to f_{ref} can be corrected for by calibrating the thrust stand using Figure 6.18 when operating in air or can be calibrated in similar way for different ambient conditions.

However, uncertainty of thrust measurement also depends on how accurately the relation between Th and F is known. From section 6.1.3 it can be remembered that for sub-sonic jet, $F = Th$ with an uncertainty of around $\pm 10\%$ has been observed in different experiments [139], [140], [231]. In the following section, measurement of Th on the capillary with a load-cell is performed and compared with F.

6.5.   Thrust verification by direct thrust measurement

The purpose of the verification experiment is

1. To measure thrust on the capillary directly and compare with the impingement force measured on the plate.

2. To verify the Th vs. P_{in} variations observed in the experiments discussed in section 6.4.

To measure thrust on the capillary, a load-cell LRF-400 from Futek [217] is used. The setup consists of a small PMMA mount where one or several capillaries can be glued such that the small reservoir inside the mount can be used as a feed-through for the inlet pressure as shown in Figure 6.25 (a) and (b). The mount is fixed on the force probe of LRF-400 load cell and cold-gas is ejected vertically upward in order to avoid non-axial loading of the mount on the force sensor. The mass of the PMMA mount and the capillaries therefore produces an offset force on the load cell and the increase in measured force, while emitting the jet, is the measure of thrust.

Since the load cell has a range of 100 mN and cannot resolve forces as low as 1 μN, one as well as multiple identical capillaries have been mounted together to increase the overall thrust

and the thrust per capillary has been evaluated from the measured force. In each experiment, first the pressure is set to ambient pressure using the 3-way switch used in the characterization of the thrust stand and the offset reading of the load cell is measured with a Keithley 2000 multimeter in slow mode for average and standard deviation of 50 readings with 200 ms integration time. Then the pressure is set to P_{in} at the pressure controller and using the 3-way switch the pressure is applied to the capillaries and average and standard deviation of 50 readings have been recorded. The standard deviation of the measured forces has been found to be within 5 μN in all the cases.

(a)   **(b)**
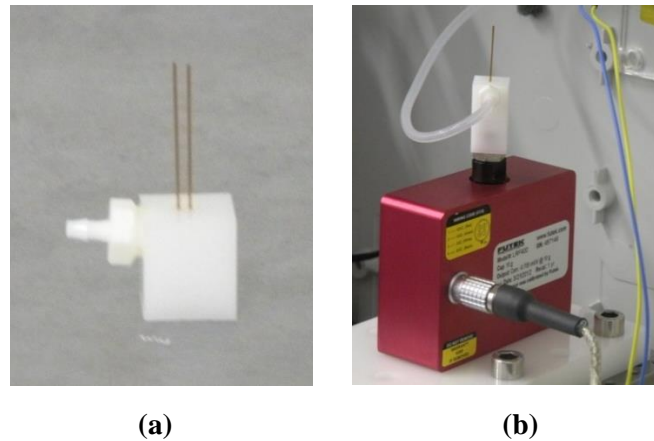
Figure 6.25: The capillary mount for measuring thrust directly on the capillary using a load-cell. The white PMMA piece works as a feed-through between the pressure inlet and th capillary and is directly atached to the load-cell as shown in (b). Three different PMMA mounts capable of mounting one, two and three capillaries are made. In (b), the load cell and the capillary assembly on the load-cell are shown.

In Figure 6.26, direct thrust per capillary measured with different number of capillaries using the load cell is shown. For comparison, measured impingement force on the plate using the FT-S100 force sensor described in section 6.4 is also plotted on the same figure. It can be seen that the thrust per capillary directly measured from one, two and three capillaries are close to the measured thrust from the intercepting plate and follow a non-linear variation with $(P_{in} - P_0)$ similar to the force measured with the FT-S100 sensor on the plate. The case of nineten capillaries ejecting together show large deviation from the results from one, two and three capillaries and increases at a slower rate with applied pressure. For the nineteen capillary case, while possibility of some blocked capillaries or mismatch among the capillaries cannot be completely discarded, the large deviation of thrust per capillary from the case of one, two or three capillaries may be due to very low hydraulic impedance which is not sufficient to retain the pressure difference $(P_{in} - P_0)$ across all the capillaries due to limited mass flow rate of the pressure controller. It can be noted here that the length of the soft tube between the outlet of the presssure controller and the inlet of the capillaries is around 25 cm and length of the capillaries is 1.8 cm. The inner radius of the soft tube is 0.5 mm and that of the capillaries is 75 μm. The ratio of cross-sectional area of a single capillary to that of the soft tube is 2.25% only whereas for the nineteen capillaries the ratio is 42.75%. At such large area ratio, the underlying asumption M_{inlet}^2 << 1 at the inlet of the capillary used in section 6.1.3 is not valid and the incompressible flow of nitrogen through the capillary cannot be assumed. Hence the resulting variation of thrust with the pressure difference is expected to be different from the parabolic profile observed with lower number of capillaries.

For up to three capllaries, the directly measured thrust in Figure 6.26 is close to the force measurement with the FT-S100 sensor on the plate. For the two capillaries case, the difference is quite large, but for one and three capillaries, the difference is within around 10%. However, the standard deviation of directly measured thrust per capillary is quite large, in the range of 5 μN for single capillary and 1 μN for three capillaries. The differences also may arrise due to relative differences in the capillaries. For example looking at Eqn. (6.8), a 1% irregularity in diameter of the capillary can produce nearly 4% change in the hydraulic impedance. Therefore, within the measured uncertainties of around 10%, it can be concluded that the measured thrust from intercepting the particles and directly meaured on the capillary are same.
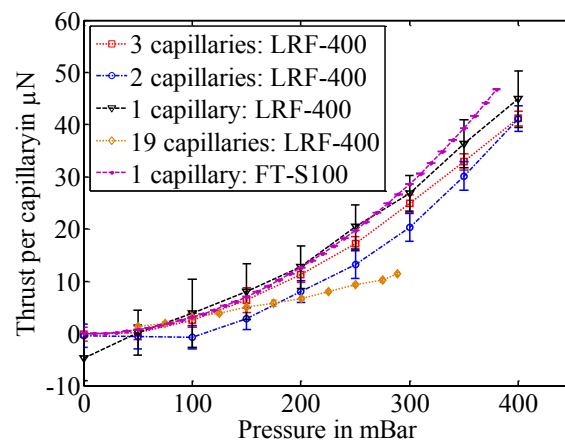
Figure 6.26: Directly measured thrust per capillary by load-cell vs. pressure difference. The average of 50 readings in each measurement done by Keithley 2000 multimeter is shown and the standard deviation of the measurement is shown as error-bar. For comparison, the measured thrust with the FT-S100 force sensor by intercepting the cold-nitrogen jet is also shown.

6.6.   Conclusion

In this chapter, atmospheric characterization of the thrust stand using a cold-nitrogen ejecting capillary has been discussed. Thrust has been generated by applying pressure to the inlet of the capillary and measured by intercepting the emitted particles with the intercepting plate. First, the stability of the output of the force sensor under its own constant weight has been verified to be within ± 10 nN by steady state measurement. However, when the force sensor pushes on the plate, significant drift of the force sensor output has been observed. Homodyne detection technique has been implemented to generate the thrust in form of sqare wave pulses at a reference frequency and using a lock-in amplifier thrust has been measured. The reference frequency and the time constant have been chosen such that the high frequency ripples excited in the plate by pulses of force and the low frequency drift and noise in the output do not interfere with the measurement. With homodyne detection, a noise floor below 10 nN has been observed for reference frequency above 3 Hz and all subsequent measurements have been performed at 4 Hz with 3 sec time constant.Thrust measurement by varying pressure difference up to 400 mBar has been performed and a minimum thrust level less than 10 nN could be measured. Thrust resolution better than 10 nN has been achieved at thrust levels below 30 μN and resolution below 20 nN above thrust levels of 30 μN. The results have been verified up to a thrust of approximately 48 μN althouth the range of

measurement can exceed even 100 μN depending on the initial offset force set by pushing the force sensor on the plate.

Accuracy of the thrust measurement has been verified by varying the position of the capillary and depending on the plate, a precision of about 89% has been obtained. The measured thrust has also been compared with a direct measurement of thrust on the capillary. A summary of the performance of the thrust stand can be listed in Table 6.5.

Table 6.5: A conservative list of properties of the thrust stand experimentally verified in the atmospheric characterization setup by the cold-gas ejecting capillary

Property	Value	Comment
Noise-floor	< 10 nN	Between 4Hz $\leq f_{ref} \leq 10$ Hz
Resolution	< 10 nN	For thrust below 30 μN
	< 20 nN	For thrust above 30 μN
Range	$\sim 2 \times (100\ \mu N - F_{OFF})^*$	Verified up to ~ 48 μN
Repeatability	$R_{p1} \sim 0.2\%$	With the same plate
	$R_{p2} \sim 2\%$	Among different plates
	$R_p \sim 2\%$	$= (R_{p1}{}^2 + R_{p2}{}^2)^{1/2}$
Minimum detectable thrust	< 10 nN	Measured at 10 nN generated thrust
Inaccuracy of impinging force measurement	$E_{r1} \sim 4\%$	Due to response time of the plate. At $f_{ref} = 4$ Hz, can be corrected by calibration.
	$E_{r2} \sim 1\%$	Due to spot-size or distance of the thruster from the plate
	$E_{r3} \sim 10\%$	Due to lateral position offset of the thruster from the centre of the plate
	$E_{r4} \sim 0.2\%$	Due to uncertainty in k_p and k_f
	$E_{r5} \sim 0.1\%$	Due to misalignment of the force sensor
Inaccuracy of thrust measurement	$E_{r6} \sim 10\%$	Due to uncertainty in the relation between F and Th
Overall uncertainty in thrust measurement	$E_r \sim 15\%$	$= (R_p{}^2 + E_{r1}{}^2 + E_{r2}{}^2 + E_{r3}{}^2 + E_{r4}{}^2 + E_{r5}{}^2 + E_{r6}{}^2)^{1/2}$

* Assuming $k_p \approx k_f$

An overall maximum uncertainty of 15% in thrust measurement has been estimated based on repeatibility of the measurements, sources addressed to affect the accuracy of measurement of the impinging force on the plate and the uncertainty in the relation between the measurd force

and thrust. This large inaccuracy is a drawback of the thrust stand, majority of which is contributed by the error E_{r1}, E_{r3} and E_{r6} i.e. the reference frequency f_{ref} (~ 4% at f_{ref} = 4 Hz), position of the thruster relative to the plate (~ 10%) and the uncertainty in the relation between F and Th (~ 10%), i.e. in the value $_|K_|$ in Eqn. (6.9). Directly measuring thrust stands can provide higher accuracy as they are indifferent of these issues. For thrusters properly aligned to the centre of the plate, the position related error in thrust measurement can be much lower than the estimated 10%. The error due to f_{ref} can be calibrated from Figure 6.18 or in a similar process in the operating conditions.

However, a better understanding of the relation between F and Th is required to reduce the inaccuracy in the value of $_|K_|$ to achieve significant reduction in E_{r6}. The thrust stand described in this chapter, however, provides features like compactness, high natural frequency, and isolation of the thrust stand from the thruster and thereby adaptability to different types of thrusters. Also with homodyne detection method described in the chapter, the thrust stand provides immunity over facility vibrations and drift in thrust measurements.

In Chapter 7, measurement of thrust from a electrospray emitter is discussed. These experiments are performed inside a vacuum chamber and without any vibration isolation. The particles emitted by the emitter are high speed charged particles as opposed to low speed neutral particles used in the atmospheric characterization setup. An estimate of the value of $_|K_|$ has been made based on sputtering of aluminium metallization from the plate, however, this has not been experimentally verified in this work. However, the performance metrics summarized in Table 6.5 can be considered as a conservative limit that the thrust stand can potentially provide.

7 Evaluation of the thrust stand for electrospray sources

In this chapter, details of evaluation of the thrust stand using an electrospray propulsion device is discussed. In the Chapter 6, experimental results on characterization of the thrust stand using a cold-nitrogen ejector has been described and the results are summarized in Table 6.5. The experiments had been performed in atmospheric conditions inside a plastic box and on a vibration isolation table. The noise floor of the measurement had been observed to be well below 10 nN when the vibration isolation was enabled and higher, but still less than, 10 nN, when the vibration isolation table was locked and the isolation was disabled. Thrust measurement up to around 50 μN by intercepting the jet of cold nitrogen by the particle intercepting plate had shown that a thrust resolution better than 10 nN is achievable up to around 30 μN thrust and better than 20 nN above this range.

Evaluation of the thrust stand with an electrospray propulsion device poses two major additional constraints on thrust measurement, which are listed below.

- Emission from electrospray devices comprises of charged ions and/or droplets at very high velocity, with kinetic energies of the order of keV. The velocity of the ions can be several orders of magnitude higher than that of a sub-sonic cold-nitrogen jet used in Chapter 6. The momentum transfer of the particles with the intercepting plate may lead to a different relation than $F = Th$ used in the previous chapter and is discussed in more detail in section 7.4.4.

- The vacuum chamber for the electrospray characterization setup is operated with a turbomolecular pump and vibrations from the pumps are directly coupled to the thrust stand and no vibration isolation is used in the setup. Additionally, vibrations originated from the building are also expected to couple to the thrust stand much more severely than in the atmospheric characterization setup used on a vibration isolation table.

It can be noted that the particle intercepting plate had been made with metalized Mylar membrane so that under charge impingement, the plate should not charge up. The natural frequency of the plate was designed and tested to be above 50 Hz (in section 5.6.2 in Chapter 5) and the thrust stand was operated in homodyne detection mode in Chapter 6 at a reference frequency where the amplitude of natural response of the plate is minimal. For electrospray sources as well, the thrust stand was designed to be able to operate in homodyne detection mode using a gate signal. It is shown in section 7.4.2 that the noise floor in the measurement is typically around 10 nN. A porous glass electrospray emitter is used for the experiments which are described in section 7.1. Initial experiments (section 7.2) on the device for its emitted beam composition and spray divergence have been performed first and highly ionic

emission has been observed. The thrust measurement setup is explained in section 7.3 and thrust measurement up to a few μN with the device is described in section 7.4.

Although, higher thrust levels can be measured at higher emitted current levels, the bombardment of the charges has damaged the plate by eroding the aluminium metallization layer from the Mylar membrane and hence tests are performed at lower current and thrust levels with a different plate. Interpretation of the thrust from direct measurement of impingement force F has been a difficult issue and is not addressed with certainty in this chapter. However, a quantitative estimation of the relation is performed from sputtering yield simulation to account for the momentum transfer mechanism of the impinging particles on the plate. This has been discussed in section 7.4.4. A comparison has also been made with indirectly measured thrust by ToF measurement and angular spread measurements which show agreement with the directly measured thrust within around 5−10% due to uncertainty in both, the interpretation of the thrust from impingement force and that in the indirect measurement technique.

7.1. The electrospray source

The electrospray source used for the experiments is a porous borosilicate source under development in LMTS-EPFL. It is desired to evaluate the thrust stand with an electrospray source that can generate thrust in the μN ranges. It can be noted that in Chapter 3 and Chapter 4, micro-fabricated capillary source and tungsten needle had been used for characterization of the ion-guide and the ToF measurement system. However, thrust per capillary from these devices can only be up to a few nN. Arrays of capillaries had also been micro-fabricated [54] and by time-of-flight measurement, the total thrust from the array had been obtained to be a few μN [63], [62].

Lately, porous glass electrospray sources have been under development, which can produce high current density, high ionic emission. In Figure 7.1 (a), a schematic of the porous glass linear emitter strips used for evaluation of the thrust stand is shown. The emitter is fabricated by Dr. Daniel Courtney from commercial borosilicate glass filter discs using milling machine, details of which can be found in Ref. [53]. It consists of trapezoidal prisms approximately 350 μm tall as shown in Figure 7.1 (b) and a half-angle approximately 30°. The apex radius of curvature is not controlled, but typically a few 10's of μm. Each emitter consists of nine strips. The extractor grid comprises of nine 350 μm wide and 9 mm long channels laser cut from 100 μm thick molybdenum sheet and aligned to the emitter strips using an optical microscope and stuck with layers of double sided kapton tape. The misalignment is typically of the order of a few 10s of μm along the length of the emitter. Before aligning and bonding the extractor grid, the emitter strips are wetted with degassed ionic liquid EMI-BF$_4$ and is kept in vacuum for filling the pores after alignment and bonding is done.

7.2. Initial characterization results of the electrospray device

Initial characterization of the porous glass electrospray device has been performed by the Dr. Daniel Courtney in LMTS-EPFL and the results discussed in this section are reported with his consent. Emitted current (I_{beam}) vs. emitter voltage (V_{em}) has first been found out for the device in positive and negative polarity of emission. Then angular spread measurements and time-of-flight measurements have also been performed before using the device for evaluation

of the thrust stand.
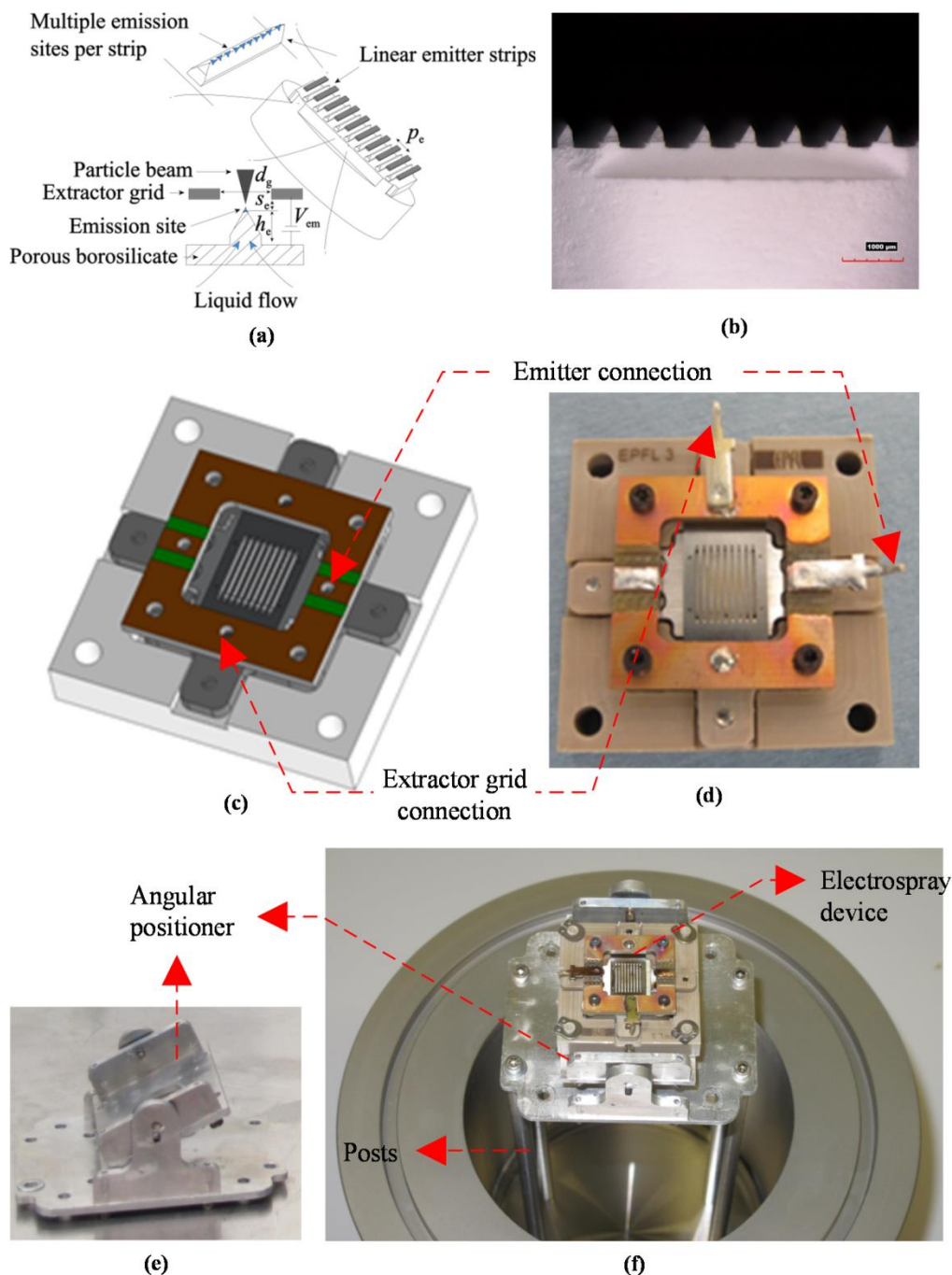
Figure 7.1: (a) Schematic cross-section of the porous borosilicate electrospray emitter. It consists of a porous borosilicate disc, milled in strips with trapezoidal shape as emission site. A 100 μm thick molybdenum extractor grid is optically aligned with the strips within a few 10's of μm. The grids have d_g = 350 μm wide and 9 mm long channels for the 9 emitter strips. (b) Side profile of the electrospray device. The height of the nine trapezoidal strips is approximately 350 μm. (c) A schematic and (d) picture of the assembly for electrical contacts and ionic liquid feed. (e) Picture of the angular positioner and (f) electrospray device mounted on the angular positioner and on the extension tube with posts. The extension tube with the electrospray device is mounted on the vacuum chamber on the right side of Figure 7.8 (b).

7.2.1. I-V characteristics

First, I_{beam} vs. V_{em} relations have been obtained in bipolar mode in which the emitter voltage is alternated between $+V_{\text{em}}$ and $-V_{\text{em}}$ with a repetition rate of 2 Hz. The voltage V_{em}, emitter current I_{em} and the extractor current I_{ex} are monitored for 3 sec at each $|V_{\text{em}}|$. The emitted beam current I_{beam} is defined as

$$I_{\text{beam}} = I_{\text{em}} - I_{\text{ex}} \tag{7.1}$$

i.e. by subtracting the current intercepted by the extractor grid from the current read on the emitter current monitor. In Figure 7.2 (a) and (b), the average I_{em} and I_{ex} are plotted against the emitter voltage $|V_{\text{em}}|$ in positive and negative polarities respectively. The error-bars on the average current values represent the standard deviation of the measured current after eliminating initial settling time immediately after each transition of V_{em} polarity, and hence represent the random noise in the current measurement and also overall variation of the currents with time during the 1.5 sec measurement time in each polarity. The extractor current from the device is typically within 5% of the emitter current; i.e. 95% of the emitter current is passed through the extractor grid as the beam current. However, it is shown in section 7.4.1 that the current intercepted by the extractor is found to be much more from the same device during thrust measurement, after several cycles of emission had been performed from the device during I_{beam} vs. V_{em} sweeps, angular current distribution scan and ToF measurements and after removing the emitter from the setup and re-installing it in the thrust measurement setup.

(a)   **(b)**
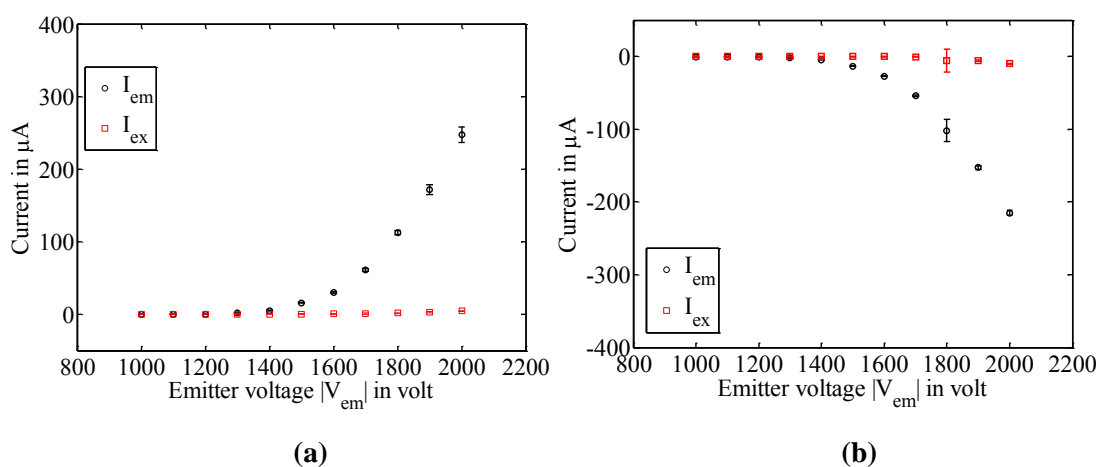
Figure 7.2: Plot of emitter current I_{em} and extractor current I_{ex} against emitter voltage $|V_{\text{em}}|$ during initial I-V sweep in bipolar mode and separated in positive (a) and negative (b) polarities. Extractor intercepts no more than 5% of the emitter current.

In Figure 7.3, (a) and (b), the I_{beam} vs. V_{em} relations are plotted in both polarities of emission from the initial I_{beam}-V_{em} measurement, after an angular spread measurement experiment and after time-of-flight measurement which are discussed later in this section. It can be seen that, the emitted beam current in both polarities is an increasing function of the emitter voltage $|V_{\text{em}}|$ and the current reaches 100's of μA as the emitter voltage is increased to more than $|V_{\text{em}}|$ = 2000 V. However, after the angle scan and flight time measurements, the emitted current reduced significantly, as is shown in section 7.4.1.

(a)　　　　　　　　　　　　　　　**(b)**
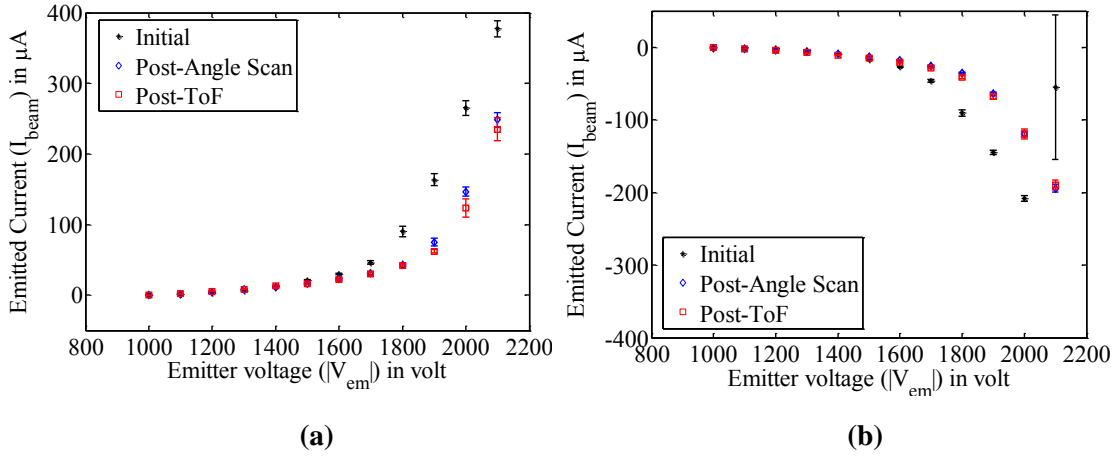
Figure 7.3: Plot of emitted beam current I_{beam} against emitter voltage $|V_{em}|$ in bipolar mode during initial I-V sweep, after angular spread scan and after ToF measurement. I_{beam} is obtained from subtraction of I_{ex} from I_{em}. The positive (a) and negative (b) polarity results are separated from the bipolar operation. The angular scan and ToF measurement will be discussed later in this section. It can be seen that the emitted beam current goes down for a given emitter voltage with increasing cycle of operation.

7.2.2. Angular scan

After initial I_{beam}-V_{em} measurements, angular spread measurements have been performed on the device. In this experiment, the angular position of the centre of the electrospray source with respect to the axis of emission (aligned to the centre of the detector) is changed parallel and perpendicular to the strips of the emitter assembly and a small fraction of the emitted current is allowed through a small aperture far downstream from the emitter and collected on a Faraday Cup detector of 12.5 mm diameter. The angles are changed from 0° (aligned with the axis of the detector) to 40° and then from 0° to -40° in steps of 5°.

(a)　　　　　　　　　　　　　　　**(b)**
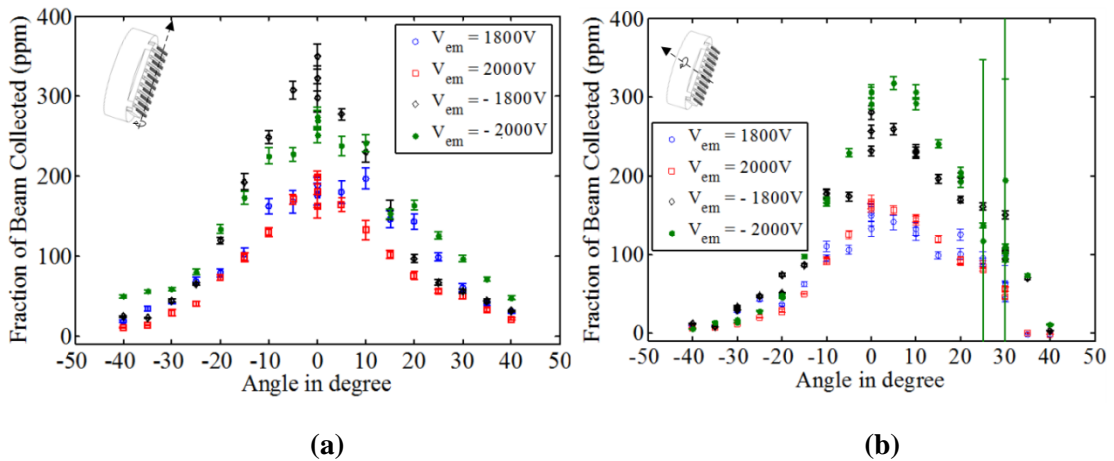
Figure 7.4. Fraction of current detected vs. the angular position of the detector when the electrospray source is rotated about an axis through its centre (a) perpendicular and (b) parallel to the direction of the strips of emitter.

In Figure 7.4 (a) and (b), the angular distribution of the current fraction (in p.p.m of the beam current I_{beam}) received on the Faraday cup detector are shown for positive and negative polarities of emission by perpendicular and parallel scans respectively. It can be seen that the

maximum current fraction received by the detector is below 400 ppm due to the very small collection area and the aperture size for allowing the charges to be detected. The parallel angular scan shows a slight angular offset of the maxima to around 5°. The relatively smaller current fractions in positive polarities can be an indication of neutralization by the secondary electrons generated from the wall of the vacuum chamber by impact of the positively charged ions. The angular distribution of the current provides a correction factor in the thrust calculation which is discussed in the section 7.2.4.2.

7.2.3. Time of flight measurement

Time-of-flight measurement of the emission has been performed in both polarities of emission from the current traces with Lecroy wavesurfer 424 oscilloscope with 40 averages on traces. The high voltage pulse generator PVX-4140 with a high voltage power supply SRS PS350 has been used to generate the gate signal to trigger the traces at time $t = 0$ and FEMTO DHPCA transimpedance amplifier has been used for converting the fast current traces into voltage for measuring with the oscilloscope. In Figure 7.5, the time-of-flight trace at $V_{em} =$ 2000 V is shown and in Figure 7.5 (b) the traces have been zoomed in close to the triggering time. It can be seen that the emission consists of predominantly monomers and dimers and a small fraction comprising of trimers; the corresponding flight times are denoted as t_0, t_1 and t_2 respectively in Figure 7.5 (b). The non-zero slope corresponding to the dimer and trimer current and spreading of the transitions corresponding to discrete ion-masses is indicative of fragmentation between the emitter and the extractor during its acceleration, a phenomenon commonly observed in electrospray emission process [35], [47], also discussed in section 4.1.2 and 4.2.3 in Chapter 4. Fragmentation downstream from the extractor should not affect the time-of-flight traces of an otherwise un-fragmented emission, because of unchanged flight speed after fragmentation.

(a)   **(b)**
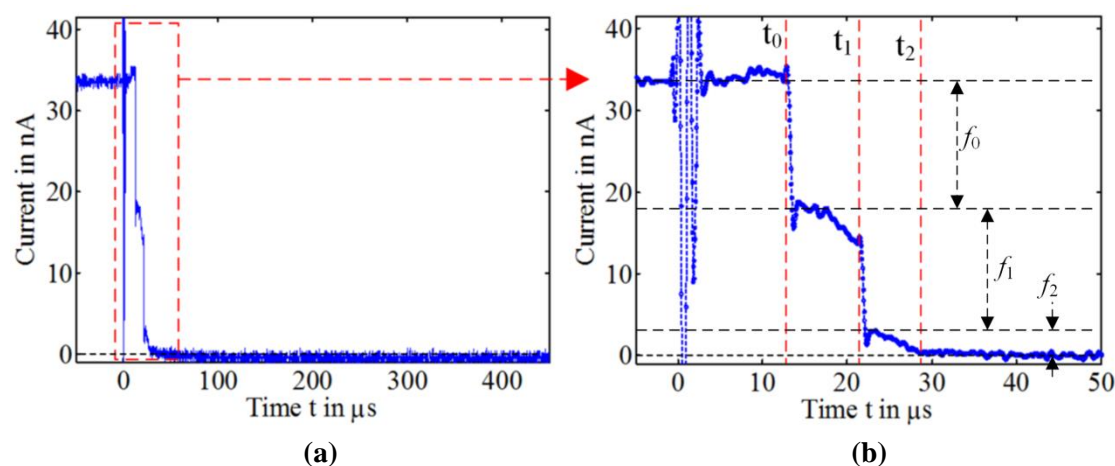
Figure 7.5: (a) Time of flight trace of the porous glass electrospray emitter at emitter voltage V_{em} = 2000 V. The gate signal (not shown here) is triggered at time t = 0 and 40 averages over samples at each V_{em} are taken. (b) Zoomed in traces show that the emission principally consists of monomers and dimers. t_0, t_1 and t_2 represent the flight times of monomers, dimers and trimers, and f_0, f_1 and f_2 represent the currents corresponding to monomers, dimers and trimers respectively. The non-zero slope corresponding to the dimer current indicates fragmentation of the dimer, leading to loss of charge without losing flight speed.

The slight increase in the current for the monomer, between $t = 0$ and $t = t_0$, is not explained, however, since they correspond to very low flight times, they do not contribute to thrust significantly and for thrust analysis, they can be ignored.

7.2.4. Thrust analysis

Looking at Figure 7.3, it can be inferred that the emitted current levels gradually decrease over repeated cycles of bipolar experiments. Hence the thrust that can be indirectly calculated from the time-of-flight measurements, angular spread and I_{beam}-V_{em} relations are not expected to be the same during direct thrust measurement. However, a few correction factors can be evaluated from the angular spread and the poly-dispersity of the emission, and assuming these parameters to be constant during thrust measurement using the thrust stand, a comparison can be made with the expected thrust at the current level during thrust measurement with the thrust stand.

Expression of thrust from an individual charge species with mass m and charge q, all emitted parallel to the axis of emission, can be recalled from Chapter 1, Eqn. (1.3)

$$Th_{\mathrm{m}} = I \sqrt{\frac{2mV_{\mathrm{em}}}{q}} \tag{1.3}$$

where I is the emitted current, qV_{em} is the assumed kinetic energy of the emitted ions neglecting energy deficits. RPA measurement of the porous glass electrospray devices suggest a 20 V to 60 V energy deficits [53] and this will contribute to 1.5–3.0% errors in estimated thrust for emitter voltage $|V_{\mathrm{em}}|$ between 1 kV and 2 kV.

7.2.4.1 Correction from ToF measurement

From the time-of-flight traces, it can be seen that the emission comprises of multiple types of ions, mostly monomer and dimers. The poly-dispersity of the emission is taken into account, when thrust is calculated from the time-of-flight traces, using the relation

$$Th_{\mathrm{ToF}} = -\frac{2V_{\mathrm{em}}}{L} \int_0^\infty t \frac{\mathrm{d}I}{\mathrm{d}t} \mathrm{d}t \tag{7.2}$$

where L is the flight length. A thrust factor γ_0 can be defined such that thrust Th_{ToF} obtained from the time of flight traces for a poly-dispersive emission with total emitted current I_{beam}, can be related to a hypothetical emission of only monomers at the same current I_{beam} such that

$$Th_{\mathrm{ToF}} = \gamma_0 \left(I_{\mathrm{beam}} \sqrt{\frac{2m_{\mathrm{monomer}}V_{\mathrm{em}}}{q}} \right) = \gamma_0 Th_{\mathrm{monomer}} \tag{7.3}$$

where m_{monomer} is the mass of a monomer, and $Th_{\mathrm{monomer}} = I_{\mathrm{beam}}(2m_{\mathrm{monomer}}V_{\mathrm{em}}/q)^{1/2}$ is the thrust from a hypothetical ideal thruster emitting monomers only, all aligned to the direction of emission. In that case, γ_0 can be obtained from the time of flight traces as

$$\gamma_0 = -\int_0^{\infty} \left(\frac{t}{t_0}\right) \frac{d}{dt}\left(\frac{I}{I_{beam}}\right) d\left(\frac{t}{t_0}\right) \tag{7.4}$$

where $t_0 = L(m_{monomer}/2qV_{em})^{1/2}$ is the flight time of the monomer. This definition of γ_0 enables a view to the consistency of the beam composition and provides a direct correction factor to be multiplied to the ideal thrust $Th_{monomer}$ obtainable from I_{beam}-V_{em} relations, had there been only monomer emission. For example, for pure monomer emission, $\gamma_0 = 1$ and for pure dimer emission, $\gamma_0 = (m_{dimer}/m_{monomer})^{1/2}$, m_{dimer} being the mass of a dimer. If only monomers and dimers are present in the emission, γ_0 depends on the relative current levels of the monomers and dimers, $I_{monomer}$ and $(I_{beam} - I_{monomer})$ respectively, as shown in Figure 7.6 for ionic liquid EMI-BF$_4$ in positive and negative polarities of emission.
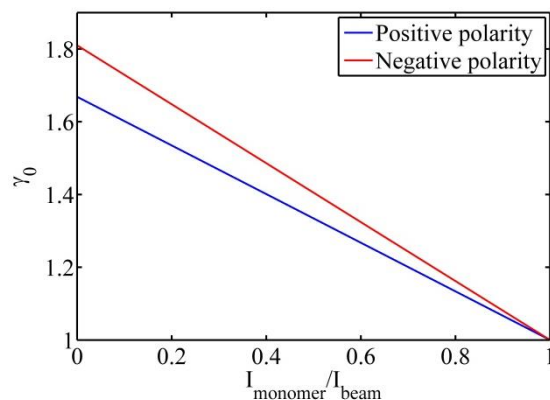
Figure 7.6: Calculated theoretical plot of thrust correction factor γ_0 for ionic liquid EMI-BF$_4$ against the ratio of monomer current to total beam current for an emission comprising of only monomers and dimers. For the same proportion of monomer and dimer current in positive and negative polarity, γ_0 is higher in negative polarity due to higher dimer to monomer mass ratio.

The value of γ_0 has been evaluated from the time-of-flight traces from in both polarities and the calculated values are listed in Table 7.1.

Table 7.1: Values of thrust correction factor γ_0 calculated from time-of-flight traces in positive and negative polarity of emission from the porous glass electrospray emitter

Positive polarity of emission				Negative polarity of emission			
V_{em} in volt	Number of time of flight traces	Mean γ_0	Standard deviation of γ_0	V_{em} in volt	Number of time of flight traces	Mean γ_0	Standard deviation of γ_0
1800	9	1.436	0.023	−1800	9	1.580	0.064
1900	3	1.454	0.017	−1900	8	1.665	0.074
2000	10	1.475	0.028	−2000	10	1.634	0.048
	Overall	1.452	0.034		Overall	1.625	0.069

The number of traces at each emission voltage is also listed in the same table and the mean value of γ_0 and its standard deviation are calculated. It can be seen that for $|V_{em}|$ between 1800 V and 2000 V, γ_0 is higher in negative polarity. However, over the emitter voltage range $|V_{em}|$ between 1800 V to 2000 V, the obtained values of γ_0 are reasonably consistent with 2.3% and 4.3% standard deviation about an average 1.452 and 1.625 in positive and negative polarity respectively. Although ToF measurements have not been performed at $|V_{em}|$ lower than 1800 V, and at non-zero angles with respect to the detector, in the effort of comparing direct thrust measurement using the thrust stand, following assumptions are made in γ_0:

- $\gamma_0 = 1.452$ in the entire range of positive emission voltages.

- $\gamma_0 = 1.625$ in the entire range of negative emission voltages.

- γ_0 is constant over the entire beam half-angle of emission in a given polarity of emission.

7.2.4.2   Correction from angular spread

To correct Th_{ToF} for angular spread, the parallel and perpendicular beam-shapes shown in Figure 7.4 (a) and (b) are first converted into a hypothetical axis-symmetric beam shape as shown in Figure 7.7 (a). First, the negative angle (θ) axis is flipped to the positive side for both, parallel and perpendicular beam shapes, and averaged to get an axis-symmetric beam shape as shown in Figure 7.7 (a). If the current at different angles are measured with a probe of area A_p by changing the angle θ from 0° to θ_{em}, from a constant distance R_p as shown in Figure 7.7 (b), the current density at the centre of the probe can be defined as
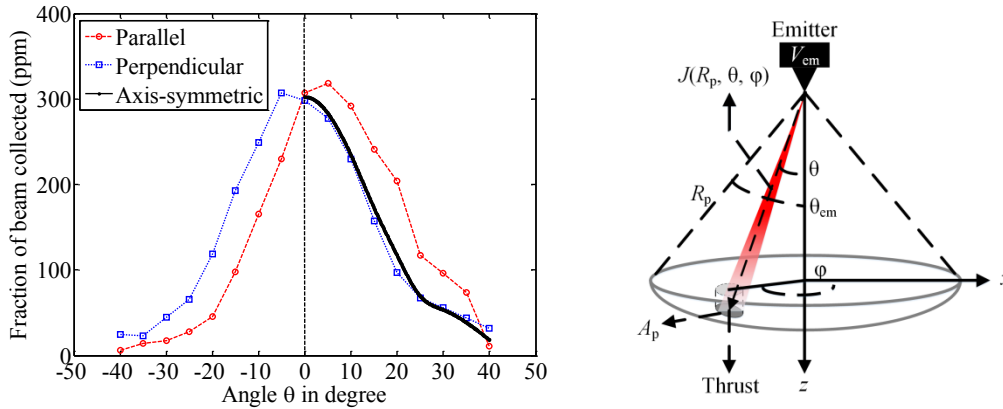
Figure 7.7: (a) Parallel and perpendicular beam scan results at $V_{em} = 2000$ V and conversion into an axis-symmetric beam shape. For the conversion, the negative angle (θ) axis is flipped to the positive side for both, parallel and perpendicular beam shapes, and averaged to get an axis symmetric beam shape. (b) Schematic of current measurement at different angles θ and representation of thrust.

$$J(R_p, \theta, \varphi) = p(\theta) \frac{I_{beam}}{A_p} \tag{7.5}$$

where, $p(\theta)$ is the axis-symmetric fraction of total beam current I_{beam} collected by the probe, calculated as described in the last paragraph and shown in p.p.m. in Figure 7.7 (a). Integrating over the entire area of the spherical surface at a distance R_p gives the total current, i.e.

$$R_p^2 \int\limits_{\theta=0}^{\theta_{em}} \int\limits_{\varphi=0}^{2\pi} J(R_p,\theta,\varphi) \sin(\theta)\, d\theta\, d\varphi = I_{beam} \tag{7.6}$$

or

$$\int\limits_{\theta=0}^{\theta_{em}} p(\theta) \sin(\theta)\, d\theta = \frac{A_p}{2\pi R_p^2} \tag{7.7}$$

Thrust, in the direction z shown in Figure 7.7 (b), due to a small current element dI in an infinitesimal area $dA = R_p^2 \sin\theta\, d\theta\, d\varphi$ on the spherical surface can be written as

$$dTh = \gamma_0 \left(\sqrt{\frac{2m_{monomer}V_{em}}{q}} \right) dI \cos(\theta)$$

$$= \gamma_0 R_p^2 \left(\sqrt{\frac{2m_{monomer}V_{em}}{q}} \right) J(R_p,\theta,\varphi)\cos(\theta)\sin(\theta)\, d\theta\, d\varphi$$

where use of Eqn. (7.3) has been made with the assumption that γ_0 is constant over the entire beam cross-section. Therefore, the total thrust can be written by integrating over the entire area over the spherical surface at a distance R_p that covers the entire emitted plume as

$$Th_{indir} = \gamma_0 R_p^2 \sqrt{\frac{2m_{monomer}V_{em}}{q}} \int\limits_{\theta=0}^{\theta_{em}} \int\limits_{\varphi=0}^{2\pi} J(R_p,\theta,\varphi) \cos(\theta)\sin(\theta)\, d\theta\, d\varphi$$

$$= \gamma_0 I_{beam} \sqrt{\frac{2m_{monomer}V_{em}}{q}} \frac{\int\limits_{\theta=0}^{\theta_{em}} p(\theta)\cos(\theta)\sin(\theta)\, d\theta}{\int\limits_{\theta=0}^{\theta_{em}} p(\theta)\sin(\theta)\, d\theta}$$

$$= \beta_0 \gamma_0 Th_{monomer}$$

$$= \beta_0 \gamma_0 I_{beam} \sqrt{\frac{2m_{monomer}V_{em}}{q}} \tag{7.8}$$

where use of definition of $Th_{monomer}$ from Eqn. (7.3) has been made. Here, an angular spread correction factor β_0 is defined from the measured axis-symmetric current fractions $p(\theta)$ as

$$\beta_0 = \frac{\int\limits_{\theta=0}^{\theta_{em}} p(\theta)\cos(\theta)\sin(\theta)\, d\theta}{\int\limits_{\theta=0}^{\theta_{em}} p(\theta)\sin(\theta)\, d\theta} \tag{7.9}$$

Therefore, incorporation of the two correction factors, β_0 and γ_0 enables from Eqn. (7.8) to evaluate the thrust assuming emission of monomer only at the same emitted current level I_{beam}. β_0 has been evaluated at $V_{em} = \pm1800$ V and $V_{em} = \pm2000$ V by numerically integrating

the numerator and denominator in Eqn. (7.9) from the distribution $p(\theta)$. In Table 7.2, the calculated values of β_0 are listed.

It can be seen that the values of β_0 obtained in both polarities of emission are very stable at around 0.92 and an approximately 8% deficit in the thrust is expected in both polarities within the range $|V_{em}|$ between 1800 V and 2000 V from thrust obtained from time-of-flight measurement only, i.e. from Th_{ToF}. In comparing with directly measured thrust from the thrust stand, the values of $\beta_0\gamma_0$ are used from Table 7.2 in Eqn. (7.8) along with the measured beam current I_{beam}.

Table 7.2: Values of angular spread correction factor β_0 for thrust from the porous glass electrospray emitter

Positive polarity of emission		Negative polarity of emission	
V_{em} in volt	β_0	V_{em} in volt	β_0
1800	0.917	−1800	0.919
2000	0.933	−2000	0.930
Overall	0.925 ± 0.008	Overall	0.926 ± 0.005

7.3. Thrust stand characterization setup with electrospray source

For evaluation of the thrust stand with electrospray source, the following modifications have been made in the setup from the atmospheric characterization setup. The modifications are based on the planned setup for using the thrust stand inside the electrospray characterization vacuum chamber as proposed in section 5.1 in Chapter 5.

7.3.1. Modification to the thrust stand

Following modifications are made in the thrust stand from the way it was used in the atmospheric characterization in Chapter 6.

- For homodyne detection, electrostatic gate is used where, by applying pulsating signal at a reference frequency, the emitted charged particles from the electrospray emitter can be blocked or allowed to impinge on the particle intercepting plate and homodyne detection can be done at the same reference frequency. The gate electrode assembly is manufactured from 1 mm thick stainless steel plates. It consists of three plates separated by 6.25 mm, each having a 50.8 mm aperture (area $A_a = 20.2$ cm^2), where the pulsating gate signal is applied to the middle electrode as shown in Figure 7.8 (a). Each of the electrodes has a stainless steel grid of 25.4 μm diameter wires and 81% optical transparency spot-welded on the plates. The other two electrodes, on both sides of the gate electrode can either be grounded or a negative potential can be applied to them in order to minimize emission of secondary electrons from the plate while charges at very high velocity are impinging on it. In the present experiments, both the electrodes are connected to a −40 V power supply for reducing secondary electron emission. The gate potential is set to $V_{gate} = \pm 3000$ V depending on the

polarity of emission such that the gate signal pulsates between 0 V and V_{gate} during homodyne measurement of thrust.

(a)

(b)

(c)
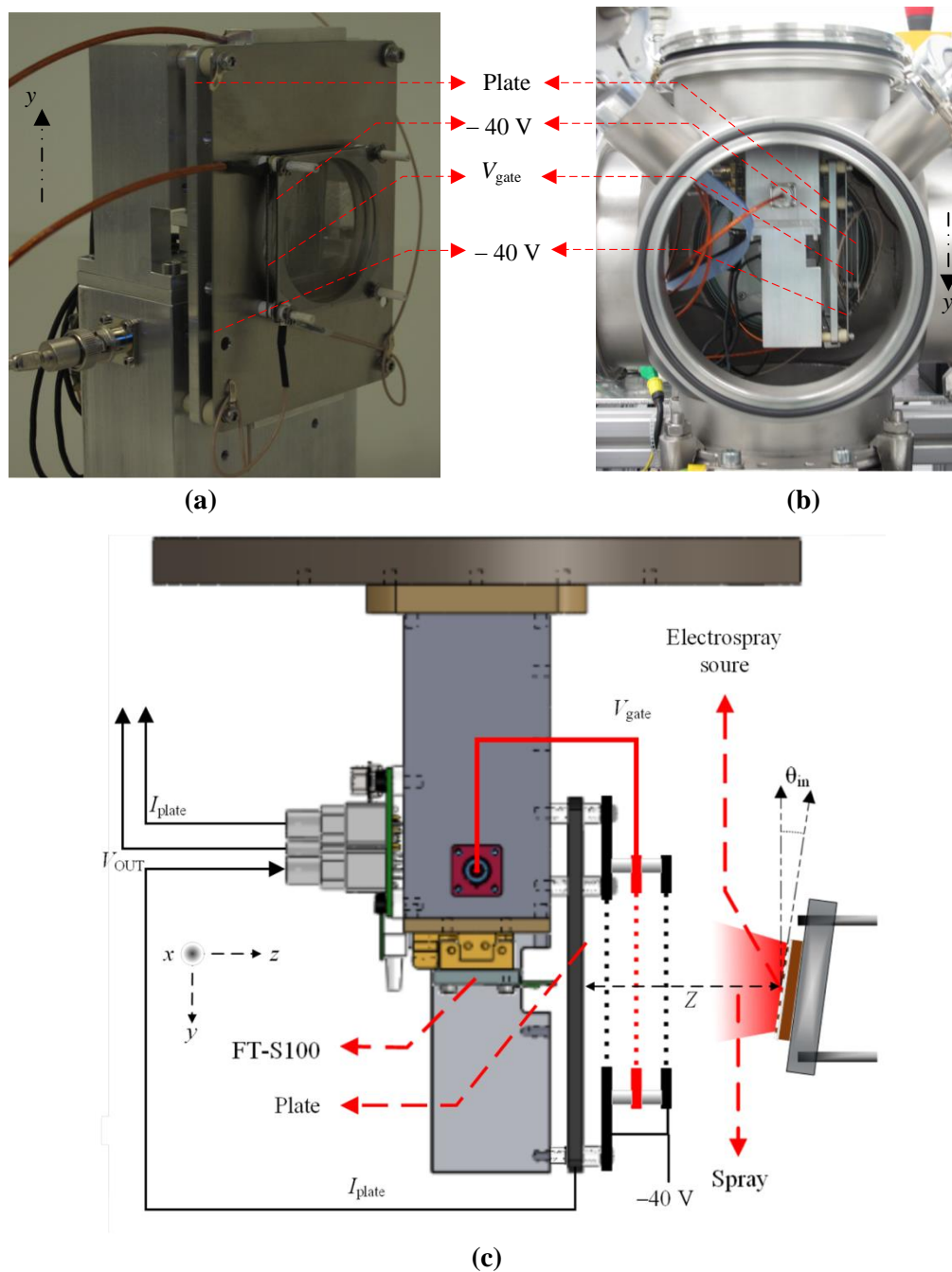
Figure 7.8: (a) The thrust stand with the gate electrode for homodyne detection and –40 V electrodes for reducing secondary emission. The gate electrode is in between the two electrodes at –40 V and a pulsating signal between levels 0 V and V_{gate} at reference frequency f_{ref} is applied to the gate electrode. The electrodes are 6.25 mm apart from each other and from the particle intercepting plate through ceramic stand-offs. (b) The thrust stand is mounted inside the vacuum chamber upside down. The electrospray device is placed on the right side. (c) A schematic of the same showing the thrust stand, the electrodes, the thruster and electrical connections to the thrust stand.

- The thrust stand is mounted on the ISO-160 flange that was modified to attach the

thrust stand to it (Figure 5.11 in Chapter 5). The stand is mounted on the base plate and then attached on the flange using vented M4 screws. The thrust stand is placed inside the vacuum chamber upside down relative to the atmospheric tests using the modified flange as the top flange of the six-way cross vacuum chamber as shown in Figure 7.8 (b).

- The support frame, the gate electrode and the -40 V electrodes are electrically isolated from each other and from the rest of the thrust stand using ceramic threaded stand-offs. The stand is electrically grounded as it is attached to the ISO-160 flange. For monitoring the current on the plate, a coaxial cable with a mini-BNC connector from the support frame is connected to the PCB of the thrust stand and from the PCB, another coaxial cable is connected to the feed-through of the vacuum chamber. Details of the configuration can be found in Chapter 5 in section 5.2.2. Details of the peripheral experimental setup are discussed in section 7.3.2.

7.3.2. The experimental setup

In Figure 7.9, a schematic of the experimental setup is shown. The thrust stand shown in Figure 7.8 is mounted inside the six-way cross vacuum chamber. Two high voltage power supply PS350 [238] are used for generating the emitter voltage V_{em} and the gate voltage V_{gate}.
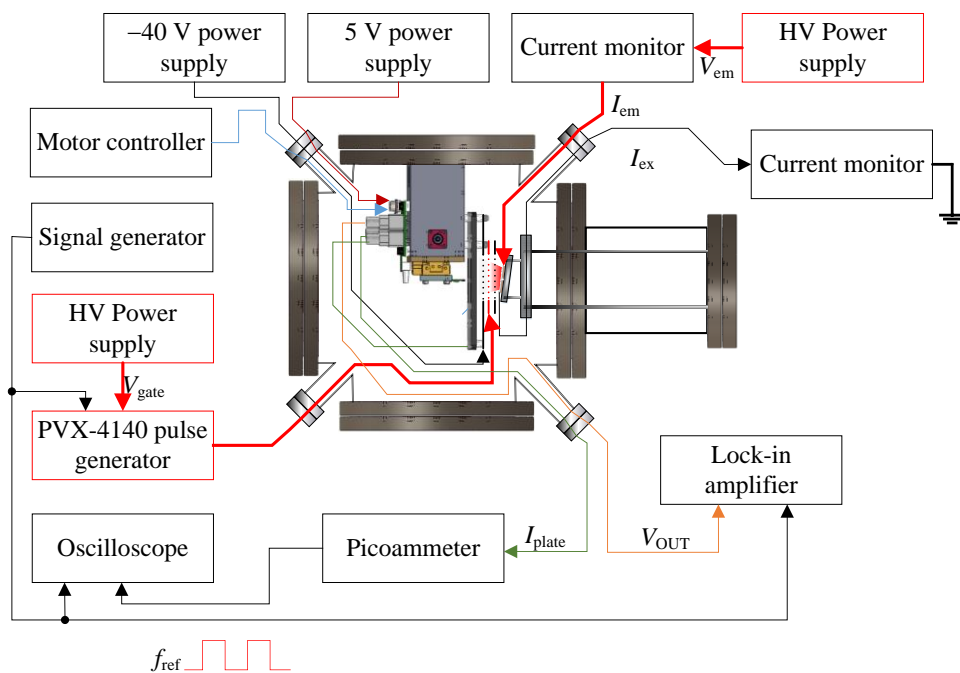
Figure 7.9: Schematic of the experimental setup for evaluation of the thrust stand for electrospray devices. The connections to the thrust stand inside the vacuum chamber have been shown in Figure 7.8.

For the gate signal, the high voltage pulse generator PVX-4140 [175] is used to generate high voltage pulses with less than 100 ns rise time. A signal generator Agilent 33220A [234] is used for generating the TTL square wave gate control signal. The gate voltage V_{gate} is set to ± 3000 V depending on the emission polarity so that when turned on, it can block all the charges irrespective of the kinetic energy of the emitted particles up to 2 keV. The same TTL

signal is used as the reference signal for the lock-in amplifier which detects the thrust at the first harmonic of the modulated thrust signal from the force sensor FT-S100. The current on the detector plate, I_{plate} can be monitored using a picoammeter (Keithley 6487 [146]) and the analog output of the picoammeter can be fed to an input channel of the oscilloscope. However, it is discussed in section 7.4 that the plate current measurements have been discarded due to damage of the picoammeter during thrust measurement. The emitter supply passes through an opto-coupler based current monitor circuit and through SHV feed-through the signal is applied to the emitter inside the vacuum chamber. The extractor connection is passed through another identical current monitor to ground. The current monitors consist of switchable transimpedance gains. For the entire set of experiments, the transimpedance gains in the emitter current monitor and the extractor current monitor are set to pre-calibrated values of 9402 V/A and 45430 V/A respectively. The relatively lower gain setting for the emitter current monitor circuit is because the extractor current is expected to be a small fraction of the relatively large emitted current.

7.4.   Thrust measurement from the electrospray source

In this section, the experimental results on thrust measurement with the thrut stand from the electrospray device are described. First, measurement of I-V characteristics of the device are repeated. Then the lock-in amplifier setting and the thrust measurement results are discussed.

Damaged Plate 2

Aluminium eroded

Unaffected Mylar
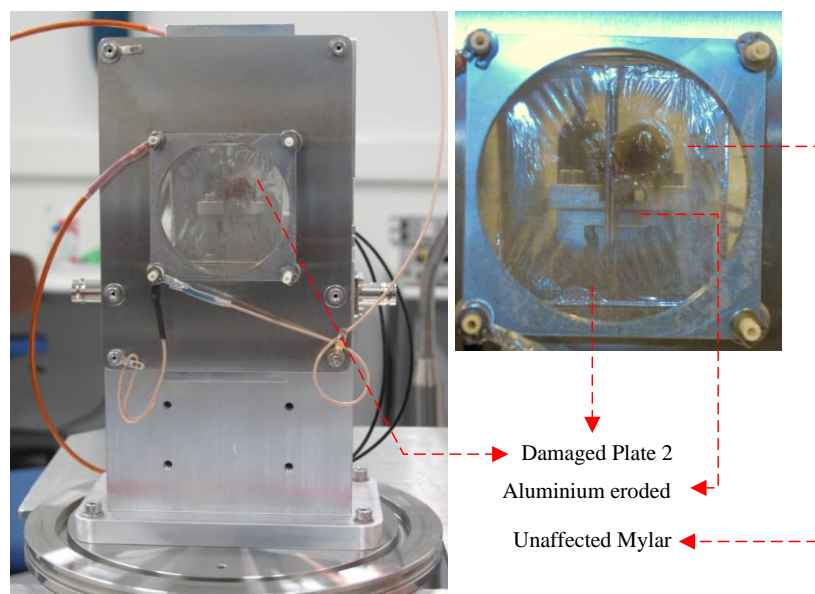
Figure 7.10: Damaged particle intercepting plate Plate 2 during initial electrospray thrust measurement. Aluminum metalization on the Mylar film is eroded due to bombardment of high speed charged particles from the electrospray source. The force sensor FEMTO-1 is also damaged due to charging of the plate under further charge bombardment. For subsequent experiments, Plate 3 with properties listed in Table 5.17 and Table 5.18 and force sensor FEMTO-2 with properties listed in Table 6.1 are used.

During initial trials, thrust measurement was performed in unipolar mode up to ~ 20 μN with beam current in the range of 100s of μA for several minutes. The electrospray source is placed on the angular positionar which was used for angular scan experiments and a 5° angular offset was given about the axis parallel to the emitter strips so that the maxima of the

current fraction in Figure 7.4 is in the direction normal to the particle intercepting plate at its centre. The distance between the emitter and the particle intercepting plate is 28 mm. It can be noted that for a 40° beam half-angle, as observed in Figure 7.4, the spot size on the plane of the particle intercepting plate is expected to be 23.5 mm in radius and the plate is expected to intercept almost all the emitted particles.

However, it was observed that, under continuous bombardment of charges with such high flux for several minutes eroded aluminium coating on the Mylar film in the particle intercepting plate Plate 2. In Figure 7.10, a picture of the damaged plate is shown. Aluminium metalization on the Mylar film on the plate is removed around the centre of the plate corresponding to the spot of the bomabardng charges whereas towards the edge of the plate, the metalization is unaffected. A more detailed discussion of the erosion is provided in section 7.4.4; however, due to removal of the metalization, the Mylar membrane was charged under further bompardment of charged particles from the emitter and as a result, the force sensor FEMTO-1 in contact with the plate was damaged due to possible arcing through the plate. Therefore, later on, the current flux and the bombarding charges' kinetic energy are reduced by limiting the emitted current to less than ±50 μA. Plate 3 has been used for subsequent thrust measurements with spring constant k_p = 46.21 N/m and natural frequency f_p = 57.54 Hz, along with force sensor FEMTO-2 with sensitivity S_F = 51.47 μN/V and spring constant k_f = 50.00 N/m as described in Table 5.17, Table 5.18 in Chapter 5 and Table 6.1 in Chapter 6 and thrust measurements are performed up to a few μN only. For protection of the picoammeter a 100 kΩ resistor is put in series. With these protections, no further visible damage in the plate is observed after thrust measurement on the plate as the current levels are limited.However, it is later found that the picoammeter was damaged during initial attempts due to arcing and the current readings from the plate have been discarded.

Another problem during initial attempts of thrust measurement has been partial damage of the electrospray source itself, in which, the emiter and the extractor grid were shorted through contaminations generated during spraying. By optical observation the contamination was later removed using a knife and all the thrust measurement results shown in the following sections are after repairing the source.

7.4.1. I-V characteristics

Before and during thrust measurement, emitted current I_{beam} vs. emitter voltage V_{em} profiles of the electrospray device is checked. In this case, unlike the bipolar initial experiments, the emitter voltage is set to V_{em} and the emitter current I_{em} and extractor current I_{ex} are monitored for 100 samples with an interval of approximately 350 ms between samples by continuously electrospraying at the set V_{em}. The measured currents at each sample are an average of 50 measurements using analog input system and the average of the 50 samples are recorded. In Figure 7.11 (a) and (b), the plot of I_{em}, I_{ex} and V_{em} are shown as function of time for V_{em} = 1800 V and V_{em} = −1800 V respectively. The emitter voltage is turned on to V_{em} at approximately 38 sec from the beginning of monitoring the currents. The average offset in the current monitor channels in the first 100 samples are recorded and then subtracted from the next 100 samples when V_{em} is applied. After completing measurement at one polarity of V_{em}, the emitter voltage is turned off and then set to the opposite polarity and the measurement is repeated.

The reason for using a prolonged unipolar spray for I-V measurements is that the same time-scales are later used during thrust measurement, which is discussed in section 7.4.3. It is described in section 7.4.2 that a time constant T_c = 1 sec and reference frequency f_{ref} = 10 Hz have been used for the lock-in amplifier for thrust measurement and typically 5 sec or more time is required for the lock-in amplifier output to settle to its final value [236] with a constant thrust input, measured by the force sensor. Therefore, for reliable measurement of thrust, at least 10 sec or more continuous spraying at a given $|V_{em}|$ is required so that stability of the measured thrust can be observed and compared with the beam current I_{beam}. This can be implemented by operating in bipolar mode with a repetition frequency set to less than 0.1 Hz and pulsating the gate signal at 10 Hz so that at each polarity of emission, the lock-in amplifier output can settle to its final value if continuous thrust is generated during the emission time. This scheme requires four high voltage power supplies, two for the emitter and two for the gate. Since the gate voltage V_{gate} pulsates between 0 to 3000 V and 0 to −3000 V, and the gate pulse generator, PVX-4140 used in the experiments, has a maximum 3500 V differential input voltage range, automatic bipolar operation has been avoided. Here, two power supplies are used; one for the emitter and one for the gate and polarity of emission and that of the gate voltage are changed manually at the power supplies after long continuous spray in each polarity.

(a)   **(b)**
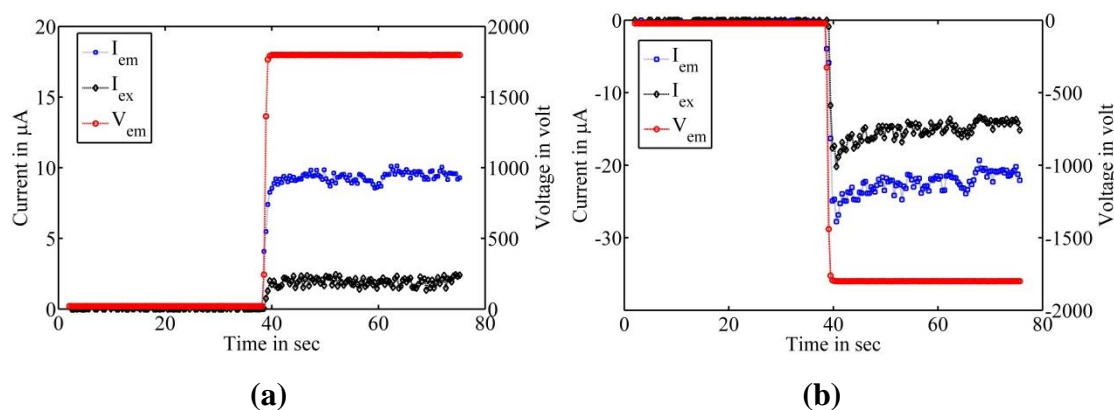
Figure 7.11: Plot of emitter current I_{em}, extractor current I_{ex} and emitter voltage V_{em} at ± 1800 V with time for I-V characteristics measurements in (a) positive and (b) negative polarity. Emitter voltage is turned on after 100 samples of current are taken with no emission for offset measurement and currents in the emitter and extractor are monitored for another 100 samples. In each polarity, the emission is continuous for approximately 38 sec.

It can be seen from Figure 7.11 that the currents are stable within a few μA, however, the current levels have decreased further from the values observed during the initial experiments described in the previous section. The fraction of emitter current intercepted by the extractor is much severer than the previous experimental results shown in Figure 7.2. Especially for the negative polarity of emission, more than 50% of the emitter current is intercepted by the extractor. This may happen due to leakage between the emitter and the extractor. It has been mentioned in the beginning of section 7.4 that the source was partially damaged before these measurements in which, an electrical short between the emitter strips and the extractor was created. Although the short was removed with a knife, a high, but non-infinite resistance between the emitter and the extractor grid may remain, leading to leakage current between the emitter and extractor. In principle, this leakage current can also produce Ohmic potential

drops in the 100 kΩ protection resistance used in emitter and extractor current monitor circuits, leading to lower potential difference between the emitter and the extractor; however, the expected Ohmic drops are only a few volts for the μA range currents and can be neglected.

Another possible reason for large extractor current can be emission at large offset angle after the device was damaged and repaired or misalignment between the emitter strips and the extractor apertures. However, optical observation of the emitter has not shown any significant misalignment and hence can be discarded as a possible source of the large extractor current.

(a)   **(b)**
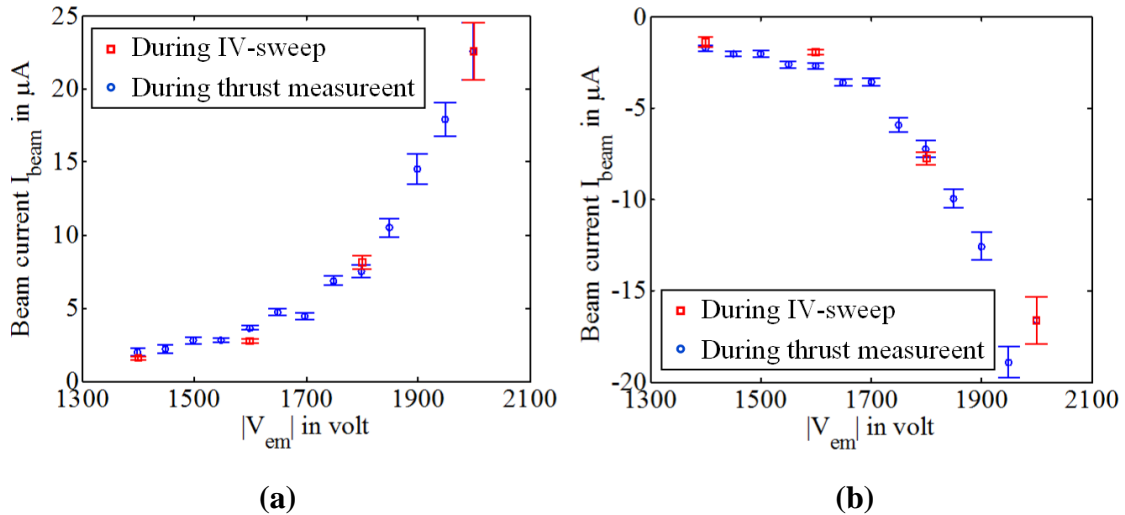
Figure 7.12: Emitted beam current I_{beam} vs. emitter voltage $|V_{em}|$ for (a) positive and (b) negative polarity of emission. These tests are performed before and during direct thrust measurement, but after the initial measurements shown in Figure 7.6.

In Figure 7.12 (a) and (b), the emitted beam current I_{beam} vs. emission voltage V_{em} are shown. I_{beam} is obtained by subtracting I_{ex} from I_{em} at each emitter voltage and averaging over 50 samples, leaving the first 50 samples immediately after onset of emission. The standard deviation of I_{beam} is shown as error bar on the mean values. On the same figures, the I_{beam} vs. V_{em} results during thrust measurement, which has been performed after the I-V sweep, are also shown. A comparison with the initial I-V measurements shown in Figure 7.3 indicates nearly an order of magnitude reduction in I_{beam} at a given V_{em} in both polarities. The drastic reduction in the current levels are attributable to unipolar emission for several minutes over 100 μA currents during initial attempts of direct thrust measurement during which the source was also partially damaged. The current levels and hence thrust can be increased to higher values by increasing the emitter voltage beyond $|V_{em}| = 2000$ V, however, increased currents resulted in damage of the Plate 2, the force sensor and possibly the picoammeter and hence currents are limited to this range only.

7.4.2. Noise floor and effect of gate signal

The gate signal pulsating between 0 V and V_{gate} produces attractive electrostatic force on the plate at the same frequency at which force on the plate is measured. Therefore, the force from the gate signal is expected to couple to the lock-in amplifier output unlike the constant −40 V potential applied to the two other grids and V_{em} applied to the emitter.

In Figure 7.13, the different electrodes and the potentials at different electrodes are schematically shown. If, for simplicity, the gate grid is assumed to be a flat wall, instead of consisting of grids like the other two grids at $V_S = -40$ V, the normal electric field E_G on the gate electrode and that on the particle intercepting plate E_P can be written in terms of V_{gate} and V_S as [239]

$$V_S + s(E_G - E_P) + E_P\left(L_{SP} - \frac{1}{2}u\right) = 0 \tag{7.10}$$

$$V_S + s(E_G - E_P) + E_G\left(-L_{GS} + \frac{1}{2}u\right) = V_{gate} \tag{7.11}$$
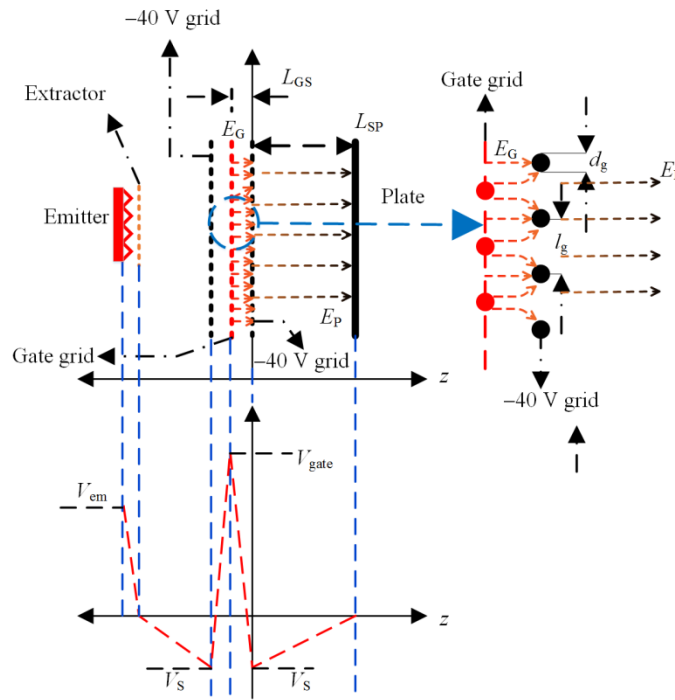
Figure 7.13: Schematic representation of the electric fields and potentials (bottom) due to the three-grid assembly between the emitter and the particle intercepting plate. The effect of the electrostatic field from the gate pulsating at a frequency f_{ref} on the plate can be analysed assuming the central gate grid as a wall and finding the electric field E_P on the plate. The grids used for the –40 V has wire diameter $d_g = 25.4$ μm, and a spacing $l_g = 254$ μm. Distance between gate electrode and the –40 V electrode is $L_{GS} = 6.25$ mm, that between the –40 V grid and the plate is $L_{SP} = 28$ mm.

if the distance $L_{SP} = 28$ mm between the plate and the first grid and $L_{GS} = 6.25$ mm between the gate and the first grid are much larger than the diameter d_g and spacing l_g of the wires in the grids shown in Figure 7.13. Here

$$s = \frac{l_g}{2\pi}\left[\frac{1}{4}\varsigma^2 - \ln\left(\varsigma\right)\right] \tag{7.12}$$

$$u = \varsigma\frac{d_g}{2} \tag{7.13}$$

where

$$\varsigma = \pi \frac{d_{\mathrm{g}}}{l_{\mathrm{g}}} \tag{7.14}$$

and ln (ς) is natural logarithm of ς. For the grid used in the setup with 81% optical transperancy, $d_{\mathrm{g}}/l_{\mathrm{g}} = 0.10$ and $d_{\mathrm{g}} = 25.4$ μm. Since $[l_{\mathrm{g}}, d_{\mathrm{g}}] \ll [L_{\mathrm{GS}}, L_{\mathrm{SP}}]$, $u \ll [L_{\mathrm{GS}}, L_{\mathrm{SP}}]$ and therefore, the electric field normal to the particle intercepting plate can be written from (7.10) and (7.11), neglecting u, as

$$E_{\mathrm{P}} = - \frac{s V_{\mathrm{gate}} + L_{\mathrm{GS}} V_{\mathrm{S}}}{L_{\mathrm{GS}} L_{\mathrm{SP}} + s(L_{\mathrm{GS}} + L_{\mathrm{SP}})} \tag{7.15}$$

where the minus sign on the right hand sign indicates that the electric field lines enter into the plate. For uniform electric field lines over the entire area A_{a} (area of the aperture of the grids) on the plate, the total electrostatic force can on the plate be written as

$$F_{\mathrm{gate}} = \frac{1}{2} \varepsilon_0 E_{\mathrm{P}}^2 A_{\mathrm{a}} \tag{7.16}$$

where $\varepsilon_0 = 8.854 \times 10^{-12}$ Farad/m is the permittivity of free space. Therefore, when the gate signal pulsates between 0 V and V_{gate}, the force on the plate is of square wave shape with amplitude given by

$$\Delta F_{\mathrm{gate}} = \frac{1}{2} \varepsilon_0 A_{\mathrm{a}} \frac{V_{\mathrm{gate}}^2}{(L_{\mathrm{GS}} + L_{\mathrm{SP}})^2} \frac{\left[\left(\dfrac{s}{L_{\mathrm{GS}}} \right)^2 + 2 \left(\dfrac{s}{L_{\mathrm{GS}}} \right) \left(\dfrac{V_{\mathrm{S}}}{V_{\mathrm{gate}}} \right) \right]}{\left[\left(\dfrac{s}{L_{\mathrm{GS}}} \right) + \left(\dfrac{L_{\mathrm{SP}}}{L_{\mathrm{SP}} + L_{\mathrm{GS}}} \right) \right]^2} \tag{7.17}$$

and reptition frequency f_{ref}. With $L_{\mathrm{GS}} = 6.25$ mm, $L_{\mathrm{SP}} = 28$ mm, $l_{\mathrm{g}} = 10 \times d_{\mathrm{g}} = 254$ μm, $V_{\mathrm{gate}} = 3000$ V and $V_{\mathrm{S}} = -40$ V, ΔF_{gate} can be calculated using Eqn. (7.14) and (7.12) to be 15.1 nN in the direction opposite to the applied thrust from the impinging particles when the source is emitting. It can be seen that, in absence of the grids having $V_{\mathrm{S}} = -40$ V, the force on the plate is

$$\Delta F_0 = \frac{1}{2} \varepsilon_0 A_{\mathrm{a}} \frac{V_{\mathrm{gate}}^2}{(L_{\mathrm{GS}} + L_{\mathrm{SP}})^2} \approx 70 \ \mu\mathrm{N} \tag{7.18}$$

Therefore, the −40 V grid significantly reduces the effect of the gate electrode on the particle intercepting plate.

Measurement of force output from the lock-in amplifier has been performed without spraying, but applying the gate signal at different reference frequencies, f_{ref} between 4 Hz and 16 Hz. Time constant T_{c} is kept at 1 sec to satisfy the condition (6.30) in Chapter 6 for this frequency range and rest of the settings are identical to that used in section 6.4 in Chapter 6 and described in Table 6.4. The gate voltage is applied after recording 20 readings of force output

from the lock-in amplifier and after the gate signal is applied, another 80 samples are recorded. In section 7.4.3, it is described that, during thrust measurements, the emitter supply is turned on after these many initial readings with the gate power supply turned on and another 100 samples of force output are recorded.

In Figure 7.14 (a), a typical measured force as a function of time is shown for $f_{ref} = 10$ Hz. It can be seen that after the gate signal is applied, the force fluctuates between 0 nN and 20 nN. On the same figure is superimposed the gate power supply reading V_{gate} where, the gate signal pulsates between 0 to $V_{gate} = 3000$ V at the reference frequency (the pulsating gate signal traces are not shown here). However, due to equivalent noise floor in the measurements, the force due to the gate cannot be distinguished from the background noise. In Figure 7.14 (b), the avarage of the 80 reading of the force sensor output is plotted against the reference frequency f_{ref} with $V_{gate} = 3000$ V and $V_{gate} = -3000$ V. The standard deviation of the 80 readings is shown as error bar on the average readings. It can be seen that the average force output with the gate signal enabled is typically around 10 nN with standard deviation of the similar magnitudes representing noise. On the same figure is shown the calculated $\Delta F_{gate} = 15.1$ nN for $V_{gate} = 3000$ V. It is seen that the measured average force is smaller than the expected value at most of the frequencies and does not show any trend of dependence on the reference frequency. The smaller observed effect of the gate signal on the force output is due to

1. Non-zero mechanical forces on the plate due to vibration in the vacuum chamber, which may or may not work opposite to the attactive force from the gate.

2. The calculations of the force ΔF_{gate} is based on the assumption that the gate electrode is a plate at V_{gate} instead of the grids and the actual electric field on the plate may be lower in magnitude than that calculated.

(a)   (b)
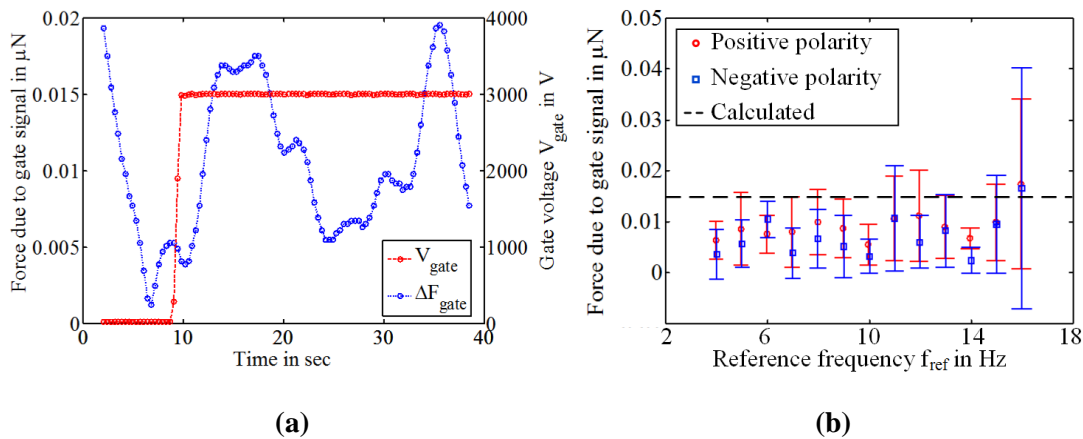
Figure 7.14: (a) Plot of V_{gate} and lock-in amplifier measured force on the plate without electrospray as a function of time with $f_{ref} = 10$ Hz. $V_{gate} = 3000$ V is applied at around 9 sec after starting the force measurements. The force reading fluctuates between 0 nN and 20 nN over the recording time. (b) Plot of average force output as a function of applied reference frequency f_{ref} with $V_{gate} = 3000$ V showing typically less than 10 nN mean value and around 10 nN standard deviation. This force partly represents the electric field from the gate signal and partly the noise floor of measurement which are indistinguishable.

From the measurements in this section it can be inferred that thrusts above 10 nN can be measured with the thrust stand with around 10 nN resolution. The large standard deviation at f_{ref} = 16 Hz in Figure 7.14 (b) in both polarities may be due to excitation of resonance in the plate due to second odd harmonic of the square wave force input. It can be remembered that inside the vacuum chamber, the damping of the plate is expected to be much lower than that measured in air and tabulated in Table 5.18 in Chapter 5. Although the operating frequency f_{ref} is much smaller than the natural frequency f_p of the plates, harmonics of the input force in proximity of the natural frequency may excite higher amplitude vibration at f_p and depending on the magnitude of the transfer function of the lock-in amplifier low-pass filter at f_p, the measured output may have non-negligible contribution from the vibration.

7.4.3. Thrust measurement with lock-in amplifier

For mesurement of thrust, the reference frequency is set to f_{ref} = 10 Hz with T_c = 1 sec to keep the transfer function magnitude of the low-pass filter to lower than −99 dB (−147 dB at f_{ref} = 10 Hz) at f_{ref}. At this point, the force sensor output can be recalled from Eqn. (6.27) in Chapter 6

$$F = 2.221 \times \left(1 + \frac{k_p}{k_f}\right) S_F R_{out} \tag{6.27}$$

where, R_{out} is the r.m.s. output voltage measured from the lock-in amplifier when thrust is applied to the plate. In Figure 7.15 (a) and Figure 7.15 (c), the plot of V_{em} and V_{gate} as a function of time during measurement of thrust at V_{em} = ±1950 V in positive and negative polarities are shown. The gate voltage is turned on to ±3000 V depending on the polarity of emission approximately after 9 sec from starting the measurements and the signal to the gate electrode is pulsating between 0 V and ±3000 V at a frequency f_{ref} = 10 Hz. The emitter voltage is turned on at approximately 38 sec from the time of start. The emission is continued for another approximately 38 sec during which 100 samples of beam current I_{beam} and force sensor output F are recorded.

In Figure 7.15 (b) and 7.15 (d), I_{beam} and F are plotted for the emission voltages corresponding to Figure 7.15 (a) and 7.15 (c) respectively. It can be seen that the force output F rises to a stable value at a slower rate than the beam current, which is due to T_c = 1 sec time constant of the lock-in amplifier. If it is assumed that despite fluctuations in the beam current levels, the beam composition (γ_0) and anglar spread (β_0) are unchanged, the force output is expected to follow the beam curent proportionately in a given polarity. However, the lock-in amplifier does not respond to the fast fluctuations of the beam current. Due to time variation of the beam current, the force output F is also expected to vary during the 38 sec of emission. Therefore, force output at a given V_{em} can be found by averaging the force readings during emission and the standard deviation of the measured F corresponds to the overall change of the beam current during measurement, fluctuations, if any, in the beam composition and angular spread i.e. in γ_0 and β_0 and the noise floor in the measurements. It can be seen that the 100 samples of force between time t = 0 sec and $t \approx$ 38 sec in Figure 7.15 (b) and 7.15 (d) before start of emission correspond to the noise floor of measurement and the effect of the gate signal, which is discussed in section 7.4.2.
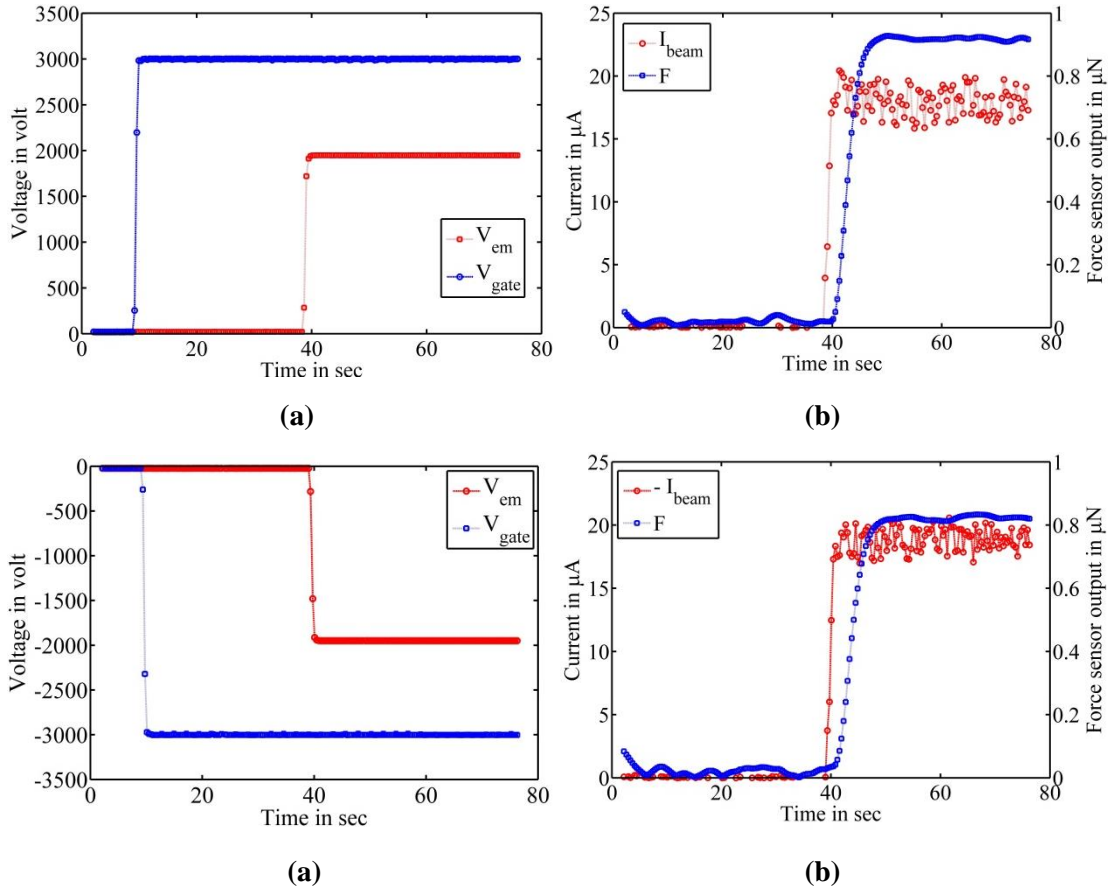
Figure 7.15: Plot of emitter voltage V_{em} and gate voltage V_{gate} with time during thrust measurement at $|V_{em}| = 1950$ V in (a) positive and (c) negative polarity of emission respectively. The gate voltage is set to $|V_{gate}| = 3000$ V for all emission voltages and is pulsated between 0 V and V_{gate} at a frequency $f_{ref} = 10$ Hz. The emitted beam current I_{beam} and force sensor output measured by the lock-in amplifier at the same reference frequency $f_{ref} = 10$ Hz are shown in (b) for positive and (d) for negative emission polarities respectively.

In order to evaluate thrust from the measured force F, the transparency of the three-grid assembly for the gate electrode and the -40 V electrodes and relation between actual thrust Th generated by the emitter and the force on the particle intercepting plate due to impingement of the emitted particles are necessary conversion factors to take into account. The relation between the force on the plate and thrust is discussed in section 7.4.4. The transparency of each grid in the three grid assembly is 81%; therefore, a combined transparency of the $\alpha_i = (0.81)^3 = 0.53$ can be calculated. This means that 53% of the emitted particles are expected to pass through the grid assembly and impinge on the plate to generate the force F. Therefore, if it is assumed that the particles impinging on the plate collide with the plate in an inelastic manner, the generated thrust can be written in terms of the measured force F as

$$Th_{\alpha i} = \frac{F}{\alpha_i} = 1.88F \tag{7.19}$$

A more accurate transparncy correction could be employed by measuring the ratio of current detected on the particle intercepting plate, I_{plate} and the current emitted, I_{beam} at every V_{em} and in that case the corrected thrust $Th_{\alpha i}$ could be written as

$$Th_{\alpha i} = \left(\frac{I_{beam}}{I_{plate}}\right) F \tag{7.20}$$

However, this has not been possible due to damage of the picoammeter and the plate current readings had been discarded.

In Figure 7.16 (a) and (b), the average thrust $Th_{\alpha i}$ obtained by correcting the average measured force F using Eqn. (7.19) is plotted against the emitter voltage $|V_{em}|$ in positive and negative polarity of emission. The average force is calculated from the last 50 samples of the force output in Figure 7.15 (b) or Figure 7.15 (d) in order to avoid spurious fluctuations, if any, in the beam current. The standard deviation of the 50 samples is shown as error-bar on the average values at each $|V_{em}|$. On the same figure is plotted the expected thrust Th_{indir} from Eqn. (7.9) using average γ_0 and β_0 from Table 7.1 and 7.2 respectively and taking average I_{beam} over the 50 samples. The error-bar in Th_{indir} represents the overall standard deviation of γ_0, β_0 from Table 7.1 and 7.2 respectively and that of measured I_{beam}, i.e.

$$\delta\{Th_{indir}\} = \underline{Th_{indir}} \left[\left(\frac{\delta\{I_{beam}\}}{\underline{I_{beam}}}\right)^2 + \left(\frac{\delta\{\beta_0\}}{\underline{\beta}}\right)^2 + \left(\frac{\delta\{\gamma_0\}}{\underline{\gamma_0}}\right)^2\right]^{1/2} \tag{7.21}$$

where $\underline{w}$ represents the mean value of w and $\delta\{w\}$ represents standard deviation of w.

(a)   (b)
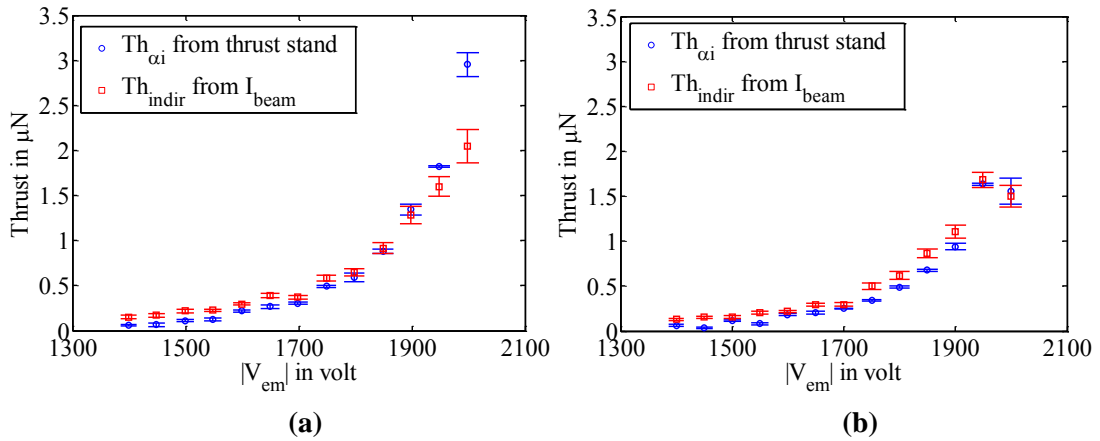
Figure 7.16: Plot of measured thrust $Th_{\alpha i}$ from the thrust stand and indirect thrust Th_{indir} calculated from measured I_{beam} using Eqn. (7.8) against emitter voltage $|V_{em}|$ in (a) positive and (b) negative polarity of emission.

It can be seen that the indirect thrust Th_{indir} calculated from Eqn. (7.9) is typically 50 nN to 150 nN higher than the measured thrust $Th_{\alpha i}$ in both polarities except for $V_{em} > 1800$ V in positive polarity of emission where the $Th_{indir} < Th_{\alpha i}$ by nearly 0.5 µN -1 µN. The non-zero offset at close to $|V_{em}| = 1400$ V emission voltage is due to emission of around 2 µA emitted beam current I_{beam} as shown in Figure 7.12 (a) and (b). For a given $|V_{em}|$, thrust in negative polarity of emission is smaller than that in positive polarity because of lower beam current I_{beam} (Figure 7.12) and lower mass of the ions. The minimum thrust $Th_{\alpha i}$ measured using the thrust stand is about 47 nN $\pm$ 8 nN at $V_{em} = 1400$ V which shows that the thrust stand can measure sub-100 nN thrusts from the electrospray source inside the vacuum chamber.

Differences between Th_{indir} and $Th_{\alpha i}$ may result from the following reasons.

1. The kinetic energy deficit of emitted particles may produce 1.5−3.0% less thrust than Th_{indir} calculated from I_{beam} and V_{em} as discussed in the beginning of section 7.2.4.

2. The beam composition and beam spreading factors, γ_0 and β_0 have been considered constant over the entire emission voltage range which may not be true or may have higher standard deviation over the entire range of emission voltages.

3. The gate signal affects the direct thrust measurement by around ± 10 nN as discussed in section 7.4.2.

4. The emitted plume's spot size on the plate and current density distribution in the cross-section of the spot may lead to a few % error in the thrust measurement. It can be remembered from Table 6.6 in Chapter 6, that the spot-size related error can be as high as 10% when the thruster axis is extremely offset (by a few mm) from the axis through the centre of the plate. However, alignment between the emitter axis and the central axis of the plate is much better than the extreme cases and is expected to produce less error.

5. The transparency factor α_i in Eqn. (7.19) has been taken as 0.53 depending on the combined transparency of three grids, each of 81% transparency. The validity of this correction factor has not been verified against I_{beam}/I_{plate} as the I_{plate} readings of the damaged picoammeter have been discarded.

6. Fragmentation of the emitted ions inside the emitter's accelerating region may lead to higher thrust than that calculated from Eqn. (7.2) or Eqn. (7.8) [240]. Depending on the fraction of solvated ions fragmenting inside the emitter's accelerating region, the flight time measurement can produce a few 10s of % less calculated thrust than that actually emitted.

7. In the expression of $Th_{\alpha i}$ in Eqn. (7.19), an inelastic collision of the impinging particles on the plate has been assumed. However, as it has been seen in Figure (7.10) and discussed in the beginning of section 7.4, erosion of the aluminium metallization indicates that the sputtered aluminium atoms may contribute to momentum to the plate, leading to higher force on the plate than that only due to the impinging ions adhering to the plate.

All these factors need verification for improved quantification of errors in measurement of both, $Th_{\alpha i}$ and Th_{indir}. It can be noted that with measurement of α_i by measuring I_{plate} during thrust measurement can improve the accuracy of the measured thrust. Estimation of fragmentation and kinetic energy deficit can be incorporated from kinetic energy and flight time measurement [240] of the emitted species. In the following section, the impact of the impinging ions on the plate is considered in some detail in order to address

1. Its effect on thrust measurements,

2. The effect of the impinging ions on the damage of the plate.

7.4.4. Effect of impact of ions on the plate

The relation $Th_{\alpha i} = 1.88 \times F$ in Eqn. (7.19) is applicable when the impinging particles transfer all their momentum to the plate by a perfectly inelastic collision. However, when high speed particles impinge on a plate, it can become neutralized by Auger transition in front of the surface, leading to secondary electron emission, or can transfer its momentum to one or more metal atoms leading to secondary electron emission, disorder, damage or sputtering of the metal atoms. The impinging atom may come to rest inside the metal or may still possess sufficient kinetic energy to escape the target [241]. Emission of electrons does not contribute

to thrust due to negligible mass. However, recoil of the ions and sputtering of the target metal atoms may contribute to the force measured on the plate. If during collision, the total linear momentum normal to the plate is conserved by perfectly elastic collision, the force measured on the plate is twice as great as the thrust generated at the emitter. For a completely inelastic collision, the measured force is same as the thrust. If $_|K_|$ is the defined as an averaged coefficient of restitution, the emitted thrust Th_{dir} thrust can be related to the measured force F as [231]

$$Th_{dir} = \frac{Th_{\alpha i}}{(1+_|K_|)} = \frac{1}{\alpha_i (1+_|K_|)} F \qquad (7.22)$$

where $0 \le {}_|K_| \le 1$. The impinging particles may be physisorbed or chemisorbed [242] depending on the mass ratio of the ions to the target material atoms, angle of incidence and kinetic energy of impinging ion. In order to evaluate $_|K_|$ for the back-scattered ions and for the sputtered atoms, sputtering yield simulation has been performed using Transport of Ions in Matter (TRIM) [243] simulator with a 20 nm aluminium metallized 2 μm thick Mylar target and an arbitrary ion of mass equal to the mass of an monomers, dimers and trimers separately, present in the emission from the electrospray device.

(a) **(b)**
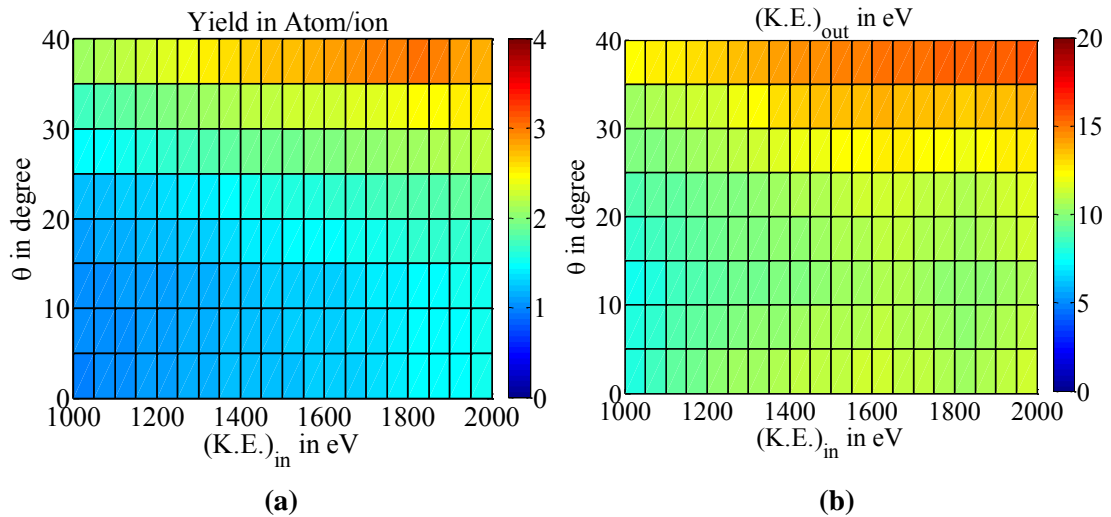
Figure 7.17: (a) Simulated sputter yield in Atom/ion and (b) kinetic energy per sputtered atom $(K.E.)_{out}$ from 20 nm aluminium metalized mylar film when an ion with mass 87 a.m.u. (equivalent to BF_4^- ion) with different kinetic energies $(K.E.)_{in}$ are indident at different angles θ. At higher angles and higher input kinetic energies, both yield and $(K.E.)_{out}$ increase.

In Figure 7.17 (a) and (b) are shown the sputtering yield (sputtered atoms per unit ion impingement) and kinetic energy of per sputtered atom $(K.E.)_{out}$ for impinging ions of mass equal to that of BF_4^- ions at different kinetic energies $(K.E.)_{in}$ and different incidence angles θ. For impinging ions with higher masses, i.e. for all other emitted charge species from EMI-BF$_4$ electrospray, the yield and $(K.E.)_{out}$ are lower than those shown in Figure 7.17. The number of back-scattered ions is found to be less than 0.1% of the number of impinging ions. It can be seen that with increasing $(K.E.)_{in}$ and θ within the range of simulations, the sputtering yield increases. Each BF_4^- ions, with $(K.E.)_{in} = 2$ keV at an angle θ = 40°, can sputter nearly three aluminium atoms with $(K.E.)_{out}$ of the order of 15 eV per atom. On the other hand, the number of impinging ions decreases with increasing angle (Figure 7.7) making less and less ions

available for sputtering at higher angles. Therefore, the total change of momentum contributed by the sputtered atoms depends on the yield and kinetic energy distribution of the sputtered atoms and the distribution of the impinging ions over the emission half-angle.
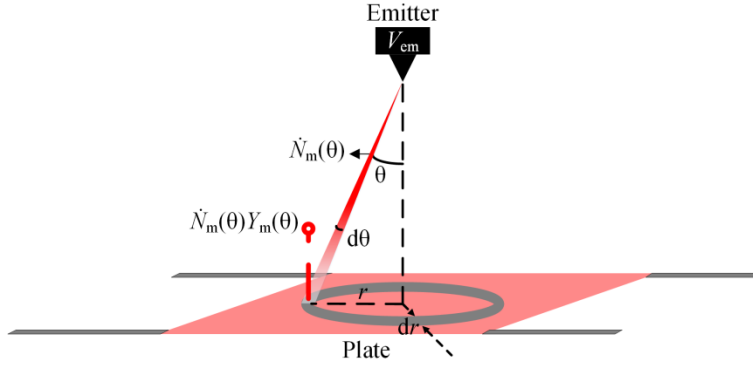
Figure 7.18: Schematic of the sputtering mechanism to find $_|K_|$.

If $\dot{N}_m(\theta)dm$ is the number of ions with mass between m and $m + dm$ and kinetic energy $(K.E.)_{in}$ incident on the plate per unit time per unit area at an angle θ as shown in Figure 7.18, and $Y_m(\theta)$ is defined as the sputtering yield in atom/ion for that particular ion species at that kinetic energy, the number of ions incident per unit time in an annular area $2\pi r dr$ on the plate is $2\pi \dot{N}_m(\theta)rdrdm$ and number of aluminium atoms sputtered per unit time from the annular area is $\dot{N}_m(\theta)Y_m(\theta)2\pi rdrdm$. If it is assumed that the aluminium atoms are sputtered perpendicular to the plane of the plate, the momentum transfer rate by the sputtered atoms on the plate can be written as

$$d\dot{p}_{m-} = \dot{N}_m(\theta)Y_m(\theta)\sqrt{[2(K.E.)_{out}\,m_{Al}]}\,2\pi rdrdm \tag{7.23}$$

where m_{Al} is the mass of an aluminium atom and the expression inside the square root symbol represents momentum of a sputtered aluminium atom. The normal momentum transfer rate by the impinging ions in the area $2\pi rdr$ is

$$d\dot{p}_{m+} = \dot{N}_m(\theta)\sqrt{[2(K.E.)_{in}\,m]}\cos\theta\,2\pi rdr\,dm \tag{7.24}$$

Integrating over the entire mass range in the emission and over the entire impingement area on the plate

$$\dot{p}_- = 2\pi L^2\sqrt{2m_{Al}}\int_m\int_\theta \dot{N}_m(\theta)Y_m(\theta)\sqrt{(K.E.)_{out}}\,\tan\theta\,\sec^2\theta\,d\theta\,dm \tag{7.25}$$

and

$$\dot{p}_+ = 2\pi L^2\sqrt{2(K.E.)_{in}}\int_m\int_\theta \dot{N}_m(\theta)\sqrt{m}\tan\theta\,\sec\theta\,d\theta\,dm \tag{7.26}$$

where $r = L\tan\theta$, L being the distance between the emitter and the plate. Back-scattered ions will contribute to $\dot{p}_-$ as well, however, as the number of back-scattered ions is found less than 0.1% of the impinging ions, their contribution to $\dot{p}_-$ are negligible compared to those due to sputtered atoms. Here, integration over θ covers the entire emission half-angle. $_|K_|$ can be written in terms of $\dot{p}_+$ and $\dot{p}_-$ as

$$_|K_| = \frac{\dot{p}_-}{\dot{p}_+}$$

(7.27)

$\dot{N}_m(\theta)$ can be represented in terms of current $I_m(\theta)$ associated with the particular type of ion measured by a current probe of area A_p at angle θ as

$$\dot{N}_m(\theta) = \frac{I_m(\theta)}{A_p q} = \frac{I_m(\theta)}{I_{beam}} \frac{I_{beam}}{A_p q} = p_m(\theta) \frac{I_{beam}}{A_p q}$$

(7.28)

where $p_m(\theta) = I_m(\theta)/I_{beam}$ represents the fraction of total beam current I_{beam} that contributes to $I_m(\theta)$ measured by the current probe. $I_m(\theta)$ is not the total current measured by the probe at θ, rather the part of the measured current that is contributed by the ions of mass m. If the distribution of impinging ion masses is independent of the emission angle, as assumed in section 7.2.4.1 and 7.2.4.2,

$$p_m(\theta) = f(m) p(\theta)$$

(7.29)

where $p(\theta)$ is the axis-symmetric current fraction distribution measured in section 7.2 and defined in Eqn. (7.5). Here $f(m)$ represents the distribution of masses in the emission, which is independent of the angle of emission. Therefore, from Eqn. (7.27),

$$_|K_| = \frac{\int_m \int_\theta f(m) p(\theta) Y_m(\theta) \sqrt{\left[\frac{(K.E.)_{out}}{(K.E.)_{in}}\right]} \tan\theta \sec^2\theta \, d\theta \, dm}{\int_m \int_\theta f(m) p(\theta) \sqrt{\left[\frac{m}{m_{Al}}\right]} \tan\theta \sec\theta \, d\theta \, dm}$$

(7.30)

By knowing $f(m)$, $p(\theta)$, $Y_m(\theta)$, and $(K.E.)_{out}$, $_|K_|$ can be evaluated. The axis-symmetric current fraction distribution $p(\theta)$ has been measured and calculated from perpendicular and parallel angular scans in section 7.2.2 and section 7.2.4.2. From the time-of-flight traces in positive and negative polarities, a simple mass distribution function $f(m)$ can be defined as

$$f(m) = 0.47 \times \delta(m - m_0) + 0.44 \times \delta(m - m_1) + 0.09 \times \delta(m - m_2) \quad \text{for positive polarity}$$

$$f(m) = 0.46 \times \delta(m - m_0) + 0.43 \times \delta(m - m_1) + 0.11 \times \delta(m - m_2) \quad \text{for negative polarity}$$

by evaluating f_0, f_1 and f_2 in both polarities from time-of-flight traces as shown in Figure 7.5 (b). Here $\delta(w)$ is delta function in w. $Y_m(\theta)$ and $(K.E.)_{out}$ have been found out for impinging ion masses of monomers, dimers and trimers in both polarities for $\theta = 0°$ to $40°$ and $(K.E.)_{in} = qV_{em} = 1$ keV to 2 keV. By numerically integrating Eqn (7.30), at each V_{em} over m and θ, $_|K_|$ has been found out as shown in Figure 7.19 (a). The total cumulative yield in atom/ion can be evaluated from the ratio of total number of sputtered atoms to the total number of impinging ions using

$$Y_{tot} = \frac{\int_m \int_\theta f(m) p(\theta) Y_m(\theta) \tan\theta \sec^2\theta \, d\theta \, dm}{\int_m \int_\theta f(m) p(\theta) \tan\theta \sec\theta \, d\theta \, dm}$$

(7.31)

and has been plotted in Figure 7.19 (b). It can be seen that $_|K_|$ is between 4.6% to 6.8% for both polarities of emission and leads to a lower value of thrust than $Th_{\alpha i}$ assuming perfectly

inelastic collision by 4.4% to 6.4%. In Figure 7.20 (a) and (b), Th_{dir} after correcting $Th_{\alpha i}$ from simulated $_|K_|$ using Eqn. (7.22) are plotted for comparison with Th_{indir} defined in Eqn. (7.8). Since inclusion of $_|K_|$ leads to $Th_{dir} < Th_{\alpha i}$, the difference between Th_{dir} and Th_{indir} increases slightly further, but still within 50 nN to 150 nN. However, the relatively large uncertainty in Th_{indir} from the discussion at the end of section 7.4.3 also has to be considered which may contribute in part to this difference as well.

The cumulative sputtering yield Y_{tot} is found to be between 1 atom/ion to 2 atom/ion within $|V_{em}| = 1$ kV and 2 kV, which can be used to estimate the erosion rate of the aluminium target. For example, during the initial attempts of thrust measurement with typically 100–200 µA current levels at around $|V_{em}| = 2000$ V, a 15–30 minute total time can be calculated to completely erode the 20 nm thick aluminium metallization layer. For thrust measurements discussed in section 7.4.3 with up to 20 µA beam current, the plate can operate without complete erosion for up to 75 minutes.

(a) **(b)**
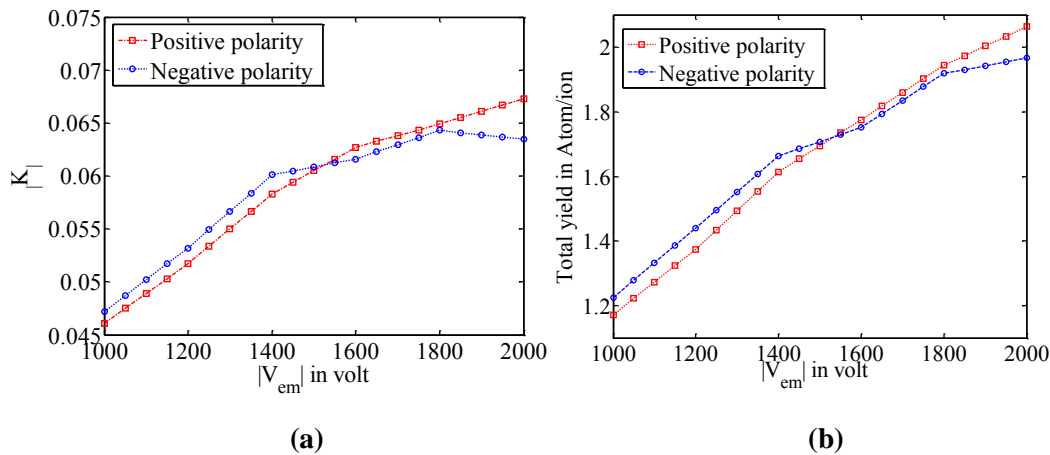
Figure 7.19: (a) Simulated $_|K_|$ and (b) total cumulative yield Y_{tot} in atom/ion as a function of emission voltage $|V_{em}|$ in positive and negative polarity of emission. $_|K_|$ and Y_{tot} have been obtained by using Eqn. (7.30) and (7.31) from TRIM simulated $Y_m(\theta)$, $(K.E.)_{out}$ and experimentally obtained $p(\theta)$ in section 7.2.4.2.

(a) **(b)**
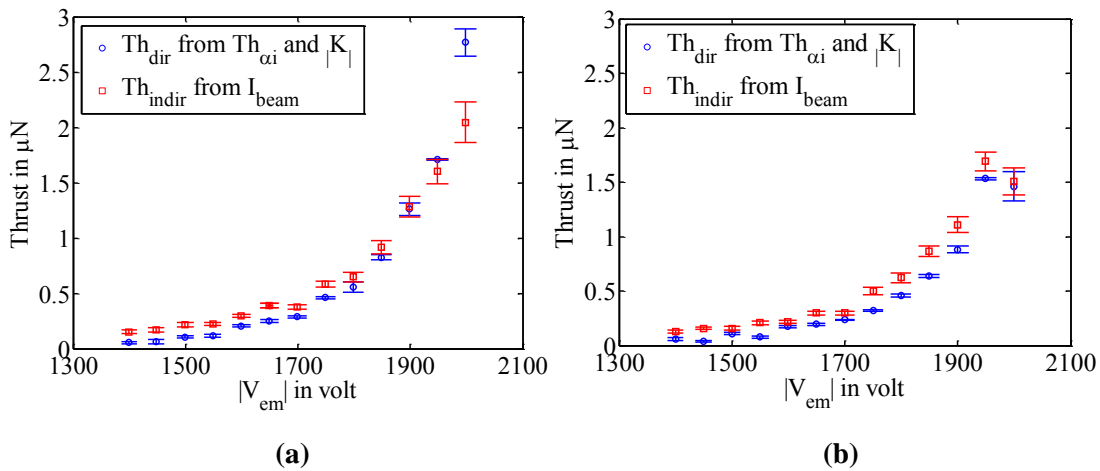
Figure 7.20: Measured thrust Th_{dir} after correcting $Th_{\alpha i}$ with the calculated values of $_|K_|$ from Figure 7.19 (a) in positive (a) and negative (b) polarity of emission. For comparison Th_{indir} are also plotted on the same figures.

The simulated physical sputter yields are typically accurate within a factor of 2 [244] and hence an equivalent standard deviation in $_{|}K_{|}$ can be expected leading to around 5−6% uncertainty in the correction factor $1/(1+_{|}K_{|})$. In [245], sputtering yield of different metal targets has been experimentally found out with inert gas ions. For krypton ions bombarding on aluminium foils (mass ratio 3.1, close to the case of ionic liquid electrospraying on aluminium), the sputtering yield is found to be around 2 atoms/ion [246], [247] consistent with the simulated results shown in Figure 7.19 (b). The kinetic energy of back-sputtered aluminium atoms is also observed to be much lower than the impinging ions' kinetic energy [247]. Resent research activities on using ionic liquid ion sources for focused ion beam application using silicon target suggest that electrochemical reaction of ionic liquid ions with target material may induce chemical reaction of the impinging ions with the plate material and increase sputter yield [167]. Sputtering yield measurement on silicon substrate using ionic liquid EMI-Tf$_2$N [248] has shown 1−3 atoms/ion sputtering yield at ion kinetic energies 10−35 keV.

The uncertainty in $_{|}K_{|}$ determined from simulations and the possibility of increased sputtering by chemical reaction of the ionic liquid ions with the target aluminium plate is therefore the major source of error in thrust measurement with the thrust stand from the electrospray thruster even if the other sources of error, such as E_{r1}, E_{r2}, E_{r3}, E_{r4} and E_{r5} defined in Table 6.5 in Chapter 6, are ignored.

7.5.   Possible improvement of thrust correction

One possible way to reduce the error in determining $_{|}K_{|}$ is to use an alternative material instead of aluminium on the particle intercepting plate which has lower sputtering yield in the similar kinetic energy and mass of the impinging ions. Lower sputtering yield reduces both, $_{|}K_{|}$ and Y_{tot}, thus reduces the effect of uncertainty in $_{|}K_{|}$ in thrust correction and also reduces chances of damaging the plate.

Use of graphite as a target material has been proposed in [142] for minimum sputtering yield (except for diamond) of the target plate in a similar indirect thrust measurement setup for a 5 kW xenon Hall thruster. Graphite is also electrically conductive; depending on type of graphite, its conductivity can vary between 0.13 MS/m to 0.03 MS/m [249], typically 2 to 3 orders of magnitude less than that of the metals listed in Table 5.11 in Chapter 5. This conductivity is sufficient to eliminate chances of charging the plate during ion bombardment.

In Figure 7.21 (a) and (b), the TRIM simulated sputtering yield in atoms/ion and kinetic energy per sputtered atom, $(K.E.)_{out}$ are plotted as a function of incident kinetic energy $(K.E.)_{in}$ and incidence angle θ of an arbitrary ion with atomic mass equal to that of BF$_4^-$ ions on a graphite (carbon) target, similar to Figure 7.17 for aluminium target. It can be seen that the sputtering yield is nearly three times lower than that observed for BF$_4^-$ equivalent ions with aluminium target. Therefore, for the same current levels, the longevity of the plate can be increased by nearly 3 times from the aluminium metallization. The number of back-scattered ions is found to be less than 0.1% of that of the incident ions here as well for up to mass of trimers and can be ignored for calculation of $_{|}K_{|}$. Similar to aluminium target in Figure 7.19 (a), $_{|}K_{|}$ can be found out using the sputtering yield and $(K.E.)_{out}$ for monomers, dimers and trimers as shown in Figure 7.22. It can be seen that $_{|}K_{|}$ is less than 1.6% for the emission voltage range between 1000 V and 2000 V, nearly three times less than that obtained with

aluminium. A similar value of momentum correction factor was calculated with graphite target in [142] as well for a xenon Hall thruster.

Graphite can be sprayed on the Mylar film [250], either to repair the eroded plate, or on initially non-metallized Mylar; however, the thickness of the graphite coating on the 2 μm thick Mylar film needs to be controlled because of increased mass and thereby reduced natural frequency. For example, the 20 nm thick aluminium layer on the Mylar film used in the thrust stand can be replaced with up to 30 nm thick graphite layer only for the same mass increase $\delta M/M_{fr}$ derived in Table 5.15 in Chapter 5. Graphite coating on PET substrate has been reported in [251] with hydrocarbon gas precursor in microwave plasma reactor with a few nm/s deposition rate which can be a useful way to coat Mylar in a controlled way.
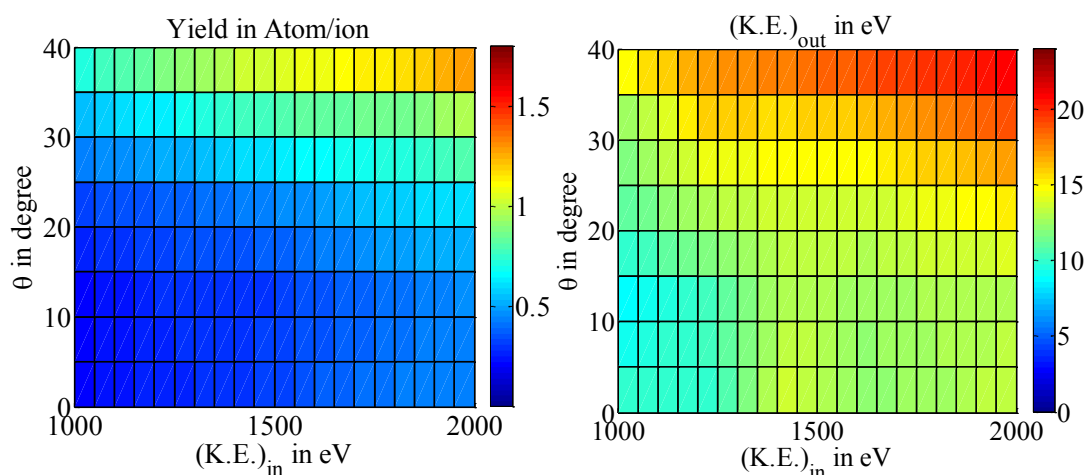
Figure 7.21: TRIM simulated plot of (a) sputtering yield in atoms/ion and (b) kinetic energy per unit sputtered atom ($K.E.$)$_{out}$ vs. kinetic energy ($K.E.$)$_{in}$ = qV_{em} and incidence angle θ of impinging ions with mass 87 a.m.u. (same as BF$_4^-$ ions) and a 20 nm thick graphite on 2 μm thick Mylar film as target. For higher mass of the ion, the yield and ($K.E.$)$_{out}$ are lower.
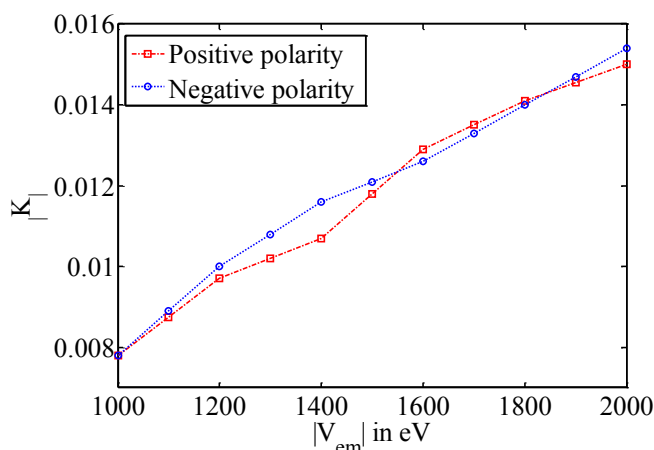
Figure 7.22: Calculated $_|K_|$ for graphite target vs. emission voltage $|V_{em}|$ for positive and negative polarities of emission of monomers, dimers and trimers from the porous glass electrospray device.

7.6.   Conclusion

In this chapter, measurement of thrust from an electrospray device using the designed thrust stand has been performed. The noise floor of the measurements in the vacuum chamber is found to be typically around 10 nN including the pulsating electrostatic force from the gate electrode. At higher current levels (above 100s of μA) and with sustained emission for several minutes, the impingement of the high energy ions on the aluminium membrane caused erosion of aluminium metalization on the particle intercepting plate, resulting in damage of the plate, the force sensor and the picoammeter employed to measure plate current. Therefore, subsequent measurements have been performed at low currents and force on the plate up to only around 2–3 μN and no further damage has been observed on the plate over the duration of the experiments. The thrust stand has demonstrated measurement of as low as 47 nN thrust from the electrospray device at $V_{em} = 1400$ V inside the vacuum chamber, which proves that sub-100 nN thrusts can be measured with the thrust stand with close to 10 nN thrust resolution from electrospray devices as well.

The measured thrust with the thrust stand has been compared with indirectly measured thrust using emission current, flight time measurement and angular spread measurements and is found to be between 50 nN to 150 nN lower than the indirectly meaured thrust at almost all emission voltages. The possible errors associated with sputtering of the metallization from the target plate has been estimated from simulations, showing that the thrust can be further 5–10% lower than that measured on the plate and corrected for the gate transparency. Measurement of sputtering yield from the target plate may reduce the uncertainty in the measured thrust.

Fast damage of the plate at high emission current levels poses a limitation on the use of the thrust stand to measure higher thrust levels. In section 7.5, use of graphite instead of aluminium has been proposed because of lower sputtering yield which reduces the error in the measured thrust due to momentum transfer mechanism on the plate and also reduces the damage of the plate. With graphite layer, higher thrusts from electroapray devices should be possible to measure without damaging the plate or the force sensor over the duration of measurement. Measurement of the transparency α_i of the grids by measuring ratio of I_{plate} and I_{beam} is essential for a more correct conversion factor for thrust, which, unfortunately, has not been possible due to damage of the picoammeter caused during thrust measurements. However, adding a series resistance between the plate and the picoammeter input can eliminate the chances of accidental damage of the picoammeter, should there be any arcing due to erosion of the conductive layer on the Mylar membrane.

8 Conclusion

Growing interest in microthrusters for small spacecrafts has set forth a new era in space exploration. The motivation behind the work in this thesis was driven by direct and indirect characterization of micro-thrusters. In Chapter 3 and Chapter 4, development of an ion-guide based ToF-MS has been described to find out emission characteristics of electrospray propulsion devices. The ion-guide consists of cascaded cylindrical electrostatic lenses inside a 65 cm long flight tube to guide electrosprayed charged particles to a small detector for flight time measurements. In Chapter 5 to Chapter 7, development of a thrust stand to measure thrust from microthrusters with sub-100 nN resolution has been described. The thrust stand works by intercepting emitted particles from the thruster with a plate and measuring the impingement force with a force sensor. The thrust stand has been characterized with the help of a cold-gas ejecting capillary and an electrospray source in Chapter 6 and Chapter 7 respectively. Achievements of the thesis along with the merits and demerits of the two systems are divided into two sections: section 8.1 for the ion-guide based ToF-MS, and section 8.2 for the thrust stand. A future scope of work has been proposed in section 8.3 to conclude the thesis.

8.1.   The ion-guide

The ion-guide enables collection of a large fraction of the emission from electrospray sources on a small detector for flight time measurement depending on the emission half-angle and kinetic energy spread among the emitted particles. It has been shown by simulation (section 3.3.1 in Chapter 3) that the ion-guide can enable detection of all mono-energetic charges up to 23° emission half-angle on a detector at a distance nearly 60 times the diameter of the detector. Experiments, performed with externally wetted tungsten emitters typically emitting mono-energetic ions within 15° emission half-angle, show that up to 80% of the emission could be collected (section 4.1.2 in Chapter 4) which is otherwise possible with a large detector plate to capture the entire plume in a wider flight tube. With internally wetted capillaries with around 40° emission half-angle, above 30% maximum collection fraction has been measured in section 4.2.3 in Chapter 4. This feature of the ion-guide enables fast real-time monitoring of the emission composition from a large section of the emission demonstrating a very high throughput ToF-MS system. Also the ion-guide reduces gain requirement of the transimpedance amplifier to convert the current traces of the in-flight charges. Increase in flight time by the ion-guide due to electric field distribution inside the ion-guide has been measured and is found to follow the simulated increase within around 10%.

The drawback of the ion-guide has been found to be large spreading in flight times due to acceptance of wide angular divergence of emission (up to 23° from simulation in section 3.3.1 in Chapter 3). A maximum flight time spread of 36% has been evaluated in section 3.3.3 in Chapter 3 for the same kinetic energy and mass of the ions depending on the emission angle

which affects the mass resolution of the mass spectrometer greatly. Measurement of flight times from externally and internally wetted electrospray emitters has shown around 10% spread in section 4.1.3 and section 4.2.4 in Chapter 4, lower than the maximum anticipated value, primarily because most of the charges are emitted in directions close to the axis of the ion-guide. Unlike a field-free drift tube for flight time measurement, the flight speed of the charge species fragmented after the accelerating region of the emitter depends on the deflecting potential applied to the ion-guide present all along the length of the flight tube. Hence identification of the charge species becomes difficult from the flight time information when fragmentation after emission is significant, as discussed in section 4.1.2 and section 4.2.3 in Chapter 4. These uncertainties inevitably lead to inaccuracies in evaluation of propulsive parameters from the flight times despite being able to collect a large fraction of the emission.

8.2. The thrust stand

The thrust stand developed in the second phase of the thesis has shown certain advantages and disadvantages over existing nano-Newton thrust stands. Major challenges in nano-Newton thrust measurement have been discussed in section 2.2 in Chapter 2 and the design of the thrust stand targeted addressing some of these challenges. The thrust stand operates by intercepting emitted particles from a micro-thruster on a plate and measuring the impingement force with a force sensor. Unlike most nano-Newton thrust stands developed in the last decade, (a survey is provided in section 2.2 in Chapter 2) this thrust stand physically isolates the thruster from the thrust measuring unit and thereby allows thrust measurement from different types of thrusters without the connections to the thruster affecting performance of the thrust stand. In the thesis, thrust measurement from two types of thrust generating devices has been described: from a cold-gas ejecting capillary in Chapter 6 and from an electrospray device in Chapter 7. The use of the same thrust stand can be extended for measurement of thrusts up to several 10s of mN by simply replacing the FT-S100 force sensor by the higher range force sensors from the same manufacturer, a list of which is provided in Table 5.4. The natural frequency of the designed thrust stand is close to 50 Hz, thereby avoiding excitation of resonance under sub-Hz to a few Hz range building vibrations and vibrations generated by pumps in a few 100's of Hz range. Homodyne thrust measurement scheme using a lock-in amplifier has been implemented in order to eliminate effect of drift and vibrations on the thrust measurement by proper choice of operating frequency where the amplitude response of the plate is minimal. A detailed design of the plate has been described in section 5.2 in Chapter 5 for the plate, trading off its natural frequency and spring constant keeping the surface area to capture the entire emitted plume as a constraint. A reproducible manufacturing process for the plate has also been proposed and used successfully in section 5.5 in Chapter 5 to produce particle intercepting plates with desired natural frequencies and spring constants.

The thrust stand has been first characterized with a cold-gas ejecting capillary in Chapter 6 and resolution better than 10 nN up to a 30 µN thrust and around 20 nN above 30 µN thrust has been achieved, which is comparable to the state-of-the-art directly measuring thrust stands summarized in Table 2.2 and the first of the indirectly measuring thrust stands discussed in section 2.2.4 in Chapter 2 to demonstrate below 3 µN resolution. The minimum thrust measured with the cold-gas ejecting capillary is below 10 nN which is also lower than any of the directly measuring thrust stands demonstrated. In Chapter 7, thrust measurement up to

around 2 μN from an electrospray propulsion device has also been demonstrated using the thrust stand. Minimum thrust measured is around 50 nN (lower than this has not been verified from the electrospray device in Chapter 7) and a noise floor around 10 nN has been observed. These results demonstrate that, even in the vacuum chamber, coupling vibrations from the turbomolecular pump directly to the thrust stand, sub-100 nN thrusts from an electrospray propulsion device can be measured with the designed thrust stand.

The advantages and high resolution of the designed thrust stand has to be traded off against the inaccuracies of indirect measurement of thrust. The relation between the impingement force on the plate and the thrust on the thruster has not been quantified with above 90% certainty for cold-gas ejecting capillary in section 6.5 in Chapter 6 due to poor resolution of a load cell used for measuring thrust directly on the capillary. Also literature review in section 6.1.3 in Chapter 6 has not confirmed the relation between cold-gas thrust and its impingement force with higher certainty. In Chapter 7, measurement of thrust from the electrospray propulsion device also indicated similar issues while comparing the measured thrust with that obtained from flight time and beam divergence measurement. Estimate of this relation has been discussed in section 7.4.4 in Chapter 7 in terms of physical sputtering yield from the target plate using TRIM simulation from ions of masses same as those of the electrosprayed ions, however, it has not been experimentally verified. Also possibility of chemical reaction of the ionic liquid ions with the plate material can produce different sputtering yield which has not been considered in the simulation, leaving room for inaccuracies of the order of 5−10% in measuring thrust.

Another disadvantage of the designed thrust stand arises from the position of the thruster relative to the plate. In case when the thruster is laterally misaligned by a large amount (above, say, 10 mm), nearly 10% reduction in measured thrust has been experimentally obtained in section 6.4.5 in Chapter 6 despite capturing the entire plume. However, for a well-aligned thruster, the error is expected to be much less. Repeatability tests with different manufactured plates have shown around 2% possible error in the measured thrust, a summary of which can be found in Table 6.5 in Chapter 6.

The third drawback of the designed thrust stand has been erosion of metallization from the Mylar film in the particle intercepting plate while measuring thrust from electrospray propulsion devices. The high speed charge species impinging on the plate eroded aluminium metallization layer from the plate, resulting in damage of the plate followed by damage of the force sensor and possibly the picoammeter attached to the plate for measuring current on the plate. This not only limited thrust measurement only in low emission current levels in Chapter 7, but also, the plate current could not be measured during thrust measurement. For safety of the picoammeter a series resistance can be used between the plate and the picoammeter input. Also possibility of using graphite instead of aluminium has been explored in section 7.5 in Chapter 7 which can reduce the erosion due to lower sputtering yield and also can reduce the error in determining thrust from the measured force.

8.3. Future scope of work

8.3.1. The ion-guide

Acceptance of wide angular spread and the kinetic energy spread in the design of the ion-

guide were consequences of each other. Although, this feature allows mass spectral analysis from a wide section of the emitted charges in a single scan, and reduces gain requirement of the transimpedance stage, they affect the mass resolution of the ToF-MS. Possibility of improving the mass resolving performance of the ion-guide can be explored by an optimal design of the ion-guide that employs Einzel lenses with lower chromatic and spherical aberration than the un-optimized symmetric lenses used in the work of the thesis. Many different asymmetric geometries of Einzel lenses have been analysed in [155] for their aberration properties. The possibility of one or multiple types of Einzel lens geometries can be explored with an eye to reducing the flight time spreading defined in Eqn. (3.6) in Chapter 3. Use of multiple power supplies for different stages of the ion-guide can also be a plausible avenue towards improving the performance of the ion-guide. It might also be useful to use the ion-guide in tandem with a sharp, variable band, kinetic energy filter without significantly compromising on the angular spread acceptance for higher mass resolution. By collimating the divergent beam, the ion-guide works somewhat similar to a 'parallelizer' as shown in Figure 2.8 in Chapter 2 [94] using octo-pole ion-guide and can be used in tandem with a reflectron for focusing the energy spread as well for achieving higher resolution.

The high transitivity of the ion-guide can be a useful means in many mass spectrometry applications as well. Examples include chromatography, pyrolysis, desorption, on-line analysis of gas mixtures etc. [101], [102] where fast attainment of the entire mass spectrum is important because of rapidly changing sample composition. For example, investigation of kinetics and mechanisms of thermal decomposition and production of intermediate radicals in pyrolysis poses an essential criterion of real-time monitoring of the mass-spectrum [103], [104]. Monitoring time evolution of growing bacteria [105], [106] and their temporal characteristics, especially for bioterror agents, require mass spectra within minutes [107] for clinical and environmental applications. For high-speed ion-imaging applications, an entire mass spectrum is required from each pixel, and imaging an entire object requires very fast attainment of the entire spectra [108]. In [156], requirement of high transitivity for ion mobility spectrometry (IMS) has been emphasized and an ion-guide has been demonstrated similar to the one reported in this thesis. Using the ion-guide with an optimized design for improved mass resolution can have promising application in such applications.

8.3.2. The thrust stand

The next steps with regards to the thrust stand can be first addressing the three disadvantages described in section 8.2. For future use of the thrust stand, a series resistance between the plate and the picoammeter is recommended in order to avoid damaging the picoammeter should there be any arcing due to complete erosion of the conductive layer of the particle intercepting plate. In-situ monitoring the sheet resistance of the conductive layer can be an useful way to monitor the degradation of the conductive layer, however, attachment of the probes on the very thin film (preferably away from the centre of the plate where sputtering yield is larger) has to be traded off against the possible change in natural frequency and spring constant of the plate and possibility of damaging the thin membrane itself. The possibilities of using graphite coating on the thin Mylar membrane, discussed in section 7.5 in Chapter 7 indicates that the performance of the thrust stand can be improved in terms of thrust measurement accuracy and also in terms of longevity of the plate in use due to lower sputtering yield. A few possible ways of modifying the design of the plate using graphite instead of, or as a replacement of, aluminium metallization has also been discussed in section

7.5. With these recommended modifications, the performance of the thrust stand can be improved significantly.

Monitoring the sputtering rate from the target plate can also be a modification that can be thought of as a future modification to the thrust stand. Sputtering rate can be monitored by measuring the mass change rate $\dot{m}_{plate}$ of the plate [252]. If $\dot{m}$ is the mass flow rate of the incident ions and $\dot{m}_{sp}$ is the mass rate of the sputtered atoms,

$$\dot{m} - \dot{m}_{plate} = \dot{m}_{sp} \tag{8.1}$$

since back-scattering of the impinging ions are negligible. $\dot{m}$ can be found out from the time of flight traces of the ions using Eqn. (2.9) in Chapter 2 and $\dot{m}_{plate}$ can be measured on the plate by measuring total mass of the plate before and after a known duration of impingement. However, for complete erosion of a few 10s of nm conductive layer corresponds to only a few 10's of µg total change in mass and may be difficult to measure on the large plate. Quartz Crystal Microbalance (QCM) [253] is a useful device to measure µg mass changes; and possibility of measurement of such small mass changes from the large plate can be explored. In [248], an alternative technique has been employed to measure sputtering yield by measuring the sputtering depth using a profilometer after a known exposure time. A review of different techniques for estimation of the sputtering yield can be found in Ref. [244], [247] as well.

Despite the difficulties faced in thrust measurement from the electrospray device in Chapter 7, which have been summarized in section 8.1 as well, the promising thrust results and the possibility of improvement of the thrust stand opens possibility of thrust measurement from a variety of thrusters using the thrust stand, exceeding even the stipulated 100 µN range discussed in the thesis. The used FT-S100 force sensor can be replaced by FT-S1000, FT-10000 or FT-S100000 from the same manufacturer (listed in Table 5.4 in Chapter 5) without any other adjustment in the thrust stand to extend the thrust range to 1 mN, 10 mN and 100 mN respectively. For example, in [143], a xenon plasma thruster has been characterized in the range 20 µN to 500 µN using a similar indirect momentum flux measurement system with 15 µN resolution. With FT-S1000 force sensor, the designed thrust stand in the thesis can be used for measuring these ranges of thrust with 50−100 nN resolution. In [142], a Hall Effect thruster has been characterised in the range of 10's of mN with a resolution of 100 µN, whereas with the thrust stand in the thesis, a FT-S100000 force sensor can be used to measure with 5−10 µN thrust resolution. These possible applications extend the use of the thrust stand to beyond micro-thrusters. Several micro-propulsion technologies, expected to dominate the small satellite propulsion [5], [12], [254] era, can be benefited from this measurement scheme due to possibility of measurement of thrust from different types of thrusters in different thrust ranges with state-of-the-art resolution and may help the research fraternity working in this domain.

Appendix A
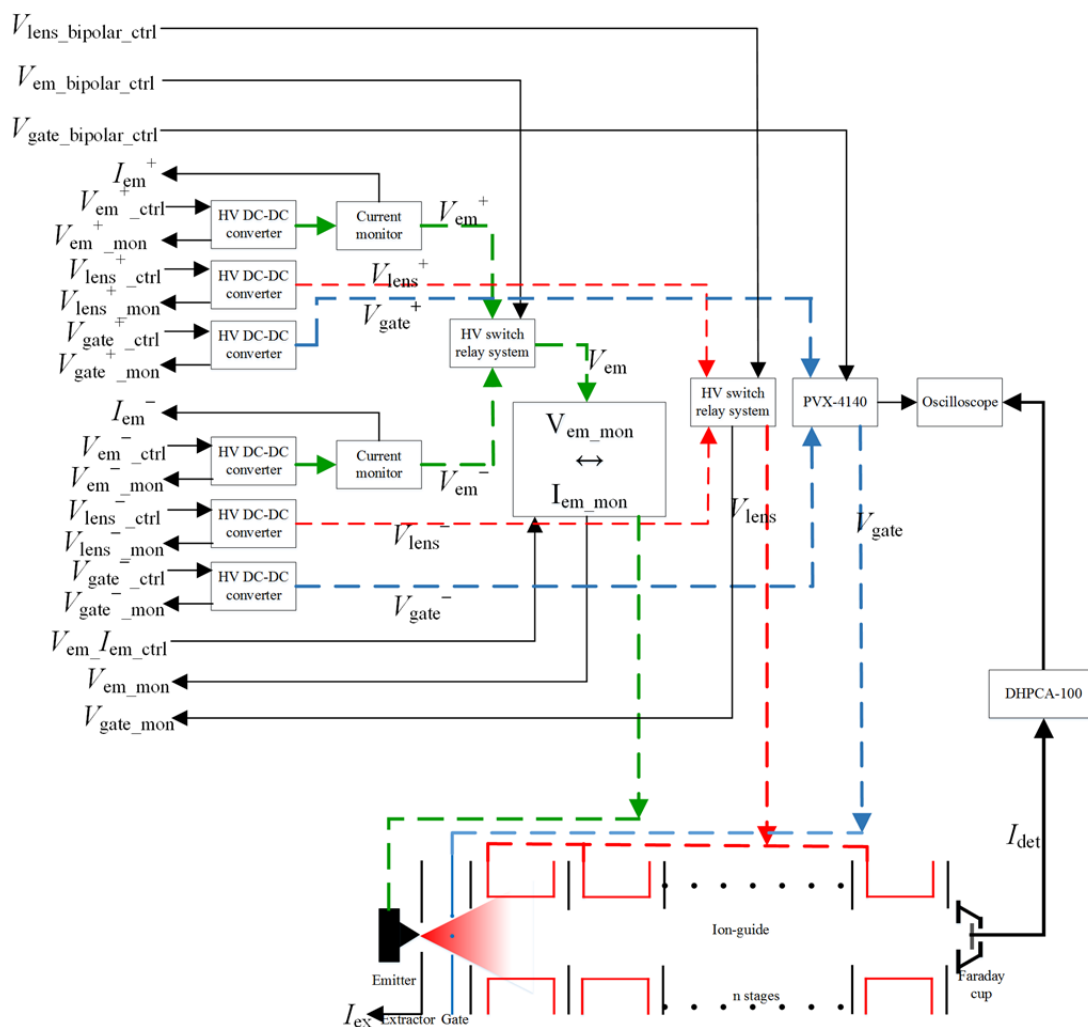
Figure A1: Schematic of the test setup for the mass spectrometric characterization of the electrospray sources using the ToF-MS with the ion-guide.

Table T1: List of signals and descriptions for the ToF-MS setup

Signal	Signal description	Notation	Range
Power supply	Emitter positive power supply	V_{em+}	0 to 2 kV
	Emitter negative power supply	V_{em-}	0 to −2 kV
	Ion-guide positive power supply	V_{lens+}	0 to 3 kV
	Ion-guide negative power supply	V_{lens-}	0 to −3 kV
	Gate positive power supply	V_{gate+}	0 to 3 kV
	Gate negative power supply	V_{gate-}	0 to −3 kV
Monitor signal	Ion-guide negative power supply	$V_{em\ mon}^{+}$	0 to 5 V
	Emitter negative voltage monitor	$V_{em\ mon}^{-}$	0 to −5 V
	Ion-guide positive voltage monitor	$V_{lens\ mon}^{+}$	0 to 5 V
	Ion-guide negative voltage monitor	$V_{lens\ mon}^{-}$	0 to −5 V
	Gate positive voltage monitor	$V_{gate\ mon}^{+}$	0 to 5 V
	Gate negative voltage monitor	$V_{gate\ mon}^{-}$	0 to −5 V
	Emitter bipolar voltage monitor	V_{em_mon}	−2 V to +2V
	Ion-guide bipolar power supply	V_{lens_mon}	−2 V to +2V
	Gate bipolar voltage monitor	V_{gate_mon}	−2 V to +2V
	Extractor current monitor	I_{ex}	−10 µA to 10 µA
	Emitter current monitor positive polarity	I_{em}^{+}	(0 to 10 V)/G_r^*
	Emitter current monitor negative polarity	I_{em}^{-}	(0 to −10 V)/G_r^*
	Detector current monitor	I_{det}	(−1 V to 1 V)/$G^{\#}$
Control signal	Emitter positive power supply control	$V_{em\ ctrl}^{+}$	0 to 5 V
	Emitter negative power supply control	$V_{em\ ctrl}^{-}$	0 to 5 V
	Ion-guide positive power supply control	$V_{lens\ ctrl}^{+}$	0 to 5 V
	Ion-guide negative power supply control	$V_{lens\ ctrl}^{-}$	0 to 5 V
	Gate positive power supply control	$V_{gate\ ctrl}^{+}$	0 to 5 V
	Gate negative power supply control	$V_{gate\ ctrl}^{-}$	0 to 5 V
	Emitter bipolar switching control	$V_{em\_bipolar\_ctrl}$	0 to 5 V
	Ion-guide switching control	$V_{lens\_bipolar\_ctrl}$	0 to 5 V
	Emitter voltage/emitter current monitor mode control	$V_{em}\_I_{em\_ctrl}$	0 to 5 V
	Gate switching	$V_{gate\_bipolar\_ctrl}$	0 to 5 V

*G_r = 10^6 V/A, 10^5 V/A, 10^4 V/A, based on selectable gain setting for the isolation amplifier
$^{\#}G$ = Gain setting of the DHPCA-100 transimpedance amplifier in V/A

Bibliography

[1]   J. Mueller, "Thruster Options for Microspacecraft: A Review and Evaluation of Existing Hardware and Emerging Technologies", Paper AIAA 97-3058, 33rd AIAA/ASME/SAE/ASEE Joint Propulsion Conference, Seattle, Washington, USA, 1997.

[2]   J. Mueller, C. Marsee, J. Polk, E. H. Yang, A. Green, V. White, D. Bame, I. Chakraborty, S. Vargo and R. Reinicke, "An Overview of MEMS-based Micropropulsion Development at JPL", *Acta Astronautica*, 52, pp. 881–895, 2003.

[3]   C. Underwood, G. Richardson and J. Savignol, "SNAP-1: A Low Cost Modular COTS-Based Nano-Satellite – Design, Construction, Launch and Early Operations Phase", Paper SSC01-VI-7, 15th AIAA / USU Conference on Small Satellites, Logan, UT, USA, Aug. 2001.

[4]   M. Richard, L. Kronig, F. Belloni, S. Rossi, V. Gass, C. Paccolat, J.P. Thiran, S. Araomi, I. Gavrilovich and H. Shea, "Uncooperative Rendezvous and Docking for MicroSats", 6th International Conference on Recent Advances in Space Technologies, RAST 2013, Istambul, Turkey, Jun. 2013.

[5]   S. Dandavino, "Microfabricated Electrospray Thrusters for a Modular Spacecraft Propulsion System", PhD Dissertation, Doctoral Program in Microsystems and Microelectronics, EPFL, 2014.

[6]   http://kk.org/cooltools/archives/7419.

[7]   "CubeSat Design Specification (CDS)", Rev. 12, The CubeSat Program, Cal Poly SLO, California Polytechnic State University. Available at: http://www.srl.utu.fi/AuxDOC/tke/radmon/cubesat_standard.pdf.

[8]   "List of CubeSats", Available at: http://en.wikipedia.org/wiki/List_of_CubeSats.

[9]   D. D. Garber, "The CubeSat Challenge: A Review of CubeSat Dependencies and Requirements for Space Tracking Systems", 2012.

[10]   R. L. Staehle, D. Blaney, H. Hemmati, D. Jones, A. Klesh, P. Liewer, J. Lazio, M. W. Lo, P. Mouroulis, N. Murphy, P. J. Pingree, T. Wilson, B. Anderson, C. C. Chow II, B. Betts, L. Friedman, J. Puig-Suari, A. Williams and T. Svitek, "Interplanetary CubeSats: Opening the Solar System to a Broad Community at Lower Cost", *Journal of Small Satellites*, vol. 2, no. 1, pp. 161-186, 2013.

[11]   C. C. Venturini, L. R. Abramowitz, J. D. Johansen, J. G. Gee and W. G. Floyd, "CubeSat Developmental Programs - Working with the Community", Paper: AIAA 2009-6501, AIAA SPACE 2009 Conference & Exposition, Pasadena, California, USA, 2009.

[12]   J. Mueller, R. Hofer, and J. Ziemer, "Survey of Propulsion Technologies Applicable to Cubesats", Jet Propulsion Laboratory, May, 2010.

[13]   S. Waydo, D. Henry and M. Campbell, "CubeSat Design for LEO-Based Earth Science Missions", IEEE Aerospace Conference, vol. 1, pp. 435−445, 2002.

[14]   R. Nugent, R. Munakata, A. Chin, R. Coelho and J. Puig-Suari, "The CubeSat: The Picosatellite Standard for Research and Education", AIAA Paper 2008-7734, AIAA SPACE 2008, San Diego, CA, USA, Sept. 2008.

[15]   D. G. Courtney, "Ionic liquid ion source emitter arrays fabricated on bulk porous substrates for spacecraft propulsion", PhD Dissertation, Department of Aeronautics and Astronautics, MIT, USA, 2011.

[16]   M. S. Rhee, C. M. Zakrzwski and M. A. Thomas, "Highlights of Nanosatellite Development Program at NASA-Goddard Space Flight Centre", Paper SSC00-X-5, 14th Annual/USU Conference on Small Satellites, Logan, UT, USA, Jan. 2000.

[17]   J. Zeleny, "The electrical discharge from liquid points, and a hydrostatic method of measuring the electric field intensity at their surfaces", *The Physical Review, Royal Society of London*, vol. 3, no. 2, pp.69−91, 1914.

[18]   G. Taylor, "Disintegration of water drops in an electric field", *Proceedings of the Royal Society of London*, vol. 280, no. 1382, pp. 383−397, 1964.

[19]   J. B. Fenn, M. Mann, C. K. Meng, S. F. Wong and C. M. Whitehouse "Electrospray ionization for mass spectrometry of large biomolecules" *Science*, vol. 246, no. 4926, pp. 64−71, 1989.

[20]   R. L. Seliger and W. P. Fleming, "Focused ion beams in microfabrication", *Journal of Applied Physics*, vol. 45, issue 3, pp. 1416−1422, 1974.

[21]   J. Perel, "Alkali Metal Ion Sources", *Journal of Electrochemical Society*, vol. 115, no. 12, pp. 343−350, 1968.

[22]   C. D. Hendricks Jr., "Charged Droplet Experiments" *Journal of Colloid Science*, 17, pp. 249−259, 1962.

[23]   http://sci.esa.int/lisa-pathfinder/39981-engineering/?fbodylongid=1901.

[24]   https://directory.eoportal.org/web/eoportal/satellite-missions/l/lisa-pathfinder.

[25]   "Laser Interferometer Space Antenna (LISA) Sciencecraft Description", LISA-SC-DD-0001, Goddard Space Flight Centre, Greenbelt, Maryland, USA, Jan. 2009.

[26]   J. K. Ziemer, T. M. Randolph, G. W. Franklin, V. Hruby, D. Spence, N. Demmons, T. Roy, E. Ehrbar, J. Zwahlen, R. Martin and W. Connolly, "Colloid Micro-Newton Thrusters for the Space Technology 7 Mission", IEEE Aerospace Conference, Big Sky, MT, USA, Mar. 2010.

[27]   J. Gonzalez, G. Saccoccia and H. von Rohden, "Field Emission Electric Propulsion: Experimental Investigations on Microthrust FEEP Thrusters", Paper IEPC 93-157, 23rd International Electric Propulsion Conference, Seatle, WA, USA, Sept. 1993.

[28]   S. Marcuccio, A. Genovese and M. Andrenucci, "Experimental Performance of Field Emission Microthrusters", *Journal of Propulsion and Power*, vol. 14, no. 5, pp. 774–781, 1998.

[29]   C. Scharlemann and M. Tajmar, "Development of Propulsion Means for Microsatellites", 43rd AIAA/ASME/SAE/ASEE Joint Propulsion Conference & Exhibit, Cincinati, OH, USA, Jul. 2007.

[30]   L. Paita, F. Ceccanti, M. Spurio, U. Cesari, L. Priami, F. Nania, A. Rossodivita and M. Andrenucci, "Alta's FT-150 FEEP Microthruster: Development and Qualification Status", Paper: IEPC-2009-186, 31st International Electric Propulsion Conference, Ann Arbor, Michigan, USA, Sept. 2009.

[31]   F. Ceccanti, L. Paita, U. Cesari, M. D. Tata, N. Giusti, P. Balducci, M. Del Pistoia, D. Nicolini and L. D. Napoli, "3200 hours Endurance Testing of the Lisa Pathfinder FT-150 Thruster", Paper: IEPC-2009-170, 31st International Electric Propulsion Conference, Ann Arbor, Michigan, USA, Sept. 2009.

[32]   C. Scharlemann, A. Genovese, N. Buldrini, R. Schnitzer, M. Tajmar, H. Früholz and R. Killinger, "Status of the Indium FEEP Micropropulsion Subsystem Development for LISA Pathfinder", Paper: IEPC-2007-122, 30th International Electric Propulsion Conference, Florence, Italy, Sept. 2007.

[33]   J. C. Beynon, E. Cohen, D. S. Goldin, M. N. Huberman, P. W. Kidd and S. Zafran, "Present status of colloid microthruster technology", *Journal of Spacecraft and Rockets*, vol. 5, no. 11 pp. 1319–1324, 1968.

[34]   K. W. Stark and A. Sherman, "Research and development in needle and slit colloid thrusters", NASA TN D-5305, Goddard Space Flight Centre, 1970.

[35]   R. Krpoun, "Micromachined Electrospray Thruster for Spacecraft Propulsion", PhD dissertation, Doctoral Program in Microsystems and Microelectronics, EPFL, 2009.

[36]   I. Romero-Sanz, R. Bocanegra, J. F. de la Mora and M. Gamero-Castaño, "Source of heavy molecular ions based on Taylor cones of ionic liquids operating in the pure ion evaporation regime", *Journal of Applied Physics*, vol. 94, issue 5, pp. 3599–3605, 2003.

[37]   D. Garoz, C. Bueno, C. Larriba, S. Castro, I. Romero-Sanz, J. F. de la Mora, Y. Yoshida and G. Saito, "Taylor cones of ionic liquids from capillary tubes as sources of pure ions: The role of surface tension and electrical conductivity", *Journal of Applied Physics*, 102, 064913, 2007.

[38]   S. Castro, C. Larriba, J. F. de la Mora, P. Lozano, S. Sümer, Y. Yoshida and G. Saito, "Effect of liquid properties on electrosprays from externally wetted ionic liquid ion sources", *Journal of Applied Physics*, 102, 094310, 2007.

[39]   P. Lozano, "Studies on the ion-droplet mixed regime in colloid thrusters", PhD Dissertation, Department of Aeronautics and Astronautics, MIT, USA, 2003.

[40]   Y.-H. Chiu, B. L. Austin, R. A. Dressler, D. Levandier, P. T. Murray, P. Lozano, M. M.-Sanchez, "Mass Spectrometric Analysis of Colloid Thruster Ion Emission from Selected Propellants", *Journal of Propulsion and Power*, vol. 21, no. 3, pp. 416–423, 2005.

[41]   P. C. Lozano, "Energy properties of an EMI-Im ionic liquid ion source", *Journal of Physics D: Applied Physics*, vol. 39, no. 1, pp. 126–134, 2006.

[42]   P. Lozano and M. Martinez-Sanchez, "On the dynamic response of externally wetted ionic liquid ion sources", *Journal of Physics D: Applied Physics*, vol. 38, no. 14, pp. 2371–2377.

[43]   P. Lozano, M. Martínez-Sánchez, "Ionic liquid ion sources: suppression of electrochemical reactions using voltage alternation" *Journal of Colloid Interface Science* 280, pp. 149–154, 2004.

[44]   P. Lozano, M. Martínez-Sánchez, "Ionic liquid ion sources: characterization of externally wetted emitters", *Journal of Colloid and Interface Science*, 282, pp. 415–421, 2005.

[45]   A. N. Zorzos and P. C. Lozano, "The use of ionic liquid ion sources in focused ion beam applications", *Journal of Vacuum Science and Technology B*, vol. 26, issue 6, pp. 2097–2102, 2008.

[46]   T. P. Fedkiw and P. C. Lozano, "Development and characterization of an iodine field emission ion source for focused ion beam applications", *Journal of Vacuum Science and Technology B*, vol. 27, issue 6, pp. 2648–2653, 2009.

[47]   C. S. Perez-Martinez and P.C. Lozano, "Visualization of beams from ionic liquid ion sources for focused ion beam applications", *Journal of Vacuum Science & Technology B*, vol. 30 no.6, pp. 06F601, 2012.

[48]   L. F. Velásquez-García, A. I. Akinwande and M. Martínez–Sánchez, "A Planar Array of Micro-Fabricated Electrospray Emitters for Thruster Applications", *Journal of Microelectromechanical System*, vol. 15, no. 3, pp. 1272–1280, 2006.

[49]   B. Gassend, L. F. Velásquez-García, A. I. Akinwande, and M. Martínez-Sánchez, "A Microfabricated Planar Electrospray Array Ionic Liquid Ion Source With Integrated Extractor", *Journal of Microelectromechanical System*, vol. 18, no. 3, pp. 679–694, 2009.

[50]   D. G. Courtney, H. Q. Li and P. Lozano, "Emission measurements from planar arrays of porous ionic liquid ion sources", *Journal of Physics D: Applied Physics*, 45, 485203 (13pp), 2012.

[51]   R. S. Legge, Jr. and P. C. Lozano, "Electrospray Propulsion Based on Emitters Microfabricated in Porous Metals", *Journal of Propulsion and Power*, vol. 27, no. 2, pp. 485–495, 2011.

[52]   C. S. Coffman, L. Perna, H. Li, and P. C. Lozano, "On the Manufacturing and Emission Characteristics of a Novel Borosilicate Electrospray Source", 49th AIAA/ASME/SAE/ASEE Joint Propulsion Conference and Exhibit, pp. 1–12, 2013.

[53]   D. G. Courtney, S. Dandavino and H. Shea, "Comparing Direct and Indirect Thrust Measurement from passively Fed and Highly Ionic Electrospray Thrusters", Submitted to *Journal of Propulsion and Power*.

[54]   C. Ataman, S. Dandavino, H. Shea, **"**Wafer-level integrated electrospray emitters for a pumpless microthruster system operating in high efficiency ion – mode", IEEE 25th

International Conference on Micro Electro Mechanical Systems (MEMS), Paris, France, pp. 1293–1296, Jan. 2012.

[55]   S. Dandavino, C. Ataman, H. Shea, C. Ryan and J. Stark, "Microfabrication of Capillary Electrospray Emitters and ToF Characterization of the Emitted Beam", IEPC-2011-131, 32nd International Electric Propulsion Conference, Wiesbaden, Germany, Sept. 2011.

[56]   R. Krpoun, K. L. Smith, J. P. W. Stark and H. R. Shea, "Tailoring the hydraulic impedance of out-of-plane micromachined electrospray sources with integrated electrodes", *Applied Physics Letters*, 94, 163502, 2009.

[57]   R. Krpoun and H. R. Shea, "Integrated out-of-plane nanoelectrospray thruster arrays for spacecraft propulsion", *Journal of Micromechanics and Microengineering*, 19, 045019, 2009.

[58]   M. Gamero-Castaño, "Characterization of the electrosprays of 1-ethyl-3-methylimidazolium bis(trifluoromethylsulfonyl) imide in vacuum", *Physics of Fluids (1994–present)*, 20, 032103, 2008.

[59]   I. Romero-Sanz and J. F. de la Mora, "Energy distribution and spatial structure of electrosprays of ionic liquids in vacuo", *Journal of Applied Physics*, vol. 95, no. 4, pp. 2123–2129, 2004.

[60]   http://cordis.europa.eu/project/rcn/96931_en.html.

[61]   C. Ryan, J. P. W. Stark, C. Ataman, S. Dandavino, S. Chakraborty and H. Shea, "MicroThrust MEMS electrospray emitters – integrated microfabrication and test results", AAAF-ESA-CNES Space Propulsion 2012, May 2012, Bordeaux, France.

[62]   S. Dandavino, C. Ataman, C. N. Ryan, S. Chakraborty, D. Courtney, J. P. W. Stark and H. Shea, "Microfabricated electrospray emitter arrays with integrated extractor and accelerator electrodes for the propulsion of small spacecraft", *Journal of Micromechanics and Microengineering*, vol. 24, no. 7, pp. 075011, 2014.

[63]   C. Ryan, A. Daykin-Iliopoulos, J. A. Stark, A. Salaverri, E. Vargas, P. Rangsten, S. Dandavino, C. Ataman, S. Chakraborty, D. Courtney, H. Shea, "Experimental progress towards the MicroThrust MEMS electrospray electric propulsion system", 33rd International Electric Propulsion Conference (IEPC), Washington DC, USA, pp. 146, Oct. 2013.

[64]   R. J. Cotter, "Time-of-flight Mass Spectrometry: Instrumentation and Applications in Biological Research", 1st Ed., ACS Professional Reference Books, Washington DC, 1997.

[65]   K. J. Terhune, L. B. King, K. He and J. Cumings, "In situ visualization of ionic liquid electrospray emission using transmission electron microscopy", 49th AIAA/ASME/SAE/ASEE Joint Propulsion Conference. San Jose, CA, 2013.

[66]   C. S. Ho, C. W.K. Lam, M. H. M. Chan, R. C. K. Cheung, L. K. Law, L. C. W. Lit, K. F. Ng, M. W. M. Suen and H. L. Tai, "Electrospray Ionisation Mass Spectrometry: Principles and Clinical Applications", *The Clinical Biochemist Reviews*, 24(1), pp. 3–12, 2003.

[67]   A. P. Bruins, "Mechanistic aspects of electrospray ionization", *Journal of Chromatography A*, 794, issue 1–2, pp. 345–357, 1998.

[68]   W. E. Steiner, B. H. Clowers, K. Fuhrer, M. Gonin, L. M. Matz, W. F. Siems, A. J. Schultz and H. H. Hill Jr., "Electrospray ionization with ambient pressure ion mobility separation and mass analysis by orthogonal time-of-flight mass spectrometry", *Rapid Communications in Mass Spectrometry,* vol. 15, issue 23, pp. 2221–2226, 2001.

[69]   J. Coles and M. Guilhaus, "Orthogonal acceleration - a new direction for time-of-flight mass spectrometry: fast, sensitive mass analysis for continuous ion sources", *TrAC Trends in Analytical Chemistry*, vol. 12, no. 5, pp. 203–213, 1993.

[70]   O. A. Mirgorodskaya and A. A. Shevchenko, "Electrospray Ionization Time-of-Flight Mass Spectrometry in Protein Chemistry", *Analytical Chemistry*, vol. 66, no. 1, pp. 99–107, 1994.

[71]   G. R. Hilton and J. L. P. Benesch, "Two decades of studying non-covalent biomolecular assemblies by means of electrospray ionization mass spectrometry", *Journal of the Royal Society*: *Interface*, vol. 9, issue 70, pp. 801–816, 2012.

[72]   M. L. Vestal, "The future of biological mass spectrometry", *Journal of the American Society for mass Spectrometry*, 22, pp. 953–959, 2011.

[73]   R. G.-Villalbaa, A. C.-Pancorbo, C. O.-Ferraros, A. V.-Martínb, J. A. Menéndez, A. S.-Carreteroa and A. F.-Gutiérrez, "Characterization and quantification of phenolic compounds of extra-virgin olive oils with anticancer properties by a rapid and resolutive LC-ESI-TOF MS method", *Journal of Pharmaceutical and Biomedical Analysis*, 51, pp. 416–429, 2010.

[74]   I. Ojanperä, M. Kolmonen and A. Pelander, "Current use of high-resolution mass spectrometry in drug screening relevant to clinical and forensic toxicology and doping control", *Analytical and Bioanalytical Chemistry*, vol. 403, issue 5, pp. 1203–1220, 2012.

[75]   A. E. Cameron and D. F. Eggers Jr., "An ion velocitron", *Review of Scientific Instruments*, vol. 19, no 9, pp. 605–607, 1948.

[76]   M. M. Wolff and W. E. Stephens, "A Pulsed Mass Spectrometer with Time Dispersion", *Review of Scientific Instruments*, vol. 24, no 8, pp. 616–617, 1953.

[77]   M. Dole, L. L. Mack, R. L. Hines, R. C. Mobley, L. D. Ferguson and M. B. Alice, "Molecular Beams of Macroions", *The Journal of Chemical Physics*, vol. 49, issue 5, pp. 2240–2249, 1968.

[78]   A. G. Bailey, "Investigation of a single spraying site of a colloid thruster", *Journal of Physics D: Applied Physics*, vol. 6, no. 2, pp. 276–288, 1973.

[79]   M. Karas and F. Hillencamp, "Laser Desorption Ionization of Proteins with Molecular Masses Exceeding 10 000 Daltons", *Analytical Chemistry*, 60, pp. 2299–2301, 1988.

[80]   K. Tanaka, H. Waki, Y. Ido, S. Akita, Y. Yoshida, T. Yoshida and T. Matsuo, "Protein and polymer analyses up to m/z 100 000 by laser ionization time-of-flight

mass spectrometry", *Rapid Communications in Mass Spectrometry*, vol. 2, issue 8, pp. 151−153, 1988.

[81] G. Lenguito and A. Gomez, "Development of a multiplexed electrospray micro-thruster with post-acceleration and beam containment", *Journal of Applied Physics*, 114, 154901, 2013.

[82] http://ixapps.ixys.com/DataSheet/pvm-4210_manual.pdf.

[83] C. Larriba, S. Castro, S., J. F. de la Mora and P. Lozano, "Mono-energetic source of kilodalton ions from Taylor cones of ionic liquids", *Journal of Applied Physics*, 101, 084303, 2007.

[84] http://ixapps.ixys.com/DataSheet/pvx-4150_data_sheet.pdf.

[85] W. C. Wiley and I. H. McLaren, "Time-of-Flight Mass Spectrometer with Improved Resolution", *Review of Scientific Instruments*, vol. 26, no. 12, pp. 1150−1157, 1955.

[86] S. Chakraborty, C. Ataman, S. Dandavino and H. Shea, "Microfabrication of an electrospray thruster for small spacecraft", PowerMEMS 2012, pp. 528−531, Atlanta, USA, 2012.

[87] M. Gamero-Castaño, "The structure of electrospray beams in vacuum", *Journal of Fluid Mechanics* 604, pp. 339–368, 2008.

[88] FEMTO DHPCA-100 datasheet. Available at http://femto.de/images/pdf-dokumente/de-dhpca-100_r10.pdf.

[89] S. Chakraborty, S. Dandavino, C.Ataman, , D. G. Courtney and H. Shea, "Development of a ToF setup with an ion-guide for characterization of electrospray microthrusters", Paper IEPC-2013-413, 33rd International Electric Propulsion Conference (IEPC), Washington, D.C. USA, Oct. 2013.

[90] S. Chakraborty, C. Ataman, D. G. Courtney, S. Dandavino, H. Shea, "A ToF-MS with a Highly Efficient Electrostatic Ion Guide for Characterization of Ionic Liquid Electrospray Sources", *Journal of The American Society for Mass Spectrometry*, vol. 25, issue 8, pp. 1364−1373, 2014.

[91] C. Ryan, "Spray results from using EMI DCA", ECM QMUL-2205, 2012.

[92] C. L. Enloe and J. R. Shell, "Optimizing the energy resolution of planar retarding potential analyzers", *Review of Scientific Instruments*, vol. 63, issue 2, pp. 1788−1791, 1992.

[93] B. A. Mamyrin, V. I. Karataev, D. V. Shmikk, and V. A. Zagulin, "The mass-reflectron, a new nonmagnetic time-of-flight mass spectrometer with high resolution", *Journal of Experimental and Theoretical Physics*, vol. 37, no. 1, pp. 45–47, 1973.

[94] http://www.chem.agilent.com/Library/usermanuals/Public/G3300-90012_TOF_Concepts_v.5.pdf.

[95] A. W. T. Bristow and K. S. Webb, "Intercomparison Study on Accurate Mass Measurement of Small Molecules in Mass Spectrometry*", Journal of the American Society for Mass Spectrometry*, vol. 14, issue 10, pp. 1086−1098, 2003.

[96] I. Ferrer and E. M. Thurman, "Measuring the Mass of an Electron by LC/TOFMS: A Study of "Twin Ions", *Analytical Chemistry*, 77 (10), pp. 3394 –3400, 2005.

[97]   http://www.tofwerk.com.

[98]   M. P. Balogh, "Debating Resolution and Mass Accuracy", LC-GC Europe, vol. 17, issue 3, pp. 152–159, 2004.

[99]   C. G. Georgakopoulos, A. Vonaparti, M. Stamou, P. Kiousi, E. Lyris, Y. S. Angelis, G. Tsoupras, B. Wuest, M. W. Nielen, I. Panderi and M. Koupparis, "Preventive doping control analysis: liquid and gas chromatography time-of-flight mass spectrometry for detection of designer steroids", *Rapid Communication in Mass Spectrom*etry, vol. 21, issue 15, pp. 2439–2446, 2007.

[100]   L. N. Williamson and M. G. Bartlett, "Quantitative gas chromatography/time-of-flight mass spectrometry: a review", *Biomedical Chromatography*, vol. 21, issue 7, pp. 664–669, 2007.

[101]   M. Guilhaus, "Principles and Instrumentation in time-of-flight mass spectrometry", *Journal of Mass Spectrometry*, vol. 30, pp. 1519–1532, 1995.

[102]   F. Mühlberger, M. Saraji-Bozorgzad, M. Gonin, K. Fuhrer and R. Zimmermann, "Compact ultrafast orthogonal acceleration time-of-flight mass spectrometer for on-line gas analysis by electron impact ionization and soft single photon ionization using an electron beam pumped rare gas excimer lamp as VUV-light source", *Analytical Chemistry*, vol. 79, no. 21, pp. 8118–8124, 2007.

[103]   Y. Kitahara, S. Takahashi, N. Kuramoto, M. Sala, T. Tsugoshi, M. Sablier and T. Fujii, "Ion attachment mass spectrometry combined with infrared image furnace for thermal analysis: evolved gas analysis studies", *Analytical Chemistry*, vol. 81, no. 8, pp. 3155–3158, 2009.

[104]   F. Basile, S. Zhang, S. K. Kandar and L. Lu, "Mass spectrometry characterization of the thermal decomposition/digestion (TDD) at cysteine in peptides and proteins in the condensed phase", *Journal of the American Society for mass Spectrometry*, vol. 22, pp. 1926–1940, 2011.

[105]   A. L. van Wuijckhuijse and B. L.M. van Baar, "Recent advances in realtime mass spectrometry detection of bacteria" In: Zourob, M., Elwary S., Turner, A. (eds.) "Principles of Bacterial Detection: Biosensors, Recognition Receptors and Microsystems", pp. 929–954. Springer, New York, 2008.

[106]   R. J. Arnold, J. A. Karty, A. D. Ellington and J. P. Reilly, "Monitoring the growth of a bacteria culture by MALDI-MS of whole cells", *Analytical Chemistry*, vol. 71, no. 10, pp. 1990–1996, 1999.

[107]   J. G. Wilkes, F. Rafli, J. B. Sutherland, L. G. Rushing and D. A. Buzatu, "Pyrolysis mass spectrometry for distinguishing potential hoax materials from bioterror agents", *Rapid Communications in Mass Spectrometry*, vol. 20, issue 16, pp. 2383–2386, 2006.

[108]   J. M. Spraggins and R. M. Caprioli, "High-speed MALDI-TOF imaging mass spectrometry: rapid ion image acquisition and considerations for next generation instrumentation", *Journal of the American Society for mass Spectrometry*, vol. 22, pp. 1022–1031, 2011.

[109] S. W. Miller and B. D. Prince, "Capillary extraction of the ionic liquid [Bmim][DCA] for variable flow rate operations" Proceedings of the 48th AIAA/ASME/SAE/ASEE Joint Propulsion Conference and Exhibit Atlanta, GA, USA, July, 2012.

[110] M. Gamero-Castaño and V. Hruby. "Electrospray as a Source of Nanoparticles for Efficient Colloid Thrusters", *Journal of Propulsion and Power*, vol. 17, no. 5, pp. 977−987, 2001.

[111] E. A. Cubbin, J. K. Zeimer, E. Y. Choueiri and R. G. Jahn, "Pulsed thrust measurement using laser interferometry", *Review of Scientific Instruments*, vol. 68, no. 6, pp. 2339−2346, 1997.

[112] K. W. Stark, T. Dennis, D. McHug and T. Williams, "Design and development of a micropound extended range thrust stand", NASA TN-7029, Aug. 1971.

[113] R. J. Radley Jr., "A performance study of a pulsed solid fuel microthruster", M. Sc dissertation, Dept. of Aeronautics and Astronautics, MIT, 1968.

[114] R. Vondra, K. Thomassen and A. Solbes, "A Pulsed Electric Thruster for Satellite Control", *Proceedings of the IEEE*, vol. 59, no. 2, pp. 271−278, 1971.

[115] E. G. Adelberger, C. W. Stubbs, B. R. Heckel, Y. Su, H. E. Swanson, G. Smith and J. H. Gunlach, "Testing the equivalence principle in the field of the Earth: Particle physics as masses below 1 μeV?" *Physical Review D: Particles and Fields*, vol. 42, no. 10, pp. 3267−3292, 1990.

[116] F. Paolucci, L. d'Agostino and S. Burgoni, "Design and performance of a micro-Newton thrust stand for FEEP", 2nd European Spacecraft Propulsion Conference, ESTEC, Noordwijk, The Netherlands, pp. 465-472, May 1997.

[117] L. Boccaletto and L. d'Agostino, "Design and testing of a micro-Newton thrust stand for FEEP", Paper AIAA 2000-3268, 36th AIAA/ASME/SAE/ASEE Joint Propulsion Conference, Huntsville, AL, USA, Jul. 2000.

[118] A. G. Bailey, J. E. Bracher, H. G. Helmke and H. J. von Rohden, "A Test Facility for Electric Microthrusters", *Review of Scientific Instruments*, vol. 43, no. 3, pp. 420−424, 1972.

[119] T. W. Haag, "Thrust stand for pulsed plasma thruster", *Review of Scientific Instruments*, vol. 68, no. 5, pp. 2060−2067, 1997.

[120] D. Nicolini, E. Chesta, J. G. del Amo and G. Saccoccia, "FEEP-5 Thrust Validation in the 10-100μN Tange with a Simple Nulled-Pendulum Thrust Stand: Integration Procedures", Paper IEPC-01-288, 27th International Electric Propulsion Conference, Pasedena, CA, USA, Oct. 2001.

[121] S. Rocca, C. Menon and D. Nicolini, "FEEP micro-thrust balance characterization and testing", *Measurement Science and Technology*, 17, pp. 711−718, 2006.

[122] E. Canuto and A. Rolino, "Nanobalance: An automated interferometric balance for micro-thrust measurement", *ISA Transactions*, 43, pp. 169−187, 2004.

[123] J. P. Lake, G. Cavallaro, G. Spanjers, P. B. Adkison and M. J. Dulligan, "Resonant Operation of a Micro-Newton Thrust Stand", Technical paper AFRL-PR-ED-TP-2002-308, Air Force Research Laboratory, Edwards AFB CA, USA, Jan. 2003.

[124]   J. K. Zeimer, "Performance Measurements Using a Sub-Micronewton Resolution Thrust Stand", Paper IEPC-01-238, 27th International Electric Propulsion Conference, Pasedena, CA, USA, Oct. 2001.

[125]   J. K. Ziemer, "Sub-Micronewton Thrust Measurement of Indium Field Emission Thrusters", Paper IEPC-03-247, 28th International Electric Propulsion Conference, Toulouse, France, Mar. 2003.

[126]   D. Packan, J. Bonnet and S. Rocca, "Thrust Measurements with the ONERA Micronewton Balance", IEPC-2007-118, 30th International Electric Propulsion Conference (IEPC), Florence, Italy, Sept. 2007.

[127]   D. Packan, J. Jarrige, P. Thobois, C. Blanchard and P.-Q. Elias, "Micronewton Balance Measurements at Onera and Application to the GAIA Mission", IEPC-2013-418, 33rd International Electric Propulsion Conference (IEPC), Washington, D.C., USA, Oct. 2013.

[128]   M. Gamero-Castaño and V. Hruby, "A Torsional Balance that resolves Sub-micro-Newton Forces", Paper IEPC-01-235, 27th International Electric Propulsion Conference, Pasedena, CA, USA, Oct. 2001.

[129]   M. Gamero-Castaño, "A torsional balance for the characterization of microNewton thrusters", *Review of Scientific Instruments*, vol. 74, no. 10, pp. 4509–4514, 2003.

[130]   A. J. Jamison, A. D. Ketsdever and E. P. Muntz, "Accurate Measurement of Nano-Newton Thrust for Micropropulsion System Characterization", Paper IEPC-01-236, 27th International Electric Propulsion Conference, Pasedena, CA, USA, Oct. 2001.

[131]   A. J. Jamison, A. D. Ketsdever and E. P. Muntz, "Gas dynamic calibration of a nano-Newton thrust stand", *Review of Scientific Instruments*, vol. 73, no. 10, pp. 3629–3637, 2002.

[132]   C. R. Phipps, J. R. Luke, W. Helgeson and R. Johnson, "A Low noise Thrust Stand for Microthrusters with 25nN resolution", *AIP Conference Proceedings*, 830, 492, pp. 492–499, 2006.

[133]   C. Phipps, J. Luke, T. Lippert, M. Hauer and A. Wokaun, "Micropropulsion Using a Laser Ablation Jet", *Journal of Propulsion and Power*, vol. 20, no. 6, pp. 1000–1011, 2004.

[134]   F. M. Hicks, "Characterization of a magnetically levitated testbed for electrospray propulsion systems", MS Thesis, Department of Aeronautics and Astronautics, MIT, USA, 2014.

[135]   Y. X. Yang, L. C. Tu, S. Q. Yang and J. Luo, "A torsion balance for impulse and thrust measurements of micro-Newton thrusters", *Review of Scientific Instruments*, 83, 015105, 2012.

[136]   J. Sony and S. Roy, "Design and characterization of a nano-Newton resolution thrust stand", *Review of Scientific Instruments*, 84, 095103, 2013.

[137]   K. A. Polzin, T. E. Markusic and B. J. Stanojev, "Thrust stand for propulsion performance evaluation", *Review of Scientific Instruments*, 77, 105108, 2006.

[138] J. P. Luna, C. H. Edwards, J. G. del Amo and B. Hughes, "Development status of the ESA Micro-Newton Thrust Balance", Paper IEPC-2011-011, 32nd International Electric Propulsion Conference, Weisbaden, Germany, Sept. 2011.

[139] C. K. Wu, H. X. Wang, X. Meng and W. X. Pan, "Aerodynamics of indirect thrust measurement by the impulse method", *Acta Mechanica Sinica*, vol. 27, issue 2, pp. 152–163, 2011.

[140] A. N. Grubišić and S. B. Gabriel, "Development of an indirect counterbalanced pendulum optical-lever thrust balance for micro- to millinewton thrust measurement", *Measurement Science and Technology*, vol. 21 no. 10, 105101, 2010.

[141] D. Bing-xiao, Z. Yong, Y. Wen and C. Xiao-qian, "Review of thrust measurement techniques for micro-thrusters", *Journal of Measurement Science and Instrumentation*, vol. 4, no. 2, pp. 103–110, 2013.

[142] B. W. Longmier, B. M. Reid, A. D. Gallimore, F. R. Chang-Diaz, J. P. Squire, T. W. Glover, G. Chavers and E. A. Bering, "Validating a Plasma Momentum Flux Sensor to an Inverted Pendulum Thrust Stand", *Journal of Propulsion and Power*, vol. 25, vo. 3, pp. 746–752, 2009.

[143] M. D. West, C. Charles and Rod W. Boswell, "A high sensitivity momentum flux measuring instrument for plasma thruster exhausts and diffusive plasmas", *Review of Scientific Instruments*, 80, 053509, 2009.

[144] Y. Takao, K. Eriguchi and K. Ono, "A miniature electrothermal thruster using microwave-excited microplasmas: Thrust measurement and its comparison with numerical analysis", *Journal of Applied Physics*, 101, 123307, 2007.

[145] Model FC-72A Faraday cup specifications, Available at http://www.kimballphysics.com/detectors/parts-listing/faraday-cups/fc-72.

[146] http://www.keithley.com/products/dcac/voltagesource/application/?mn=6487.

[147] W. S. Choong, "Investigation of a Multi-Anode Microchannel Plate PMT for Time-of-Flight PET", *IEEE Transactions on Nuclear Science*, vol. 57, no. 5, pp. 2417–2423, 2010.

[148] J. C. Schwartz M. W. Senko and J. E. P. Syka, "A Two-Dimensional Quadrupole Ion Trap Mass Spectrometer", *Journal of the American Society for Mass Spectrometry*, vol. 13, no. 6, pp. 659–669, 2002.

[149] G. Andersson, "Angle resolved ion scattering spectroscopy at surfaces of pure liquids: topography and orientation of molecules", *Physical Chemistry Chemical Physics*, vol. 7, issue 15, pp. 2942–2947, 2005.

[150] C. Bamberger, U. Renz and A. Bamberger, "Digital imaging mass spectrometry", *Journal of the American Society for Mass Spectrometry*, vol. 22, issue 6, pp. 1079–1087, 2011.

[151] S. Ebata, M. Ishihara, K. Kumondai, R. Mibuka, K. Uchino and H. Yurimoto, "Development of an ultra-high performance multi-turn TOF-SIMS/SNMS system MULTUM-SIMS/SNMS", *Journal of the American Society for Mass Spectrometry*, vol. 24, issue 2, pp. 222–229, 2013.

[152] J. C. May and D. H. Russell, "A mass-selective variable-temperature drift tube ion mobility-mass spectrometer for temperature dependent ion mobility studies", *Journal of the American Society for Mass Spectrometry*, vol. 22, issue 7, pp. 1134–1145, 2011.

[153] N. C. Contino, E. E. Pierson, D. Z. Keifer and M. F. Jarrold, "Charge detection mass spectrometry with resolved charge states", *Journal of the American Society for Mass Spectrometry*, vol. 24, issue 1, pp. 101–108, 2013.

[154] http://nasa.olin.edu/projects/2011/efl/background.html

[155] G. H. N. Riddle, "Electrostatic Einzel lenses with reduced spherical aberration for use in field emission guns", *Journal of Vacuum Science and Technology*, vol. 15, issue 3, pp. 857–860, 1978.

[156] K. J. Gillig, B. T. Ruotolo, E. G. Stone and D. H. Russell, "An electrostatic focusing ion guide for ion mobility-mass spectrometry", *International Journal of Mass Spectrometry*, vol. 239, issue 1, pp. 43–49, 2004.

[157] R. C. Blasé, J. A. Silveira, K. J. Gillig, C. M. Gamage and D. H. Russell, "Increased ion transmission in IMS: a high resolution, periodic-focusing DC ion guide ion mobility spectrometer", *International Journal of Mass Spectrometry*, vol. 301, issue 1, pp. 166–173, 2011.

[158] S. Guan and A. G. Marshall, "Stacked-ring electrostatic ion guide", *Journal of the American Society for Mass Spectrometry*, vol. 7, issue 1, pp. 101–106, 1996.

[159] B. Wolf, P. D. Mudgett and R. D. Macfarlane, "A New Method for Electrostatic Ion Deflection", *Journal of the American Society for Mass Spectrometry*, vol. 1, issue 1, pp. 28–36, 1990.

[160] R. Solouki, K. J. Gillig and D. H. Russell, "Detection of High-Mass Biomolecules in Fourier Transform Ion Cyclotron Resonance Mass Spectrometry: Theoretical and Experimental Investigations", *Analytical Chemistry*, 66 (9), pp 1583–1587, 1994.

[161] P. A. Limbach, A. G. Marshall and M. Wang, "An electrostatic ion guide for efficient transmission of low energy externally formed ions into a Fourier transform ion cyclotron resonance mass spectrometer", *International Journal of Mass Spectrometry and Ion Processes*, vol. 125, issue 2–3, pp. 135–143, 1993.

[162] P. V. Bondarenko and R. D. Macfarlane, "A new electrospray-ionization time-of-flight mass spectrometer with electrostatic wire ion-guide", *International Journal of Mass Spectrometry and Ion Processes*, 160, pp. 241–258, 1997.

[163] C. Guimbaud, D. Labonnette, V. Catoire and R. Thomas, "High-pressure flowing-afterglow setup validated by the study of the CO_3^- + HNO_3 reaction", *International Journal of Mass Spectrometry*, vol. 178, issue 3, pp. 161–171, 1998.

[164] M. A. Röttgen, K. Judai, J.-M. Antonietti and U. Heiz, "Conical octopole ion guide: Design, focusing and its application to the deposition of low energetic clusters", *Review of Scientific Instruments*, 77, 013302, 2006.

[165] D. Gerlich, "Inhomogeneous RF fields: A versatile tool for the study of processes with slow ions", Available at https://www.tu-chemnitz.de/physik/ION/Publications/ger92.pdf.

[166] http://www.kimballphysics.com/ev-parts.

[167] C. Perez-Martinez, S. Guilet, N. Gogneau, P. Jegou, J. Gierak and P. Lozano, "Development of ion sources from ionic liquids for microfabrication", *Journal of Vacuum Science & Technology B*, 28, L25, 2010.

[168] http://www.lewvac.com.

[169] https://www.idex-hs.com/catalogsearch/result/?q=N-124S.

[170] http://www.edwardsvacuum.com/pumpingstations/index.htm#index.

[171] C. Perez-Martinez, , S. Guilet, J. Gierak and Paulo Lozano, "Ionic liquid ion sources as a unique and versatile option in FIB applications", *Microelectronic Engineering*, vol. 88, issue 8, pp. 2088–2091, 2011.

[172] http://oldwww.epotek.com/SSCDocs/datasheets/H20S.PDF.

[173] Regulated products. Available at: http://www.emcohighvoltage.com/ regulated-power-supply.php.

[174] Precision, Wide Bandwidth 3-Port Isolation Amplifier: AD210. Available at: http://www.analog.com/static/imported-files/data_sheets/ AD210.pdf.

[175] http://ixapps.ixys.com/Datasheet/pvx-4140_data_sheet.pdf.

[176] DAQ M series. Available at http://www.ni.com/pdf/manuals/371931f.pdf.

[177] NI 9264, Available at : http://sine.ni.com/nips/cds/view/p/lang/en/nid/203424.

[178] http://cotorelay.com/product/9000-series-molded-sip-reed-relays.

[179] S. Castro, J. F. de la Mora, "Effect of tip curvature on ionic liquid emission from Taylor cones of ionic liquids from externally wetted tungsten tips", *Journal of Applied Physics* 105, 034903, 2009.

[180] http://www.gautrain.co.za/about/uploads/2010/04/Volume-03-Chapter-12a-Noise-Vibration-Part-2.pdf.

[181] N. Yazdi, F. Ayazi and K. Najafi, "Micromachined Inertial Sensors", *Proceedings of the IEEE*, vol. 86, no. 8, pp. 1640−1659, 1998.

[182] F. Rudolf, "A micromechanical capacitive accelerometer with a two-point inertial-mass suspension", *Sensors and Actuators*, vol. 4, pp. 191–198, 1983.

[183] F. Rudolf, A. Jornod, J. Bergqvist and H. Leuthold, "Precision Accelerometers with μg Resolution", *Sensors and Actuators*, vol. A21−A23, pp. 297−302, 1990.

[184] C. Lu, M. Lemkin and B. E. Boser, "A Monolithic Surface Micromachined Accelerometer with Digital Output", *IEEE Journal of Solid-State Circuits*, vo. 30, no. 12, pp. 1367−1373, 1995.

[185] N. C. Loh and M. A. Schmidt, "Sub-10 cm^3 Interferometric Accelerometer With Nano-g Resolution", *Journal of Microelectromechanical Systems*, vol. 11, no. 3, pp. 182−187, 2002.

[186] P. M. Zavracky, B. McClelland, K. Warner J. Wang, F. Hwtley and B. Dolgin, "Design and process considerations for a tunneling tip accelerometer", *Journal of Micromechanics and Microengineering*, 6, pp. 352–358, 1996.

Bibliography

[187]   http://www.macrosensors.com/BBP_BBT.html.

[188]   http://www.microstrain.com/displacement/s-dvrt.

[189]   http://www.philtec.com/products/targetmotion.html.

[190]   http://www.mtiinstruments.com/products/accumeasure5000.aspx.

[191]   http://www.lionprecision.com/capacitive-sensors/cap-products.html.

[192]   G. Binnig, C. F. Quate and Ch. Gerber, "Atomic Force Microscope", vol. 56, no. 9, pp. 930–934, 1986.

[193]   http://www.scu.edu/engineering/centers/nano/upload/Dimension3100D-Manual.pdf.

[194]   W. Denk and W. W. Webb, "Optical measurement of picometer displacements of transparent microscopic objects", *Applied Optics*, vol. 29, no. 16, pp. 2382–2391, 1990.

[195]   S. Yang and T. Saif, "Micromachined force sensors for the study of cell mechanics".*Review of Scientific Instruments*, 76, 044301, 2005.

[196]   J. Rajagopalan, A. Tofangchi and M. T. A. Saif, "Linear High-Resolution BioMEMS Force Sensors With Large Measurement Range", *Journal of Microelectromechanical Systems*, vol. 19, no. 6, pp. 1380–1389, 2010.

[197]   C.J. Anthony, J. Bowen, G. Torricelli, E.L. Carter, M.C.L. Ward, C. Binns, "AFM characterisation of silicon-on-insulator push-in plates for Casimir force measurements", *Micro & Nano Letters*, vol. 3, no. 1, pp. 7–11, 2008.

[198]   J. A. Harley and T. W. Kenny, "A High-Stiffness Axial Resonant Probe for Atomic Force Microscopy", *Journal of Microelectromechanical Systems*, vol. 10, no. 3, pp. 434–441, 2001.

[199]   http://www.lot-qd.de/files/downloads/femtotools/eu/microforcesensors/FT-S_Microforce_Sensing_Probes_eu.pdf.

[200]   http://www.novatechloadcells.co.uk/ds/f329.htm.

[201]   http://www.xidex.com/images/stories/PDF_Files/Force_Sensor_End_Effector110321.pdf.

[202]   http://www.femtotools.com/index.php?id=technology-probe.

[203]   http://www.standa.lt/products/catalog/vacuum_compatible_stages?item=378&prod=Vacuum_Compatible_Motorised_Translation_Stages_DC&print=1.

[204]   http://www.newmarksystems.com/linear-positioners/nls4-series.

[205]   http://www.newport.com/Agilis-Series-Piezo-Motor-Driven-Linear-Stages/685167/1033/info.aspx#tab_Specifications.

[206]   http://www.attocube.com/attomotion/industrial-line/ecs3030.

[207]   "Agilis™ Series: Piezo Motor Driven Components", Available at http://assets.newport.com/webDocuments-EN/images/UsrMan-AG-UC2-UC8-Agilis-PiezoComp.pdf.

[208]   http://www.lewvac.com.

[209] http://en.wikipedia.org.

[210] https://www.alfa.com/en/GP140W.pgm?task=product&srchtyp=ELEM&PSvalue=Al uminum%20foil&element=Al&group=972.00000.

[211] http://www.mcmaster.com/#aluminum-foil/=vafr84.

[212] http://asm.matweb.com/search/SpecificMaterial.asp?bassnum=MQ304A.

[213] Minhang Bao, "Analysis and Design Principles of MEMS Devices", 1st edition, Elsevier, The Netherlands, 2005.

[214] S. Kalpakjian and S.R. Schmid, "Manufacturing Processes for Engineering Materials", 5th edition, Pearson Education, 2005.

[215] http://www.adhesivesresearch.com/wp-content/uploads/2013/10/8154-Data-Sheet.pdf.

[216] http://www.goodfellow.com/catalogue/GFCat4I.php?ewd_token=5zAC71K1JH9x7Y OFvHqMA82H3upgEl&n=jUtitQ6rhZkhHxgO9o08r8dvJiUtrJ&ewd_urlNo=GFCatS eaReb6&Catite=ES301820&CatSearNum=2.

[217] http://www.futek.com/files/pdf/Product%20Drawings/lrf400.pdf.

[218] http://www.keyence.com/products/measure/laser-1d/lk-g5000/models/lk-h022/index.jsp.

[219] "_active vibration isolation desktop unit halcyonics_micro series". Available at: http://www.halcyonics.de/sales-support/downloads/halcyonics-product-line/flyer_halcyonics__micro_series.pdf.

[220] http://www.sgt-nl.com/Labtools.aspx.

[221] http://www.fluigent.com/microfluidic-flow-control-system.

[222] G. P. Sutton and O. Bibilarz, "Rocket Propulsion Elements", 7th Edition, Willey-Interscience Publication, 2001.

[223] A. Anis, "Cold Gas Propulsion System – An Ideal Choice for Remote Sensing Small Satellites", Chapter 20 in "Remote Sensing - Advanced Techniques and Platforms", Edited by B. Escalante, ISBN 978-953-51-0652-4, 2012.

[224] T. J. Craft, L. J. W. Graham and B. E. Launder, "Impinging jet studies for turbulence model assessment − II. An examination of the performance of four turbulence models", *International Journal of Heat and Mass Transfer*, vol. 36, issue 10, pp. 2685–2697, 1993.

[225] P. J. Lamont and B. L. Hunt, "The impingement of underexpanded, axisymmetric jets on perpendicular and inclined flat plates", *Journal of Fluid Mechanics*, vol. 100, issue 03, pp. 471−511, 1980.

[226] S. Ashforth-Frost, K. Jambunathan, C. F. Whitney, "Velocity and turbulence characteristics of a semiconfined orthogonally impinging slot jet", *Experimental Thermal and Fluid Science*, vol. 14, issue 1, pp. 60–67, 1997.

[227] K. Jambunathan, E. Lai, M. A. Moss and B.L. Button, "A review of heat transfer data for single circular jet impingement", *International Journal of Heat and Fluid Flow*, vol. 13, issue 2, pp. 106–115, 1992.

[228] J. W. Gauntner, P. Hrycak, J. N. B. Livingood, "Survey of literature on flow characteristics of a single turbulent jet impinging on a flat plate", NASA Technical Note, NASA TN D-5652, 1970.

[229] C. duP. Donaldson and R. S. Snedeker, "Study of free jet impingement. Part 1. Mean properties of free and impinging jets", *Journal of Fluid Mechanics*, vol. 45, issue 02, pp. 281−319, 1971.

[230] P. Hill and C. Peterson, "Mechanics and Thermodynamics of Propulsion", 2nd Edition, Addison-Willey Publishing Company, 1992.

[231] S. Hoffman and J. J. Janos, "Force due to air and helium jets impinging normal to a plat plate for near-vacuum and sea-level ambient pressures", NASA TN D-7002, NASA Langley Research Centre, 1971.

[232] http://www.keithley.com/products/dcac/dmm/broadpurpose/?mn=2000.

[233] http://www3.imperial.ac.uk/pls/portallive/docs/1/7293024.PDF

[234] Agilent 33220A arbitrary waveform generator datasheet, Available at http://literature.cdn.keysight.com/litweb/pdf/5988-8544DEE.pdf.

[235] MCP9700 Datasheet, Available at http://ww1.microchip.com/downloads/en/DeviceDoc/21942e.pdf.

[236] "MODEL SR850 DSP lock-In Amplifier", Available at http://www.thinksrs.com/downloads/PDFs/Manuals/SR850m.pdf.

[237] "SMC 3 port solenoid valve catalog", Available at http://content2.smcetech.com/pdf/V100.pdf.

[238] http://www.thinksrs.com/products/PS300.htm.

[239] O. Bunemann, T. E. Cranshaw and J. A. Harvey, "Design of Grid Ionization Chambers", *Canadian Journal of Research*, 27 a(5) pp. 191−206, 1949.

[240] D. G. Courtney and H. Shea, "Accounting for Fragmentation in Time of Flight Spectroscopy Based Calculations of Ionic Electrospray Thruster Performance", Accepted in *Journal of Propulsion and Power*.

[241] E. V. Kornelsen, "The Ionic Entrapment and Thermal Desorption of Inert Gases in Tungsten for Kinetic Energies of 40 EV to 5 KEV", *Canadian Journal of Physics*, vol. 42, issue 2, pp. 364-381, 1964.

[242] P. Kisliuk, "The sticking probabilities of gases chemisorbed on the surfaces of solids", *Journal of Physics and Chemistry of Solids*, vol. 3, issue 1−2, pp. 95–101, 1957.

[243] http://www.srim.org.

[244] P. C. Stangeby, "The Plasma Boundary of Magnetic Fusion Devices", *Institute of Physics*, Bristol, England, U.K., 2000.

[245] O. Almén and G. Bruce, "Collection and sputtering experiments with noble gas ions", *Nuclear Instruments and Methods*, vol. 11, pp. 257–278, 1961.

[246] O. Almén and G. Bruce, "Sputtering experiments in the high energy region", *Nuclear Instruments and Methods*, vol. 11, pp. 279–289, 1961.

[247] P. Sigmund, "Recollections of fifty years with sputtering", *Thin Solid Films*, vol. 520, issue 19, pp. 6031–6049, 2012.

[248] M. Gamero-Castaño and M. Mahadevan, "Sputtering yields of Si, SiC, and B4C under nanodroplet bombardment at normal incidence", *Journal of Applied Physics*, 106, 054305, 2009.

[249] "Properties and Characteristics of Graphite", May 2013, Entegris Inc, Available at: https://www.entegris.com/resources/assets/6205-7329-0513.pdf.

[250] http://www.mgchemicals.com/downloads/tds/tds-839-l.pdf.

[251] N. Boutroy, Y. Pernel, J. M. Rius, F. Auger, H. J.von Bardeleben, J. L. Cantin, F. Abel, A Zeinert, , C. Casiraghi and A.C. Ferrari, J. Robertson, "Hydrogenated amorphous carbon film coating of PET bottles for gas diffusion barriers", *Diamond & Related Materials*, 15 pp. 921 – 927, 2006.

[252] R. P. Doerner, D. G.Whyte and D. M. Goebel, "Sputtering Yield Measurements During Low Energy Xenon Plasma Bombardment," *Journal of Applied Physics*, vol. 93, no. 9, pp. 5816–5823, 2003.

[253] S. K. Vashist and P. Vashist, "Recent Advances in Quartz Crystal Microbalance-Based Sensors", *Journal of Sensors*, vol. 2011, article ID 571405, 13 pages, 2011.

[254] D. Spence, E. Ehrbar, N. Rosenblad, N. Demmons, T. Roy, S. Hoffman, D. Williams, V. Hruby and C. Tocci, "Electrospray Propulsion Systems for Small Satellites", Paper SSC13-VII-5, Small Satellite Conference, 2013.

Curriculum Vitae

Subha Chakraborty

Address :	15 Av. de la Gare, Neuchatel 2000, Switzerland
Contact no:	(+41) 79 488 2210
E-mail id:	subha.chakraborty@epfl.ch
Institute :	lmts.epfl.ch
Nationality:	Indian

Academic Background:

(2011 to 2015):	**PhD candidate** at the **Microsystems for Space Technologies Laboratory (LMTS), IMT-EPFL, Neuchatel, Switzerland**.
	Thesis title: **"An Electrostatic Ion-guide and a High-resolution Thrust-stand for Characterization of Micro-propulsion Devices"**.
	Thesis advisor: **Prof. H. Shea**
(2008 to 2011):	**Master of Science** at **Indian Institute of Technology, Kharagpur, India**.
	Thesis title: **"Study of Electrostatically actuated surface micro-machined cantilevers and their application in digital logic gates"**
(2003 to 2006):	**Bachelor of Technology** at **Institute of Radio Physics and Electronics, University of Calcutta**
	Focus: **Microelectronics, micro-optics, RF and microwave engineering**
(2000 to 2003):	**Bachelor of Science** at **University of Calcutta;**
	First class Honours in **Physics.**

Professional experience

Microsystems for Space Technologies Laboratory (LMTS), EPFL:

- **Time of Flight Mass Spectrometer** with an **ion-guide**
  - **Time of flight mass spectrometer** development for high sensitivity mass-spectrometry.
  - **Ion-guide-based ion-focusing technique** for maximizing detectability

- o **High voltage switching** and **detection circuit** and **test setup automation**
- o **Ion trajectory simulations, Matlab, Comsol Multiphysics, Solidworks, Circuit simulators.**
- **Nano-Newton thrust measurement setup development for microsatellites.**
  - o Development of a compact novel **nano-Newton thrust bench** using MEMS force sensor for **characterizing microthrusters**.
  - o **Ultra-low-noise** thrust stand with a 10 nN resolution.
- **Micro-fabrication experience**
  - o Experience in **optical lithography, wet-etching, dry etching (DRIE), porous silicon process.**
  - o Experience in **Laser micromachining**, **chip bonder**, **spot-welding**.

Indian Institute of Technology, Kharagpur, India

- **Design** and **characterization** of **surface-micromachined logic gates.**
- Expertize in **MEMS simulation** tools (**CoventorWare**, **COMSOL**)
- Hands-on experience in **Laser Doppler vibrometry (LDV), Scanning electron microscopy (SEM), wafer prober, wire bonder.**

Indian Space Research Organization

- Worked as a **Scientist** in **Laboratory for Electro-optics Systems** (LEOS), **Indian Space Research Organization** (ISRO) for two years from 2006 to 2008 in the field of spacecraft sensors.
- Worked on **Charge Coupled Device** (**CCD**) based **Star Sensors**.
- Electro-optical characterization of CCD, electronic driving circuit development for Star Sensor.

Publication:

Journals & Letters

1) Subha Chakraborty, Caglar Ataman, Daniel G. Courtney, Simon Dandavino, Herbert Shea**, "A ToF-MS with a Highly Efficient Electrostatic Ion Guide for Characterization of Ionic Liquid Electrospray Sources"**, *Journal of The American Society for Mass Spectrometry*, vol. 25, issue 8, pp 1364-1373, 2014.

2) Subha Chakraborty and T. K. Bhattacharyya, "**Development of surface micro-machined binary logic inverter for ultra-low frequency MEMS sensor applications**", *Journal of Micromechanics and Microengineering,* **IOP,** 20 (2010) 105026 (15pp).

3) S. Chakraborty and T. K. Bhattacharyya, "**Solution of Euler-Bernoulli equation using a semi-analytical technique for steady state deflection of microelectromechanical cantilever under electrostatic actuation**", *Micro & Nano Letters,* **IET,** vol. 5, issue 4, pp. 215–218, 2010.

4) S. Chakraborty, K.B.M. Swamy, S. Sen, T. K. Bhattacharyya, "**An experimental analysis of electrostatically vibrated array of polysilicon cantilevers**", *Microsystem Technologies,* **Springer,** vol. 16, no. 12, pp. 2131–2145, 2010**.**

5) Subha Chakraborty, A. Bhattacharya and T.K. Bhattacharyya, "**An experimental analysis of pull-out voltage of electro-statically actuated micro-cantilever beam based on contact-stiction model**", *Micro & Nano Letters*, Vol. 6, Iss. 1, pp. 43–47, 2011**.**

6) S. Dandavino, C Ataman, C N Ryan, S Chakraborty, D Courtney, J P W Stark and H Shea, "**Microfabricated electrospray emitter arrays with integrated extractor and accelerator electrodes for the propulsion of small spacecraft**", *Journal of Micromechanics and Microengineering,* 24(2014), 075011, (13pp).

Conferences

1) Subha Chakraborty Simon Dandavino, Caglar Ataman, Daniel G. Courtney and Herbert Shea, "**Development of a ToF setup with an ion-guide for characterization of electrospray microthrusters**", *International Electric Propulsion Conference (IEPC 2013).*
(Sessions best paper award)

2) S. Chakraborty, C. Ataman, S. Dandavino and H. Shea, "**Microfabrication of an Electrospray Thruster for small spacecrafts**", **PowerMEMS 2012**, Atlanta, GA, USA, pp. 528-531, 2012.

3) Subha Chakraborty and T. K. Bhattacharyya, *"***Development of MEMS based Universal Gate for Signal Processing Circuit in Low Frequency Sensor Applications***", IEEE TechSym 2010*, Kharagpur, India, April 3rd to April 4th, 2010, pp: 129-136.

4) S. Chakraborty, A. Ray Chaudhuri, Tarun. K. Bhattacharyya, "**Design and Analysis of MEMS Cantilever Based Binary Logic Inverter**", *IEEE International Conference on Advances in Computing, Control, and Telecommunication Technologies, ACT 2009,* Trivandrum, December 2009, pp: 184-188.

5) S. Chakraborty, A. Ray Chaudhuri, Tarun. K. Bhattacharyya, "**Transient Analysis of MEMS Cantilever Based Binary Inverter and Design of a Ring Oscillator**", *4th International Conference on Computers & Devices for Communication CODEC-09,* Kolkata, December 2009, pp: 1-4.

6) Subha Chakraborty and T. K. Bhattacharyya, *"***Development of Surface-micromachined Binary Logic Gate for Low Frequncy Signal Processing in MEMS based Sensor Applications***", MicroTech Conference and Expo, 2010*, CA, USA, June 21-25, 2010, paper id: 1502.

7) Subha Chakraborty and Tarun Kanti Bhattacharyya, "**A novel surface micro-machined voltage comparator for mixed signal operation in MEMS sensor**"**,** accepted in 11th *International Symposium on RF MEMS and RF Microsystems (MEMSWAVE)*, Otranto, Italy, 28th-30th June 2010, paper id: MEMS_S2_2.

8) Subha Chakraborty and Tarun Kanti Bhattacharyya, "**Development of a Micro-Mechanical Logic Inverter for Low Frequency MEMS Sensor Interfacing**", **accepted** in **IEEE VLSI conference** to be held from 2nd Jan to 7th Jan in Chennai, India.

9) **S.** Dandavino**,** C. Ataman, S. Chakraborty, H. Shea, C. Ryan, and J. P. W. Stark, **"Design and fabrication of the thruster heads for the MicroThrust MEMS electrospray propulsion system". 33rd International Electric Propulsion Conference,** Washington, D.C., USA., pp. 1–8, 2013.
(Sessions best paper award)

10) S. Dandavino**,** C. Ataman, S. Chakraborty, H. Shea, C. Ryan and J. P. W. Stark, **"Progress Towards a Miniaturized Electrospray Thruster for Propulsion of Small Spacecraft", 48th AIAA/ASME/SAE/ASEE Joint Propulsion Conference and Exhibit,** Atlanta, USA,